Superconducting Cavities for Circuit Quantum Electrodynamics

A Dissertation
Presented to the Faculty of the Graduate School
of
Yale University
in Candidacy for the Degree of
Doctor of Philosophy

by
Matthew James Reagor

Dissertation Director: Professor Robert J. Schoelkopf

December 2015

Superconducting Cavities for Circuit Quantum Electrodynamics

Matthew James Reagor

2015

The components of a circuit Quantum Electrodynamics (cQED) system are mesoscopic and engineered. As a consequence, strong interactions are nearly automatic, making cQED a viable platform for quantum information processing. However, strong interactions also persist to the unintended elements that originate from the engineering of any device. These spurious interactions decohere a cQED system and will ultimately limit the performance of future superconducting quantum processors. This thesis explores novel architectures for cQED that eliminate decoherence. We leverage three-dimensional (3D) microwave cavities to shape resonant fields into low-loss configurations. Previously, such techniques have resulted in highly coherent superconducting qubits. We extend this approach to realize a novel quantum memory for qubits based on superconducting cavity resonators. Our cavity memory architecture exceeds millisecond lifetimes for superpositions that are written by a superconducting qubit to the memory. This type of device will enable future studies of fault-tolerant quantum information processing with highly coherent, resource efficient memory systems, as well as fundamental tests of quantum optical dynamics.

Contents

List of Figures

List of Tables

Acknowledgements

In compiling these acknowledgments, I am humbled by the cast of people I have been fortunate enough to call friends. I owe a great deal to Robert Schoelkopf. As my thesis advisor, Rob introduced me to superconductors, microwave circuits, and low-noise measurements. Rob has taught me how to ask questions, how to simplify problems, and how to work out the details of an experiment with the big picture in focus.

I am indebted to Michel Devoret for being so generous with his time and brilliance. Walking into Michel's office has always been a personal thrill, and walking out has always meant a wonderful, fleeting sense of enlightenment. Daniel Prober has been a mentor to me since my first day in Becton. His active fostering of the best possible culture among the research groups here has been instrumental to all of our achievements. Luigi Frunzio has a genuine passion for teaching and made the work in this thesis possible. Without Luigi, I would have ended up doing theoretical physics. I would then have been lucky to know Liang Jiang. Liang can explain difficult concepts with remarkable ease, and his creativity shines through in every conversation. In addition, I would like to thank all of the above colleagues, as well as Konrad Lehnert, for participating in the preparation of this thesis.

I would like to thank Wolfgang Pfaff for teaching me how to run an experiment with thoughtfulness and organization; how to write and manage useful code; how to illustrate beautiful plots and figures; and how to have a good time doing it all. Working alongside Wolfgang has been an absolute pleasure for the last few years. When Reinier Heeres arrived at Yale, he completely disrupted the software infrastructure of the lab, and I feel lucky to have learned cQED experiments in the post-Heeres era. Besides his depth of knowledge from software to fabrication and more, Reinier also possesses an honest

frankness that has elevates discourse. Jacob Blumoff and Kevin Chou have always the first people I turn to when I needed a second opinion, on anything. They are awesome people to solve problems with. Few people have had as much impact on how I think about Josephson junctions and quantum mechanics as Zaki Leghtas and Gerhard Kirchmair. It has been inspiring to work with folks who approached concepts (that I thought I already knew) with a radically different framework.

Uri Vool and Michael Hatridge were always happy to listen to new results, provide feedback, and give encouragement too, which has picked me up many times throughout this thesis. Teresa Brecht has always had aptitude for hard technical problems. Her dedication and skill is inspiring. I would especially like to thank 'Uncle' Chris Axline who has saved my dogs from trouble on an uncountable number of occasions. He has also been a remarkable labmate (e.g. Chris built an emergency operating system for the physical infrastructure of our building). In addition, Chris has contributed his a phenomenal talent on various hardware collaborations. Eric Holland has been a friend who I can talk through any situation with, and I am truly indebted to him for listening to ups and downs and helping me keep a level head. Maria Rao and Giselle DeVito have made the fourth floor of Becton feel like a second home. I have shared that home with too many great colleagues for me to recognize all of their important contributions here.

I had the good fortune to spend time with Eric Dufresne, Joseph Zinter, Jean Zheng, and Larry Wilen, as well as many talented staff members, in my capacity as a teaching fellow in the Center for Engineering Innovation and Design. Piggybacking off their awesome classes, I have worked on problems from gastrointestinal surgery to regulating climate for leaf-cutter ants. Those experiences have shaped my character in profound ways.

Finally, I would like to thank my family for their love and support. My wife, Jennifer Reagor, has been a part of this journey since its beginning. Her support has been a constant source of joy throughout.

Publication list

This thesis is based in part on the following publications:

1. H. Paik, D. I. Schuster, L. S. Bishop, G. Kirchmair, G. Catelani, A. P. Sears, B. R. Johnson, M. J. Reagor, L. Frunzio, L. I. Glazman, S. M. Girvin, M. H. Devoret, and R. J. Schoelkopf, 'Observation of High Coherence in Josephson Junction Qubits Measured in a Three-Dimensional Circuit QED Architecture,' Physical Review Letters 107, 240501 (2011),

2. M. Reagor, H. Paik, G. Catelani, L. Sun, C. Axline, E. Holland, I. M. Pop, N. A. Masluk, T. Brecht, L. Frunzio, M. H. Devoret, L. Glazman, and R. J. Schoelkopf, 'Reaching 10 ms single photon lifetimes for superconducting aluminum cavities,' Applied Physics Letters 102, 192604 (2013).

3. Z. Leghtas, S. Touzard, I. M. Pop, A. Kou, B. Vlastakis, A. Petrenko, K. M. Sliwa, A. Narla, S. Shankar, M. J. Hatridge, M. Reagor, L. Frunzio, R. J. Schoelkopf, M. Mirrahimi, and M. H. Devoret, 'Confining the state of light to a quantum manifold by engineered two-photon loss,' Science 347, 853 (2015).

4. E. T. Holland, B. Vlastakis, R. W. Heeres, M. J. Reagor, U. Vool, Z. Leghtas, L. Frunzio, G. Kirchmair, M. H. Devoret, M. Mirrahimi, and R. J. Schoelkopf, 'Single-photon Resolved Cross-Kerr Interaction for Autonomous Stabilization of Photon-number States,' In press at Physical Review Letters (2015).

5. T. Brecht, M. Reagor, Y. Chu, W. Pfaff, C. Wang, L. Frunzio, M. H. Devoret, and R. J. Schoelkopf, 'Demonstration of Superconducting Micromachined Cavities,' Applied Physics Letters 107, 192603 (2015).

6. M. Reagor, W. Pfaff, C. Axline, R. W. Heeres, N. Ofek, K. Sliwa, E. Holland, C. Wang, J. Blumoff, K. Chou, M. J. Hatridge, L. Frunzio, M. H. Devoret, L. Jiang, and R. J. Schoelkopf, 'Quantum Memory with Near-Millisecond Coherence in Circuit QED,' ArXiv e-prints (2015), 1508.05882 [quant-ph].

CHAPTER 1

Introduction

Heike Kamerlingh Onnes began seeking applications for superconductivity soon after he discovered the effect. Kamerlingh Onnes believed that his coils, which carried electrical currents without resistance, could act as permanent magnets of arbitrarily large strength [1]. Such magnets could in turn spawn new discoveries and technologies. When Kamerlingh Onnes's coils were looped on themselves, they could sustain currents at near-Ampere levels long after their generation. For a demonstration at London's Royal Society, Kamerlingh Onnes's coils were shown to be strongly magnetic after being transported by plane (in liquid helium) from Kamerlingh Onnes's Leiden laboratory, where the currents had been generated [2]. Yet, Onnes's magnets would always decay, eventually. To his frustration, Kamerlingh Onnes found that his superconducting coils had finite current-carrying capacity too, breaking-down sharply at some threshold currents. For the remainder of his career, Kamerlingh Onnes made incremental progress with increasingly pure samples and new superconductors toward his goal of more powerful superconducting magnets [1].

We celebrated the 100^{th} anniversary of Kamerlingh Onnes's discovery in 2011. We recognize now that Kamerlingh Onnes's threshold currents were critical magnetic field effects. These would only be explained after World War I, and Kamerlingh Onnes's retirement. The vision of useful superconducting magnets was eventually fulfilled though: they are now found in most hospitals, where they enable life-saving MRI scans.

Superconductivity is a great example of a quantum mechanical phenomenon that can be used for improving a classical technology. The effect's quantum description can be completely ignored in most applications. Engineers can swap copper wire for superconducting wire with minor woes. Indeed, Onnes was ignorant of, but confident in, the quantum mechanical description of supercurrents [2]. For emerging quantum technologies, such as quantum-enhanced metrology, cryptography, or computational systems, the end-user must purposefully control the quantum evolution of system.

In many ways, makers of quantum technologies benefit from more than a century of quantum mechanics. We take for granted that the 'spookiness' [3] has largely been removed from the conversation. However, the path to universal quantum computation traverses untested physics*. No experiment has yet shown that the fundamental tenets quantum error correction are correct [4], and further, that they will persist to the logical error levels required for large quantum algorithms [5]. Already though, the pursuit of quantum information science has inspired new ways of thinking about other physical systems, such as the interplay of quantum error correction and black holes [6].

In many ways, this thesis continues in Kamerlingh Onnes's tradition. We are still fabricating superconducting circuits and finding new techniques to extend the persistence of their currents. There are a few key differences though. For one, Kamerlingh Onnes coils had an inductance of nearly 10 mH. They thus sustained flux of approximately 10 mWb, or twelve orders of magnitude larger than the magnetic flux quantum ($h/2e \approx$2 fWb), which sets the scale of most experiments on quantum circuits. A second, crucial difference here is that at these small excitation levels, circuits can oscillate with many phases at once, quantum mechanically.

This thesis concerns the onset of quantum effects in circuits and how they may be leveraged to take precision measurements of quantum processes and for performing quantum computation. In particular, we argue that harmonic oscillators can be remarkable objects and demonstrate their application as coherent quantum memories for superconducting circuits.

* Though, perhaps it is encouraging that Helium was only discovered on Earth a decade after Kamerlingh Onnes began his pursuit of absolute zero.

1.1 Overview of this thesis

We see how circuits can behave quantum mechanically in Chapter 2. We find that purely linear circuit elements are relatively boring objects, beyond the existence of a noisy ground state in these systems. However, adding nonlinearity to a resonant circuit gives it color [7]. Superconducting circuits can acquire strong nonlinearities from the Josephson effect [8]. We present a modern, detailed description of the arguably simplest Josephson quantum circuit, the transmon [9, 10]. By examining the response of this circuit to resonant and detuned drives, we show how a transmon can be treated as an artificial atom. Finally, we show how coupled Josephson circuits can lead to an interesting conditional nonlinearity that is also a hallmark of Cavity Quantum Electrodynamics (CQED) [11].

Motivated by the existence of nonlinear coupling, we show how otherwise-linear circuits can be remarkable quantum objects in Chapter 3. Linearity provides the means to excite many degrees of freedom in these systems at once, and each quanta of energy in the circuit adds new capacity for quantum information [12, 13]. We describe how such systems can be measured and controlled via a conditional nonlinearity. The consequence of decoherence mechanisms in these systems is also important. We argue that particular states of linear circuits could be used to defeat these loss mechanisms with an oscillator-based scheme for quantum error correction.

Next, we study the physical realization of these circuits in Chapter 4, considering four types of linear resonators in detail: coplanar transmission line resonators, rectangular waveguide cavities, cylindrical waveguide cavities, and coaxial $\lambda/4$ cavities. We present each resonant mode structures and sensitivity to various loss mechanisms to understand its dissipation. As architectures for implementing circuit QED, we weigh the benefits and trade-offs of each system. We conclude the chapter with the design of a robust cavity quantum memory, based on one of these resonators.

In Chapter 5, we discuss the experimental techniques for the individual design, fabrication, and characterization of these circuit elements. We provide details on how superconducting cavity resonators are prepared in order to minimize their dissipation. Then, we describe the techniques for extracting the resonator's quality from circuit-network analysis. Finally, we present an overview of how transmons are fabricated and measured.

Putting all of these ideas together, this thesis culminates in the experimental realization of a transmon strongly coupled to a highly coherent cavity quantum memory, Chapter 6. We describe the calibration and characterization of the coupled system. The chapter

includes measurement techniques for extracting of the cavity's lifetime and coherence. In particular, we trace two important decoherence effects in the cavity to the transmon. The results in this chapter pave the way for implementing many of the ideas in Chapter 3.

We conclude this thesis, Chapter 7, with an outlook on coherence in cQED and future experiments with these systems. In particular, we consider leveraging the full atom-like capabilities of transmons, as described in Chapter 2, as an opportunity to achieve more precise control over nearly-linear, highly coherent quantum circuits.

CHAPTER 2

Circuit QED

Circuit Quantum Electrodynamics (cQED) is a toolbox for implementing nontrivial quantum circuits that can be precisely designed and controlled. We begin this chapter by putting the quantum mechanics of circuits on solid theoretical footing. We first describe how the circuit operators of voltage and flux can be quantized. Then, the theoretical framework of the Josephson effect and its realization as a nonlinear circuit element is introduced. Finally, we show how circuits coupled with Josephson elements can achieve QED effects.

This chapter benefits from a long history of excellent theses and pedagogical reviews on the subject of Josephson quantum circuits. In particular, the beginning of this chapter closely follows the seminal work by Devoret [7] and especially the recent treatment by Girvin [14]. We rely on this foundation to advance a modern description of QED as a natural consequence the Josephson effect beginning in Section 2.3.2. By treating our cQED system as a 'Black Box' [10], we are able to describe driven, coupled, nonlinear, quantum circuits with a single framework. The consequence (Section 2.4) is an intuitive set of quantum behaviors and 'selection rules' for a circuit that can potentially possess many degrees of freedom.

In order to explore the rich behavior of a single cQED system (an otherwise-linear circuit with one Josephson element), this chapter does not review the many other types of

quantum circuits or superconducting qubits in detail. For this purpose, we refer the reader to the reviews by Clarke and Wilhelm [15] and also the review by Devoret and Schoelkopf [16].

2.1 Building blocks of cQED

Circuits made of capacitors and inductors have equivalent descriptions in mechanical systems of masses and springs. We use that analogy throughout this section to justify our intuition and make connections to other experimental techniques. For instance, voltage (V) and flux (Φ) are collective phenomena. Typically in a circuit, a countless number of charge carriers generate our measured V or Φ. Fortunately, we are able to abstract away the microscopic forces that act on these solid-state charge carriers. This is analogous to treating a many-atom chunk of material as a single mass with a single momentum: as long as the inter-mass dynamics (lattice vibrations) occur at a sufficiently high frequency, we can approximate these modes to be their ground state. Indeed, for aluminum circuits, the equivalent modes (plasma oscillations of free charge carriers) occur at frequencies above $\omega/2\pi \gtrsim 10^{15}$ Hz [17], five orders of magnitude higher frequencies than we consider here in this thesis. The collective motion approximation is therefore well justified.

Superconductivity plays the vital role of suppressing dissipation in our circuits. Perhaps more importantly, an ideal superconductor also gives us access to a dissipationless nonlinear circuit element, which we describe in Section 2.2. In both of these cases, the gap of the superconductor (Δ) gives us another ground state to consider, allowing more rigor to the collective motion approximation [18]. The gap of our circuit's superconductor also sets a limit to the temperatures and excitation energies that can be used [18]. The frequencies associated with the break down of superconductivity are much smaller than the onset of plasma oscillations considered above. When working with aluminum for instance, drives above $\omega/2\pi \gtrsim 2\Delta/h$ ($\approx 80 - 100$ GHz for aluminum) can efficiently excite quasiparticles above the gap.

Our operating frequencies are bounded below by the requirement that our resonant circuits be in their quantum mechanical ground states. To achieve a Boltzmann factor suppression of the first excited state to approximately one percent, we require then that $\omega/2\pi \gtrsim 5k_BT$. At the operating temperatures of a commercial dilution refrigerator ($T \sim 20$ mK), that requirement translates to $\omega/2\pi \gtrsim 2$ GHz. These considerations therefore place our quantum circuits squarely in the microwave domain.

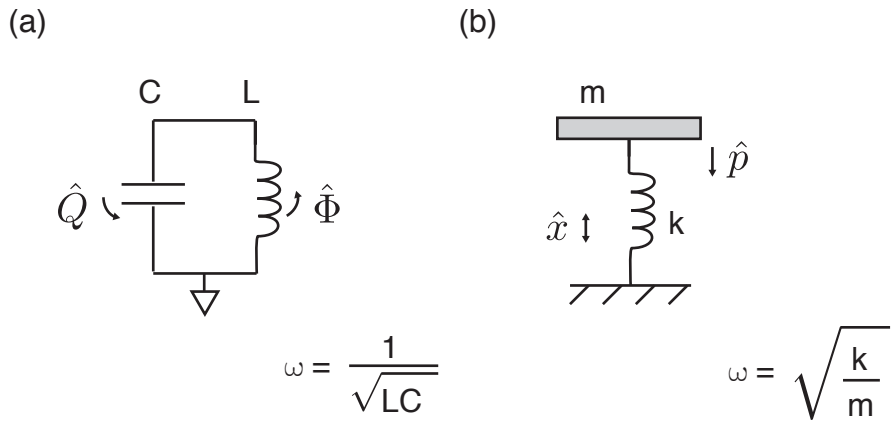

Figure 2.1: Quantum harmonic oscillators. **(a)** An electrical harmonic oscillator is constructed by placing a capacitor (C) in parallel with an inductor (L). The conjugate variables that describe the resulting oscillation are the charge on the capacitor $\hat{Q}$ and flux through the inductor $\hat{\Phi}$. The natural frequency of this oscillator is related to these two circuit elements by $\omega = 1/\sqrt{LC}$. **(b)** The analogous mechanical circuit to the LC oscillator is a simple mass-spring system with mass m and inverse-spring constant k^{-1}. In this oscillator, the displacement of the spring $\hat{x}$ and the momentum of the mass $\hat{p}$ form the equivalent conjugate variables to the system as charge and flux in the electrical circuit. The mechanical oscillator has the resonant frequency $\omega = \sqrt{k/m}$.

2.1.1 The quantized circuit

To quantize a circuit we proceed in the canonical fashion [7, 14] by finding a Hamiltonian for the system and its conjugate variables, which will become our quantum operators. The foundational circuit to this thesis is the linear oscillator (Fig. 2.1). This circuit combines a capacitor (C) in parallel with an inductor (L). On resonance, energy sloshes between a charging energy ($E_C = Q^2/2C$) and an inductive energy ($E_L = \Phi^2/2L$). For the mass-spring system, energy likewise oscillates between kinetic energy ($p^2/2m$) and potential energy ($x^2/2k^{-1}$). Combining the circuit's kinetic energy (E_C) and potential energy (E_L) terms to form a Lagrangian [14] gives

$$\mathcal{L} = \frac{Q^2}{2C} - \frac{\Phi^2}{2L}. \tag{2.1}$$

Because these elements share a node in the circuit, we can use the flux-voltage relation [7]

$$\Phi(t) \equiv \int_{-\infty}^{t} V(\tau)d\tau = \int \frac{Q(\tau)}{C}d\tau \tag{2.2}$$

to rewrite the charging energy as

$$\mathcal{L} = \frac{C\dot{\Phi}^2}{2} - \frac{\Phi^2}{2L}. \tag{2.3}$$

We recognize that flux through the inductor ($\Phi = L\dot{Q}$) is the conjugate variable of charge [14], since

$$\frac{\delta\mathcal{L}}{\delta\dot{\Phi}} = L\dot{Q} = \Phi. \tag{2.4}$$

Therefore, we have a classical Hamiltonian for this circuit that is

$$H = \Phi\dot{Q} - \mathcal{L} = \frac{\Phi^2}{2L} + \frac{Q^2}{2C}. \tag{2.5}$$

Now, we are now ready convert these variables to quantum mechanical operators (e.g. $\Phi \Rightarrow \hat{\Phi}$) and the Hamiltonian as well ($H \Rightarrow \hat{H}$). Additionally, we can factor Equation 2.5, using

$$\hat{x}^2 + \hat{y}^2 = (\hat{x} + \imath\hat{y})(\hat{x} - \imath\hat{y}) - \imath\left[\hat{x}, \hat{y}\right] \tag{2.6}$$

to eventually simplify our circuit's description, now giving

$$\hat{H} = \left(\frac{\hat{\Phi}}{\sqrt{2L}} + \imath\frac{\hat{Q}}{\sqrt{2C}}\right)\left(\frac{\hat{\Phi}}{\sqrt{2L}} - \imath\frac{\hat{Q}}{\sqrt{2C}}\right) - \frac{\imath}{2\sqrt{LC}}\left[\hat{Q}, \hat{\Phi}\right]. \tag{2.7}$$

The conjugate relationship between flux and charge in Equation 2.4 gives us the commutation rules for free as $\left[\hat{Q}, \hat{\Phi}\right] = -\imath\hbar$ [7]. The symmetric form of Equation 2.7 suggests defining a simpler operator $\hat{a}$ such that

$$\hat{a} = \frac{1}{\sqrt{\hbar\omega}}\left(\frac{\hat{\Phi}}{\sqrt{2L}} - \imath\frac{\hat{Q}}{\sqrt{2C}}\right), \tag{2.8}$$

where $\omega \equiv 1/\sqrt{LC}$. This substitution wonderfully allows us to recast the Hamiltonian [14] as

$$\hat{H} = \hbar\omega\left(\hat{a}^\dagger\hat{a} + \tfrac{1}{2}\right). \tag{2.9}$$

We recognize this Hamiltonian as a simple harmonic oscillator with a frequency ω, and

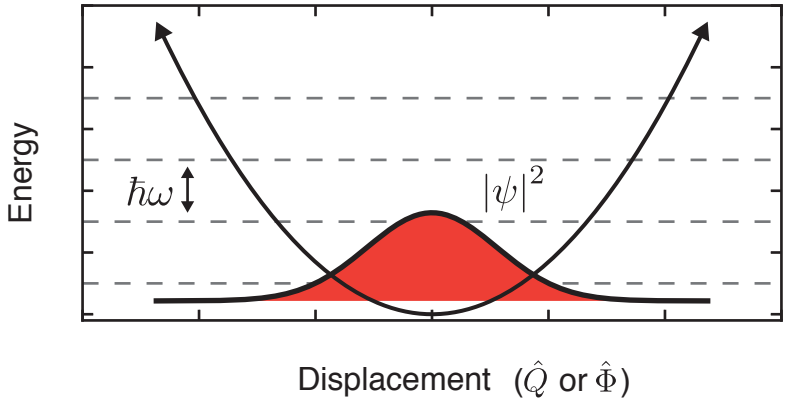

Figure 2.2: Energy levels of the quantum harmonic oscillator. The quadratic potential yields evenly spaced energy eigenstates ($\Delta E = \hbar\omega$). The ground state of the system is Gaussian distributed in the conjugate variables of motion, e.g. charge $\hat{Q}$ and flux $\hat{\Phi}$. Note that the circuit has finite probability $|\psi|^2$ of being detected at a nonzero value of $\hat{Q}$ or $\hat{\Phi}$ for the ground state. This phenomenon is known as zero-point fluctuations of the circuit and leads to a number of important consequences as we see in this chapter.

where the operator $\hat{a}$ is the annihilation operator and $\hat{a}^\dagger\hat{a} = \hat{n}$, the number operator. Further, we can invert Equation 2.8 and its Hermitian conjugate [14] to rewrite the flux through the inductor and charge on the capacitor as

$$\hat{\Phi} = \sqrt{\frac{\hbar Z}{2}}\left(\hat{a}^\dagger + \hat{a}\right) \tag{2.10a}$$

$$\hat{Q} = -\imath\sqrt{\frac{\hbar}{2Z}}\left(\hat{a}^\dagger - \hat{a}\right), \tag{2.10b}$$

where $Z = \sqrt{L/C}$ is the impedance of the circuit.

It is worth pointing out that the relationship between circuits and mechanical degrees of freedom is more than an analogy. The first experiments to explore the ideas of Quantum Non-Demolition (QND) measurements were attempts to observe gravitational waves in the excitation of massive mechanical oscillators, transduced by LC oscillators [19] as

$$\hat{H} = \frac{\hat{p}^2}{2m} + \frac{1}{2}m\hat{x}^2 + \frac{\hat{\Phi}^2}{2L} + \frac{\hat{Q}^2}{2C} + \hbar g\hat{x}\hat{Q}. \tag{2.11}$$

where the term interaction term $\hat{H}_{int} = \hbar g \hat{x} \hat{Q}$ is created by the mass being suspended between two plates of a capacitor; displacing the mass changes the capacitor's charge distribution. Today, electromechanical systems are exploiting this coupling term in to explore the quantum dynamics of massive objects [20].

We now turn to solving for the ground state of the LC oscillator, which will prepare us for studying driven circuits in Section 2.1.3 and nonlinear LC systems in Section 2.3.

2.1.2 Gaussian states in an LC oscillator

As for all harmonic oscillators, our circuit acquires non-zero variance of charge and flux, even in its ground state, i.e.

$$\langle 0|\hat{\Phi}^2|0\rangle \equiv \Phi_{\text{ZPF}}^2 \neq 0. \tag{2.12}$$

These zero-point fluctuations can be related to the flux quantum ($\Phi_0 \equiv h/2e$) and the resistance quantum ($R_{\text{Q}} \equiv h/2e^2$) [7] as

$$\Phi_{\text{ZPF}} = \Phi_0 \sqrt{\frac{Z}{2\pi R_{\text{Q}}}} \tag{2.13a}$$

$$Q_{\text{ZPF}} = e \sqrt{\frac{R_{\text{Q}}}{2\pi Z}}. \tag{2.13b}$$

The circuit's impedance therefore determines the relative strength of these fluctuations. We recognize in Equation 2.13 that a low impedance circuit has less flux noise but more charge noise.

The shape of ground state wave function ($|\psi_0\rangle$) is interesting as well [21]. If we make use of the differential operator in quantum mechanics, e.g. $\hat{Q} = -\imath\hbar\,(\partial/\partial\Phi)$, then the statement $\hat{a}|\psi_0\rangle = 0$ can be written as

$$\left(\frac{\Phi}{\sqrt{2L}} + \frac{\hbar}{\sqrt{2C}}\frac{\partial}{\partial\Phi}\right)|\psi_0(\Phi, Q)\rangle = 0. \tag{2.14}$$

A similar expression holds for Q, and both of these equations have a Gaussian solution. When normalized, this gives for the ground state

$$|\psi_0(\Phi, Q)\rangle = \frac{1}{\sqrt{2\pi\Phi_{\text{ZPF}}Q_{\text{ZPF}}}} \times e^{-(\Phi^2/4\Phi_{\text{ZPF}}^2 + Q^2/4Q_{\text{ZPF}}^2)} \tag{2.15}$$

Because the Gaussian distribution is normalized by the zero-point fluctuations, it is often

convenient to describe the circuit in a dimensionless quadrature representation as

$$\hat{X} \equiv \frac{1}{\sqrt{\hbar Z}} \times \hat{\Phi} = \frac{1}{\sqrt{2}} \left(\hat{a} + \hat{a}^\dagger\right) \tag{2.16a}$$

$$\hat{Y} \equiv \sqrt{\frac{Z}{\hbar}} \times \hat{Q} = -\imath \frac{1}{\sqrt{2}} \left(\hat{a} - \hat{a}^\dagger\right), \tag{2.16b}$$

such that which simplifies the wave function of the ground state to a highly symmetric two-dimensional Gaussian form

$$|\psi_0(X,Y)\rangle = \frac{1}{\sqrt{2\pi}} \times e^{-(X^2+Y^2)/4}. \tag{2.17}$$

The ground state is only one eigenvector of $\hat{a}$. Actually, there are infinitely many such solutions of the form

$$\hat{a}\,|\psi\rangle = \alpha\,|\psi\rangle \tag{2.18}$$

where α is a complex number. All of these wavefunctions are Gaussian distributed in (X,Y) with the same standard deviation as the ground state, but have some displaced centroid $(X_0, Y_0) = (\Re(\alpha), \Im(\alpha))$ as

$$|\psi(X,Y)\rangle = \frac{1}{\sqrt{2\pi}} \times e^{-((X-X_0)^2+(Y-Y_0)^2)/4}. \tag{2.19}$$

These states are given the name coherent states [22], and such states play a number of important roles in this thesis.

We can use the eigenvector relation (Eq. 2.18) to learn about the photon statistics of a coherent state. In particular, knowing the complex eigenvalue α gives us the ability to exactly describe the distribution of the state across the entire Hilbert space of the mode. To see how, we begin by stating the eigenvalue relationship more precisely in Fock-space [21],

$$\hat{a}\,|\alpha\rangle = \hat{a} \sum_n C_n\,|n\rangle = \alpha\,|\alpha\rangle\,. \tag{2.20}$$

Using the definition of the annihilation operator, $\hat{a}\,|n\rangle = \sqrt{n}\,|n-1\rangle$, we have that

$$C_n = \frac{\alpha}{\sqrt{n}} C_{n-1} = \frac{\alpha^2}{\sqrt{n(n-1)}} C_{n-2} = \ldots = \frac{\alpha^n}{\sqrt{n!}} C_0. \tag{2.21}$$

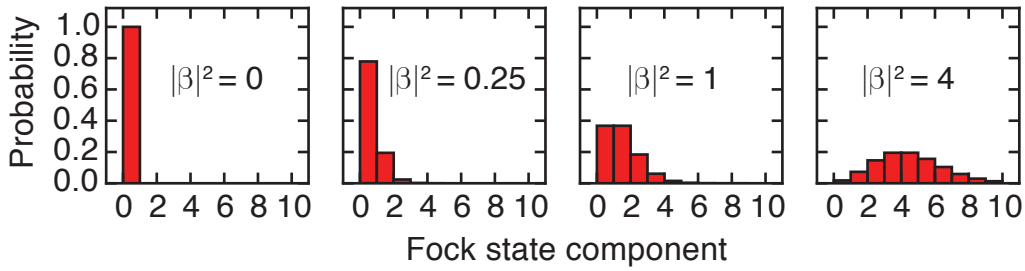

Figure 2.3: Photon number statistics of coherent states. The probability of the oscillator to contain exactly n photons (P_n) for coherent states of amplitude β is a discrete Poisson distribution, truncated here for visibility at $N = 10$. The distribution broadens at larger displacements since the variance is equal to the mean number of photons $|\beta|^2$.

Then, we can express the coherent state in the Fock basis as

$$|\alpha\rangle = \exp(-|\alpha|^2/2) \sum_n \frac{\alpha^n}{\sqrt{n!}} |n\rangle, \tag{2.22}$$

where the normalization factor is found by the constraint that $\sum |C_n|^2 = 1$Equation 2.22 can be used to calculate any expectation value of the field quadratures. For instance, the probability of detecting a coherent state in a specific Fock state $|m\rangle$ (P_m) is Poisson distributed as

$$|C_m|^2 = \exp(-|\alpha|^2) \frac{|\alpha|^{2m}}{m!}. \tag{2.23}$$

The mean photon number $\bar{n}$ can also be calculated from the distribution of P_m to be

$$\bar{n} \equiv \langle \alpha | \hat{a}^\dagger \hat{a} | \alpha \rangle = |\alpha|^2. \tag{2.24}$$

Equation 2.20 can further be used to show that two coherent states also have a variance of their number distribution $\Delta n^2 = \bar{n}$; that such states minimize quadrature uncertainties ($\Delta X^2 \Delta Y^2 = 1/4$); and that they form an overcomplete set of states on the Hilbert space of the mode.

In the next subsection, we describe how these states are the natural consequence of classical drives.

2.1.3 Arbitrary classical drives on linear circuits

In this section, we consider the effect of an arbitrary, but linear, classical drive on an LC oscillator. Such a drive can only take a coherent state in the oscillator, e.g. its ground state, to another coherent state [23]. That transformation be can described by a unitary operator, called the displacement operator [22],

$$\hat{D}(\alpha)|0\rangle = |\alpha\rangle, \tag{2.25}$$

where α is the amplitude of the displacement and $|\alpha|^2$ is the resulting average photon occupancy.

A derivation for the form of the displacement operator that is particularly useful for our purposes is given by Girvin [14]. Consider that, as discussed in Section 2.1.2, any coherent state is equivalent to the vacuum state up to a transformation of coordinate systems. Therefore, a finite amplitude coherent state is at the origin of some X', Y' plane. We have confidence then that we can obtain a precise description of $\hat{D}(\alpha)$ by requiring that this operator offsets the coordinate system of a state by $-\alpha$ but otherwise leaves it unaffected. Following Girvin, for this type of transformation, we can use Taylor's theorem that for a function of one variable

$$f(x) = f(a) + f'(a)\,(x-a) + \frac{f''(a)}{2}\,(x-a)^2 + ... \tag{2.26}$$

Furthermore, we can express this infinite series equivalently as an exponentiated differential operator, a form attributed to Lorentz, as

$$f(x) = e^{(x-a)\frac{d}{dx}} f(x)\Big|_{x=a}. \tag{2.27}$$

For a given initial state wave function, $|\beta\rangle$, transforming the coordinates by $\hat{X} \Rightarrow \hat{X} - \alpha$ can be written explicitly [14] as

$$\hat{D}(\alpha)|\beta\rangle = \exp(-\alpha\frac{d}{dX})|\psi(X)\rangle\Big|_{X=\beta}. \tag{2.28}$$

We use that $Y = (\imath/2)(d/dX)$ to write the displacement operator as

$$\hat{D}(\alpha)|\beta\rangle = \exp(-2\imath\alpha\hat{Y})|\beta\rangle = \exp(-\alpha(\hat{a} - \hat{a}^\dagger))|\beta\rangle. \tag{2.29}$$

We can show a number of interesting properties about $\hat{D}$, but perhaps the most important is to check that $\hat{D}$ on the vacuum state produces the correct coherent state. We rewrite the displacement operator in a more convenient form $\hat{D}(\alpha) = \exp(-|\alpha|^2)\exp(+\alpha\hat{a}^\dagger)\exp(-\alpha\hat{a})$ [22]. Since $\hat{a}|0\rangle = 0$, we only have to keep the $\hat{a}^\dagger$ terms:

$$\hat{D}(\alpha)|0\rangle = \exp(-|\alpha|^2)\exp(+\alpha\hat{a}^\dagger)|0\rangle, \tag{2.30}$$

and we use a Taylor series in the exponentiated operator [21] to yield

$$\begin{aligned}\hat{D}(\alpha)|0\rangle &= \exp(-|\alpha|^2)\sum_n \frac{\left(+\alpha\hat{a}^\dagger\right)^n}{n!}|0\rangle \\ &= \exp(-|\alpha|^2)\sum_n \frac{\alpha^n}{\sqrt{n!}}|n\rangle\end{aligned} \tag{2.31}$$

which is indeed the same form for $|\alpha\rangle$ as Equation 2.22.

A formal proof that Gaussian states of circuits are only trivially affected by an arbitrary drive is adapted from [23] in Appendix A. However, an intuitive toy model is as follows. Consider an arbitrary current source coupled to the flux of our inductor as shown in Figure 2.4. The evolution of the circuit will be governed by

$$\hat{H}(t) = \hbar\omega\hat{a}^\dagger\hat{a} - I(t)\hat{\Phi} = \hbar\epsilon(t)\hat{\Phi} \tag{2.32}$$

where we have introduced ϵ in order to work with more convenient units. We proceed by taking a rotating frame to remove the harmonic oscillator term [11], leaving

$$\hat{H}_1(t) = \hbar\epsilon(t)\tilde{\Phi}, \tag{2.33}$$

where now $\tilde{\Phi}$ has rotating ladder operators $\tilde{a} = \hat{a}e^{-\imath\omega t}$.

Any physical drive, i.e. presenting finite dissipation to the circuit, will result in a drive that is a differentiable function. Therefore, we can find an infinitesimally small time δt over which the Hamiltonian is approximately time independent. The circuit, initialized in some coherent state $|\beta_0\rangle$, will therefore evolve via the unitary propagator

$$|\beta_{\delta t}\rangle = \hat{U}_{drive}|\beta_0\rangle \approx e^{-\imath\hat{H}\delta t/\hbar}|\beta_0\rangle = e^{-\imath\epsilon_0\delta\tilde{\Phi}}|\beta_0\rangle \tag{2.34}$$

Under these conditions, the propagator is cast as a displacement operator with $\delta\alpha = \epsilon_0\delta t$. Then, the tilde on $\hat{\Phi}$ simply determines the angle of the displacement. Taking many

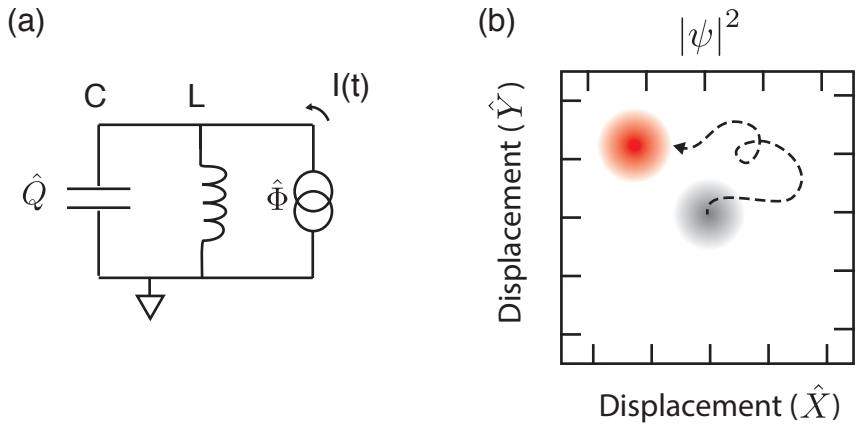

Figure 2.4: Effect of an arbitrary drive on a damped oscillator. (a) An LC oscillator is biased with a time-dependent current drive. Here, damping is provided by the finite input impedance of the current source. The driving current couples to the conjugate flux variable to add a potential to the system as $\hat{H}_{drive}(t) = -I(t)\hat{\Phi}$. The resulting state of the resonator can be shown to be a coherent state for all times. **(b)** The probability of detecting the oscillator at a given displacement ($\hat{X}$,$\hat{Y}$) is shown (red) for a given trajectory of $I(t)$. The linear bias pushes the oscillator from its ground state (grey) to some coherent state $|\beta\rangle$. However, at all times this trajectory can be equally described by displacing the origin of the resonator along the dashed line. The oscillator remains in its ground state while the axes $\hat{X}, \hat{Y}$ are translated. Nonlinearity is needed in the system to create more interesting states.

snapshots of this process, we can build up the trajectory of an arbitrary drive. Furthermore, we will always be stuck in a minimum uncertainty Gaussian state that resembles the quantum vacuum.

In the next section, we meet our first nonlinear circuit element, the Josephson junction. Such an element allows for even simple drives to generate states of our circuit that exhibit striking quantum mechanical properties, markedly different than the simple noise addition of the uncertainty principle.

2.2 Josephson junctions

A Josephson tunnel junction is created by sandwiching a thin insulating layer between two superconductors [8]. Supercurrents tunneling between the two superconductors obey the

Josephson equations [18, 24]. In particular, the current and voltage across the barrier is related to the phase difference between the two superconductors (δ) as

$$I = I_0 \sin\varphi \tag{2.35a}$$

$$\frac{d\varphi}{dt} = \frac{2\pi V}{\Phi_0} \tag{2.35b}$$

where the constant of proportionality I_0 is the critical current of the junction. We will describe later how such tunnel junctions are made in the practice (Section 5.2.1). For now, we focus on the new types of circuits we can make with this element.

2.2.1 Nonlinear inductance

Clearly, the Josephson relations are nonlinear. To see how such a junction can act like an inductor, consider the definition of inductance, $L \equiv V/\dot{I}$. Taking the time-derivative of the current-phase relation (Eq. 2.35a) gives

$$\frac{dI}{dt} = I_0 \cos\phi \times \frac{d\varphi}{dt} = \frac{2\pi I_0 V}{\Phi_0}\cos\varphi \tag{2.36}$$

where we have used the second Josephson relation (Eq. 2.35b) to compute the time-derivative of the phase [7]. These simple calculations allow us to define the Josephson inductance L_J as

$$L_J = \frac{\Phi_0}{2\pi I_0 \cos\varphi}. \tag{2.37}$$

Often, the $\cos\varphi$ term is ignored to quote a 'Josephson inductance' value for a given tunnel junction (L_0) in nH. For the typical devices we will discuss in this chapter, $L_0 \approx 1-10\,\text{nH}$.

Many quantum circuits make use of the full sinusoidal capabilities provided by the Josephson effect [25, e.g. and references therein]. However, we restrict ourselves in this thesis to the small phase ($\varphi \ll 1$) limit. In that limit, we have an inductance that is approximately

$$L_J \approx \frac{\Phi_0}{2\pi I_0}\left(1 + \frac{\varphi^2}{2} + \mathcal{O}(\phi^4)\right). \tag{2.38}$$

The effective inductance of a Josephson junction increases at higher phase bias. This is shown schematically in Figure 2.5. We could imagine constructing an LC oscillator using such a circuit element as the inductor. Then, the resonant frequency of the circuit should

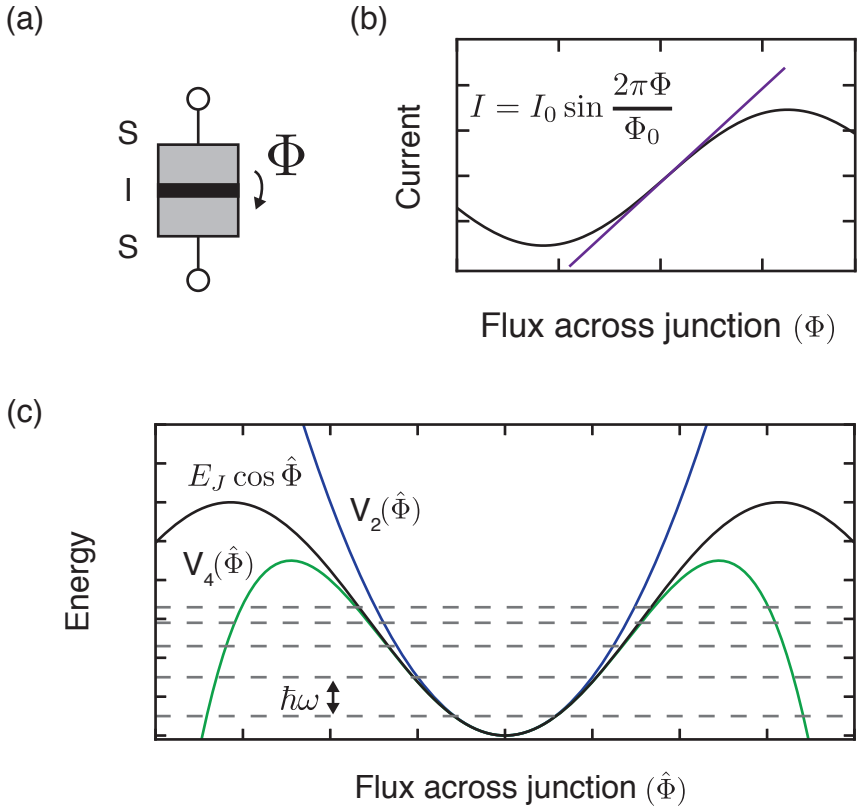

Figure 2.5: Josephson effect as a circuit element. (a) A Josephson junction is formed by separating two superconducting electrodes by a small layer of insulating material. The resulting junction serves as a nonlinear circuit element. **(b)** The current-flux relationship of the Josephson effect is sinusoidal. We can ascribe an inductance to our new circuit element as $L_J \equiv \Phi/I$, which is linear to first order (purple). At larger values of Φ the linear term over-estimates the inductance of the junction. **(c)** The basic sinusoidal potential leads to low-lying energy states that have an anharmonic spectrum. The successive approximations to this potential are a quadratic $V_2(\hat{\Phi})$ and quartic $V_4(\hat{\Phi})$ Hamiltonian terms described in this chapter.

depend on amount of energy circulating in it. Remarkably, that intuition describes the quantum properties of such a circuit, as we will see next.

2.2.2 Quantized Josephson effects

It is often more convenient to work in the flux basis when evaluating the behavior of the Josephson element [7]. We can equally describe the phase across the junction as a flux

$$\Phi = \Phi_0 \varphi. \tag{2.39}$$

We can then quantize phase on an equal footing to charge and flux as before, i.e. $\hat{\varphi} = \hat{\Phi}/\Phi_0$ [7]. Furthermore, the energy added to our system by a current and voltage at a junction is given by $\Phi_0 I$, or

$$\hat{H}_J = -E_J \cos\left(\hat{\Phi}/\Phi_0\right), \tag{2.40}$$

where

$$E_J = \frac{\Phi_0^2}{2\pi L_0} \tag{2.41}$$

is the Josephson energy. In the small flux limit limit ($|\langle\hat{\Phi}\rangle| \ll \Phi_0$), we can expand the cosine Hamiltonian of the Josephson junction in higher order operator terms with rapidly decreasing magnitude [10], as

$$\hat{H}_J \approx E_J \left[1 - \frac{1}{2}\left(\frac{\hat{\Phi}}{\Phi_0}\right)^2 + \frac{1}{4!}\left(\frac{\hat{\Phi}}{\Phi_0}\right)^4 + ...\right] \tag{2.42}$$

The small flux limit is satisfied for

$$\bar{n}\frac{\Phi_{\mathrm{ZPF}}}{\Phi_0} \ll 1. \tag{2.43}$$

Recalling that $\Phi_{\mathrm{ZPF}} \propto \sqrt{Z}$ (Eq. 2.13), we see that this limit can be satisfied for small impedances in addition to small $\bar{n}$.

In the next section, we will see that the fourth order term in this expansion is sufficient to give an LC oscillator full Hilbert state addressability [10], alleviating the problems of simple harmonic circuits.

2.3 Quantum Josephson circuits

This thesis relies on the nonlinearity of Josephson elements to address individual transitions of quantized circuits as if they were artificial atoms [26, e.g. and references therein] . The many other uses of Josephson junction circuits for quantum mechanical applications, such

as quantum limited amplifiers [27, e.g.], lossless frequency converters [28], or reconfigurable circulators [29], is beyond the scope of this chapter.

In addition, we will describe a single type of Josephson atom, the transmon, in detail. However, there are many other realizations of artificial atoms using Josephson circuits. We refer the reader to the reviews in [15, 16, and references therein] for information about these devices.

2.3.1 Black Box Quantization of a Josephson circuit

One of the simplest Josephson circuits is shown in Figure 2.6. A clever scheme to approximately diagonalize this circuit by leveraging the small-phase limit was introduced by Nigg [10] and is called Black Box Quantization (BBQ). For the circuit in Figure 2.6, the small-phase limit is equivalent to the large-capacitance limit since $Z \propto C^{-1/2}$. The idea in [10] is to treat the linear part of the junction and accompanying circuit ($\hat{H}_0$) separately from the nonlinear part of the junction ($\hat{H}_{nl}$). We proceed by finding the normal modes of the circuit (ω_0's) and then introducing the nonlinearity later as a perturbation. More precisely,

$$\hat{H} = \frac{\hat{\Phi}^2}{2L} + \frac{\hat{Q}^2}{2C} + \hat{H}_{nl} = \hbar\omega_0 \hat{a}^\dagger \hat{a} + \hat{H}_{nl}, \tag{2.44}$$

where the nonlinear part of the Hamiltonian ($\hat{H}_{nl}$) is given by

$$\hat{H}_{nl} = E_J \left[1 - \cos(\hat{\varphi})\right] - \frac{E_J}{2}\varphi^2. \tag{2.45}$$

It is important to note that up to charging effects (see Section 2.3.2), Equation 2.44 is still exact. From here, treating the nonlinearity as a perturbation will be a powerful tool to solving the dynamics of our circuit. In particular, Equation 2.43 gives a prescription for how many terms in this expansion we need to keep. The majority of thesis, and also the majority of cQED, concerns the lowest order terms in the nonlinear Hamiltonian [9], terms proportional to φ^4. However, at the conclusion of this chapter, we show how the neglected terms can be enhanced.

The circuit in Figure 2.6 is an ideal transmon artificial atom [30]. In the next section, we show show how the nonlinearity of the Josephson junction allows us to address its individual levels and later, how to operate the transmon as a qubit [9, 31].

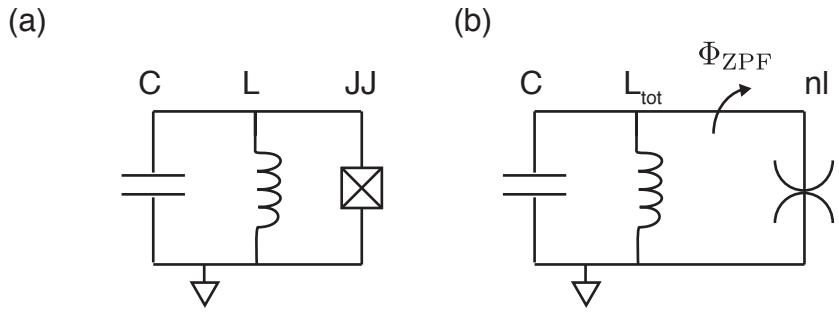

Figure 2.6: Quantizing the Josephson LC oscillator. **(a)** A parallel LC oscillator is shunted by the nonlinear admittance of a Josephson junction (box element). **(b)** The effect of the Josephson junction is separated into two components, the linear term is absorbed into the the total inductance of the LC oscillator, and a new element is introduced (spider element) that contains only the nonlinear terms of the junction's response to flux ($\hat{H}_{\mathrm{nl}}$) [10]. The solution to the Hamiltonian is determined, up to a scaling term E_J, by the magnitude of zero point fluctuations in the flux variable, or equivalently, the impedance of the LC resonator, provided that the charging energy is negligible.

2.3.2 Transmon artificial atoms

The circuit in Fig. 2.6 is susceptible to low-frequency charge offsets since the junction presents a high impedance tunnel barrier to unpaired electrons. This offset charge shifts the total charge operator by $\hat{Q} \Rightarrow \hat{Q} + Q_{ofs}$ in Equation 2.44. The perturbation ($\hat{H}_Q$) on the Hamiltonian is two new terms

$$\hat{H}_Q = \frac{(\hat{Q} + Q_{ofs})^2}{2C} - \frac{\hat{Q}^2}{2C} = \left(\frac{Q_{ofs}}{C}\right)\hat{Q} + \frac{(Q_{ofs})^2}{2C}. \tag{2.46}$$

The first term on the right hand side of the final expression accounts for the static voltage induced by the offset charge. The second is a renormalization of the energy that could be discarded, unless the offset charge is fluctuating, which is always observed experimentally [32, e.g.]. Charge fluctuations cause dephasing for our circuit. These effects can be solved for analytically, as discussed in detail [30], but, by working in the large capacitance limit, we become exponentially insensitive to these charge offsets. This limit, where

$$E_J \gg Q_{ofs}^2/2C \sim e^2/2C \equiv E_C, \tag{2.47}$$

is called the transmon limit. For $E_J \lesssim E_C$, this is known as a Cooper Pair Box (CPB) charge qubit [33] and is sensitive to charge noise.

2.3.3 Driving a transmon atom

What is the fate of our nonlinear circuit under the drive we considered for the LC oscillator in Section 2.1.3? The total Hamiltonian for the driven transmon atom is similar to original expression (Eq.2.32), except with the addition of an $\hat{H}_{nl}$ term (Eq. 2.45) of the junction. Now, the driven system evolves under

$$\hat{H} = \hbar\omega\hat{a}^\dagger\hat{a} - \hbar\epsilon(t)(\hat{a} + \hat{a}^\dagger) + E_J\left[1 - \cos(\hat{\varphi})\right] - \frac{E_J}{2}\hat{\varphi}^2, \tag{2.48}$$

where the driving term is equivalent to Equation 2.32. Because of the cosine term, this system evolves in a nontrivial manner.

Let us proceed by assuming a sinusoidal drive at ω_d. To calculate the effect of this drive, let us perform the following transformations (for details, see for instance [34]). First, we go into a rotating frame of the transmon ω. This is accomplished by the unitary operator [11],

$$\hat{U} = \exp(+\imath\omega t\hat{a}^\dagger\hat{a}), \tag{2.49}$$

which transforms our Hamiltonian as

$$\tilde{H} = \hat{U}\hat{H}\hat{U}^\dagger + \hat{U}\left[-\imath\frac{d}{dt}, \hat{U}\right]. \tag{2.50}$$

The resulting Hamiltonian is

$$\tilde{H} = \hat{H}_1 + \hat{U}\hat{H}_{nl}\hat{U}^\dagger \tag{2.51}$$

where $\hat{H}_1$ is our previous driven LC oscillator Hamiltonian (Eq. 2.33). Therefore, we have only to calculate the evolution of the nonlinear part of the Hamiltonian,

$$\tilde{H}_{nl} = e^{\imath\omega t\hat{a}^\dagger\hat{a}}\hat{H}_{nl}e^{-\imath\omega t\hat{a}^\dagger\hat{a}}. \tag{2.52}$$

We can rewrite the cosine term as

$$\cos\hat{\varphi} = \frac{1}{2}\left(e^{\imath\hat{\varphi}} + e^{-\imath\hat{\varphi}}\right). \tag{2.53}$$

Note that each of these exponential functions resembles a displacement operator, such

that

$$e^{\imath\hat{\varphi}} = e^{\imath\varphi_0(\hat{a}+\hat{a}^\dagger)}, \tag{2.54}$$

which has the same form as $\hat{D}(\imath\varphi_0)$ for a real number φ_0. Working with the exponential form simplifies calculations significantly since a displacement about any angle θ is still a displacement. More explicitly,

$$e^{i\theta\hat{a}^\dagger\hat{a}}\hat{D}(\alpha)e^{-i\theta\hat{a}^\dagger\hat{a}} = \hat{D}(\alpha e^{-i\theta}). \tag{2.55}$$

For $\theta = \omega t$, then, we see that our rotating frame has the effect of bringing the time dependence of the rotating frame into the cosine. Defining a rotating φ operator as

$$\tilde{\varphi} = \varphi_0\left(\tilde{a} + \tilde{a}^\dagger\right), \tag{2.56}$$

we then have

$$\tilde{H}_J = E_J\cos(\tilde{\varphi}). \tag{2.57}$$

Combining these terms, we are left with the rotating frame Hamiltonian

$$\tilde{H}(t) = \hbar\epsilon(t)\left(\tilde{a} + \tilde{a}^\dagger\right) + E_J\left[1 - \cos\left(\tilde{\varphi}\right)\right] - \frac{E_J}{2}\tilde{\varphi}^2, \tag{2.58}$$

We can use another unitary transformation to enter into the displaced frame of the drive [34]. This unitary has the form

$$\hat{U}_D = e^{-\xi(t)\hat{a}^\dagger + \xi^*(t)\hat{a}} \tag{2.59}$$

where $\xi(t)$ is a displacement amplitude. If the displaced mode has an energy decay rate κ, there is a clever choice of ξ such that the frame becomes stationary [35]. That condition is satisfied for the differential equation

$$\frac{d\xi}{dt} = -\left(\frac{\kappa}{2} + \imath\omega_0\right)\xi - \imath\epsilon(t) \tag{2.60}$$

If our drive is a simple, continuous wave (CW) drive at frequency ω_d, the solution to this differential equation is

$$\xi = -\frac{\imath\epsilon_0 e^{-\imath\omega_d t}}{\kappa_0 + \imath|\omega_d - \omega_0|}. \tag{2.61}$$

The squared-amplitude $|\xi|^2$ is effectively the number of drive photons. However, the amplitude ξ itself is quickly rotating.

By choosing our displaced frame as Equation 2.60 we are left with a displaced, rotating Hamiltonian that has a readily simplified form. Without any further approximations, the driven transmon atom Hamiltonian is

$$\tilde{H} = E_J \left[1 - \cos\left(\varphi_0(\tilde{a} + \tilde{a}^\dagger + \xi + \xi^*)\right)\right] - \frac{E_J \varphi_0^2}{2}(\tilde{a} + \tilde{a}^\dagger + \xi + \xi^*)^2 \tag{2.62}$$

To see the utility of the above expression, we again work in the small φ_0 limit. Now, we can expand Equation 2.62 in powers of φ and examine the allowed transitions of the circuit, as well as other 'real atom'-like effects. We expand the cosine using the Taylor series

$$\cos\vartheta = \sum_{k=0} \frac{(-1)^k}{(2k)!}\vartheta^{2k}. \tag{2.63}$$

When expanding the Hamiltonain (Eq. 2.62), the zeroth and second order terms will drop from our expression. We are left with

$$\tilde{H} = -E_J \sum_{k=2}^{\infty} \frac{(-1)^k \varphi_0^{2k}}{(2k)!} \left(\tilde{a} + \tilde{a}^\dagger + \xi + \xi^*\right)^{2k}. \tag{2.64}$$

To make further progress, we need make a few approximations. The first is that we will in practice only want to keep a finite number of terms. In fact, the lowest order (fourth order) already provides a rich set of physics to explore [34].

$$\tilde{H} \approx -\frac{E_J \varphi_0^4}{4!} \left(\tilde{a} + \tilde{a}^\dagger + \xi + \xi^*\right)^4 \tag{2.65}$$

The binomial theorem has useful generalizations for non-commuting operators, in particular Weyl operators $\left[\hat{A}, \hat{B}\right] = 1$, such as $\hat{a}$ and $\hat{a}^\dagger$. We can normal-order a polynomial of two Weyl operators [36] using

$$\left(\hat{A} + \hat{B}\right)^n = \sum_{m=0}^{n} \sum_{k}^{\mathrm{Min}[n, n-m]} C_{nmk} \hat{B}^{m-k} \hat{A}^{n-m-k} \tag{2.66}$$

where C_{nmk} is a combinatorial coefficient, given by

$$C_{nmk} = \frac{n!}{2^k k!(m-k)!(n-m-k)!}. \tag{2.67}$$

Because $\xi(t)$ is a complex number as opposed to an operator (representing the location of the displaced frame), ξ will commute with the other Hamiltonian terms. However,

by ignoring the noise terms associated with the drive, we are working in the limit of an infinitely stiff pump.

We make our second approximation before trying to solve the resulting dynamics. In the expansion, we will only keep energy conserving terms like $\tilde{a}^\dagger\tilde{a}$ or $\xi^*\xi$, since, for these terms, the quickly rotating parts (e.g. $e^{\imath\omega t}$) cancel, making these terms stationary. In the absence of drives ($\xi = 0$), our transmon Hamiltonian reduces to

$$\tilde{H} \approx -\frac{E_J\varphi_0^4}{4}\hat{a}^\dagger\hat{a}^\dagger\hat{a}\hat{a} \equiv -\frac{K}{2}\hat{a}^\dagger\hat{a}^\dagger\hat{a}\hat{a}. \tag{2.68}$$

This is a Kerr-type nonlinearity [37, 38], where the energy spectrum of the system depends quadratically on the transition level. If we look at the difference between neighboring Fock states, the splitting increases linearly as

$$E_{n+1} - E_n = -\frac{K}{2}\left(n(n+1) - n(n-1)\right) = -nK \tag{2.69}$$

Right away, we can see that if we have narrow enough frequency resolution, we may be able to resolve such an intrinsic energy splitting in spectroscopy. In later subsections, we will show that this intuition is correct but incomplete: spectroscopy on a Kerr-medium will turn out to be much richer than Equation 2.69 would suggest.

Another way to think of the Kerr nonlinearity is to consider a mean field frame about $\langle\hat{n}\rangle \approx \bar{n}$ [11]. We can reorder the nonlinearity as

$$\tilde{H} = \frac{K}{2}\left((\hat{a}^\dagger\hat{a})^2 - \hat{a}^\dagger\hat{a}\right) \tag{2.70}$$

Going into another rotating frame, at $\omega_{\bar{n}}$, will remove the second term on the right hand side. Another way to say that is that an oscillator with a Kerr-type nonlinearity has mean-field frequency that is proportional to the energy stored in the oscillator.

In the next subsections, we consider the effects of resonant and detuned drives $\omega_d \neq \omega_0$ on the transmon. We will see how our transmon atom can be excited or acquire an AC stark shift from drives.

2.3.4 Exciting a transmon atom

While the displaced frame treated us well when we were considering steady-states of the transmon, we abandon that transformation for the moment to consider a weak ($|\epsilon_0| \ll K$), resonant drive ($\omega_d = \omega_0$). We are particularly interested in how this drive affects the atom

to lowest level approximations. In the rotating frame of the ground state and drive, we have

$$\tilde{H} \approx -\frac{\hbar K}{2}\left(\hat{a}^\dagger\hat{a}^\dagger\hat{a}\hat{a}\right) + \hbar\epsilon_0\left(\hat{a}^\dagger + \hat{a}\right). \tag{2.71}$$

In the case of the linear LC oscillator, the drive term would displace the system until reaching equilibrium with the oscillator's decay rate. However, now higher states of the transmon are detuned from the drive, i.e.

$$|\epsilon_0| \ll |\Delta_{1\to 2}| = K, \tag{2.72}$$

where $\Delta_{1\to 2}$ is the detuning between the drive frequency and the $1 \to 2$ transition. Because of this detuning, the drive only dresses the higher states of the transmon virtually, giving them an AC Stark shift (as we will see in section 2.3.4). Our weak drive cannot actually excite these higher states at all.

The result is that transmon will undergo Rabi oscillations [39], where the population cycles between the ground and first excited state of the transmon. If we ignore the dressing effects of the higher-states, we can truncate our consideration to the lowest two levels of the transmon, treating it a qubit. Indeed, working with this reduced Hilbert space allows us to recover all of the simple Pauli matrix descriptions of qubits [39]. We can define Pauli operators

$$\hat{\sigma}_x \cong \hat{X} \tag{2.73a}$$

$$\hat{\sigma}_y \cong \hat{Y} \tag{2.73b}$$

$$\hat{\sigma}_z \cong 2\hat{a}^\dagger\hat{a}, \tag{2.73c}$$

where the congruency ($\cong$) is used to call attention to the crucial exception that the creation and annihilation operators are taken to only act on the lowest two states of the Hilbert space, i.e. $\hat{a}^\dagger|1\rangle \equiv 0$.

We can recast the truncated, resonantly driven Hamiltonian in a familiar form [39], as

$$\hat{H} = \frac{\hbar\epsilon_0}{2}\hat{\sigma}_x. \tag{2.74}$$

This effect is well described as a continuous rotation about the two-level system's Bloch sphere about the x-axis. The drive takes $|g\rangle$ to $|e\rangle$ in a time

$$T_{\text{Rabi}} = \frac{2\pi}{\epsilon_0} \tag{2.75}$$

Changing the phase of $|\epsilon|e^{\imath\theta}$ changes the Bloch-sphere angle that the procession will follow, e.g. along $\hat{\sigma}_y$ for $\theta = \pi/2$. Therefore, any point on the Bloch-sphere can be reached with this simple treatment. We will examine more of the consequences of this procession later (Section 3.3.2). First though, there are a few more striking physical consequences that occur beyond the two-level atom description that are worth exploring.

Climbing the ladder

If we initialize the transmon in an excited Fock state, say the N^{th} Fock state, a choice of drive frequency can force Rabi oscillations between the $|N\rangle$ and $|N \pm 1\rangle$ states, allowing us to 'climb the ladder' of the transmon [40]. To see this, let us go into the rotating frame of given by

$$\omega_N = \omega_0 - \frac{K}{2}N(N-1). \tag{2.76}$$

If we consider just the nearest laying states we can write the undriven Hamiltonian as

$$\tilde{H}_0 = K\left[(N-1)\hat{\Pi}_{N-1} - N\hat{\Pi}_{N+1}\right], \tag{2.77}$$

where we have introduced the projection operator Π_N for simplicity, defined as

$$\hat{\Pi}_N = |N\rangle\langle N|. \tag{2.78}$$

Now, if we drive the transmon that detuned from our reference frame by $\Delta_d = \omega_d - \omega_N$, our driven Hamiltonian now has quickly oscillating terms. But, if we detune the drive by $\Delta_d = (N-1)K$ or $\Delta_d = -NK$ then we recover the two-level system description with the selected Fock state acting as $|g\rangle$ or $|e\rangle$. For example, taking $\Delta_d = -NK$ yields a similar expression to Equation 2.74 except now the Pauli matrix converts population between $|N\rangle$ and $|N+1\rangle$:

$$\tilde{\sigma}_x = |N\rangle\langle N+1| + |N+1\rangle\langle N| \tag{2.79}$$

It is clear by induction ($0 \Rightarrow 1$ and $N \Rightarrow N+1$) that all transmon levels can be reached in this fashion. In addition, because we can halt the Rabi oscillation at any point on a Bloch sphere, population can be spread across many levels of the transmon's Hilbert space, which can have arbitrary phase. The resulting state will be of the form

$$|\psi\rangle = \sum_n C_n|n\rangle. \tag{2.80}$$

However, for large states (spanning hundreds of excitations) with high symmetry, this process is cumbersome because each Fock state must be prepared individually. Later, we will see how another nonlinearity can provide some amount of parallelization to our toolbox (Section 3.3.2).

AC Stark effect in a transmon atom

The AC Stark effect describes the response of an atom to a rapidly rotating external field [41]. In this process, the atom acquires a dressing due to the detuned drive ($\Delta = \omega_d - \omega_0$), causing the spectrum of the atom to change. Dressed-state splitting has deep connections to nonlinearity. Recall that the 'spectrum' of the harmonic LC oscillator was unaffected by any drive. Observing that a circuit exhibits the AC Stark effect, as in Schuster et al. [42], is evidence that the system interacts with light in a highly nontrivial manner.

Consider Equation 2.65 with a very detuned drive ($\Delta \gg K$), such that the only terms valid in the Rotating Wave Approximation (RWA) [39] are $\hat{a}^\dagger\hat{a}$ and $\xi^*\xi$. We use the expansion coefficients (Eq. 2.67) to write down that

$$\tilde{H}_{\text{stark}}(t) \approx -\frac{K}{2}\left(\hat{a}^\dagger\hat{a}^\dagger\hat{a}\hat{a} + \hat{a}^\dagger\hat{a}|\xi(t)|^2\right). \tag{2.81}$$

Thus, the transmon has acquired a new dressed frequency that is proportional to the power contained in the AC drive. The new frequency is detuned by

$$\Delta_{\text{stark}}(t) = -\frac{K}{2}|\xi(t)|^2 \tag{2.82}$$

For a CW drive, we can use Equation 2.61 to write

$$\Delta_{\text{stark}} = -\frac{\bar{K}}{2} \times \left(\frac{\epsilon_0^2}{\kappa_0^2 + (\omega_d - \omega_0)^2}\right). \tag{2.83}$$

Essentially, even virtual photons (i.e. $|\xi(t)|^2 \gg 0$ but $|\hat{a}^\dagger\hat{a}| \approx 0$) can load the Kerr nonlinearity.

AC Stark effect in a two-level atom

In the weak driving ($\epsilon \ll K$), small detuning ($\Delta \ll K$) limit, wherein the transmon is well-approximated as a two level system, we can solve for the AC Stark effect as commonly

done for qubits [39]. The Hamiltonian is thus

$$\hat{H} = \frac{\hbar\Delta}{2}\sigma_z - \frac{\hbar\epsilon_0}{2}\sigma_x \tag{2.84}$$

The new, dressed eigenstates have energies

$$E_\pm = -\frac{\hbar\epsilon_0}{2} \pm \frac{\hbar}{2}\sqrt{\epsilon_0^2 + \Delta^2}. \tag{2.85}$$

For $\Delta \gg \epsilon_0$ we have shifted the ground state energy by

$$\delta E_- \approx \frac{\hbar\epsilon_0^2}{4\Delta^2} + \mathcal{O}\left(\frac{\epsilon_0}{\Delta}\right)^4 \tag{2.86}$$

2.3.5 Selection rules and multi-photon transitions

It turns out that we can take short cuts on our way up the ladder too. At higher order approximations, multi-photon transitions become allowed at certain drive frequencies [9]. For fourth-order approximations to our transmon atom, we will show explicitly that two-photon transitions between second-nearest neighbors is allowed. We then give a recipe for extending these ideas to arbitrary transitions, allowing us to define selection rules for our artifical atom.

For a second-order transition, we need terms in the Hamiltonian which connect second-nearest neighbors like

$$\hat{H}_{\text{two-photon}} = \hbar\epsilon_0\left((\hat{a}^\dagger)^2 + \hat{a}^2\right). \tag{2.87}$$

To see how these can come about, we start from the rotating, displaced picture at fourth-order (Eq. 2.65). There will always be terms in the binomial expansion of this Hamiltonain which have the form

$$\hat{H}_2 \propto \left(\xi^2(\hat{a}^\dagger)^2 + (\xi^*)^2\hat{a}^2\right). \tag{2.88}$$

These terms are usually thrown out by the RWA. However, consider a drive at a frequency halfway between a given Fock state and its second-nearest neighbor, $\omega_d = \frac{1}{2}(\omega_{N+2} + \omega_N) = \frac{1}{2}(\omega_N - N^2K)$. Then, two-photon terms like the above rotate at

$$\xi^2(t)(\tilde{a}^\dagger)^2 = \xi^2(\hat{a}^2)e^{2\imath(\omega_d - \omega_N)t} = \xi^2(\hat{a}^2)e^{-\imath N^2 K t} \tag{2.89}$$

But, we see that since the $|N+2\rangle$ state has an energy difference with the $|N\rangle$ state of $\delta E = -N^2K$, that time dependence is actually the correct rotating frame for the

$N \rightarrow N+2$ transition! Importantly, the selection rule is proportional to $|\xi|^2$, meaning that the Rabi rate now given by the square of the drive strength, now a function of ϵ_0^2.

In practice, this is a useful way to characterize the anharmonicity of a transmon circuit in spectroscopy [9]. At sufficiently large drive strengths (enough that ϵ_0^2 can saturate the transition), the detuning between a two-photon transition and a single-photon transition gives us value of K directly ($\Delta f = K/2$). Furthermore, this type of transition is easily distinguished from the single-photon transition because the $|\epsilon_0|^2$ dependence reduces line-broadening. Thus, the higher-order terms tend to be more narrow in spectroscopy, as shown in Section 5.2.6.

Sixth order expansion will give terms that are of the form $\xi^3(\hat{a}^3)$ and that a drive at the appropriately chosen frequency can drive this term proportional to $|\epsilon_0|^3$, and these transitions can be observed as well [43]. Indeed, all transitions of the transmon atom would be accessible by continuing this pattern. However, an $\mathcal{O}^{th}$ order transition is exponentially hard to drive. Therefore, at some high order, we will break the approximation that $\epsilon_0 \ll K$. Hence, these processes will no longer be selective. We will essentially start driving many transitions at once, instead of driving single Rabi-like oscillations in Fock-space.

2.4 Coupling quantum circuits

Adding more degrees of freedom to our circuit, in the form of additional components, can enable new functionality. For instance, circuits with multiple superconducting qubits can be used to execute quantum algorithms [44] or quantum error correction [45–48]. Moreover, circuits with dissimilar types of components [49] can be useful for applications such as quantum memory [50–52] or quantum communication [53].

One particularly important class of coupled circuits is a superconducting qubit coupled to a linear resonator. This is a scheme known as circuit QED (cQED) [54, 55] for its close analogues with Cavity QED (CQED) [11]. A cQED-type architecture protects superconducting qubits from spontaneous emission [56], allows for multi-qubit gates [57, 58], and enables high fidelity, QND measurements of qubit states [59, 60]. In this section, we describe the theory of coupled transmon-resonator circuits, closely following the approach used in Section 2.3.1 to describe a single transmon.

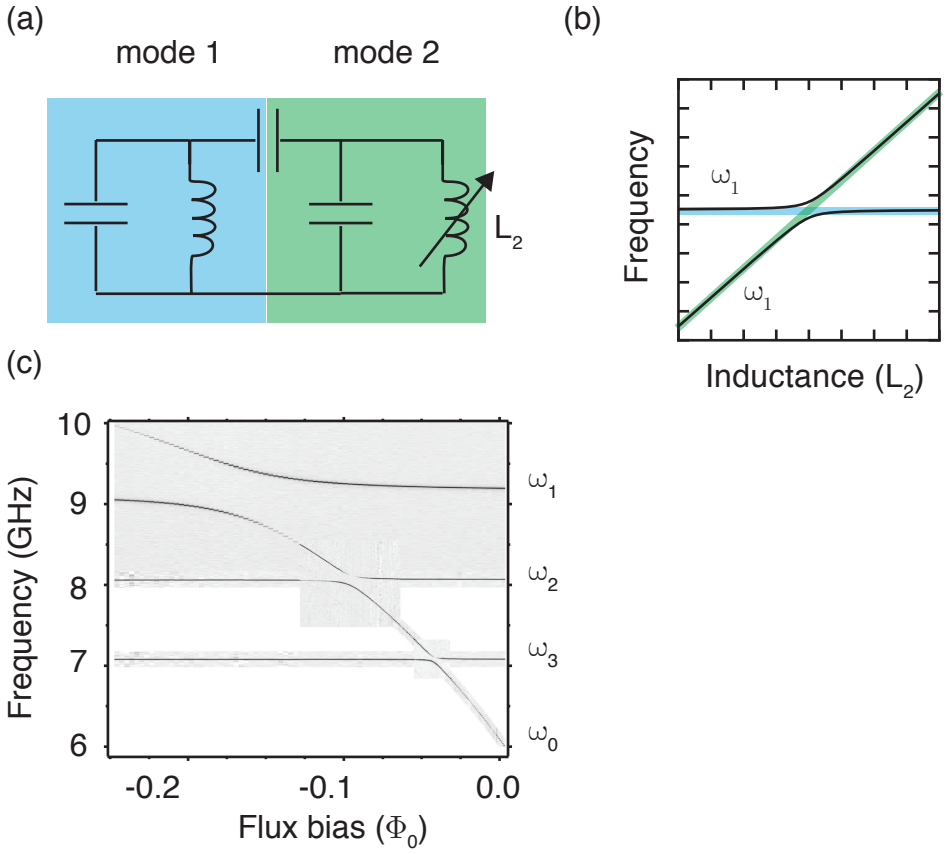

Figure 2.7: Classical dressing of a linear circuit. **(a)** Two parallel LC resonators are joined by a capacitor to form a simple coupled-circuit. Because of their interaction, neither mode preserves its independence. This effect can revealed by sweeping any circuit element, e.g. mode two's inductor L_2, and observing the new eigenmodes of the system. **(b)** The linear circuit can be exactly diagonalized. The spectrum is shown as a function of L_2, with shading representing the behavior of the two modes in the absence of coupling. The resulting eigenmodes are $\omega_\pm = (\omega_1 + \omega_2 \pm \sqrt{g^2 + \Delta^2})/2$, where Δ is the detuning and g is the coupling strength. Near resonance ($\Delta = 0$), a level repulsion of $\omega_+ - \omega_- = 2g$ is caused by the interaction. The techniques in this chapter that diagonalize linear parts of more complicated systems capture effects such as this mode-splitting. The splitting between these two LC modes is a classical effect and can be observed with standard circuit elements on printed circuit boards. **(c)** Spectroscopy data of the realization of avoided crossings in cQED. A flux-tunable transmon qubit is tuned through resonance of several other modes. The size of the avoided crossings is a classical parameter, although the evolution of the system at any of these bias points is highly quantum. (Figure used with permission from [45]. See Copyright Permissions.)

2.4.1 Black Box Quantization for many modes

The techniques for treating the Josephson nonlinearity as a perturbation can be extended to systems with many coupled elements [10]. Before (Section 2.3.1), we proceeded by diagonalizing the linear Hamiltonian, then introducing a term $\hat{H}_{nl}$ to account for a nonlinear inductance of the junction. For coupled circuits, we must solve a system of many hybridized LC modes. However, the result will always be expressible as some number of resonant modes [61], although the frequencies and characteristic impedances for an LC resonance may be altered by the coupling. The linear Hamiltonian, after this diagonalization, can therefore be written as

$$\hat{H}_{tot} = \hbar \sum_n \tilde{\omega}_n \hat{\mathcal{A}}_n^\dagger \hat{\mathcal{A}}_n \tag{2.90}$$

where $\hat{\mathcal{A}}_n$ represents the annihilation operator of the n-th, re-diagonalized mode. Because these new eigenmodes are the same as their classical counterparts (Fig. 2.7), classical circuit analysis is sufficient to solve this part of the system.

All we need now to treat the effects of our Josephson junction is the dressing of these modes as seen at the 'port' of the junction. Essentially, each mode will contribute some amount of flux toward the junction, as

$$\hat{\Phi} = \sum_n \Phi_{\mathrm{ZPF}}^n \left(\hat{\mathcal{A}}_n^\dagger + \hat{\mathcal{A}}_n \right) \tag{2.91}$$

Luckily, we already know how to find the required Φ_{ZPF}^n parameters too!

We saw earlier that the magnitude of the zero-point fluctuations was simply related to the effective impedance of the circuit by Equation 2.10a. We now see that the relevant characteristic impedance is the mode's impedance as seen by the junction. To find these zero-point fluctuation values, we simply need to determine impedance of each mode.

Imagine that we had an impedance-probe at the junction looking out, which could measure across a wide-range of frequencies. At each normal mode of the circuit, our admittance would cross zero (giving us $\tilde{\omega}_n$). Further, the slope of the admittance trace at that zero-crossing is related to the mode's effective characteristic impedance [10], as

$$\left(\frac{dY}{d\omega} \right) \Big|_{\omega=\tilde{\omega}_n} = \frac{2j}{\tilde{\omega}_n Z_{\mathrm{eff}}} \equiv Y_n' \tag{2.92}$$

By rearranging Equation 2.92, we find a simple way relate the effective impedance that sets the scale of the zero-point fluctuations to a measurable, at least in theory, circuit

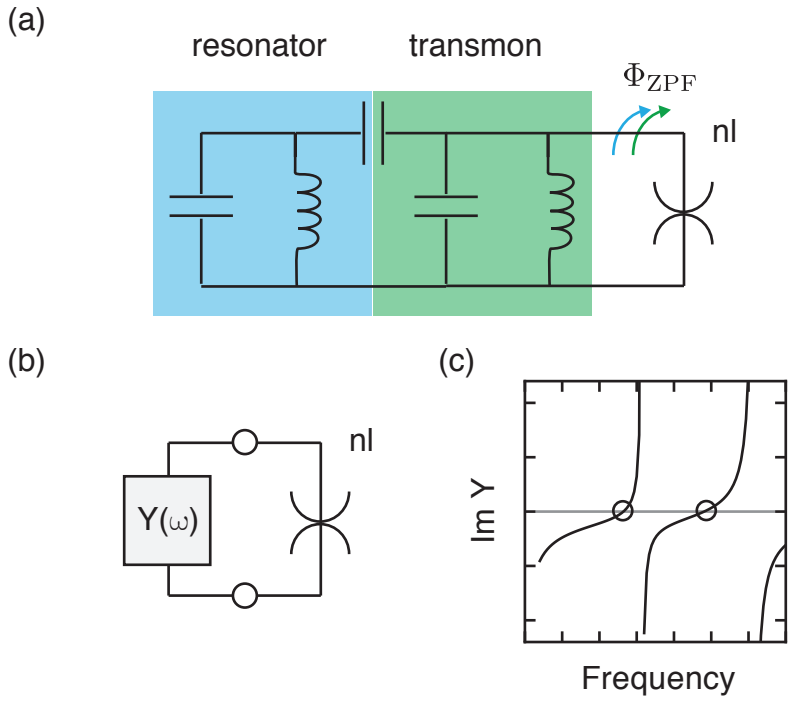

Figure 2.8: Black box quantization of many modes. (a) The most basic circuit QED schematic is a mostly-linear LC oscillator (resonator) coupled to a strongly nonlinear LC oscillator (transmon). Both acquire their nonlinearity from a single Josephson element, which also provides the cross mode-mode nonlinearity (such as cross-Kerr term χ) to the system. **(b)** To simplify the quantum mechanical treatment of the coupled system, first the classical circuit is diagonalized and lumped into a 'black box' admittance term $Y(\omega)$. **(c)** The characteristic impedance of each resonant mode in the black box, as viewed from the junction, sets the participation of that mode in the junction's nonlinearity. That impedance can be predicted from studying the classical circuit model of the system. The problem reduces to finding the zero-crossings of the imaginary part of the admittance and the slope of the function there (circles).

parameter. Now, the magnitude of the zero-point fluctuations are given by

$$\Phi^n_{\mathrm{ZPF}} = \frac{\Phi_0}{\sqrt{2\pi R_Q \tilde{\omega}_n Y'_n}}, \tag{2.93}$$

where R_Q is the resistance quantum. Because Y'_n is a classical, linear circuit parameter, traditional circuit simulators are also able predict Φ^n_{ZPF} natively, even for complex circuits [10].

Our total Hamiltonian now reads

$$\hat{H} = \hbar \sum_n \tilde{\omega}_n \hat{\mathcal{A}}^\dagger_n \hat{\mathcal{A}}_n + \hat{H}_{nl} \tag{2.94}$$

where $\hat{H}_{nl}$ is defined equivalently to before (Eq. 2.45), except we replace the simple flux operator by our new expression for total flux across the junction (Eq. 2.91) [10], giving the full Hamiltonian as

$$\hat{H}_{nl} = E_J \left[1 - \cos\left(\sum_n \varphi_n \left(\hat{\mathcal{A}}^\dagger_n + \hat{\mathcal{A}}_n \right) \right) \right] - \frac{E_J}{2} \left[\sum_n \varphi_n \left(\hat{\mathcal{A}}^\dagger_n + \hat{\mathcal{A}}_n \right) \right]^2 \tag{2.95}$$

where again, we will find it simpler to work in a unitless parameter $\varphi_n \equiv \Phi^n_{\mathrm{ZPF}}/\Phi_0$. Indeed, the sum over all fluxes shows up as the operator $\hat{\varphi}_{\mathrm{tot}}$, including for the quadratic term on the right hand side.

The real utility of this total Hamiltonian becomes clear when we consider the fact that distinct modes commute: $\left[\hat{\mathcal{A}}_n, \hat{\mathcal{A}}_m\right] = \delta_{n,m}$. Therefore, our frame transformations from before can be done in parallel on this potentially massive Hamiltonian right away. Going into the co-rotating frame, such that $\tilde{\mathcal{A}}_n = \hat{\mathcal{A}}_n e^{\imath\tilde{\omega}_n}$, allows us to expand the total Hamiltonian like before.

For simplicity, let us treat in some detail the simple case of two modes, truncated at the fourth order. We can write the truncated Hamiltonian (similar to Eq. 2.65) as

$$\tilde{H} \approx \frac{\hbar E_J}{24} \left[\varphi_a \left(\tilde{a}^\dagger + \tilde{a} \right)^4 + \varphi_b \left(\tilde{b}^\dagger + \tilde{b} \right) \right]^4 \tag{2.96}$$

We use the RWA to find the dominant terms of this Hamiltonian [11]. In particular, because our modes are detuned, we can discard terms like $\tilde{a}^\dagger \tilde{b}$ in the expansion of the quartic Hamiltonian. Collecting terms like $\tilde{a}^\dagger \tilde{a}$ and $\tilde{b}^\dagger \tilde{b}$, we see that each mode will acquire

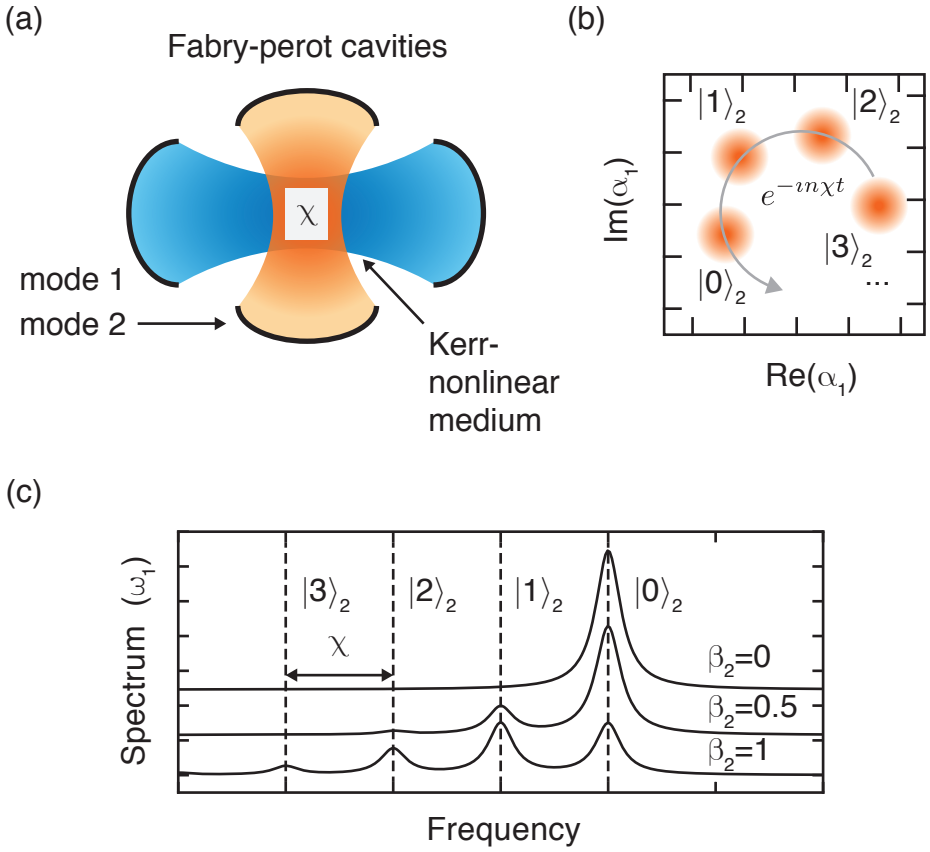

Figure 2.9: Cross-Kerr nonlinear effects. (a) Two prototypical oscillators, modes one and two (shown as Fabry Perot-type resonators), store energy in a Kerr nonlinear medium. In that nonlinear medium, the phase velocity of resonant light depends on the total energy stored, leading to an effective length for the resonators which is dependent on the energy stored in the other. A strongly nonlinear version of this system is realized in cQED architectures with remarkable consequences. **(b)** If mode two is in a superposition of several Fock states, for instance as a coherent state $|\beta\rangle_2$, any state in mode one, shown as a single Gaussian state, acquires a differential phase for each Fock state $|m\rangle_2$ at a rate χ, where χ is the strength of the cross-Kerr nonlinearity. **(c)** With strong nonlinearity ($\chi \gg \kappa$, where κ is the linewidth of the modes), the system enters the number-split regime of cross-Kerr interaction. Each energy eigenstate of mode two $|m\rangle_2$ is associated with its own transition frequency in mode one. Shown are frequency spectra of mode one for three different coherent states in mode two.

a Kerr term proportional to

$$K_k = \frac{E_J \varphi_k^4}{4} \tag{2.97}$$

This is a little strange. Our circuit under consideration began as a transmon sub-circuit coupled to many LC oscillators, but somehow, we ended up with just a bunch of transmons! In retrospect, this might not be too surprising since a transmon, in our treatment, has been a nonlinearly-shunted LC oscillator. Surely then, by introducing the same nonlinearity to the other LC oscillators, they might be expected to dress with the Josephson effect in a similar manner.

At fourth order, we acquire a new type of Hamiltonian term as well that has interesting consequences for our circuit. We now find terms in the expansion that are a cross-Kerr type nonlinearity [62], as

$$\tilde{H}_{\text{int}} = -E_J \varphi_a^2 \varphi_b^2 \hat{a}^\dagger \hat{a} \hat{b}^\dagger \hat{b}. \tag{2.98}$$

We define the cross-Kerr interaction strength as $\chi_{ab} \equiv E_J \varphi_a^2 \varphi_b^2$. Note that χ is related to the geometric mean of the two Kerr terms as

$$\chi_{ab} = 2\sqrt{K_a K_b}. \tag{2.99}$$

This makes intuitive sense since this nonlinear interaction is set by how hybridized each mode is to the single Josephson junction in the problem. That same hybridization also sets K_n.

For two modes with a large detuning, χ_{ab} is the dominant coupling term. This regime is known as the dispersive regime of cQED [62], a Hamiltonian that has also obtained with CQED [11]. Now, if mode a is excited, for example in the Fock state $|1\rangle_a$, our dispersive Hamiltonian indicates that the frequency of mode b will shift downward by exactly χ, since $\langle \hat{a}^\dagger \hat{a} \rangle = 1$ for Equation 2.98. A more interesting behavior is achieved whenever one of the modes is in a superposition of Fock states. Then, an entangling interaction occurs [11], whereby a superposition of Fock states in one mode forces the other mode to be in a conditional superposition of many frequencies, as we will discuss in detail in Chapter 3. In the next section, we show how this conditional frequency shift can be used to devise a QND measurement of the qubit state.

2.5 Detecting the state of a transmon

It might be interesting to probe a transmon directly with a Vector Network Analyzer (VNA), for instance, measuring the atom in reflection, similar to the scheme of Hoi et al. [63]. In this case, when the VNA (at weak probe powers) sweeps through a transition frequency of an occupied level of our transmon, a single probe photon (at most) will be exchanged with the transmon. Detecting a missing photon (absorption) or an extra photon (emission) would inform us of the former state of the transmon. However, practically this is a demanding requirement. Additionally, the real impedance of the VNA would introduce unnecessary dissipation to the transmon, as we will discuss later in Section 4.2.1.

Instead, we will couple our simple transmon circuit to a filter element, an ancillary LC oscillator [54, 55], and probe the response of the oscillator to infer information about the state of the transmon [14, 64]. To detect the state of mode a, we need to determine mode b's frequency with sufficient precision to determine whether it is ω_b or $\omega_b - \chi$. There are some nice properties of this proposal. First, if we can drive mode b with many photons, our frequency detector does not need to be sensitive to fluorescence-like signal levels as considered before. Also, this detection can be QND to good approximation [59, 60]. This is opposed to schemes which rely on absorption or fluorescence, which detect a change of state. Finally, if the readout mode is more strongly coupled to the detection apparatus, it will filter real impedance of the detector from the transmon atom, extending the possible lifetimes in the transmon mode [56].

Now, however, our readout mode has acquired some transmon-like behavior as shown in the previous section. However, for a carefully designed circuit, we can largely ignore these effects, and pretend that our filter retains its linearity. This is a reasonable approximation for the readout mode whenever

$$K_b |\langle \hat{b}^\dagger \hat{b} \rangle|^2 \ll 1/T_{\text{exp}} \tag{2.100}$$

where T_{exp} is the timescale for the experiment. Essentially, for a weak nonlinearity, the number-state dependent phase accumulation by the Kerr effect may take more time to acquire than we are sensitive to.

To use the conditional frequency shift of the readout mode ($\delta\omega = \chi$) as a detection mechanism, sufficient frequency precision is required. Therefore, the measurement time

will be on the order of $T_{\text{exp}} \approx 1/\chi$. By Equation 2.100, we then require that

$$\chi_{ab} \gg K_b \langle \hat{b}^\dagger \hat{b} \rangle. \tag{2.101}$$

Therefore, we must design circuits that have a large χ_{ab}/K_b ratio. Using Equation 2.99, we find that these requirements can be distilled to working with a transmon having high anharmonicity, such that

$$\mathrm{K}_a \gg K_b |\langle \hat{b}^\dagger \hat{b} \rangle|^2. \tag{2.102}$$

Essentially, the above constraint is the extent to which we can assign the label 'transmon' to one mode and 'resonator' to the other. In practice, this inequality is easily satisfied because usually only the transmon mode is galvanically connected to the junction. For instance, we will study a sample in detail in Chapter 6 that fulfills this requirement up to $\langle \hat{b}^\dagger \hat{b} \rangle \approx 500$.

To show how the simplest readout schemes operate, consider our coupled Hamiltonian, with the transmon truncated at its lowest two levels (Eq. 2.73), and ignoring the resonator's nonlinearity [54]. In the interaction picture, the Hamiltonian is given by

$$\tilde{H}_{\text{disp}} = \frac{\chi_{ab}}{2} \hat{b}^\dagger \hat{b} \hat{\sigma}_z. \tag{2.103}$$

This expression is equivalent to the dispersive limit of the Jaynes-Cummings model for CQED [11], albeit derived with a different set of systems, assumptions and approximations.

A typical technique for measuring the frequency of a resonator is to measure the reflection coefficient of signals from the device [14, 64]. That coefficient is given by

$$r = \frac{\Delta_b - \imath\kappa/2}{\Delta_b + \imath\kappa/2} \tag{2.104}$$

where Δ_b is the detuning between the probe and the resonator. For a probe tone tuned halfway between the response of mode b to the transmon ($\omega_d = \omega_b - \chi/2$), r can be rewritten to account for the state-dependent shift [14] as

$$r = \frac{\chi \hat{\sigma}_z - \imath\kappa/2}{\chi \hat{\sigma}_z + \imath\kappa/2}. \tag{2.105}$$

If we define a the angle $\theta = \kappa/\chi$ we can simplify the reflection as a rotation in the IQ plane as

$$r = e^{-\imath\theta\hat{\sigma}_z}. \tag{2.106}$$

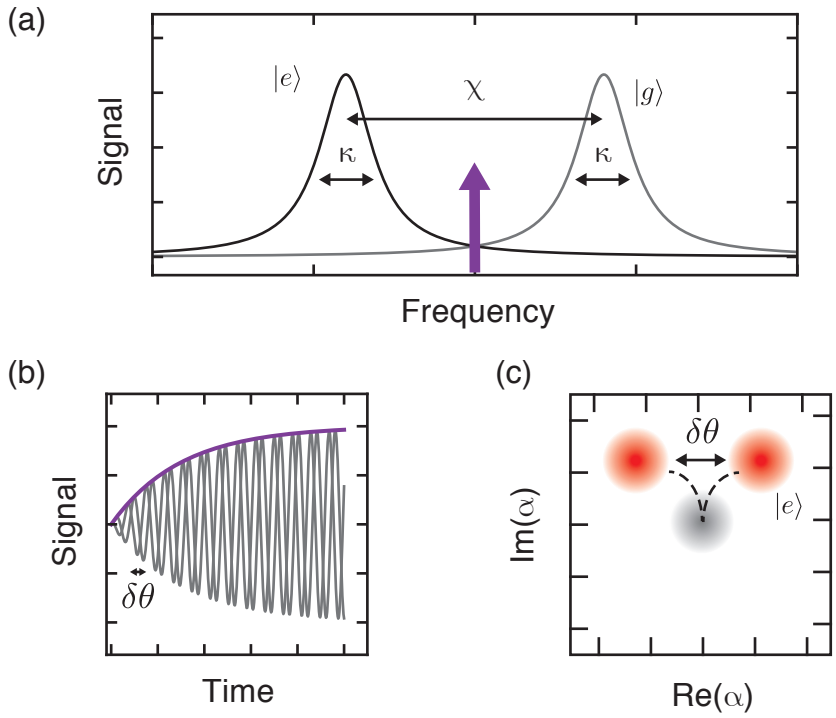

Figure 2.10: Reading out the state of a transmon. (a) The frequency of the readout resonator depends strongly on the state of the transmon qubit. The frequency shift χ can be much greater than the linewidth of the mode κ. To probe the state of the transmon, a common technique is to drive halfway between these two frequencies (purple arrow). Then, the state of the transmon is encoded in the phase of the outgoing signal. **(b)** A readout pulse builds up energy in the resonator that is leaked out to the measurement chain. For the readout probe frequency shown in (a), the two states of the transmon yield identical ring-up type envelopes. **c)** The amplitude and phase of these signals are digitized, via techniques described in a later chapter, and the measurement results are histogrammed. The relative counts between the two distributions gives the probability the qubit was detected in the ground or excited state (P_g and P_e).

For a coherent input state, in the absence of the resonator's Kerr nonlinearity, this phase angle is independent of the displacement size [14]. Therefore, phase contrast, our measurement signal, will increase with larger displacements. We can quantify the information contained in the reflected signal as the orthogonality of the resultant coherent states. If the two states of the transmon ($|0\rangle_a, |1\rangle_a$, or equivalently $|g\rangle, |e\rangle$) are mapped onto a phase difference θ, the coherent states can be detected in unique states to the extent that

$$\langle \alpha e^{+\imath\theta} | \alpha e^{-\imath\theta} \rangle = 0 \tag{2.107}$$

We give the practical details of this detection scheme later in Section 5.2.4.

2.5.1 Selection rules for many-wave mixing

We conclude our study of the simplest coupled-oscillator Josephson circuits with some striking effects that can be observed by stimulating otherwise negligible processes in the circuit with pumps.

We rely on the commutativity of our different modes in order to go into a co-rotating, co-displaced frame [34], such that all modes can be driven by some field, transforming our operators as

$$\tilde{\mathcal{A}}_n \rightarrow \tilde{\mathcal{A}}_n + \xi_n. \tag{2.108}$$

Our total Hamiltonian recovers a generalized form of Equation 2.62. A remarkable set of interactions can be driven between the elements of our many-transmon artificial molecule.

If we take the simplest experiment, driving a single mode off resonantly, the χ interaction at fourth order approximation ends up every mode an AC Stark shift [34]. Driving the n-th mode shifts the m-th mode by an amount

$$\Delta_m = -\chi_{nm} |\xi_n|^2. \tag{2.109}$$

Also, similar the multi-photon transitions of a single transmon, strong pumps can drive multi-photon processes in the coupled circuit [34]. For example, a pump on mode n at a frequency $\omega_d = \frac{1}{2}(\omega_m - \omega_n)$ would make stationary any terms in the Hamiltonian of the form

$$\hat{H}_{swap} = -\chi_{nm} \left[\xi^2 \tilde{\mathcal{A}}_n{}^\dagger \tilde{\mathcal{A}}_m + (\xi^*)^2 \tilde{\mathcal{A}}_n \tilde{\mathcal{A}}_m{}^\dagger \right] \tag{2.110}$$

We see that this Hamiltonian term can be used to swap single photons between modes, such as the transmon and resonator, by exchanging energy with two probe photons (four-wave

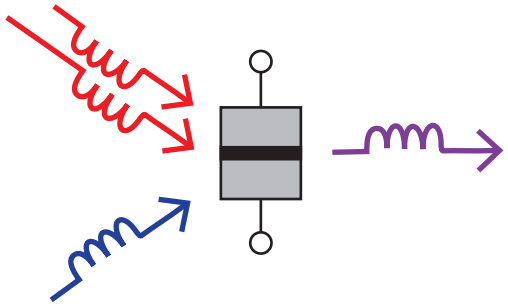

Figure 2.11: Josephson junction as a scattering site. Many Hamiltonian terms are discarded by energy conservation considerations during the polynomial treatment of a Josephson junction's cosine potential. However, in the presence of drives, these otherwise neglected terms can dominant the evolution of the system. Pumping a single junction at multiple frequencies can lead to a versatile set of mode conversions via many-wave mixing.

mixing). For a cold resonator with fast decay constant, this technique can be used for to reset another mode [34]. Or, driven between two coherent modes, this pump can be used for SWAP-based quantum logic [65]. Interestingly, these SWAP interactions typically require resonant operation [65] (and thus frequency tunability), which can complicate circuit implementations. Here, we get that physics 'for free' from the quartic term of our cosine expansion.

As another example, take the pump frequency $\omega_d = (2\omega_m - \omega_n)$. Energy-conserving terms now include

$$\hat{H}_{swap} = -\chi_{nm}\left[\xi\left(\tilde{\mathcal{A}}_n^{\dagger}\right)^2\tilde{\mathcal{A}}_m + \xi^*\left(\tilde{\mathcal{A}}_n\right)^2\tilde{\mathcal{A}}_m^{\dagger}\right] \tag{2.111}$$

Just by changing the frequency of the pump, we have altered the four wave mixing such that now one photon from mode m is converted to two photons in mode n and vice-versa, by exchanging energy with a single pump photon. This parametric process was used in Leghtas et al. [34] to drive an oscillator directly to a cat state.

There is an infinite number of interesting processes we can stimulate with many-wave mixing [37]. The recipe is simple enough to be extended to even higher order terms beyond quartic. These experiments will push the cosine expansion in new ways. Single Josephson junction circuits seem to be an endless playing field for fundamental quantum optics.

Before diving into the physical implementation of these systems, the next chapter explores the consequences of quantum information in resonators. Future chapters will

discuss the specifics of transmon-resonator design Chapter 4 as well as techniques for their fabrication and measurement Chapter 5. Then we will combine these ideas to describe a novel type of quantum memory that has state-of-the-art coherence for cQED, in Chapter 6.

CHAPTER 3

Quantum information in harmonic oscillators

HArmonic oscillators are very simplest quantum mechanical objects, as we saw in Chapter 2. However, the infinite Hilbert space of a harmonic oscillator can be leveraged for powerful applications in quantum information processing [66, and references therein]. We begin this chapter by motivating oscillator-based quantum information schemes with an example from modern classical communication techniques [67]. We then turn our attention to quantum states in oscillators, describing how to characterize such states [11] and how to create them using the ideas from Chapter 2 [68, 69]. Finally, we review recent progress toward one exciting application for qubit-coupled resonators, the so-called cat-codes for quantum error correction. [70].

Many of the concepts throughout this chapter are general to the control and measurement of oscillators. Whenever possible, we show how the dispersive interaction described in the previous chapter enables the particular process at hand. Many other qubit-resonator interactions are possible and have their own set of advantages and disadvantages [26, and references therein]. In particular, resonant SWAP gates between qubits and resonators, in which single excitations are swapped or manipulated, have been used to demonstrate a remarkable set of experiments [71]. Side-band pulses can also be used to create non-classical qubit-resonator states [72–74] and mediate quantum information storage in an oscillator [75].

3.1 Photons carrying classical bits

This chapter is influenced by the modern signal processing techniques of digital phase-shift-keying (PSK) [67], which is reviewed here to highlight its similarities to quantum schemes, as pointed out in [68].

Fiber optic cables are ideal transmission channels for long distance communication because they are low-distortion and low-loss. However, installing fiber optics cables and repeaters is an expensive endeavor. Techniques that maximize the capacity of each signal channel are crucial to enabling modern high speed communication at large scale. PSK relies on the fact that telecommunications signals are carried by waves. By comparing the phase-difference (ϕ_0) between an incoming signal and a reference clock, we can determine ϕ_0 to some, potentially high, precision. That precision sets the number of points in phase space that can be used as classical bits.

An additional benefit of phase encoding is that it is naturally robust against small amounts of signal loss, as compared to amplitude encoding which is maximally sensitive to loss. As long as the signal remains above the noise floor such that ϕ_0 can be determined to the requisite precision, PSK is robust against dissipation. This idea is analogous and important for quantum mechanical versions of PSK, as we will see later in this chapter.

As shown in Figure 3.1, quadrature-PSK encoding (QPSK) is one example of such an encoding scheme. The sender of a QPSK message chooses one of four offset-phases $\phi_0 \in [\pm\pi/4, \pm 3\pi/4]$, such that the sent message is

$$s(t) = V_0 \cos(\omega t + \phi_0). \tag{3.1}$$

The receiver mixes down the message against two orthogonal basis functions (sine and cosine) to recover the phase symbol

$$I_m = \int_0^{T_s} \cos(\omega t) \times V_0 \cos(\omega t + \phi_0) dt \tag{3.2a}$$

$$Q_m = \int_0^{T_s} \sin(\omega t) \times V_0 \cos(\omega t + \phi_0) dt \tag{3.2b}$$

It simplifies demodulation to choose the integration time to be a full period $T_s = 2\pi/\omega$, though this is not a requirement of QPSK. Then,

$$(I_m, Q_m) \in \frac{V_0 T_s}{2\sqrt{2}} \{(-1,1), (1,1), (1,-1), (-1,-1)\} \tag{3.3}$$

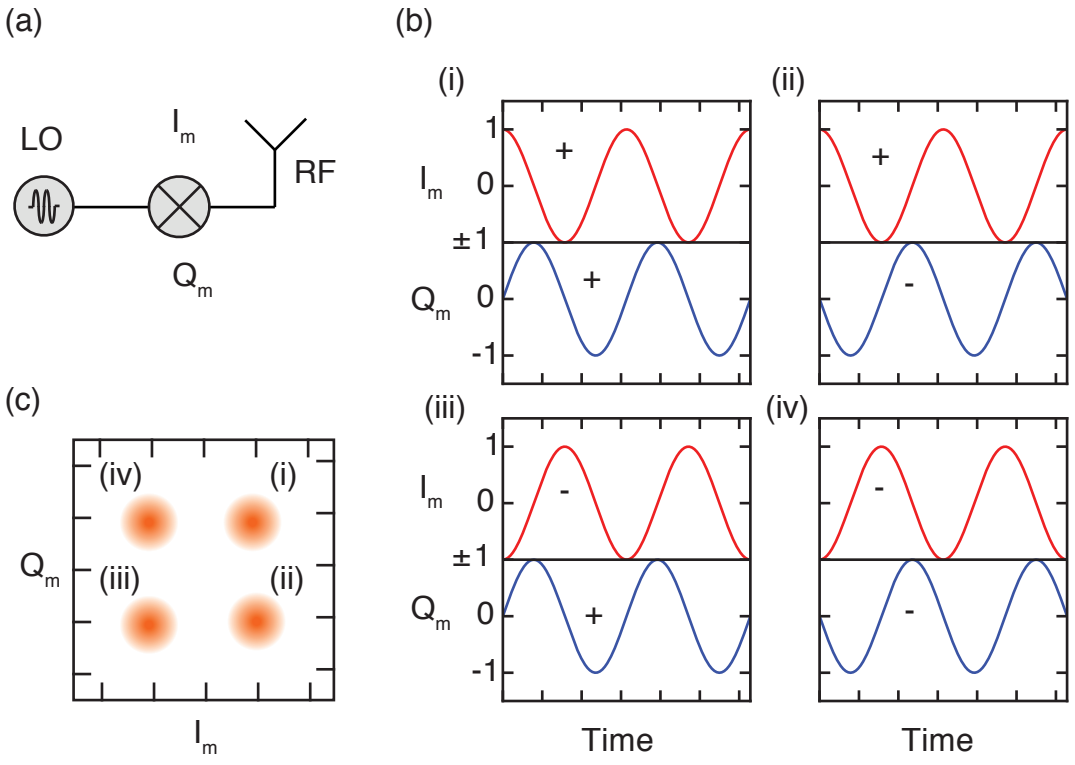

Figure 3.1: Phase shift-keying (PSK) of classical signals. (a) In transmit mode, a local oscillator (LO) is mixed with two sinusoidal voltages I_m and Q_m that carry a four-bit message encoded in the phase of these oscillating voltages for a predetermined amount of time. The modulated output signal (RF) is sent across a channel to the receive party. The receiver works in reverse. There, the RF chain carries a modulated input signal that is down-converted to phase-information containing components (I_m,Q_m) by a local oscillator. **(b)** Four bits are encoded in a single time channel by setting the initial phase of independent sinusoidal functions as $\phi_0 \in \{0, 2\pi\}$, which relies on the orthogonality of the cosine and sine functions. **(c)** Each transmitted symbol will be modulated or demodulated to a location on the IQ plane that falls on the PSK constellation shown. For signal strengths greater than the noise of the system, many bits can be encoded in each symbol, provided that the constellation points do not overlap to the precision of a given error threshold.

where we enumerated the results for phases increasing from $\phi_0 = -3\pi/4$. Noise sets the limit on the density of phase-space at our disposal. A common PSK constellation can include between 16 and 32 bins for ϕ_0. Therefore, in one integration window, the symbol contains up to 32 bits of information.

A subtle issue with PSK is that the rapid switching of the phases between symbols can cause issues if any of the components, such as optical repeaters and amplifiers, have finite bandwidth or linearity [67]. To combat these problems, only certain transitions between symbols are allowed and information becomes encoded in the pattern of symbols, rather than single symbols themselves. Indeed, this idea indeed has also been considered for finite-nonlinearity PSK analogues in the quantum domain.

If we had quantum control over a PSK-type communication channel, it is not too hard to imagine one could encode a similar number of *quantum bits* of information for each symbol. The sender only needs a component which can phase-shift a coherent state into a superposition, i.e. modulate a signal to phase multiple phases at once. Remarkably, such control has already been demonstrated. At the conclusion of this chapter, we will review an experiment that has achieved the quantum version of QPSK, and we examine some important applications of such an encoding.

First however, we need a more sophisticated suite of tools to describe quantum states in continuous variables systems.

3.2 State tomography of an oscillator

For an infinite-level system, full state tomography [39] is impossible [21]. In practice, we will truncate any oscillator under study at some N-th level [11]. We require that any population in higher levels is negligible to sufficiently describe the state. To see why this is justified, consider a coherent state of amplitude $|\beta\rangle$, the probability of finding population at a high Fock state ($N \gg |\beta|^2$) is given by Equation 2.21, which falls off precipitately. For instance, for the coherent state $|\beta|^2 = 9$, if we truncate our tomography at $N = 18$, the total population in higher states is only 0.5%.

Further, coherent states are an overcomplete decomposition of the oscillator's Hilbert space [21]. Zurek showed that for state tomography, the minimum grid-size for a given precision is related to the size of the allowed N-th level truncation of the Hilbert space [76]. Essentially, any features in state tomography will be required to have slower variation than some $\delta\alpha$ [76]. Therefore, most tomography schemes proceed by gridding the Hilbert space

into a series of IQ-blocks of size $\delta\alpha \times \delta\alpha$ that are accessed with a displaced measurement operator [11], examples of which we will describe starting in Section 3.2.2.

3.2.1 Fock state distribution

The simplest, but potentially incomplete, tomography that can be conducted on the state of a resonator is obtained by measuring the probability distribution of Fock states, each P_n, up to some truncation. Such a tomography scheme is useful for detecting non-Gaussian statistics in a resonator state [62] and for calibrating control drives [38] as we discuss in Section 6.2.1.

In the strong dispersive regime of cQED, spectroscopy on the qubit reveals the P_n distribution automatically [62]. Essentially, because the qubit acquires a large frequency shift for each resonator Fock state $\chi \gg \gamma_2$ (where γ_2 is the full qubit linewidth), the relative area of the n-th number-state resolved transition line (the 'n^{th} number-peak') gives P_n. Assuming a sufficiently weak drive on the qubit and assuming that the linewidth of the qubit is $\gamma_2 \approx 1/T_1$, the spectrum of the qubit is given by [64]

$$\mathcal{S}[\omega] = \frac{C}{2\pi} \sum_n \left(\frac{P_n \gamma_2}{(\frac{1}{2}\gamma_2)^2 + (\omega - \omega_0 - n\chi)^2} \right) \tag{3.4}$$

where C is a scaling term to account for the readout efficiency and ω_0 is the frequency of the transmon conditioned on zero photons in the resonator, i.e. the transition $|g,0\rangle \rightarrow |e,0\rangle$. We use this technique to confirm the preparation of non-classical states in Chapter 6.

We caution the reader that pulsed spectroscopy is recommended for this tomography technique. The alternative, which would seek to quantify the statistics of a steady-state resonator drive by measuring the spectroscopy signal of a transmon in parallel, leads to several complications [64]. First, the presence the resonator drive will Stark shift the transmon spectrum (Section 2.3.4), shifting the observed resonator and qubit spectra as

$$\begin{aligned} \Delta_{\text{stark},r} &= -K_r |\xi_r|^2 \\ \Delta_{\text{stark},q} &= -\chi |\xi_r|^2 \end{aligned} \tag{3.5}$$

where $|\xi_r|^2$ is the resonator drive intensity, K_r is the Kerr of the resonator, χ is the dispersive coupling strength between the qubit and resonator. Importantly, this is a different term in the Hamiltonian than $\chi \hat{a}^\dagger \hat{a} \hat{b}^\dagger \hat{b}$ that provides number splitting (i.e. is quantized). As soon as the drive, ξ is turned off (as for pulsed spectroscopy) this term

will disappear. Furthermore, as described in Section 2.5.1, drive terms in the Hamiltonian can stimulate previously discarded conversion terms. This can yield additional features in spectroscopy, making interpretation difficult. Yet, as long as the experiment is conducted carefully and pulsed, the protocol for determining χ in spectroscopy is straightforward.

By measuring the transmon's spectrum then, we can determine whether the distribution of P_n is Poissonian (coherent states), super-Poissonian (e.g. thermal states), or sub-Poissonian (e.g. Fock states) [62]. Examples of ideal distributions are given in Figure 3.2. Since a single Fock state carries no phase information, a P_n distribution is sufficient to completely characterize such states. However, for states that lack rotational symmetry in the IQ plane, additional information is needed to characterize the system.

3.2.2 Husimi Q functions

The Husimi Q function [77] is a quasiprobability distribution that quantifies the oscillator's population at a given point in IQ grid $(\mathcal{R}(\alpha), \mathcal{I}(\alpha))$ as the overlap between the input oscillator state and a coherent state of amplitude $|\alpha\rangle$. More precisely, for the input state $|\psi\rangle$, the Q function at grid-point α can be written as

$$Q(\alpha) \equiv \frac{1}{\pi}|\langle\alpha|\psi\rangle|^2 \tag{3.6}$$

To see how this quantity is extracted experimentally, we can rearrange the above as [21]

$$Q(\alpha) = \frac{1}{\pi}|\langle 0|D^\dagger(\alpha)|\psi\rangle|^2 = \frac{1}{\pi}|\langle 0|D(-\alpha)|\psi\rangle|^2. \tag{3.7}$$

We see that, by symmetry, the task of measuring the overlap of $|\psi\rangle$ with a finite amplitude coherent state reduces to measuring the overlap of $|\psi'\rangle = D(-\alpha)|\psi\rangle$ with the zeroth Fock state (P_0), which we saw in the previous subsection was possible. Examples of Husimi Q functions are given in Figure 3.3.

Rather than spectroscopy, we can measure P_0 more efficiently [38] by driving the transmon with a number-selective π pulse that is narrow frequency (FWHM $\ll \chi$) and resonant on the $|g,0\rangle \rightarrow |e,0\rangle$ transition, followed by a measurement of the qubit state. This technique can be quantum non-demolition (QND) [78, 79], meaning that regardless of the input state, a measurement of the transmon in the excited state $|e,0\rangle$ will herald the preparation of a zeroth Fock state. Measuring the resulting transmon state in $|g\rangle$ will

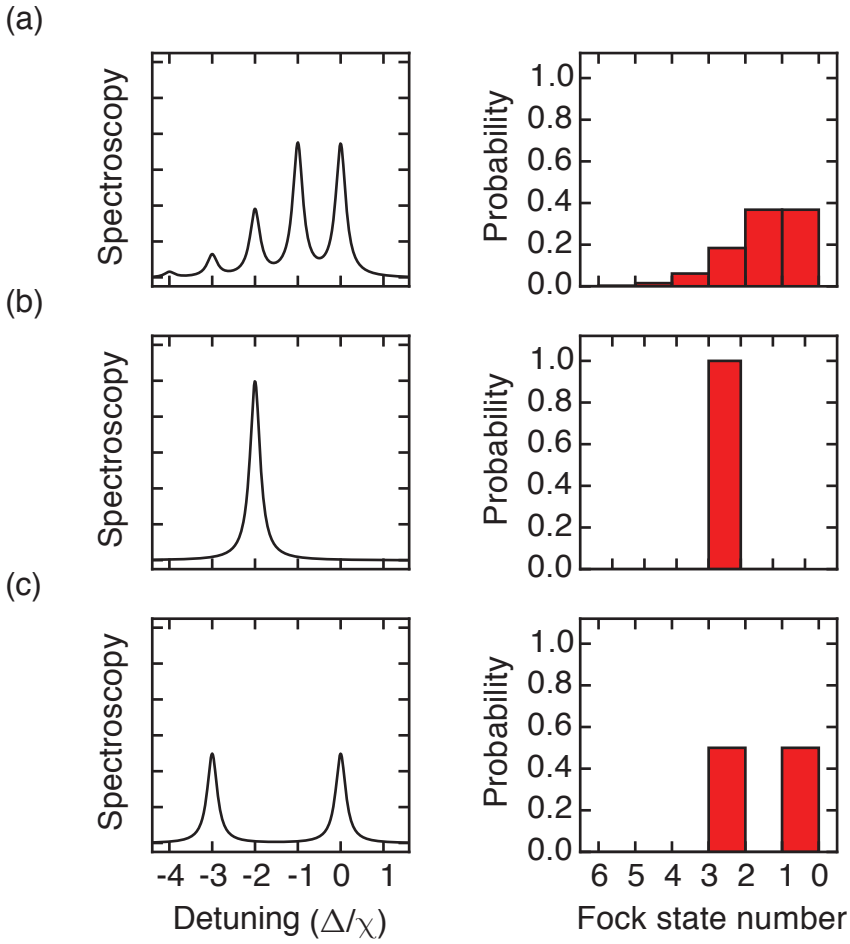

Figure 3.2: Quantifying the statistics of a resonator state. (left) Examples are given of various qubit spectra under different preparations of resonator states. **(right)** The corresponding probability distribution of resonator Fock states (P_n) that would be inferred from the associated qubit spectrum. **(a)** The resonator is in a coherent state of $\beta = 1.0$ and obeys Poissonian number statistics. **(b)** The resonator is in a single Fock state $|3\rangle$ and displays sub-Poissonain number statistics (the variance in $\hat{n}$ of zero is less than the mean value of three). **(c)** The resonator is either in a superposition of $|0\rangle$ and $|3\rangle$ or in a statistical mixture of the two states. A simple probability distribution P_n is not sufficient to distinguish these two cases.

project the state into a vacuum subtracted version of the input state [79], i.e.

$$|\psi\rangle_{\text{final}} = \mathcal{N}\left(|\psi\rangle_{\text{input}} - C_0|0\rangle\right) \tag{3.8}$$

where C_0 is the initial state's amplitude in $|0\rangle$. The $\mathcal{N}$ accounts for the renormalization of the state to maintain $\sum_{n=1}^{\infty}|C_n|^2 = 1$, where the new amplitudes are scaled to account for the missing population the vacuum.

In general, more information can be extracted about the oscillator state if the qubit is found to be in $|g\rangle$ since some other C_m remains nonzero with statistics that are directly related to the input state [79]. However, for tomography protocols which only seek to measure the state of an oscillator, it is more accurate to instead recycle the system, waiting for it to return to equilibrium before preparing another input state and measuring it. The trade off for discarding additional information is that the resulting tomography can be interpreted without concern for uncontrolled measurement backaction, such as qubit decay during measurement [80].

The Husimi Q function can also be generalized to extract a more sensitive set of information about an oscillator input state [11]. Instead of probing just the overlap with a coherent state (equivalently a displaced $|0\rangle$ Fock state), one can measure the overlap with any displaced Fock state as

$$Q_n(\alpha) = \frac{1}{\pi}|\langle n|D(-\alpha)|\psi\rangle|^2 \tag{3.9}$$

It follows that Q_m of the m-th Fock state is identical to the Gaussian profile of the Q_0 of the vacuum.

Any one of the generalized Q_n functions is a complete representation of the input state's density matrix [21]. However, some quantum features tend to be suppressed in this type of tomography. Figure 3.4 shows that a way of recovering that sensitivity is to combine many Q_n distributions into a single observable across an oscillator's Hilbert space, such as the parity operator [38, 71], defined as

$$\hat{P} \equiv e^{\imath\pi\hat{n}}. \tag{3.10}$$

Measuring the expectation of some operator $\langle\hat{O}\rangle$ at a location in IQ space α is equivalent to

$$\langle\hat{O}\rangle_\alpha = \text{Tr}\left(D^\dagger(\alpha)\rho D(\alpha)\hat{O}\right), \tag{3.11}$$

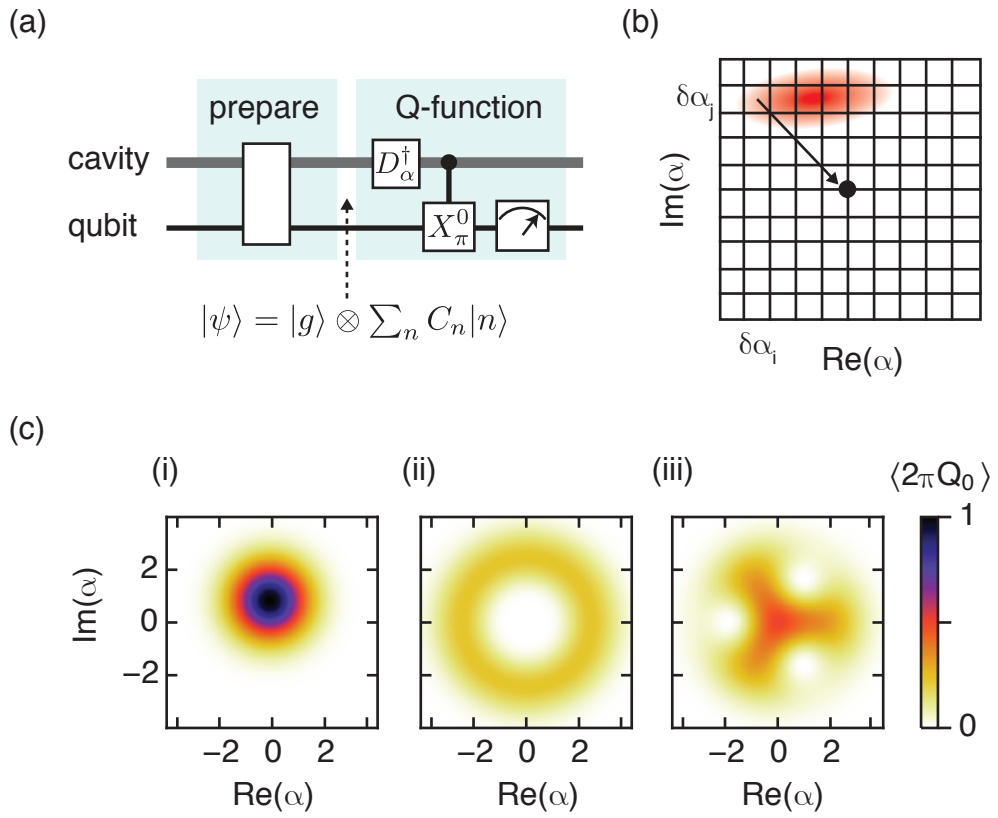

Figure 3.3: Husimi Q distribution of resonator states. (a) Experimental sequence to perform Husimi Q tomography on a resonator state. The tomography is performed after some arbitrary preparation step, which leaves the qubit unentangled with the resonator. To measure the Q function at a displacement α, a displacement of $D^\dagger(\alpha) = D(-\alpha)$ is used to bring that region of the state to the origin. Then, a number selective qubit rotation is performed that flips the qubit to the excited state only if zero photons are present. Measurements are repeated to acquire the quasiprobability distribution across many values of the displaced mode. **(b)** Graphical representation of Q function measurement. The IQ plane of the resonator is broken up into grids, where each block represents a displacement value used in the experimental sequence. **(c)** Examples of Q functions. The Husimi Q representation of the resonator states previously considered in Figure 3.2 can reveal more information. **(i)** A coherent state of $\beta = 1i$ is distinguishable from $\beta = -1i$. **(ii)** The Q function of the $|3\rangle$ Fock state has no further information since the state has complete phase uncertainty. **(iii)** The superposition of $|0\rangle$ and $|3\rangle$ is distinguished from a statistical mixture by the existence of a rotational asymmetry in the state's Q function.

which can be expanded as

$$\langle \hat{O} \rangle_\alpha = \sum_n \langle n | \left(D^\dagger(\alpha) \rho D(\alpha) \hat{O} \right) | n \rangle. \tag{3.12}$$

Fock states are eigenstates of the parity operator: $\hat{P}|n\rangle = (-1)^n |n\rangle$. So the above expansion reduces [21] to

$$\langle \hat{P} \rangle_\alpha = \sum_n (-1)^n \langle n | \left(D^\dagger(\alpha) \rho D(\alpha) \right) | n \rangle. \tag{3.13}$$

Rearranging the density matrix gives a simple form for this expectation value as

$$\langle \hat{P} \rangle_\alpha = \sum_n (-1)^n |\langle n | D^\dagger(\alpha) | \psi \rangle|^2 \tag{3.14}$$

which we recognize as a sum over Q_n as defined in Equation 3.9. We finally have that

$$\langle \hat{P} \rangle_\alpha = \pi \sum_n (-1)^n Q_n(\alpha) \tag{3.15}$$

Again, we truncate this series at some N above which Q_N tends to zero at small displacements ($|\alpha|^2 \lesssim N$). By measuring many generalized Q_n functions, we are able to extract directly a useful quantity to describe our state. In fact this particular observable is directly related to another type of tomography, the Wigner function. In the next subsection, we meet the Wigner function and a more direct measurement technique for $\langle \hat{P} \rangle_\alpha$.

3.2.3 Wigner tomography

The Wigner function [21] is a quasiprobability distribution that is formally defined as

$$W(\alpha) = \frac{2}{\pi} \langle \hat{P} \rangle_\alpha. \tag{3.16}$$

The function takes values in the range of $W(\alpha) \in [-2/\pi, 2/\pi]$, and it is normalized such that

$$\int W(\alpha) d\alpha^2 = \pi. \tag{3.17}$$

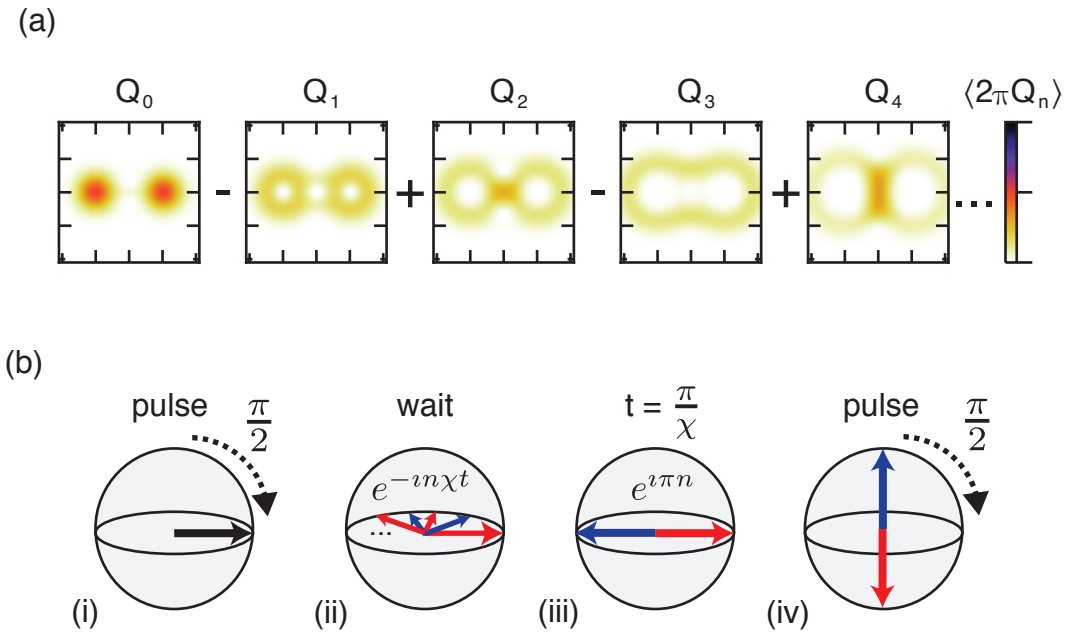

Figure 3.4: Two techniques for measuring parity. (a) Parity can be determined by an alternating sum of generalized Q_n functions [21]. This is a graphical representation of Equation 3.15 for an even superposition of coherent states $|\psi\rangle = |\beta\rangle + |-\beta\rangle$. The first panel, which is Q_0, does not contain noticeable information about the superposition. However, the higher even functions Q_2, Q_4 have weight at the center, whereas the odd functions Q_1, Q_3 have zeros at the center, indicating that the state has a strong positive parity at the origin. This shows explicitly what is meant by parity having more quantum phase sensitivity. **(b)** An alternative method for measuring parity in a 'single-shot' is shown [68, 81]. An initial $\pi/2$ pulse puts the qubit on the equator of the Bloch sphere. If the resonator state has many photons (colored Bloch vectors), the qubit will dephase by the dispersive interaction. At a revival time $t = \pi/\chi$, the Bloch vectors associated with odd photon numbers (blue) will have acquired a π phase shift, while the evens (red) will have acquired $2\pi n$ of phase. At this time, a final $\pi/2$ maps the parity information onto the qubit state. A measurement of the qubit state thus makes a projective parity measurement of the resonator state.

With these conventions, a number of useful relations hold. Most importantly, the density matrix of a given state is given by an integral over the Wigner function [21] as

$$\rho = \frac{2}{\pi} \int W(\alpha) D(\alpha) \hat{P} D^{\dagger}(\alpha) d\alpha^2 \tag{3.18}$$

Thus by probing the Wigner function experimentally, we gain direct insight into the density matrix of the oscillator's state. It can further be shown that the Q_0 function is related to the Wigner function as

$$Q_0(\alpha) = \frac{2}{\pi} \int W(\beta) e^{-2|\alpha-\beta|^2} d\beta^2. \tag{3.19}$$

This convolution is simply a Gaussian filter over W. Therefore, we expect the Wigner function is more sensitive to detecting structure in the IQ plane. Indeed, the Wigner function has an additional, useful detection property for quantum states: no oscillator classical state can have negativity in its Wigner function [82]. It has also been demonstrated theoretically that a negative Wigner function can be a resource for a quantum information processing speed-up [83, 84].

In order to assemble a state's Wigner function, we could in principle measure each Q_n and compute Equation 3.15. However, this requires tens of P_n's to be measured at each point on the IQ grid which is burdensome. Instead, the dispersive interaction gives us the opportunity to make projective measurements of $\hat{P}$ directly [81].

Figure 3.5 shows how a projective parity measurement is conducted with the dispersive Hamiltonian, used for Rydberg atoms with CQED [81] and for transmon atoms with cQED [68]. The goal of the protocol is to flip the qubit if and only if the resonator is in an even (or odd) parity state. The measurement begins with an unselective $\pi/2$ pulse on the qubit (FWHM $\gg N\chi$) that brings the qubit's Bloch vector to the equator. As we saw earlier, if many Fock states in the resonator are populated, the qubit no longer has a well defined frequency. Consequently, each Bloch vector associated with a different Fock state will acquire phase a different rate, $\phi = \hat{n}\chi t$ [85]. A second $\pi/2$ pulse will become more ineffective as these states spread out, appearing as a Gaussian T_2 decay. Yet, this system revives in a very special way after a characteristic time $T_p = \pi/\chi$ [68]. Examining the total state at $t = T_p$, we have

$$|\psi(t = T_p)\rangle = \sum_n C_n \left(|g, n\rangle + e^{\imath\pi\hat{n}}|e, n\rangle\right). \tag{3.20}$$

We see that at the time T_p, each odd Fock state acquires a π phase shift, while each even Fock state returns to the initial point on the Bloch equator (2π phase). Therefore, a second $\pi/2$ pulse, along the same axis will bring the even subspace to the excited state, while the odd subspace is rotated to the ground state. To summarize, this protocol transforms the system as

$$\sum_n C_n|g,n\rangle \Rightarrow \sum_{n\in\text{odds}} C_n|g,n\rangle + \sum_{n\in\text{evens}} C_n|e,n\rangle. \tag{3.21}$$

Now, the probability of detecting the qubit in the excited state (P_e) is directly related to the probability that the resonator had an even parity. So the expectation of the parity operator is simply now

$$\langle\hat{P}\rangle \propto P_e - P_g. \tag{3.22}$$

The lack of equality in the above expression arises from our inability to conduct this parity mapping and qubit readout with unit efficiency. However, we can calibrate out these inefficiencies by taking tomography of a known state, such as the vacuum state, and normalizing our tomography to the visibility of this signal [68]. While this lacks the robustness required for claiming violating quantum measurement inequalities [79], it is often useful to separate out state preparation fidelity from tomographic errors.

As shown in Figure 3.5, the full protocol for performing Wigner tomography in the dispersive regime of cQED is a combination of parity measurements and displacements on the resonator. It is illustrative to compare the distributions across Figure 3.2, Figure 3.3, and Figure 3.5 to see how the same resonator state can be described in many ways.

3.2.4 Flying state tomography

An important class of techniques have been developed to perform tomography on photonic states that are not confined to resonators but rather traveling down a measurement chain [86, 87]. Once a state is 'flying', the experimentalist may lack many of the tools we previously took for granted, including coherent control over the mode (access to $D(\alpha)$), a photon-number resolving detector (access to P_n), or a direct parity meter (access to $\langle\hat{P}\rangle$). Instead, the complete density matrix of a propagating field can be reconstructed using a technique known as optical homodyne tomography.

Homodyne detection is implemented by combining a field under study (E_s) with a strong local oscillator ($E_\text{LO}e^{-\imath\omega t+\imath\phi}$) at a beam splitter [87], which produces two outputs

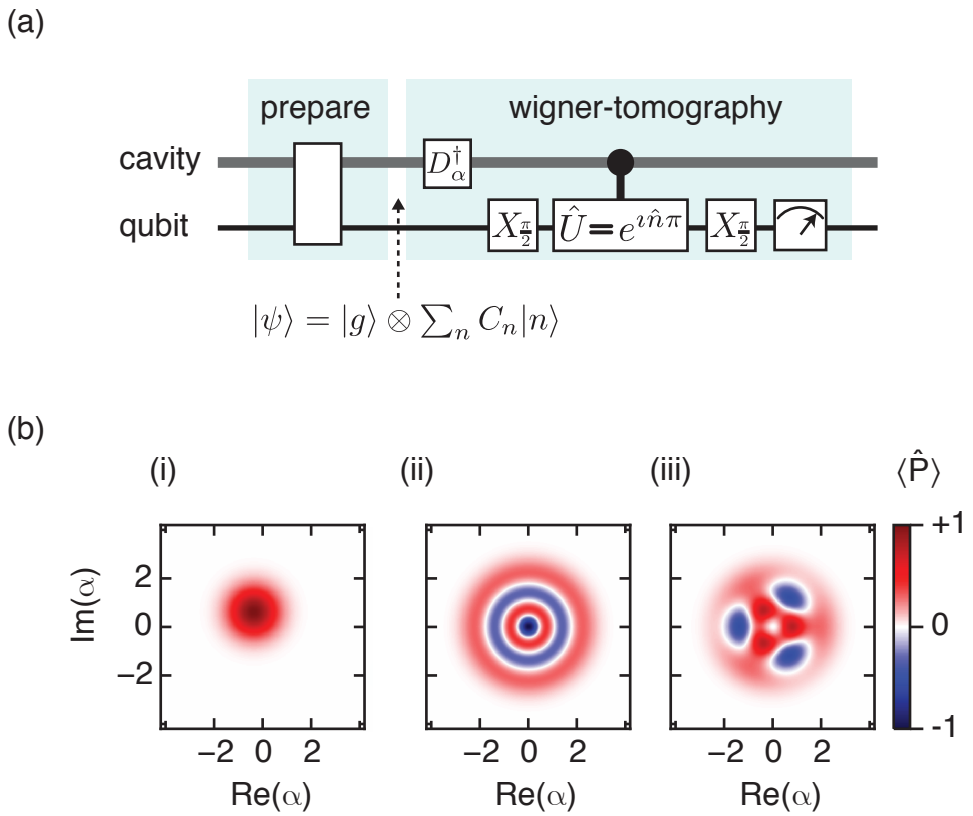

Figure 3.5: Wigner tomography in cQED. (a) Experimental sequence to perform Wigner tomography on a resonator state. As in the sequence for Husimi-Q functions, we begin with some arbitrary state in the resonator that is unentangled with the qubit. Like Q-functions, Wigner tomography is measured across different displacement values α. A displacement of $D^\dagger(\alpha) = D(-\alpha)$ brings a section of the Hilbert space interest to the origin. Then, two unselective qubit $\pi/2$ pulses, separated by a delay time $t = \pi/\chi$, maps the parity of the resonator to the qubit state. Measurements are repeated to acquire the quasiprobability distribution across many values of the displaced mode. **(b)** Examples of Wigner functions. The Wigner representation of the resonator states previously considered in Figure 3.2 and Figure 3.3. The Wigner function can reveal more information than either of these techniques. **(i)** A coherent state of $\beta = 1i$ has a smaller Gaussian width in a Wigner function as compared to the Husimi Q distribution, making Wigner a more sensitive technique for resolving small differences in amplitude or phase. **(ii)** The Wigner function of the $|3\rangle$ Fock state again has no further information compared to P_n or the Q function. However, an important feature of negativity in the Wigner function clearly distinguishes this state from a classical one. **(iii)** The superposition of $|0\rangle$ and $|3\rangle$ is distinguished from a statistical mixture by the existence of a rotational asymmetry and distinct regions of negativity in the quasiprobability distribution.

that, for balanced detection (using a 50/50 beam splitter), are given by

$$E_{\pm} = \frac{1}{\sqrt{2}}(E_{\mathrm{LO}}e^{-\imath\omega t+\imath\phi} \pm E_{\mathrm{s}}). \tag{3.23}$$

In optical detection schemes, these arms are measured by sensitive square-law detectors. If the field under study has quadratures that oscillate at ω, the time dependence is averaged out from the signals. Subtracting the outputs from the two detectors gives the experimentalist access to

$$|E_-|^2 - |E_+|^2 = 2E_{\mathrm{LO}}E_{\mathrm{s}}(\phi). \tag{3.24}$$

Varying the phase of the LO traces out the statistics of the field under study across the IQ plane [87]. Alternatively, performing a heterodyne measurement ($\omega_{\mathrm{s}} \neq \omega_{\mathrm{LO}}$) reveals both quadratures in parallel, at the cost of a quanta of added noise.

To be more precise, we can define a set of scaled, rotated quadratures [87], as

$$\begin{aligned} \hat{x}_\phi &= \frac{1}{\sqrt{2\bar{n}_{\mathrm{LO}}}}\left(\hat{X}\cos\phi + \hat{Y}\sin\phi\right) \\ \hat{y}_\phi &= \frac{1}{\sqrt{2\bar{n}_{\mathrm{LO}}}}\left(-\hat{X}\sin\phi + \hat{Y}\cos\phi\right) \end{aligned} \tag{3.25}$$

where $\hat{X}, \hat{Y}$ are defined as in Equation 2.16. Our homodyne protocol consists of a series of measurements to obtain a distribution at each ϕ that is a histogram of amplitudes $P_\phi(X_\phi)$. Because the probability distribution of any observable is given by an integral over the state's Wigner function, we have that

$$P_\phi(x_\phi) = \int_{-\infty}^{\infty} W(-x_\phi\cos\phi + y_\phi, x_\phi\sin\phi + y_\phi\cos\phi)dy_\phi. \tag{3.26}$$

The Wigner function can be obtained by inverting the above integral with a Radon transform [88]. Treating noise, detector inefficiencies, and finite numbers of measurements can also be treated by approximate inversion techniques [87] such as the maximum likelihood method [89].

For detectors that are linear, as opposed to square-law, a similar set techniques are available [90]. If we count the number of integrated measurements that fall in an IQ-bin, e.g. $[\mathcal{R}(\alpha_i + \varepsilon), \mathcal{I}(\alpha_i + \varepsilon)]$, we have essentially measured the overlap of the signal under study with a coherent state with amplitude α_i. By the definition of the Husimi Q function

(Eq. 3.7), we recognize that this measurement probes Q_0 for a traveling wave. Next, we consider an important type of linear detector-based flying state tomography, the dispersive readout scheme of cQED [64].

Dispersive readout as tomography

Performing a measurement of the qubit state in the dispersive regime of cQED can be accomplished by interrogating a strongly-coupled, harmonic readout mode. As described in Section 2.5, we analyze the output field of the readout mode in order to discriminate the qubit state-dependent phase imparted during the interaction time. In the following discussion, we relate this concept to the types of tomography considered here.

We can write the input-output relations [91] for a resonator populated with some state $A(t)$ as

$$a_{\mathrm{out}}(t) = \sqrt{\kappa}A(t) - a_{\mathrm{in}}(t), \tag{3.27}$$

where a_{in} and a_{out} are input and output modes, respectively (for details, see for instance [90]). We integrate that signal with a Heaviside step windowed function $f(t) = \sqrt{\kappa}e^{-\kappa t/2\Theta(t)}$ to obtain our signal mode [92] as

$$a = \int f(t)a_{\mathrm{out}}(t)dt. \tag{3.28}$$

Our linear amplification chain provides gain (G) to our signal and introduces a noise mode $\hat{h}$ that acts as a noise term so that our final complex amplitude signal operator is given by

$$\hat{S} = \sqrt{G}(a + \hat{h}) \tag{3.29}$$

The resulting histograms are a Husimi Q function on $\hat{S}$ which are scaled from the original signal quasiprobability distribution as $Q_{\mathrm{out}}(S)$ [90], so that

$$Q_{\mathrm{out}}(\sqrt{G}\alpha) = \frac{1}{G}Q_{\mathrm{in}}(\alpha) \tag{3.30}$$

The added noise from the vacuum mode can be shown to enter as a convolution, which for the Gaussian states typically used for readout, only results in in a broadening of the Gaussian distribution, as a thermal field. For signal chains that contain low-noise HEMT amplifiers, the full added thermal field corresponds to $\sim 20\,\mathrm{K}$, while for chains that include near-quantum limited parametric amplifiers, it can be below 1 K [93].

To perform a dispersive measurements on a transmon qubit, we require that the two measurement distributions $Q_{\text{out}}(S_g)$ and $Q_{\text{out}}(S_e)$ are well separated. As the resonator is displaced to some coherent state $|\beta\rangle$, we rely on the dispersive interaction to impart a relative phase shift conditional on the state of the qubit [64]. The resu broadened Gaussian histograms as $\delta\phi \sim \chi\tau$ where τ is some the effective signal decay time on the order of $\bar{n}/\kappa$. Two coherent states of equal amplitude, but rotated by $\delta\phi$ have the separation

$$|\langle\beta e^{\imath\delta\phi}|\beta\rangle|^2 = e^{-|\beta-\beta e^{\imath\delta\phi}|^2} = e^{-2|\beta|^2\sin^2(\phi/2)} \tag{3.31}$$

Importantly, for strong projective measurements, we see that for a given phase shift, a larger amplitude coherent tone will be a more effective measurement. However, if the system has nonlinearity in the readout chain, either in the readout resonator or in the saturation of the amplifier, there will be some optimal strength that is difficult to predict a priori.

3.3 Dispersive control

Now that we have several methods for quantifying non-classical fields within a resonator, we turn our attention to creating such states. We review a few recent ideas for creating target states in a harmonic oscillator by leveraging the dispersive interaction. First, we present a method for mapping the superposition state of a qubit onto the phase of a displaced oscillator state, the so-called QCMap gate [94]. QCMap is a powerful technique to create a superposition of many Fock states in a single gate application [68]. Next, we show how individual Fock states can be manipulated with a Selective-on Number Arbitrary Phase (SNAP) gate [69, 95]. SNAP can be used to build arbitrary states in a stepwise fashion, similar to the SWAP gates discussed in Section 2.5.1.

3.3.1 QCMap gate

Essentially, the QCMap works in the reverse of the parity measurement we presented in Section 3.2.3. Rather than map the parity of the resonator onto the state of the qubit for detection, we map the state of the qubit onto the parity of a displaced resonator state [94]. In particular, QCMap can be used to put qubit states of the form $|\psi\rangle_q = C_g|g\rangle + C_e|e\rangle$ onto superpositions of coherent states $|\psi\rangle_r = C_g|\beta\rangle + C_e|-\beta\rangle$. If the qubit had been in a equal superposition, $C_g = \pm C_e$, the resonator is taken to a parity eigenstate, having a either

all even photons (+) or odd photons (−), while preserving Poissonian statistics centered around $|\beta|^2$. Such a state is commonly referred to as a cat state [11], since the phase of a large coherent state approaches a classical variable. Indeed, the size of the resulting superposition is arbitrary in the gate's functionality and is only set by system imperfections. Therefore, QCMap is an interesting testbed for quantum to classical transitions [68], in addition to being a potentially useful quantum memory operation [70], as we consider at the conclusion of this chapter.

To perform a QCMap operation, we initialize the system with the qubit in $|\psi\rangle_q$ and the resonator in a coherent state $|\beta\rangle$, such that the total system state vector is

$$|\psi\rangle = (C_g|g\rangle + C_e|e\rangle) \otimes |\beta\rangle \tag{3.32}$$

The dispersive interaction will evolve the ground and excited states of the combined system with a frequency difference χ that we can absorb into the definition of the coherent state

$$|\psi(t)\rangle = C_g|g, \beta\rangle + C_e|e, \beta e^{\imath\chi t}\rangle. \tag{3.33}$$

After a time $T_p = \pi/\chi$, again the dispersive Hamiltonian will yield a π phase shift between the two subspaces, leaving

$$|\psi(t = T_p)\rangle = C_g|g, \beta\rangle + C_e|e, -\beta\rangle. \tag{3.34}$$

At this point, the system is in a Schrödinger cat state [11], since measuring the two-level state of the qubit would provide complete information over the nearly-classical coherent state phase variable. In analogy to the famous Gedanken experiment, the qubit acts as a spontaneously decaying atom which determines the fate of our feline-like phase.

We complete the QCMap gate by removing the entanglement between qubit and resonator. This is done in two steps. First, a non-selective displacement $D(\beta)$ is performed on the resonator to yield

$$|\psi\rangle = C_g|g, 2\beta\rangle + C_e|e, 0\rangle. \tag{3.35}$$

Then, a qubit rotation that is selective on the zeroth Fock state, as in Section 3.2.2, takes $|e, 0\rangle \rightarrow |g, 0\rangle$, leaving

$$|\psi\rangle = |g\rangle \otimes (C_g|2\beta\rangle + e^{\imath\phi}C_e|0\rangle), \tag{3.36}$$

where the phase term accounts for a Berry phase that can be acquired depending on the relative trajectory of the qubit rotation. The resonator is left in a state that is commonly

referred to as an amplitude-cat [11] for obvious reasons. A final displacement $D(-\beta)$ restores the symmetry to the system, and, fixing the Berry phase at $\phi = 0$, gives

$$|\psi\rangle = |g\rangle \otimes (C_g|\beta\rangle + C_e|-\beta\rangle). \tag{3.37}$$

In a pioneering experiment [68], this procedure was confirmed to take an arbitrary qubit state to an arbitrary resonator state of the above form. Additionally, extensions of the simple QCMap gate can be constructed for evolution times $t = T_p/m$, which can be used to create m-legged cat states. We discuss the connection between these states and error correction in the final section of this chapter.

3.3.2 SNAP gate

The Selective-on Number Arbitrary Phase (SNAP) gate allows for universal quantum control over a harmonic oscillator by making active use of the dispersive interaction [69, 95]. A SNAP gate is constructed by driving the qubit on a closed trajectory on its Bloch sphere. The backaction of the enclosed area imparts a Barry phase on the system $|g\rangle \rightarrow e^{\imath\phi}|g\rangle$ [96]. The key observation for SNAP is that the qubit only undergoes such an evolution conditionally on a Fock state in the resonator, taking $|g, m\rangle \rightarrow e^{\imath\phi}|g, m\rangle$. This phase accumulation is differential between the selected Fock state and the rest of the resonator's state vector [95]. Classical drives on the resonator can be used to interfere these differential phases. By interleaving displacements with SNAP rotations then, one can build up complex quantum sates in the resonator. For instance, a single SNAP gate and two displacements on the resonator is sufficient to generate an $N = 1$ Fock state in the resonator [69]. We present this example in detail to get an understanding of the SNAP framework.

An intuition for the protocol can be gained by considering a qubit trajectory that is along a single axis, e.g. a 2π-pulse along the qubit's x-axis. This great-circle trajectory accumulates a π phase shift on the state [96]. Therefore, if the pulse is selective on the m^{th} Fock state, the amplitude C_m will acquire a sign flip [69]. An additional small displacement can be thought of as a mixing of neighboring Fock states, which might now be out of phase and therefore interfere in a nontrivial way. In practice, the size of the displacement operations are numerically optimized to maximize the fidelity of the final state [95].

We show how these operations can be combined explicitly for the creation of a Fock state. First, a displacement of $D(1.14)$ on the resonator generates a coherent state in the resonator that has

$$\begin{aligned}|\psi\rangle_r =& 0.522|0\rangle + 0.595|1\rangle + 0.480|2\rangle \\ &+ 0.316|3\rangle + 0.180|4\rangle + \mathcal{O}(0.1)[\geq |5\rangle].\end{aligned} \tag{3.38}$$

The qubit rotation imparts a Barry phase of $\phi = 2\pi$ on the $|0\rangle$ state, leaving the resonator in

$$\begin{aligned}|\psi\rangle_r =& -0.522|0\rangle + 0.595|1\rangle + 0.480|2\rangle \\ &+ 0.316|3\rangle + 0.180|4\rangle + \mathcal{O}(0.1)[\geq |5\rangle].\end{aligned} \tag{3.39}$$

A final displacement operation $D(-0.56)$ takes the resonator to

$$\begin{aligned}|\psi\rangle_r =& -0.048|0\rangle + 0.990|1\rangle + 0.003|2\rangle \\ &+ 0.133|3\rangle + 0.002|4\rangle + \mathcal{O}(0.01)[\geq |5\rangle].\end{aligned} \tag{3.40}$$

Indeed, a perfect set of operations can prepare the $N = 1$ Fock state with $P_1 = 0.98$ [95]. This preparation fidelity can be further improved by additional SNAP operations. Unfortunately, as we discuss in Chapter 6, system imperfections can limit the resulting state fidelity before the fundamental limits of these operator-level considerations. It is worth remarking too that the nontrivial statistics of the small remaining population $P_3 \gg \sum_{n\neq 1} P_n$ arises from the interference effects inherent in the SNAP gate.

For a full proof of the universality of this protocol, we refer the reader to [95]. However, we present a simpler argument here based on continuous variables quantum computation [97]. Because it is straightforward to impart an infinitesimal phase on each number state, we can scale the imparted phases such that they are polynomial in n. We can thus generate an artificial n^{th}-order nonlinearity. This was actually demonstrated with SNAP experimentally for a fourth-order nonlinearity in [69]. Because such a nonlinearity causes increasing orders of operators by commutation [97], e.g.

$$\left[K(\hat{X}^2 + \hat{Y}^2)^2, \hat{X}\right] = \frac{1}{2}\left(\hat{X}^2\hat{Y} + \hat{Y}\hat{X}^2 - 2\hat{Y}^3\right), \tag{3.41}$$

we simply need to alternate SNAP gates will classical drives to synthesize an arbitrarily high order Hamiltonian [97].

So far, we have seen how to characterize and control the Hilbert space of our linear,

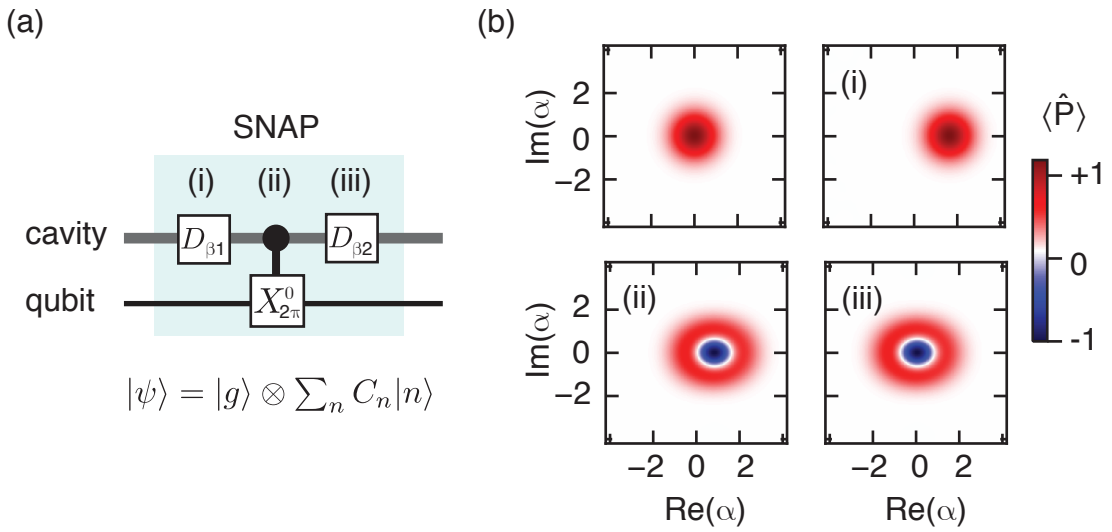

Figure 3.6: Creating nonclassical states via SNAP. (a) An experimental sequence for arbitrary state preparation in a resonator via SNAP. This technique interleaves classical displacements on the resonator with number-selective Berry phases on the qubit. Because the Berry phase is number-selective, resonator Fock states can be interfered by applications of the displacement operator, which can leave the resonator in a highly nonclassical state. **(b)** Step-by-step creation of a Fock state via two displacements and a single qubit rotation. A coherent state is generated from driving the resonator with classical drives. By rotating the phase on the vacuum state by π, the resonator is left in a displaced $|1\rangle$ Fock state. A final displacement returns the Fock state to the origin.

continuous variables resonator. To explore the utility of such a resource, in Section 3.5, we review a proposal for quantum error correction for oscillators [70] and experimental progress towards its realization. First though, we put on solid footing why such schemes are necessary.

3.4 Decoherence in an oscillator

Quantum states in resonators are always eventually spoiled by interactions with the environment. For instance, resonator photons can be exchanged with a thermal bath, or the phase of a quantum superposition can be randomized by unitary evolution. The cost of relying on the large Hilbert space of an oscillator is that the sensitivity to these interactions increases rapidly for macroscopic superposition states [11].

In this section, the effect of energy exchange between a general resonator density matrix

and a thermal bath is considered, treating the resonator as an open quantum system. Phase noise is treated in a similar manner, introducing a phase scattering process with the bath to compute its effects.

Previously, we evoked terms like an energy decay rate κ without a rigorous quantum mechanical description. In order to recover that description, we rely on the Lindblad form of the quantum master equation (QME) [35]. This allows us to solve for the evolution of the density matrix of the resonator given some spurious process. The model assumes the existence of a bath system whose degrees of freedom are sufficiently numerous that the evolution of the bath is not greatly affected by its interaction with the resonator (Markov approximation) [35]. Under this condition, the generic Lindblad form of the QME gives the evolution of the resonator density matrix as

$$\frac{d\rho}{dt} = \frac{-\imath}{\hbar}\left[\hat{H}, \rho\right] + \sum_{k\neq 0}\left(\hat{L}_k\rho\hat{L}_k^\dagger - \frac{1}{2}\hat{L}_k^\dagger\hat{L}_k\rho - \frac{1}{2}\rho\hat{L}_k^\dagger\hat{L}_k\right), \tag{3.42}$$

where L_k are jump operators which describe the interaction with the bath. Specific examples of these decoherence mechanisms are given next.

3.4.1 Energy decay

The basic form of energy damping is an exchange interaction between the resonator and a bath [35] as

$$\hat{H}_{int} = \sum_k \Omega_k^*\hat{c}_k^\dagger\hat{a} + \Omega_k\hat{c}_k\hat{a}^\dagger, \tag{3.43}$$

where the rates Ω_k determine the amount energy exchange. We can define a set of jump operators $\hat{L}_\uparrow$, $\hat{L}_\downarrow$ that account for the resonator gaining or losing a photon from a bath [35]. These are

$$\hat{L}_\uparrow = \sqrt{\kappa_\uparrow}\hat{a}^\dagger \tag{3.44a}$$

$$\hat{L}_\downarrow = \sqrt{\kappa_\downarrow}\hat{a}. \tag{3.44b}$$

If the bath reservoir is a temperature T, Boltzmann's Law requires that these rates are related by a Boltzmann factor

$$\frac{\kappa_\uparrow}{\kappa_\downarrow} = e^{-\hbar\omega_0/k_bT} \tag{3.45}$$

where ω_0 is the frequency of the resonator and k_b is Boltzmann's constant. By Planck's Law, the thermal state should have an average number of photons in each mode as

$$n_{th} = \frac{1}{e^{\hbar\omega_0/k_bT} - 1} = \frac{1}{\kappa_\downarrow/\kappa_\uparrow - 1}. \tag{3.46}$$

Rearranging this expression gives

$$\kappa_\downarrow = (1 + n_{th})\kappa \tag{3.47a}$$

$$\kappa_\uparrow = n_{th}\kappa, \tag{3.47b}$$

where a single decay rate κ is used to normalize the up and down rates. We recognize the $\bar{n}\kappa$ terms to account for the hopping of a (thermally) displaced field.

We can write down a Lindblad equation to describe this evolution of the resonator under this interaction [35] as

$$\begin{aligned}\frac{d\rho}{dt} =& -\frac{\imath}{\hbar}\left[\hbar\omega_0\hat{a}^\dagger\hat{a}, \rho\right] \\ &- \frac{(1+n_{th})\kappa}{2}\left(\hat{a}^\dagger\hat{a}\rho + \rho\hat{a}^\dagger\hat{a} - 2\hat{a}\rho\hat{a}^\dagger\right) \\ &- \frac{n_{th}\kappa}{2}\left(\hat{a}\hat{a}^\dagger\rho + \rho\hat{a}\hat{a}^\dagger - 2\hat{a}^\dagger\rho\hat{a}\right).\end{aligned} \tag{3.48}$$

To go further, we can consider the populations of individual Fock states, essentially sandwiching the above expression as

$$\frac{dP_n}{dt} = \langle n|\frac{d\rho}{dt}|n\rangle, \tag{3.49}$$

which gives a rate equation for P_n [35] as

$$\frac{dP_n}{dt} = \Gamma_\uparrow P_{n+1}(t) + \Gamma_\downarrow P_{n-1}(t) - \left[\left(\frac{n}{n+1}\right)\Gamma_\uparrow + \left(\frac{n+1}{n}\right)\Gamma_\downarrow\right]P_n(t). \tag{3.50}$$

The rates are calculated to be

$$\Gamma_\uparrow = (1 + n_{th})(n+1)\kappa \tag{3.51a}$$

$$\Gamma_\downarrow = n_{th}n\kappa. \tag{3.51b}$$

In equilibrium, we require that the probabilities are stationary ($dP_n/dt \equiv 0$), which

immediately gives us a condition on the probabilities as a function of the thermal field

$$\frac{P_n}{P_{n-1}} = \frac{n_{th}}{1+n_{th}} \tag{3.52}$$

which is again a simple Boltzmann factor as one would naively expect.

Importantly though, Equation 3.50 allows us to consider states out of equilibrium [35]. If some state in the resonator has a mean number of photons $\bar{n} \neq n_{th}$, the state will evolve towards equilibrium as

$$\frac{d\bar{n}}{dt} = \sum_k k \frac{dP_k}{dt}(t) = -(\bar{n} - n_{th})\kappa. \tag{3.53}$$

This is a quite remarkable result, meaning that any excited state of the resonator will have an expected energy that decays as an exponential [20]

$$E(t) = \hbar\omega_0 \bar{n}(t) = \hbar\omega_0((\bar{n}_0 - n_{th})e^{-\kappa t} + n_{th}), \tag{3.54}$$

where $\bar{n}_0$ is the initial mean field in the state.

The exponential shape of Equation 3.54 is reminiscent of two-level system T_1 decays with $T_1 = 1/\kappa$ [39]. In fact, we can immediately conclude that if the resonator has $\bar{n}_0 = 1$, regardless of the actual distribution of P_n, the averaged energy decay will be equivalent to a T_1 experiment, provided that $\bar{n}(t)$ is the extracted quantity experimentally.

In general, the off diagonal components of ρ, which contain the coherences between Fock states, decay in a highly nontrivial manner under amplitude damping [11]. As an example, we consider the effect of energy decay on an equal superposition cat-state of the form $|\psi\rangle = \mathcal{N}(|\beta\rangle + |-\beta\rangle)$, the initial density matrix is

$$\rho(t=0) = \frac{1}{2}\left[|\beta\rangle\langle\beta| + |-\beta\rangle\langle-\beta| + |\beta\rangle\langle-\beta| + |-\beta\rangle\langle\beta|\right] \tag{3.55}$$

Here, the cross terms ($\rho_{[\beta,-\beta]}$ and $\rho_{[-\beta,\beta]}$) contain the coherences between the two coherent states. Under the action of Equation 3.61, the coherent state amplitudes acquire a trivial decay term [11]

$$|\beta(t)\rangle = |\beta e^{-\kappa t/2}\rangle \equiv |\tilde{\beta}\rangle. \tag{3.56}$$

However, the coherence between the coherent states decays much more rapidly [11], as

$$\rho_{[\beta,-\beta]}(t) = e^{-2\bar{n}(1-\exp(-\kappa t))}\rho_{[\tilde{\beta},-\tilde{\beta}]}(0). \tag{3.57}$$

Therefore, the true 'T_2' of the state, i.e. the rate of phase information loss, is for short times ($\kappa t \ll 1$) given by

$$T_2 \approx \frac{1}{2\bar{n}\kappa}. \tag{3.58}$$

For macroscopic superpositions, $\bar{n} \gg 1$. Therefore, $T_2 \ll T_1$, even though energy decay is the only decoherence mechanism present!

3.4.2 Phase noise

The Lindblad formalism is applicable to phase noise as well [35]. In this case, the interaction with the bath does not exchange resonator photons between the modes (as in the case of energy decay). Instead, the effect is a modification of the resonator's resonant frequency as a scattering process, in which a bath quantum is created or destroyed while the resonator photon number is conserved,

$$\hat{H}_{int} = \sum_k \Omega_k^* \hat{c}^\dagger \hat{a}^\dagger \hat{a} + \Omega_k \hat{c} \hat{a}^\dagger \hat{a} \tag{3.59}$$

where the rates Ω_k determine the amount of frequency perturbation by the reservoir. We can define a pair of jump operators that account for emitting and absorbing bath quanta in order to acquire exchange energy, but at zero temperature, we are left with a single operator

$$\hat{L}_\phi = \sqrt{2\Gamma_\phi}\hat{a}^\dagger \hat{a}. \tag{3.60a}$$

$$\tag{3.60b}$$

Here, the QME is given by [35]

$$\begin{aligned} \frac{d\rho}{dt} = &-\frac{\imath}{\hbar}\left[\hbar\omega_0 \hat{a}^\dagger \hat{a}, \rho\right] \\ &- \Gamma_\phi \left(\rho(\hat{a}^\dagger \hat{a})^2 + (\hat{a}^\dagger \hat{a})^2 \rho - 2\hat{a}^\dagger \hat{a} \rho \hat{a}^\dagger \hat{a}\right). \end{aligned} \tag{3.61}$$

We are particularly interested in the evolution of off-diagonal elements of the form

$$\frac{d\rho_{nm}}{dt} = \left(-\imath\omega_0(n-m) - \Gamma_\phi (n-m)^2\right)\rho_{nm}. \tag{3.62}$$

Again, we find an exponential damping of our solution. Here,

$$\rho_{nm}(t) = e^{-\imath\omega_0(n-m)t} e^{-\Gamma_\phi (n-m)^2 t} \tag{3.63}$$

We find that random modulations of the resonator frequency washes out coherence rapidly for distant coherences ($|n-m| \gg 1$). Therefore, macroscopic superpositions will be highly susceptible to dephasing. We can define a pure dephasing time $T_\phi = 1/\Gamma_\phi$, such that the total 'T_2' of the resonator is then

$$\frac{1}{T_2} = \frac{1}{2T_1} + \frac{1}{T_\phi} \tag{3.64}$$

However, we caution the reader that the simple decay of two level systems is only applicable to resonators when we truncate the Hilbert space of the resonator to the same number of levels as we will do in Chapter 6.

3.5 Quantum error correction on cat-codes

All quantum error correction schemes rely on storing quantum information across redundant degrees of freedom and accessing joint properties of the system to correct errors [98, e.g.]. It was recognized by Leghtas et al. [99] that because the Hilbert space of a resonator is infinite, a single resonator could provide a resource-efficient subspace for storing redundant quantum information. In this section, we present a code that corrects for photon-loss in cat states of a cQED resonator [70, 99]. These so-called cat-codes are the basis for a logical quantum computing scheme.

3.5.1 Cyclic photon-loss

Photon-loss is a dominant error channel in circuits [9, 100]. However, coherent states are eigenstates of the annihilation operator [21]. If a photon is lost from a resonator in a coherent state, nothing happens. Instead, the state deterministically loses amplitude at rate $\kappa/2$, which can be corrected after some time dt with a displacement of amplitude $\epsilon = \kappa dt/2$. Certainly, for a classical bit of information, this is an appealing property.

It turns out that superpositions of coherent states have an interesting consequence for photon-loss mechanisms too [99]. Consider the even parity eigenstate

$$|\psi\rangle = \frac{1}{\sqrt{2}}\left(|\beta\rangle + |-\beta\rangle\right). \tag{3.65}$$

Losing a photon in this state results in a phase flip,

$$\hat{a}|\psi\rangle = \frac{1}{\sqrt{2}}\left(|\beta\rangle - |-\beta\rangle\right). \tag{3.66}$$

This phase flip takes us to the odd parity subspace. Parity measurements therefore, can act as a photon-loss error detector, without collapsing the state since $|\psi\rangle$ remains always in a parity eigenstate [99]. Remarkably, this error tracking scheme has been experimentally demonstrated in cQED [80]. However, the two-legged cat [11] can only encode a classical bit of information (whether the parity is +1 or -1). To encode a quantum bit, each parity subspace needs to contain an entire logical Bloch sphere [99].

One basis that can encode superpositions within a parity subspace are four-legged cats. Two pairs of orthogonal coherent states form a PSK-like constellation to provides logical states $|0\rangle_L$ and $|1\rangle_L$ as

$$\begin{aligned} |0\rangle_L &= \mathcal{N}\left(|\beta\rangle + |-\beta\rangle\right) \\ |1\rangle_L &= \mathcal{N}\left(|\imath\beta\rangle + |-\imath\beta\rangle\right), \end{aligned} \tag{3.67}$$

where $\mathcal{N} \approx 1/\sqrt{2}$ since the states that form the basis are only approximately orthogonal. Now, a full quantum bit of information can be encoded in the state

$$|\psi\rangle_L = C_0|0\rangle_L + C_1|1\rangle_L. \tag{3.68}$$

This logical state is a four-legged cat, with phases and weights of each leg determining the projected vector on the logical Bloch sphere [70]. Because our logical states are chosen in the even parity subspace, all logical states have only even Fock weights [11], as

$$|\psi\rangle_L = \sum_{n\in\text{evens}} C_n|n\rangle \tag{3.69}$$

Therefore the loss of a single photon will leave us in an odd parity basis. It is convenient to define logical error states [70] as

$$\begin{aligned} |\tilde{0}\rangle_L &= \mathcal{N}\left(|\beta\rangle - |-\beta\rangle\right) \\ |\tilde{1}\rangle_L &= \mathcal{N}\left(|\imath\beta\rangle - |-\imath\beta\rangle\right). \end{aligned} \tag{3.70}$$

Detecting any of these error states will indicate that an error has occurred in the memory.

To see how errors can be decoded, consider the action of the annihilation operator

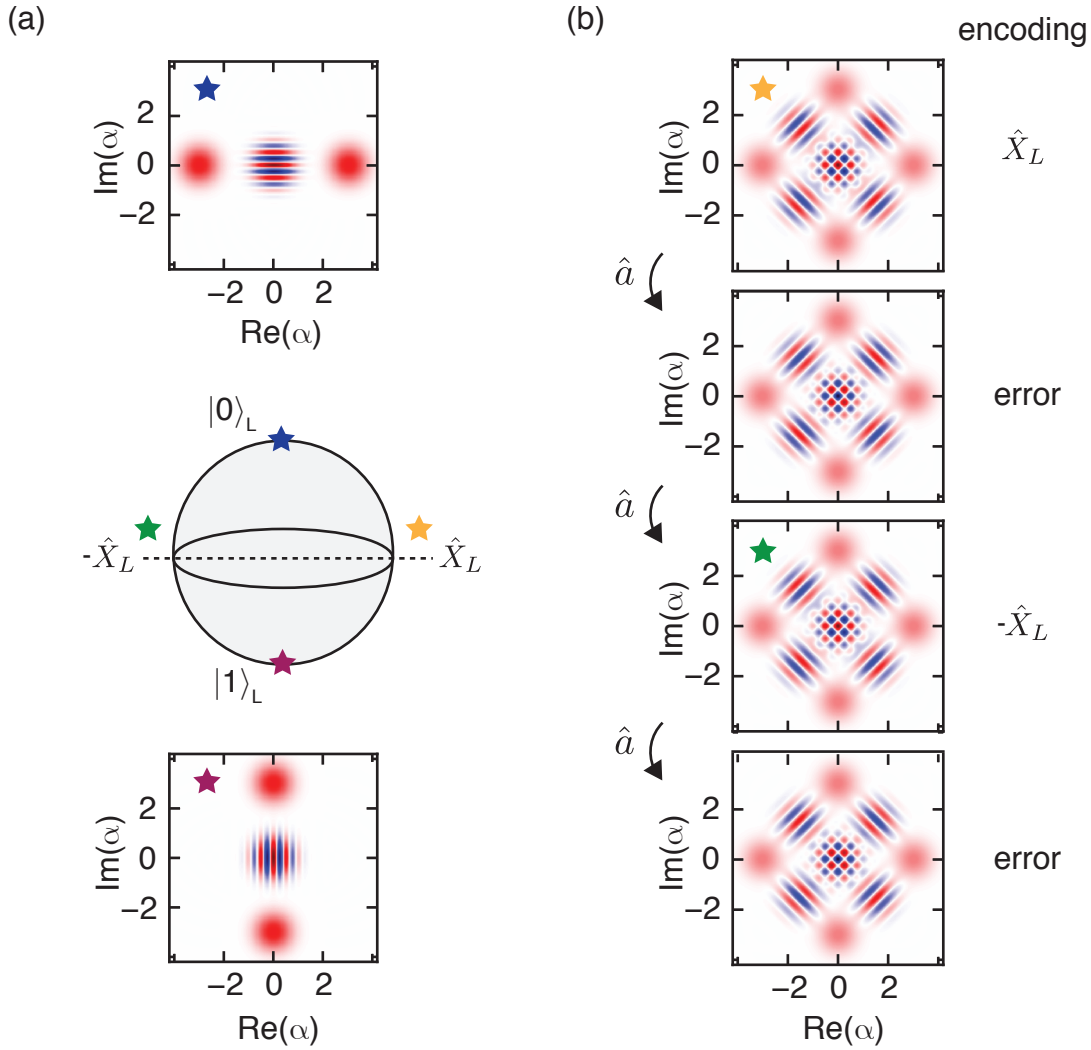

Figure 3.7: Cat-code logical qubit encoding. (a) The cardinal points on a logical Bloch sphere are taken to be the even superposition of real valued coherent states $|\pm beta\rangle$ and imaginary valued coherent states $|\pm ibeta\rangle$, as defined in Equation 3.70. The Wigner function of the logical states $|0\rangle_L$ (blue star) and $|1\rangle_L$ are shown for $|\beta| = 3$. **(b)** The effect of repeated photon loss events on an encoded qubit state. At the origin, we see that every photon loss event flips the parity of the state at the origin. After one loss, the negative parity here indicates an error state. However, a second photon loss even leads to an undetected error, since the state is back in the logical basis but at a new point on the logical Bloch sphere.

on the logical qubit state. We define a counter state $|\psi^{(k)}\rangle_L$ in order to keep track of successive photon loss events:

$$|\psi^{(k)}\rangle_L \equiv (\hat{a})^k |\psi\rangle_L. \tag{3.71}$$

Remembering that for coherent states $\hat{a}|\alpha\rangle = \alpha|\alpha\rangle$, we encounter a series of phase flips for the logical qubit

$$|\psi^{(0)}\rangle_L = C_0|0\rangle_L + C_1|1\rangle_L \tag{3.72a}$$
$$|\psi^{(1)}\rangle_L = C_0|\tilde{0}\rangle_L + \imath C_1|\tilde{1}\rangle_L \tag{3.72b}$$
$$|\psi^{(2)}\rangle_L = C_0|0\rangle_L - C_1|1\rangle_L \tag{3.72c}$$
$$|\psi^{(3)}\rangle_L = C_0|\tilde{0}\rangle_L - \imath C_1|\tilde{1}\rangle_L \tag{3.72d}$$
$$|\psi^{(4)}\rangle_L = C_0|0\rangle_L + C_1|1\rangle_L \tag{3.72e}$$

We recognize immediately that $|\psi^{(0)}\rangle_L = |\psi^{(4)}\rangle_L$. Therefore, the photon-loss process is cyclic in our basis [70]. Consequently, our state is never destroyed by photon loss, though the deterministic energy loss still occurs at rate κ. Techniques for overcoming energy decay are under active investigation [34]. These schemes rely on parametrically driving the system (Section 2.5.1) to 're-pump' the energy back into the resonator deterministically.

Major milestones still remain for the nascent cat-codes. Although encoding a qubit state onto a four-legged cat has been achieved [68], universal control over a logical cat-qubit, for instance using the techniques in [69], is an important next step for the scheme. Additionally, extending the QND error-tracking scheme [80] to a full quantum bit in a four-legged cat will be a significant accomplishment. Furthermore, building on the parametric drives already demonstrated for cat-codes [34] to demonstrate four-photon processes will be essential for the long-term success of oscillator-based QEC schemes. Finally, putting all of these pieces together, and showing overall gains in qubit performance, will be an incredible triumph.

CHAPTER 4

Photon boxes for cQED

Microwave resonators are an enabling technology in circuit QED. On their own, resonators can serve as a test bed for studying material losses [101–104]. The lessons gained from these measurements guide the development of cQED devices [105, 106]. Coupled to superconducting qubits, low-loss resonators can act as quantum memories [52, 75, 107] or as buses for exchanging quantum information between qubits [57, 58]. Resonators are also implemented to enable high fidelity measurements of qubit states [64] and to protect superconducting qubits from radiative losses [56].

This thesis is primarily concerned with one of these applications in particular, the quantum memory performance of a resonator. Therefore, we begin this chapter by presenting a generalized framework for to describe how loss mechanisms affect resonators. With that context, we present the design and development of a suite of low-loss microwave resonators and discuss the challenges and opportunities of a number of resonator geometries. This chapter culminates in the discovery of a viable technique for achieving state-of-the-art quantum memory performance for a superconducting-qubit-coupled device [52].

4.1 Quantizing a distributed mode

In earlier chapters, our circuits were compiled from discrete components such as inductors and capacitors. We showed how such elements could lead to a quantized Hamiltonian

which governed their quantum behavior. However, such lumped-element components do not exist in reality [108]. 'Inductors' and 'capacitors' are only approximate reactances, appropriate whenever the size of the component is much less than a wavelength. In practice, all circuit elements have some complex impedance that is neither completely capacitive nor inductive. (nor even purely reactive for that matter). Further, the concept of electromagnetic resonance is much more general than parallel or series circuits. We will see in this chapter that even with the same frequency and impedance, two microwave oscillators can have very different physical properties, influencing their utility for cQED.

We are left with the need to generalize our Hamiltonian description from before. While a careful treatment is possible for any specific arrangement of metal and dielectric, we use two observations to simplify our work here, which are derived explicitly for a transmission line in [14]. The first observation is that our electromagnetic mode should be well described by a wave velocity $\nu_p = 1/\sqrt{\ell c}$, where ℓ and c are the inductance and capacitance per unit length along some propagation axis (usually taken as $\hat{z}$). Then, our circuit has well defined flux and charge that oscillate at frequency ω as

$$\hat{\Phi}(\mathbf{x},t) = \hat{\Phi}(x,y)e^{j(\omega t+\beta z)} \tag{4.1a}$$

$$\hat{Q}(\mathbf{x},t) = \hat{Q}(x,y)e^{j(\omega t+\beta z)}, \tag{4.1b}$$

where $\beta = \omega/\nu_p$ is the propagation constant. The second observation that allows us to write down the quantum mechanical description of such a system is the treatment of boundary conditions [14]. Each resonator has a particular set of boundary conditions that forces these wave equations to a set of discrete eigenmodes. Otherwise, the system would lack a meaningful, discrete resonance.

These distinct eigenmodes form a complete, orthogonal set of functions for flux and charge in a closed geometry. A given distribution of electromagnetic energy can be written as a sum over these modes [14], such that

$$\hat{\Phi}(\mathbf{x},t) = \sum_n C_n \hat{\Phi}_n(x,y)e^{j(\omega_n t+\beta_n z)} \tag{4.2a}$$

$$\hat{Q}(\mathbf{x},t) = \sum_n C_n Q_n(x,y)e^{j(\omega_n t+\beta_n z)}. \tag{4.2b}$$

The boundary conditions and geometry of the resonator determine the frequency and spatial distribution of each eigenmode. We have a Hamiltonian for this generalized photon

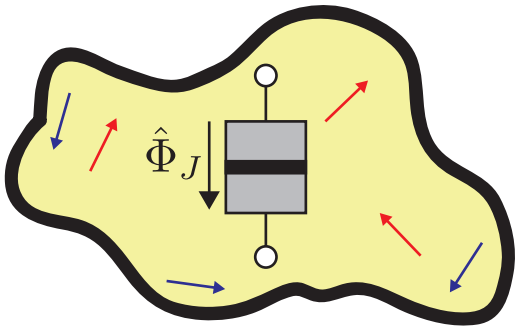

Figure 4.1: Black box quantization of a distributed mode. The LC oscillator circuits in Chapter 2 are useful toy models that capture the physics of QED. In reality however, only the Josephson element can usually be treated as a lumped element. Distributed resonators can have complicated mode structures, but once the eigenmodes of the linear system are known, we recover the equations of motion that would otherwise describe simple LC elements.

box as

$$\hat{H} = \hbar \sum_n \omega_n \hat{a}_n^\dagger \hat{a}_n, \tag{4.3}$$

where each eigenmode has a distinct, commuting set of creation and annihilation operators.

We can also generalize a circuit's coupling to a lumped-element Josephson junction in this language [109]. The linear part of the Josephson inductance may add another set of eigenmodes to the system and perturb the existing ones, but we can account for this using similar techniques as before [10]. We just need to re-diagonalize the modes. After the linear system has been solved, we only need to know the location of the junction ($\mathbf{x} = \mathbf{x_J}$) to find the flux across the junction (i.e. the difference in flux at $+\varepsilon$), as

$$\hat{\Phi}_J = \sum_n C_n \left(\hat{\Phi}_n(\mathbf{x_J}) - \hat{\Phi}_n(\mathbf{x_J} + \varepsilon) \right). \tag{4.4}$$

It is this quantity that we use the for nonlinear part of the Hamiltonian (Eq. 2.45) that gives us the rich physics we saw in the previous chapter. We see in later chapters explicitly how this term is calculated by full 3D simulations.

4.2 Quality factors and participation ratios

The quality factor of a resonator (Q) sets the ultimate limit for the resonator's performance as a quantum memory or bus. The quality factor is defined as

$$Q \equiv \omega \frac{\text{Total energy stored}}{\text{Total power dissipated}} = \omega T_1, \tag{4.5}$$

where T_1 is the energy decay time and is inversely related to the energy decay rate ($T_1 = 1/\kappa$). Therefore, the ultimate quantum coherence that a resonator can posses is $T_2 = 2T_1 = 2Q/\omega$. If a full circuit model is available, the quality factor can be calculated by

$$Q = \frac{1}{Z_0 \mathrm{Re}Y}\Big|_{\omega=\omega_0}, \tag{4.6}$$

where Z_0 is the characteristic impedance of the resonator (defined in Eq. 2.92).

As shown in Figure 4.2, many sources of loss can contribute to a total quality factor. The power dissipated in each of these loss mechanisms combines to make the the total power dissipated in the circuit equal to

$$\Gamma_{\text{tot}} = \sum_n \Gamma_n, \tag{4.7}$$

where each loss mechanism consumes power at rate Γ_n. Because the average total energy stored in the resonator is a single quantity, we can write the quality factor as

$$\frac{1}{Q} = \frac{1}{\omega E_{\text{tot}}} \sum_n \Gamma_n. \tag{4.8}$$

A more convenient way to express the phenomenology of many sources of loss adding to the total quality factor is to work in unitless quality factors defined as $Q_n = \omega E_{\text{tot}}/\Gamma_n$, so that the total quality factor can be expressed [110, e.g.] as

$$\frac{1}{Q} = \sum_n \frac{1}{Q_n}. \tag{4.9}$$

Note that Q_n is represents net result of source of loss, combining both the lossiness of the source and the sensitivity of the resonator to the loss mechanism. Changing geometries while holding all of the materials properties constant will change Q_n. Clearly, there is a need

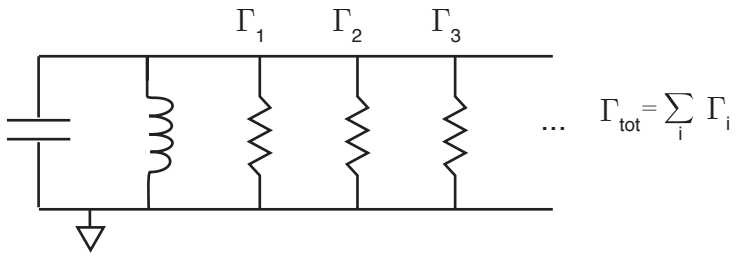

Figure 4.2: General loss mechanisms for a resonator. For a physical circuit, many loss mechanisms can contribute to the damping of energy in the system. The dissipation of each of these elements adds to the total dissipation rate of the circuit. We can make progress in understanding a given total dissipation rate through experiments which selectively probe one such mechanism, such as conductor loss.

to express the sensitivity of a given resonator to a certain loss mechanism independently of the lossiness of the given mechanism.

This notion is already common for cavity resonators limited by conductor loss, where a geometrical factor $\mathcal{G}$ is expressed in Ohms such that the observed quality factors are $Q \approx \mathcal{G}/R_{\square}$ [111], where $R_{\square}$ is the sheet resistance of the conductor used to fabricate the resonator. For typical waveguide cavity geometries and frequencies, $\mathcal{G} \approx 100\,\Omega$ such that typical room temperature conductors, e.g. copper with $R_{\square} \approx 0.1\,\Omega/_{\square}$, gives room temperature quality factors of $Q \approx 1000$. Designs with higher $\mathcal{G}$ achieve a higher Q for a given metal. We generalize this notion to generic loss mechanisms next, as participation ratios.

Participation ratios are a useful framework for quantifying loss in any device [112]. The idea is to use straightforward accounting to interpret decay rates in a way that educates a circuit designer about the losses in the system. These ratios can lead to surprising conclusions about what limits a given performance [105, 106]. Comparing many variations of one main geometry can test scaling hypotheses about certain loss mechanisms [104]. In addition, comparing results from two entirely different geometries can inform a circuit designer about different types of loss present in both.

To accomplish this accounting, we simply re-express Q_n to tease apart the geometry

dependence from the loss tangent of a mechanism, as a participation ratio

$$p_n = \frac{\text{Energy stored in mechanism}}{\text{Total energy stored}}. \tag{4.10}$$

Now, if the loss mechanism has a loss tangent $\tan\delta_n$, then

$$Q_n = \frac{1}{p_n \tan\delta_n} = \frac{q_n}{p_n}. \tag{4.11}$$

If the resonator stores all of its energy in a single degree of freedom its participation ratio is unity, $p_x = 1$, which implies that $Q = q_x$. The key to designing a low-loss circuit is to know what systems have high q_n and store as much of the energy there as possible. In subsection 4.2.3, we will see how $\mathcal{G}$ is explicitly connected to one of these ratios.

Let us look at a few classic loss mechanisms for a superconducting microwave resonator, using the language of participation ratios.

4.2.1 External loss

All resonators share a loss mechanism that is a direct consequence of coupling signals into and out-of such circuits [111]. If a circuit is coupled to a port, the real part of the port's admittance will damp the mode to some degree. In fact, it is a common technique to actually over-couple a cQED resonator for readout purposes. Here, we show how this arises for a simple toy model.

In Figure 4.3, an LC oscillator is capacitively coupled to a $50\,\Omega$ load, which can be an access channel for drives or a path for signal to leak into the measurement chain. Following Schuster [62], the coupling capacitor transforms the real impedance of the load, which we can recast as a parallel admittance as

$$Y_{ext} = \frac{1}{R + 1/j\omega C_{ext}} = \frac{j\omega C_{ext}}{1 + j\omega C_{ext} R}. \tag{4.12}$$

For weak coupling ($\omega C_{ext} \ll R$), Y_{ext} can be approximated as

$$Y_{ext} \approx j\omega C_{ext} + \omega^2 C_{ext}^2 R. \tag{4.13}$$

The total admittance of the circuit is then

$$Y_{tot} = \frac{1}{j\omega L} + j\omega C_{tot} + \omega^2 C_{ext}^2 R, \tag{4.14}$$

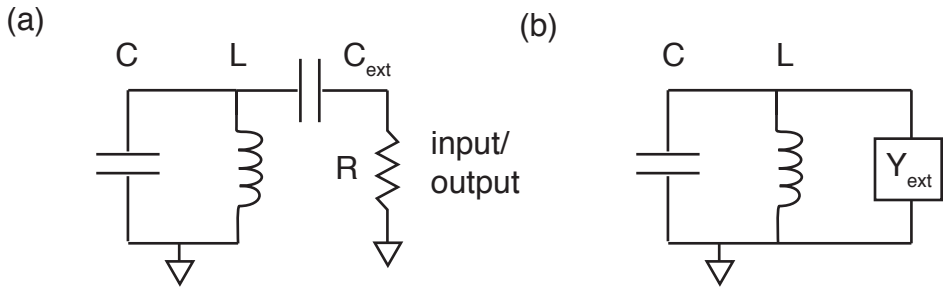

Figure 4.3: Treating external dissipation. (a) All systems which are probed by an external port are damped in the process. We introduce the toy model of an LC oscillator capacitively coupled to a 50 Ω load to capture this effect. **(b)** In order to solve for the induced dissipation rate on the resonator, we recast the series coupling impedance to a parallel admittance, whose real part enters the calculation for Q_{tot} as shown in this section.

where $C_{tot} = C + C_c$. To use Equation 4.6, we need the characteristic impedance

$$Z_0 \equiv \omega \mathrm{Im} Y' \big|_{\omega=\omega_0} = \sqrt{\frac{L}{C_{tot}}}, \tag{4.15}$$

since $\omega_0 = 1/\sqrt{LC_{tot}}$. Then, we are ready to express a quality factor for the circuit

$$Q_{ext} \approx \frac{1}{\omega_0^2 C_{ext}^2 Z_0 R}. \tag{4.16}$$

When coupling to distributed modes, the same idea from this toy model holds. Introducing a real impedance to the circuit for control or readout purposes will be associated with some external dissipation.

4.2.2 Dielectric loss

On resonance, a circuit stores an equal part of its energy in the mode's electric and magnetic fields [111]. Let us first quantify loss mechanisms which dissipate energy in the electrical quadrature in the form of lossy dielectrics. A good room temperature PCB has a dielectric loss of $\tan\delta \approx 2 \times 10^{-3}$ [113], while crystalline sapphire might have loss lower than $\tan\delta \lesssim 1 \times 10^{-6}$ [114, 115].

There are two main channels for dielectric loss in a cQED experiment. First, energy is stored in the substrate that holds the artificial atom itself [115]. In addition, electrical

energy is stored at the surface of the superconducting metals, e.g. an oxide layer ALO_x and at the surface of the substrate [105, 106]. Both of these electrical surfaces can be lossy.

These mechanisms are well described by participation ratios, albeit at very different scales. We compute the dielectric participation ratio as

$$p_{\text{diel}} = \frac{\int_{\text{diel}} \epsilon |E|^2 dV}{\int_{\text{tot}} \epsilon |E|^2 dV} \tag{4.17}$$

where the numerator integrates over the dielectric of interest, while the denominator accounts for all of the electrical energy stored in the device. Bulk dielectric participation ratios tend to be in the range of $p_{\text{diel}} \approx 0.01 - 1$, as we will enumerate in later sections for various geometries. Surface dielectrics, on the other hand, tend to have smaller participation by virtue of their significantly smaller physical volume.

It is often to useful to compute a simplified integral for surface participation. At a superconducting surface, the tangential component of the electric field must go to zero (so that no voltage builds up on the conducting surface). Therefore, we only need to consider the behavior of the perpendicular electric field at these interfaces. To calculate the electric field inside of the surface layer ($\mathbf{E}_{\text{surf}}$), we rely on the continuity of the $\mathbf{D}$-field to find $\mathbf{E}_{\text{surf}} = \mathbf{E}_{\text{vol}}(\epsilon_{\text{vol}}/\epsilon_{\text{surf}})$, where $\mathbf{E}_{\text{vol}}$ is the electric field in the vacuum. We can approximate the integral in Equation 4.18 for this type of surface interface, considering a thin oxide layer, as

$$p_{\text{diel}} \approx \frac{t_{\text{ox}} \int_{\text{surf}} |E_{\text{vol}}|^2 dA}{\epsilon_{r,\text{ox}} \int_{\text{tot}} |E_{\text{vol}}|^2 dV} \tag{4.18}$$

where t_{ox} is the surface oxide thickness, $\epsilon_{r,\text{ox}}$ is the relative dielectric constant, and E_0 is the field strength in the vacuum. We point out that if the interface had been different, e.g. metal-dielectric-metal, the above expression would require modifying the ratio of $\mathbf{E}_{\text{surf}}/\mathbf{E}_{\text{vol}}$ accordingly.

We can estimate the magnitude of the surface participation ratio for a generic resonator geometry by considering that the determining contribution is the ratio of volumes represented by $t_{\text{ox}}A$ and V, where A is the surface area of the resonator's conductor, and V is the total volume of the device. Therefore, a common rule-of-thumb estimation for p_{diel} of surface oxide is $p_{\text{diel}} \sim t_{\text{ox}}A/\epsilon_{r,\text{ox}}V$. For an infinite parallel plate capacitor, this expression

is exact, and p_{diel} reduces to a ratio of the oxide thickness to the plate separation L, as

$$p_{\mathrm{diel}} = 2t_{\mathrm{ox}}/L. \tag{4.19}$$

These rules of thumb are useful for estimating the performance of very different types of microwave resonators. We can see immediately for instance, if a resonator stores all of its electrical energy in a parallel plate-like element, a larger separation of electrodes will likely exhibit smaller participation and thus a smaller dissipation or a higher Q for the same materials properties.

Next, we will look at loss in the other quadrature (magnetic fields), with conductor loss. We will compare participation ratios for a number of different geometries in a later section.

4.2.3 Conductor loss

Conductor loss dominates the Q of most microwave resonators made with normal metal [111]. However, because we have access to superconductors for cQED experiments, we expect many orders of magnitude higher Q should be attainable [116]. Still, if our superconducting resonators have finite temperature [18, 117], contain non-equilibrium quasiparticles [118–120], or contain vortices [18], these devices will have some finite conductivity. Therefore, it is hard to exclude a limited conductivity of our resonators as a main source of dissipation in some situations.

We have already met the geometrical factor for cavity resonators $\mathcal{G}$. The definition of $\mathcal{G}$ in Ohms makes it difficult to treat on equal footing with other participation ratios. We define it here [111] to show how closely related the two concepts are

$$\mathcal{G} \equiv \frac{\omega\mu_0 \int_{\mathrm{tot}} |H|^2 dV}{\int_{\mathrm{surf}} |H|^2 dA}. \tag{4.20}$$

We recognize that there is again a surface to volume ratio at the core of this expression. The total magnetic quality factor is given by $Q_m = \mathcal{G}/R_{\square}$, and we can rearrange the above integral into unitless pieces as,

$$Q_m = \left(\frac{\omega\mu_0\delta}{R_{\square}}\right) \frac{\int_{\mathrm{tot}} |H|^2 dV}{\delta \int_{\mathrm{surf}} |H|^2 dA}, \tag{4.21}$$

where we have introduced a generic skin depth δ to the numerator and denominator that

represents the exponential decay of magnetic field into our conductor. In the parenthesis, we have a term $\omega\mu_0\delta$ which can be interpreted as a surface reactance X_S [121], since μ_0 has units of inductance per meter. Then, the quantity in the parenthesis is a unitless ratio of $X_S/R_\square$ which we can understand as an effective conductor quality factor q_{cond} for the metal [100]. For normal metals, $q_{cond} = 1$ [111]. In fact, switching to a more conductive normal metal increases Q by reducing the δ in the denominator of the integral-ratio. That unitless ratio of integrals is p_{cond}, as

$$p_{cond} = \frac{\delta \int_{\text{surf}} |H|^2 dA}{\int_{\text{tot}} |H|^2 dV}, \tag{4.22}$$

which we will explore in detail next.

The conductor participation ratio has a long history in superconducting circuits, where it also known as the kinetic inductance fraction (α) [122]. For a superconducting resonator, the correct δ is the penetration depth λ [121]. Because this parameter defines a circuit's sensitivity to conductor loss, it also describes the circuit's sensitivity to quasiparticles. Circuits with large p_{mag} are used as detectors for astronomy, called Microwave Kinetic Inductance Detectors (MKID's) [122], where quasiparticle signals are used to detect a photon flux.

Unlike dielectric participation ratios, p_{cond} can be revealed experimentally for a superconductor through direct means [121, 122], as we describe in detail in Chapter 5.

4.2.4 Contact resistance

Any cQED experiment is assembled from parts that are individually fabricated, for instance SMA connectors that route signals between devices and cabling [62]. The connections between components which carry RF energy can introduce dissipation in the form of spurious contact resistance at seams [123]. Seam loss is especially important whenever bolting two halves of a cavity together to form a high Q resonator [100, 124] or whenever assembling and introducing wire bonds to planar circuitry [125].

Following Brecht et al. [123], we model this loss as a generic conductance G whose loss-profile is constant as $g_\varnothing = G/L$ along a seam of length L. The conductance dG of a small section dl along the seam is

$$dG = g_\varnothing dl. \tag{4.23}$$

The incremental power dissipated by a small amount of current along dl by dG will be

$$dP = \frac{1}{2}\frac{(dI)^2}{dG} = \frac{1}{2}\frac{(J_\perp dl)^2}{g_\varnothing dl} = \frac{J_\perp^2 dl}{2g_\varnothing}, \tag{4.24}$$

where dI is the current flowing across dl, and the surface current $J_\perp$ is given by a magnetic field tangential to the current $H_\parallel$ as

$$J_\perp = \hat{n} \times H_\parallel. \tag{4.25}$$

Therefore, the total dissipated power can be written as

$$P_\varnothing = \int dP = \frac{1}{2g_\varnothing}\int H_\parallel^2 dl. \tag{4.26}$$

Then, the quality factor of the mode due to this loss mechanism [123] is

$$Q_\varnothing = \frac{\omega\mu_0 \int H^2 dV}{P_\varnothing} = \omega\mu_0 g_\varnothing \frac{\int H^2 dV}{\int H_\parallel^2 dl} = \frac{g_\varnothing}{y_\varnothing}. \tag{4.27}$$

The above expression has a very similar form as the participation ratios discussed earlier. However, allowing units in the dissipation term $g_\varnothing$, unlike $\tan\delta$ for example, prevents us from having to make further assumptions about the dissipation. Additionally, we can define an effective admittance per unit length for the seam as

$$y_\varnothing \equiv \frac{\int H_\parallel^2 dl}{\omega\mu_0 \int H^2 dV}. \tag{4.28}$$

The term $y_\varnothing$ acts like the participation ratio for seam loss, giving a quality factor that is inversely proportional to $y_\varnothing$ as

$$Q_\varnothing = \frac{g_\varnothing}{y_\varnothing}. \tag{4.29}$$

We observe that locating cavity joints at regions of small magnetic field, or at least small current density across the seam (small $y_\varnothing$), is important for maximizing $Q_\varnothing$ and thus Q_{tot} [123].

4.2.5 Summary of loss mechanisms

The examples in this section have not exhausted all of the possible dissipation mechanisms in cQED devices. However, participation-ratio accounting techniques are a general framework.

If a new loss mechanism is encountered, it can likely be described as an effective lossy capacitor (p_{diel}), lossy inductor (p_{cond}), or discrete conductance element $g_{\varnothing}$.

In the remainder of this chapter, we present four types of resonator that have applications to cQED. For each resonator, we provide derivations and estimates for the participation ratios studied here. In addition, we also explicitly state how Q_{ext} is calculated and understood for each device. Finally, we discuss how transmon-type qubits can be coupled to each type of photon box to realize cQED devices.

4.3 Planar resonators

Planar, thin-film resonators begin life as a bare dielectric wafer. Then, the conducting circuit is patterned on the wafer through either photolithography or electron-beam lithography. These steps are similar to the ones reviewed in a later chapter for transmon lithography. For now, let us consider the electrodynamics of one popular type of planar resonator, the CPW transmission line resonator [126, 127].

4.3.1 Resonant modes of a CPW

A transmission line is constructed from two conductors, where one acts as a ground plane and the other as a signal-carrying center-pin [111]. The impedance of the line Z_0 is determined by the inductance and capacitance per unit length as

$$Z_0 = \sqrt{\frac{\ell}{c}}. \tag{4.30}$$

Electromagnetic radiation traveling down such a transmission line a length z acquires phase as $e^{j\beta z}$. Upon encountering an impedance discontinuity ($Z \neq Z_0$), the signal is reflected with a complex reflection coefficient [111]

$$\frac{V^-}{V^+} = \frac{Z - Z_0}{Z + Z_0}. \tag{4.31}$$

where V^+, V^- are the incoming, outgoing waves. If the discontinuity is an short circuit ($Z = 0$) or an open circuit ($Z = \infty$) the magnitude of this reflection coefficient is unity, meaning that the boundary is equivalent to an infinitely sharp potential well.

Not surprisingly then, two such reflections (open-open, open-short, etc.) are sufficient to create a standing wave [62]. For the case of an open-open line, the fundamental

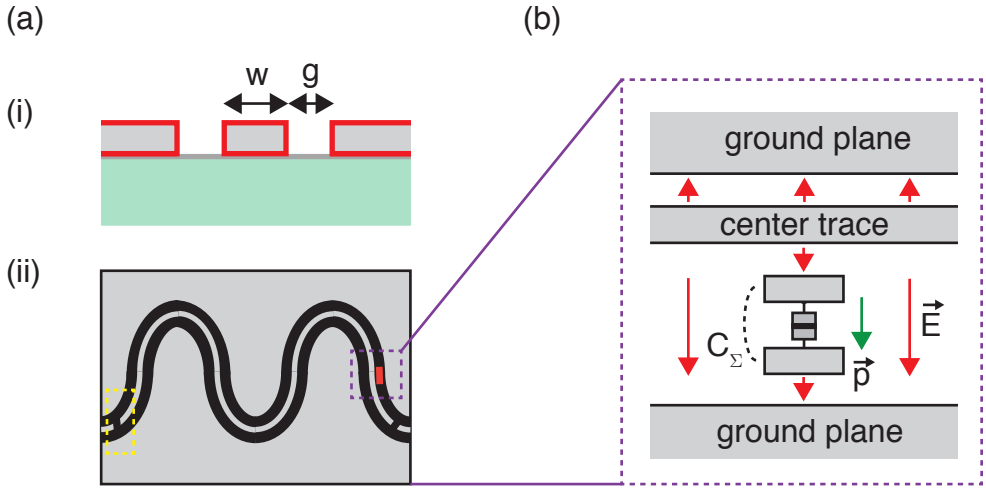

Figure 4.4: Planar resonators and transmons. **(a)** Cartoon of planar device. **(i)** Side view. Metal (silver), typically niobium or aluminum, is patterned on a substrate (green), typically silicon or sapphire. The impedance of resulting circuits is determined by the ratio of the width w of metal traces to the gap g separating the trace from the ground plane. The impact of lossy material (red outline) is also determined by the dimensions of the circuit. **(ii)** Top view. A gap in the center trace (yellow box) acts as a coupling capacitor and creates the conditions for resonance. The bend in the CPW line achieves a smaller physical package with negligible effect in the microwave domain. A transmon (red) is located between the center trace and ground plane. **(b)** Zoom of the transmon-resonator integration. The dynamics are mediated by the dipole coupling of the transmon element ($\mathbf{p}$) and the fields of the CPW mode ($\mathbf{E}$). The nonlinearity of the Josephson junction is shunted by the capacitance of the transmon (C_Σ).

resonance has a wavelength $\lambda_0 = 2L$, where L is the length of transmission line. If the boundary condition was instead open-short, the fundamental resonance occurs for $\lambda_0 = 4L$. Most planar resonators are one of these types.

For CPW resonators, a transmission line is formed by a central conductor of width w, separated by a gap g from a ground plane [127]. These values are chosen to achieve a certain characteristic impedance for the transmission line, usually $Z_0 \approx 50\,\Omega$. Typical values for CPW design parameters are $w \sim 10 - 100\,\mu$m and $g \sim 1 - 50\,\mu$m. State-of-the-art CPW resonators reach internal quality factors of $Q_{int} \sim 10^6$ [103].

4.3.2 Input-output coupling

We treated reflections from a resonator's open boundary condition as an infinite potential well in the previous subsection to aide in our quantization of planar circuits. However, to get microwave signals into and out-of CPW resonators, the impedance only ever approximates infinite. A common technique is to implement a small break in the center conductor [62, 128], introducing a gap between the resonator and the signal carrying transmission line. Then, the termination impedance is given by a coupling capacitance,

$$Z_c = 1/j\omega C_c. \tag{4.32}$$

We see that as C_c is reduced to zero, Z_c tends to infinity, and the reflection coefficient will return to unity. A full circuit model can predict an external quality factor Q_{ext} from the dimensions of the discontinuity [62]. However, because the two-dimensional treatment of planar circuits is an approximation, fringing fields may lead to spurious, unintended loss if not treated properly [128].

4.3.3 Planar transmons

Transmons on planar circuity tend to have dimensions that are much smaller than a wavelength ($50\,\mu\text{m} \ll \lambda \sim 5\,\text{mm}$) [129]. Therefore, a lumped-element approximation is well-suited to evaluate the Hamiltonian parameters, e.g. χ_{ij}, K_i. As shown in Figure 4.4, a capacitance network is typically used to calculate parameters [62, op. cit. Section 3.3], such as the transmon anharmonicity

$$K_q \approx \frac{e^2}{2C_\Sigma}, \tag{4.33}$$

where C_Σ is the capacitance of the total network given by

$$C_\Sigma = C_g + C_{||}, \tag{4.34}$$

and C_g the gate capacitance is from the center trace to the ground plane across the transmon and $C_{||}$ is the capacitance directly between the two transmon antenna pads. Additionally, the self-capacitance of the resonator C_r must be known in order to properly normalize the coupling strength.

The capacitance network can also be used to predict the magnitude of the cross-Kerr

coupling strength between qubit and resonator (χ_{rq}) and next order Hamiltonian terms [62, op. cit. Section 3.3]. For instance, the strength of the dispersive interaction is

$$\chi_{rq} \approx \frac{g^2 \omega_q}{4\Delta(\Delta - K_q)}, \tag{4.35}$$

where

$$g \equiv e\frac{C_g}{C_\Sigma}\sqrt{\frac{\omega_r}{2C_r}}. \tag{4.36}$$

The two-dimensional circuit approximation allows even complicated, many-transmon circuits to be designed. There has been a steady increase in the number of transmons on a planar circuit [16, and references therein], with current state-of-the-art circuits having nine individual transmon elements [46].

The performance of planar transmons has steadily improved too [16, and references therein]. Recent experiments have shown many transmon circuits where all of the transmons had $T_1 \gtrsim 20\,\mu$s [46]. Continued development of materials and designs for these circuits promises even more exciting physics results from this architecture.

4.3.4 Losses

Loss mechanisms in planar resonators and transmons have been the subject of many experimental investigations [103, 104, 130–133]. A common trend from these results is that larger features yield lower loss devices until a radiation limit [134] is reached. Careful participation ratio accounting allows different experimental groups to compare materials with a common set of explicit assumptions about a given loss mechanism [105, 131]. We give such a table at the end of this chapter (Table 4.2).

To approximate participation ratios for planar circuits, we can apply our rule-of-thumb estimates for a CPW's p_{diel} and p_{cond}. Consider the case of surface dielectric loss at the interface between the metal of the planar circuit and the vacuum between conductors. We can roughly approximate the capacitance of the CPW as a parallel plate capacitor. Then, for a CPW with gap size g (as Fig. 4.4), the interface would participate (Eq. 4.19) as $p_{diel} \sim 2t_{ox}/\epsilon_r g$, where $t_{ox} = 3\,$nm, $g = 10\,\mu$m and $\epsilon_r = 10$ [105], gives $p_{diel} \approx 3 \times 10^{-5}$. If instead, we consider the interface between the metal of the CPW and the substrate of the circuit, the boundary conditions give a factor of ϵ_r larger p_{diel}, indicating that this interface is particularly important for achieving high quality circuits.

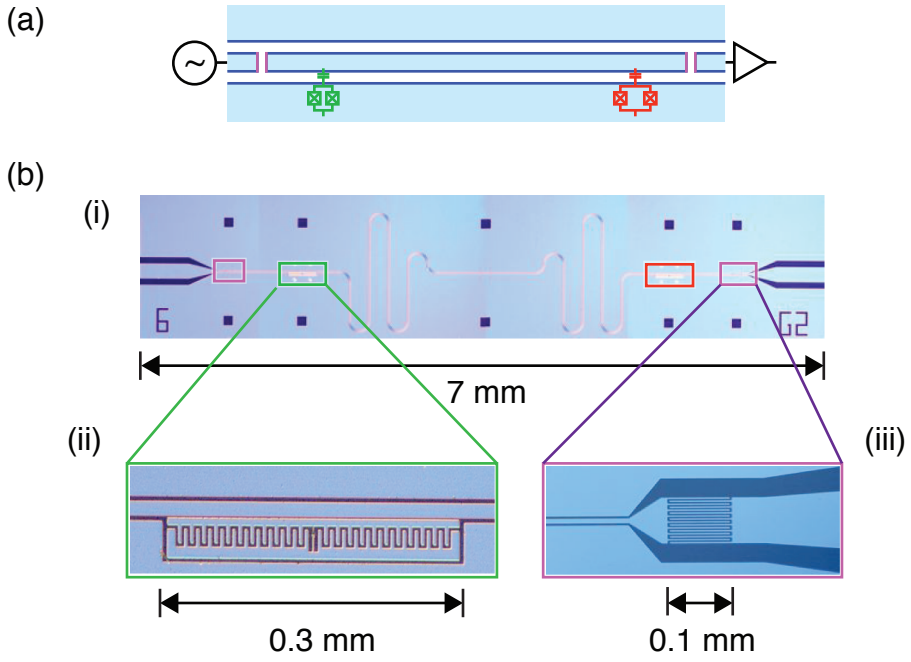

Figure 4.5: Experimental realization of planar circuit elements. (a) A schematic of a two-transmon cQED device. Control and measurement signals are input through the left, weak port, and measurement results are demodulated in transmission. **(b) (i)** Optical image of the physical circuit. **(ii)** A planar transmon is defined with an interdigitated capacitor. **(iii)** The output capacitor is also interdigitated to achieve sufficiently fast signal acquisition. (Figure used with permission from [58]. See Copyright Permissions.)

For a more accurate calculation, edge effects need to be treated carefully with a two-step technique [135]. The fields of larger features ($\delta x \gtrsim 10\,\mu$m) are numerically calculated independently of smaller features, such as edges. An interpolation is used based on local scaling arguments to arrive at a global participation ratio [135].

4.4 Rectangular cavity resonators

Since the pioneering experiments that demonstrated strong, dispersive coupling between a transmon and a three-dimensional (3D) rectangular cavity resonator [114], these cavities have become a staple of cQED, an architecture that has become known as '3D cQED.' We give an overview of these devices here.

One of the contributions made in this thesis has been the careful treatment of coupling signals to these devices as described in Section 4.4.2. Other important implementation details can be found in [43].

4.4.1 Resonant modes

Rectangular waveguides can be treated exactly in their three-dimensional propagating field profiles [111], unlike the two-dimensional transmission line circuits whose modes are treated by approximation. Given a single conductor with rectangular cross-section and dimensions (a, b), the fundamental propagating mode is the TE_{10}. The non-zero field components are

$$E_y = E_0 \sin \frac{\pi x}{a} e^{-j\beta z} \tag{4.37a}$$

$$H_z = H_0 \cos \frac{\pi x}{a} e^{-j\beta z} \tag{4.37b}$$

$$H_x = \frac{j\beta a}{\pi} H_0 \sin \frac{\pi x}{a} e^{-j\beta z}, \tag{4.37c}$$

where the wave impedance

$$Z_{\mathrm{TE}} \equiv -\frac{E_y}{H_x} = \frac{\omega\mu}{\beta} \tag{4.38}$$

relates the two fields such that the scaling between the electric and magnetic fields is

$$|E_0| = \frac{\omega\mu a}{\pi} |H_0|. \tag{4.39}$$

Like the planar transmission line, boundary conditions can establish resonances in the rectangular waveguide. If the waveguide is shorted on two planes, separated by a distance d, the frequency of the fundamental mode (TE_{101}) is

$$f_0 = \frac{c}{2\pi\sqrt{\mu_r \epsilon_r}} \sqrt{\left(\frac{\pi}{a}\right)^2 + \left(\frac{\pi}{d}\right)^2}. \tag{4.40}$$

For standard cQED frequencies ($f_0 \sim 10\,\mathrm{GHz}$), this corresponds to cavity dimensions of $a, d \sim 20\,\mathrm{mm}$ [114]. The fields of the mode are obtained from Equation 4.37 by mapping the $\hat{z}$ dependence into a sinusoid.

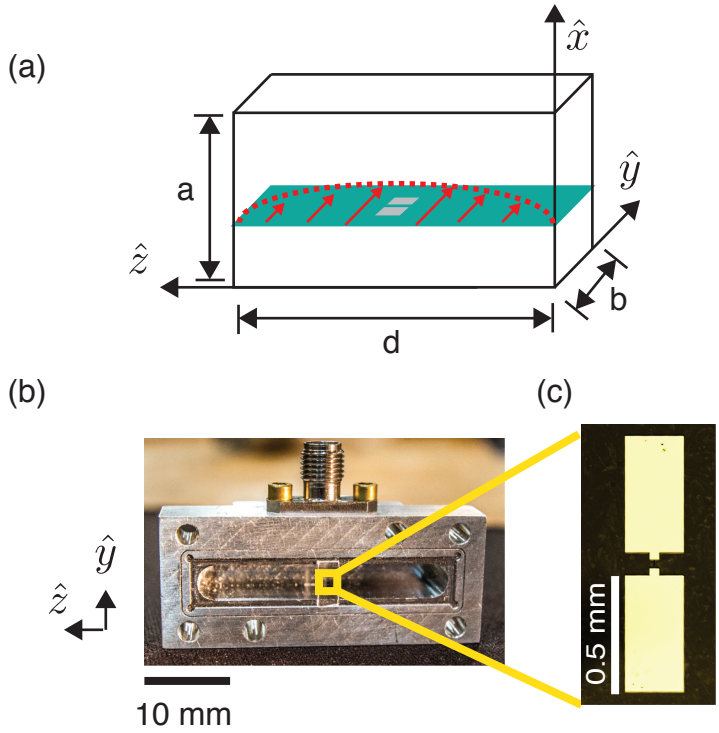

Figure 4.6: Rectangular cavities and the 3D transmon. **(a)** The dimensions of a rectangular cavity ($a \times b \times d$) determine the spectrum of resonant modes. A cartoon of the electric field of the fundamental TE_{011} mode is shown in red arrows. The transmon (silver) is located on a substrate (green). **(b)** Image of a 3D cQED device. An SMA connector delivers signals as described in Section 4.4.2. The sapphire chip that holds a transmon qubit is visible in the center of the cavity. **(c)** Optical microscope image of a 3D transmon. (Figure used with permission from [120]. See Copyright Permissions.)

4.4.2 Input-output coupling

A contribution to the understanding of the coupling mechanism for rectangular cavities was developed for this thesis. The scheme is shown in Figure 4.7 [114]. Coaxial transmission line (TL) carries signals between room-temperature and the device. At the device, an abrupt transition is made between the TL and a narrow section of circular waveguide of radius $r_0 \approx 1\,\text{mm}$, which delivers the signal to the cavity. Many waveguide modes are excited by the abrupt TL-waveguide transition. In particular, azimuthal symmetry allows any TM_{0m} mode of the waveguide to participate [136].

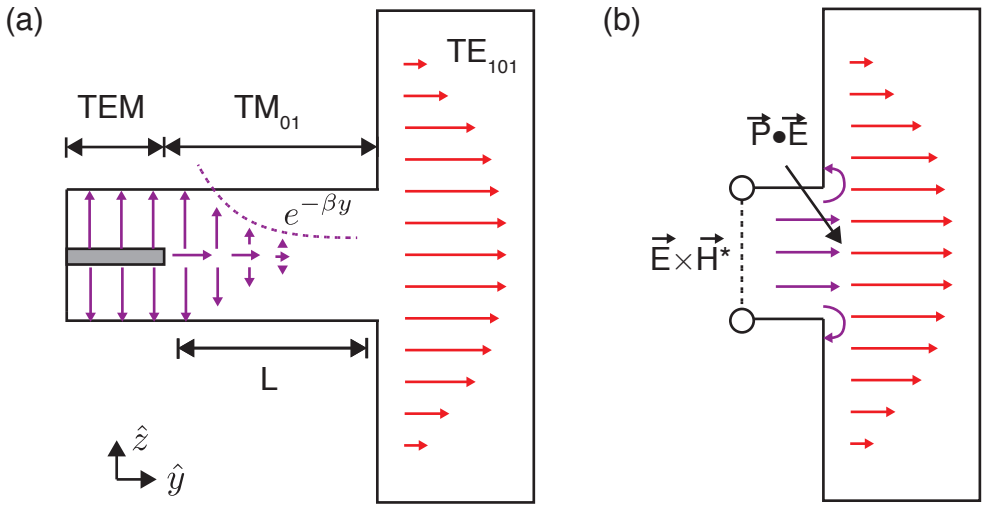

Figure 4.7: Input-output coupling for rectangular cavities. (a) Coupling to the rectangular cavity is achieved by transforming signals from the coaxial line (TEM) to a propagating circular waveguide mode (TM_{01}), which has a decay length given by the cutoff propagation constant β. **(b)** Coupling between the circular waveguide and the rectangular cavity is well-described by a circular aperture since the radius of the circular waveguide is small $r_0 \ll \lambda$. Then, the coupling is treated as a dipole excitation problem as shown in Equation 4.44.

Importantly, these TM_{0m} modes have propagation constants [111] given by

$$\beta_{TM0m} = \sqrt{k^2 - \left(\frac{p_{0m}}{r_0}\right)^2}, \tag{4.41}$$

where p_{0m} is the m^{th} zero of the zeroth Bessel function $J_0(x)$ (for instance, the first zero of this function occurs at $x = p_{01} \approx 2.41$). The propagation constants become imaginary when

$$\omega < \frac{p_{0m}c}{r_0}, \tag{4.42}$$

with c the speed of light. Below this cutoff frequency for a given mode, the corresponding signal component is exponentially attenuated in the length of the waveguide section. Because the TM_{01} mode has the lowest cutoff frequency, it dominates the transport of our signals. For the radius of sub-cutoff waveguide used for such cavities ($r_0 = 1.2\,\text{mm}$), the dominant mode has $|\beta_{TM01}| \approx 2\,\text{mm}^{-1}$, meaning that the propagating fields lose a factor of e in their amplitude every 0.5 mm of waveguide, or equivalently, that the propagating energy is reduced a factor of e every 0.25 mm of waveguide.

The external quality factor then should be expected to scale exponentially in the length of the waveguide section L as

$$Q_{ext} \propto e^{-2\beta_{TM01}L}. \tag{4.43}$$

Indeed, measurements confirm this scaling, as we show in Appendix C. To go further than a scaling-law argument, we need to consider the coupling between the circular waveguide and the rectangular cavity.

Bethe introduced a technique for describing coupling via aperture as a dipole radiation problem [137]. We recognize that our circular waveguide impinging on the rectangular waveguide resembles this problem closely [138]. For Bethe, the aperture was an infinitely thin sheet of metal separating two waveguides. This concept has been extended to the case of thick walls by considering the waveguide effects within the aperture [139]. We approximate the field of the TM_{01} waveguide at the cavity ($y = 0$) as the result of a circular aperture, which has the electric dipole moment [138] as

$$\mathbf{P} \approx \frac{2}{3}\epsilon_0 r_0^3 \mathcal{E} \delta^3(\mathbf{x} - \mathbf{x}_0)\hat{\mathbf{y}}, \tag{4.44}$$

where $\mathbf{x}_0$ is the location of the aperture, and $\mathcal{E}$ is the amplitude of the electric field of the TM_{01} mode with units of V/m. By treating the waveguide mode as a infinitesimal dipole element, we require that $r_0 \ll \lambda$.

To see how this dipole radiation affects our resonator, consider the expansion of the electric field in the cavity as

$$\mathbf{E} = \sum_i e_i \mathbf{E}_i, \tag{4.45}$$

where the convenient normalization is introduced [138] so that

$$\int \mathbf{E}_i \cdot \mathbf{E}_j dV = \delta_{i,j}. \tag{4.46}$$

Then, at the resonance frequency of mode i, the stored energy is

$$W_{tot} = 2W_e = 2\epsilon_0 |e_i|^2. \tag{4.47}$$

We point out that the amplitude e_0 has units of V$\sqrt{\text{m}}$ in order for the above relations to be valid. For the fundamental TE_{101} mode, we have

$$\mathbf{E}_0 = \frac{2}{\sqrt{abd}} \sin\frac{\pi x}{a} \sin\frac{\pi z}{d}\hat{\mathbf{y}}. \tag{4.48}$$

Now, let us consider driving the cavity on resonance with the fundamental mode (ω_0) with our dipole. An arbitrary current distribution in the cavity $\mathbf{J}$ (oscillating at ω_0) generates a field in the cavity dominated by the amplitude e_0 [138, op. cit. Eq. 7.132], given by

$$e_0 \approx -j\omega\mu_0 \frac{\int \mathbf{J}\cdot\mathbf{E}_0 dV}{k_0^2\left(\frac{1-j}{Q}\right)}, \tag{4.49}$$

where Q is the total quality factor of the resonator. The presence of a finite quality factor prevents the fields from diverging in the presence of our drive. Although, we have already seen that any real drive necessitates damping anyway: $Q = Q_{ext}$ if there are no other losses present.

Our dipole radiation is equivalent to the current $\mathbf{J} = j\omega_0\mathbf{P}$ [138]. Therefore, we can readily compute

$$\int \mathbf{J}\cdot\mathbf{E}_0 dV = j\omega_0 \int_V \left(\frac{2}{3}\epsilon_0 r_0^3 \mathcal{E}\delta^3(\mathbf{x}-\mathbf{x}_0)\right)\left(\frac{2}{\sqrt{abd}}\sin\frac{\pi x}{a}\sin\frac{\pi z}{d}\right)dV, \tag{4.50}$$

which gives an excitation amplitude for the mode of

$$|e_0| \approx \frac{\omega_0^2\mu_0 Q}{\sqrt{2}k_0^2}\left(\frac{2}{3}\epsilon_0 r_0^3\mathcal{E}\right)\left(\frac{2}{\sqrt{abd}}\sin\frac{\pi x_0}{a}\sin\frac{\pi z_0}{d}\right). \tag{4.51}$$

We can simplify the above expression using $k_0 = \omega_0\sqrt{\epsilon_0\mu_0}$ to cancel a few terms, leaving

$$|e_0| \approx \frac{4r_0^3 Q\mathcal{E}}{3\sqrt{2abd}}\sin\frac{\pi x_0}{a}\sin\frac{\pi z_0}{d}. \tag{4.52}$$

It is easily verified that our expression has the right units for the mode amplitude.

To finish the derivation, let us calculate the power radiated into the circular waveguide from the resonator. We can calculate this power via the Poynting vector [138] as

$$P_{rad} = 2\int (\mathbf{E}\times\mathbf{H})\cdot\hat{\mathbf{y}}dS. \tag{4.53}$$

The fields of the TM_{01} that contribute to the Poynting vector are

$$\mathbf{E}_\rho = -\frac{j\beta}{k_c}\mathcal{E}J_0'(k_c\rho)\hat{\rho} \tag{4.54a}$$

$$\mathbf{H}_\phi = -\frac{j\omega_0\epsilon_0}{k_c}\mathcal{E}J_0'(k_c\rho)\hat{\phi}, \tag{4.54b}$$

where β is $\beta_{TM01} \approx \imath k_c = \imath p_{01}/r_0$. We can make use of the fact that $J_0'(x) = -J_1(cx)$ and the useful identity for Bessel functions

$$\int_0^a \left(J_n(\frac{p_{nm}x}{a})\right)^2 xdx = \frac{a^2}{2} J_{n+1}^2(p_{nm}). \tag{4.55}$$

The power radiated into the waveguide is then

$$P_{rad} = \imath \left(\frac{2\pi\omega_0\epsilon_0 r_0^3 \mathcal{E}^2}{p_{01}}\right) J_2^2(p_{01}). \tag{4.56}$$

Here though, the Poynting vector is imaginary [111]. This means that terminating the cavity in a waveguide below cutoff only introduces reactance to the mode! None of the energy is actually dissipated, but the effective volume of the mode has increased. We can make sense of this result by remembering that an infinite transmission line is equivalent to a discrete termination by the characteristic impedance of the line. Below cutoff, the waveguide has an imaginary impedance as shown by Equation 4.56. Introducing an infinite sub-cutoff waveguide introduces no dissipation since all of the mode is eventually reflected.

In reality, it is the real impedance of our terminated coaxial line ($R = 50\,\Omega$) that introduces the dissipation to the system as

$$P_{dis} = \frac{V_0^2}{2R}, \tag{4.57}$$

where V_0 is the voltage on the transmission line, given by

$$V_0 = \mathcal{E}\varrho\frac{2\pi R}{\eta_0}(1-\Gamma), \tag{4.58}$$

and where ϱ is the radius of the inner conductor of the coax, $\eta_0 = \sqrt{\mu_0/\epsilon_0}$ is the vacuum impedance, and Γ is a reflection coefficient that we leave unevaluated for the time being. We point out that an analytical treatment of the fringing field can yield a value for Γ, as in [136].

Now, we have an external quality factor given by

$$Q_{ext} \approx \frac{2\omega\epsilon_0|e_0|^2}{P_{dis}} = 2\omega\epsilon_0 \left[\frac{4r_0^3 Q_{ext}\mathcal{E}}{3\sqrt{2abd}} \sin\frac{\pi x_0}{a} \sin\frac{\pi z_0}{d}\right]^2 \left[\frac{\eta_0}{2\pi\mathcal{E}\varrho R(1-\Gamma)}\right]^2 (2R) \tag{4.59}$$

Solving for Q_{ext}, simplifying the expression, and grouping terms, gives us

$$Q_{ext} \approx \frac{3}{8}\pi^2 \left[\frac{R(1-\Gamma)^2}{\omega\mu_0 r_0}\right] \left(\frac{abd}{r_0^3}\right) \left(\frac{\varrho^2}{r_0^2}\right) \left[\sin\frac{\pi x_0}{a}\sin\frac{\pi z_0}{d}\right]^{-1} \tag{4.60}$$

Let us walk through these terms one at a time. We observe that the term in the first bracket is a ratio of the termination resistance to an effective impedance of the dipole. The next term is a ratio of 'volumes' between the cavity and dipole. Then, we have a transformer term that accounts for the transformation to the coaxial line. Finally, all of these effects are modulated by the location of the aperture in the cavity.

Collecting all of the aperture radius terms in the denominator of Equation 4.60 gives $Q_{ext} \propto r_0^{-6}$. This is the scaling observed experimentally and in simulation, as reported in [123].

To evaluate our expression Q_{ext}, we use the values of the standard rectangular devices ($abd \approx 3 \times 10^3\,\text{mm}^3$) and apertures ($r_0 \approx 1\,\text{m}$) and coaxial lines ($\varrho \approx 0.4\,\text{mm}$) [114]. We expect then that the strongest coupling obtainable via this type of aperture coupling, for ($x_0 = a/2$, $z_0 = d/2$, $\Gamma = 0$), is $Q_{ext} \gtrsim 1000$. For the design shown in Figure 4.6, the coupler is actually offset from the maximum, centered at $x_0 = 0.12\,\text{in}$, which gives another factor of approximately four in Q_{ext}. Additionally, we expect some mismatch due to the the coaxial TL-waveguide. The observed maximum Q_{ext}, for the coaxial probe still within the circular waveguide, is $Q_{ext} \approx 10^4$. This suggests that discontinuity of the coax transition reflects approximately half the signal ($\Gamma \approx 1/2$).

An advantage of this coupling scheme is that the exponential nature of the scaling allows for a wide range of Q_{ext} to be achieved [140]. Additionally, the exactness of the TM_{01} mode, e.g. no breaks in the waveguide, prevents crosstalk and unwanted dissipation channels [134]. Therefore, large ratios of Q_{ext} can be designed into a single experiment, which is an enabling technique for many cQED experiments [80, e.g.].

4.4.3 3D transmon

By moving to a waveguide cavity, the effective mode volume is greatly increased. This gives the Q performance gain by decreasing the participation ratios [105, 106]. That larger volume necessitates a larger transmon in order to conserve the dipole coupling element g between resonator and qubit [114]. Unlike planar transmons though, 'radiation' losses are

suppressed by the fact that the 'package' of the 3D cavity is the resonator itself. Therefore, only the Hamiltonian dictates the size constraints on the device.

The 3D transmon has longer coherence ($T_1 \sim T_2 \sim 100\,\mu$s) than other superconducting qubits, likely for several reasons [114, 141]. First, rectangular waveguide cavities present a relatively a 'clean' RF environment for the transmon. In comparison to the packaging for planar transmons, the qubit sees no wirebonds, epoxy, or circuit board, all of which could present dissipation to planar transmons [62]. In addition, the larger dimensions of the 3D transmon are beneficial to the participation ratios of the mode [105, 106]. Precise calculations show that 3D transmons can be less sensitive to surface dielectric loss and to quasiparticles by an order of magnitude [105]. If these loss mechanisms are the root cause of dissipation in planar transmons, a similar factor for an improvement in lifetime should accompany the 3D transmon. Finally, the two transmon regimes store energy in their substrates at approximately equal proportions. Encouragingly, the high coherence obtained in 3D transmons effectively rules out bulk dielectric loss as a limiting factor for planar devices at their observed values.

'Scaling-up' 3D transmon circuits is one sense as easy as for planar circuits. For instance, [Sears APS] has shown preliminary results from an 3D architecture which has 48 transmon elements coupled to a single 3D cavity [142]. Implementing individual qubit control and readout with this architecture might be more of a challenge since the 'empty box' approach of rectangular cavities lends itself mostly to always-on couplings. Yet, clever proposals exist for leveraging that type of coupling for tailoring subsets of multi-qubit measurements as well as constructing many-qubit gates [143]. The 3D transmon thus poses a viable architecture for next-generation experiments with multi-qubit parity eigenstates and error correction [144].

Moreover, the flexibility of the 3D architecture lends itself to creativity in experimental implementation. For instance, waveguide Purcell filters have been integrated in such devices and exhibit fundamentally new spectral filtering [60]. These filters have led to record fidelities for QND measurements on cQED systems [60]. Having access to a 3D-distributed mode has made it possible to couple 3D transmons to new degrees of freedom, such as ferromagnetic magnons [145], opening the door to using new, coherent systems as quantum memories of transmon qubits [49, and references therein].

Finally, the 3D transmon can also be taken as a proof-of-principle demonstration that solid state qubits can be coupled to waveguide cavities, which themselves are interesting objects. Superconducting cavities can be significantly longer lived that state-of-the-art

superconducting qubits [116], reaching single photon lifetimes as long as 100 ms [146]. If these lifetimes can be combined with the strong coupling of cQED, a number of fascinating consequences will immediately follow, the first likely being the realization of extremely effective quantum memories [49]. However, as we show in the next subsection, the rectangular waveguide architecture might not be sufficiently robust for this vision.

4.4.4 Losses

Because the fields of a rectangular waveguide are analytically solvable, we can determine what dissipation is introduced to a rectangular cavity by a given loss mechanism. To simplify our discussion, we take the rectangular cavity dimensions ($a = 17.8\,\text{mm}$, $b = 5.1\,\text{mm}$, $d = 35.6\,\text{mm}$) [114] for this discussion.

Dielectric loss

Consider a layer of lossy dielectric on the walls of our cavity. For the TE_{101} mode, the field is constant in $\hat{y}$. Therefore, the (x, z) integrals in the definition of p_{diel} drop, leaving simply

$$p_{\text{diel}} = \frac{2t_{ox}}{\epsilon_r b} \tag{4.61}$$

where t_{ox} and ϵ_r are the thickness and relative dielectric constant of the dielectric layer. For typical assumptions [105], $t_{ox} = 3\,\text{nm}$, $\epsilon_r = 10$ and resonator size $b = 5\,\text{mm}$, we find $p_{\text{diel}} \sim 10^{-7}$. Therefore, a bad dielectric $q_{\text{diel}} \sim 10$ will limit these devices at the $Q \sim 10^8$ level.

Conductor loss

Similarly, the sensitivity to quasiparticles is readily available [100]. The integrals in p_{mag} are straightforward to evaluate using the definitions for H_x and H_z in Equation 4.37 giving

$$p_{\text{mag}} = \frac{\omega_0 \mu_0 \lambda}{\eta} \frac{2\pi^2(2a^3b + 2bd^3 + a^3d + ad^3)}{(kad)^3 b}. \tag{4.62}$$

For a penetration depth of 50 nm [100], we have a magnetic participation ratio of $p_{mag} = 3 \times 10^{-5}$.

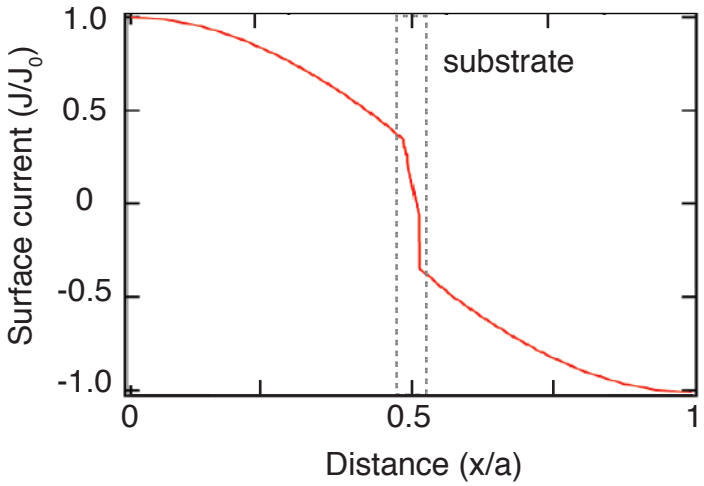

Figure 4.8: Perturbation of surface currents induced by substrate. The otherwise-sinusoidal surface currents acquire a sharp kink by the perturbation of the substrate. The slope of this curve is essentially the sensitivity to asymmetry for seam dissipation as Equation 4.64, which is significantly steeper than the unperturbed resonant mode.

Seam loss

Finally, the sensitivity of rectangular cavities to dissipative seams can be calculated as well [123]. Let us first assume that the two halves of the cavity are joined together in the $\hat{y}-\hat{z}$ plane as shown in Figure 4.6 [114]. The magnetic field terms that contribute to $y_{\varnothing}$ are those parallel to the seam. Along the seam at $z=0,d$ however, this component would be H_y, which is zero for the TE_{101} mode. Therefore, the relevant integral is only along the $\hat{n}=\hat{y}$ plane, where H_z is nonzero. We have then that

$$\begin{aligned} y_{\varnothing} &= \frac{1}{\omega\mu_0}\frac{2\int|H_z|^2dl}{\int|H|^2dV} = \frac{1}{\omega\mu_0}\frac{2\left(\frac{\pi}{k\eta a}\cos\frac{\pi x_{\varnothing}}{a}\right)^2\frac{2d}{\pi}}{(abd/(16\eta^2))} \\ &= \frac{1}{\omega\mu_0}\left(\frac{64\pi}{k^2a^3b}\right)\left[\cos\left(\frac{\pi x_{\varnothing}}{a}\right)\right]^2 \end{aligned} \tag{4.63}$$

For the choice of seam location $x_{\varnothing}=a/2$ (as we do in practice) the seam admittance goes to zero. Therefore, the design of the rectangular cavity is ideally such that no surface currents flow across the seam. However, we expect a machining accuracy of up to δx ~50 μm for these parts as the result with careful machining techniques. We can

approximate that the seam is located at $x_{\varnothing} = a/2 + \delta x$. The resulting seam participation is

$$y_{\varnothing} \approx \frac{1}{\omega \mu_0} \left(\frac{64\pi^3}{k^2 a^3 b} \right) \left(\frac{\delta x_{\varnothing}}{a} \right)^2 . \tag{4.64}$$

With the expected machining accuracy, we find that $y_{\varnothing} \approx 1.8\,/\Omega$m.

This result is actually quite alarming. For the rectangular geometry and aluminum cavity assembly process, we have 'calibrated' our g_{seam} by taking several measurements of quality factors at different, intentional δx values [123]. We find there that for aluminum $g_{seam} \approx 10^4\,/\Omega$m. Therefore, asymmetry at the level of machining tolerance may play a dominant role in rectangular cavities at the $Q_{\varnothing} \approx 5 \times 10^7$. Strikingly, this is average value for measured Q_{tot} in high purity aluminum, indicating that assembly may so far be the ultimate limit of these cavities.

An observation that made a substantial impact on the direction of this thesis is that the effect of seam loss is enhanced, as shown in Figure 4.8, by the presence of the dielectric substrate of the 3D transmon. This perturbation concentrates the surface currents at the location of the substrate, which is also usually also the location of the seam. The concentrated currents account for a factor of approximately ten in the slope of the cosine of H_z locally, which is equivalent to a factor of 100 in $y_{\varnothing}$. For a fixed seam quality, a machining tolerance of δx ~50 μm would therefore be expected to limit cavities at the level of $Q_{\varnothing} \approx 5 \times 10^5$, which is near the observed values for Q_{tot} for sapphire-loaded cavities. Simulations suggest that factors of two in $Q_{\varnothing}$ are possible for smaller pieces of dielectric. Rethinking the mode structure is therefore important for extending $Q_{tot} > 10^7$ in the presence of dielectric and seams.

4.5 Cylindrical cavity resonators

In order to avoid the issues of assembly, a new type of cavity was explored for cQED applications in this thesis [100]. We point out that is no coincidence that the long history of high quality factor cavity resonators began with measurements on cylindrical [147, and references therein]. In particular, it was recognized that one mode of these boxes, the TE_{011} mode [148], has no dielectric participation $p_{diel} = 0$ and zero currents flowing across the corners of the geometry. The latter observation allows the cylindrical cavity to be assembled as in Figure 4.9, with joints at the corners of the cylinder, such that p_{seam}=0.

By design, we are left with only conductor loss to limit the internal quality factor of the resonator [148].

With the rectangular cavities, we found that working with higher purity aluminum, and treating the surfaces before measurement, higher quality factors can be achieved [100]. Cylindrical cavities were developed during this thesis to probe what materials properties were improved via this technique, and moreover, if the extremely high quality factors $Q > 10^8$ were achievable in a standard cQED experimental setup. These type of resonators may eventually provide access to very long-lived resources in full cQED experiments. However, their primary purpose here is a platform for materials testing. At the conclusion of this section, we present a number of challenges that a cQED experimentalist faces toward qubit-integration.

4.5.1 Resonant modes

The fields of the TE_{011} mode are [111, op. cit. Eq. 6.54]

$$H_z = H_0 J_0(\frac{p_{11}\rho}{a}) \sin\frac{\pi z}{d} \tag{4.65a}$$

$$H_\rho = -\frac{\beta a H_0}{p_{11}} J_1(\frac{p_{11}\rho}{a}) \cos\frac{\pi z}{d} \tag{4.65b}$$

$$E_\phi = -\frac{jk\eta a H_0}{p_{11}} J_1(\frac{p_{11}\rho}{a}) \sin\frac{\pi z}{d}, \tag{4.65c}$$

where a is the radius, d is the height, and as before p_{nm} is the m^{th} zero of $J_n(x)$ ($p_{11} \approx 3.83$). Immediately, we recognize that at the side walls ($\rho = a$), $J_1(p_{11}) = 0$ implies that the electric field is zero there. In addition, on the lid ($z = 0, d$), $\sin(0) = 0$ or $\sin\pi = 0$ gives zero electric field there, too. Therefore, the electric field vanishes at all cavity surfaces. Hence,

$$p_{diel} = 0. \tag{4.66}$$

Furthermore, at the corners of the geometry, ($z = 0, d$) and ($\rho = a$), we have that

$$H_z\Big|_{\text{corner}} = H_\rho\Big|_{\text{corner}} = 0. \tag{4.67}$$

Therefore, a joint located at the corners of this cavity has $y_\varnothing = 0$ for this special mode. Combining these two ideas we thus expect the TE_{011} mode to be solely limited by conductor loss [148]. Furthermore, because of the large volume to surface ratio of the mode, we

expect p_{mag} to be quite small. For all of these reasons, we expect that the TE_{011} mode should indeed achieve high Q_{tot}.

Additionally, the cylindrical geometry supports a diversity of modes whose ordering can be altered by the ratio of the cavity diameter to its height [111]. However, at best, the TE_{011} mode is the sixth lowest mode [111, op. cit. Fig. 6.9]. The frequency of the mode is given by

$$f_0 = \frac{c}{2\pi}\sqrt{\left(\frac{p_{11}}{a}\right)^2 + \left(\frac{\pi z}{d}\right)^2} \tag{4.68}$$

Since $J_0'(x) = -J_1(x)$ though p_{11} is essentially double-counted in the ordering of modes [148]. Therefore, the TE_{011} is degenerate with pair of TM_{111} modes for all aspect ratios of cavity.

We use a shape perturbation to split this degeneracy [100]. We introduce a ring-shaped extrusion to the mode at the corners (visible in Fig. 4.9). There, the TE_{011} mode is largely unaffected, while the TM_{111} experiences an effectively smaller volume. We can calculate the expected shift for small perturbations [111, op. cit. Eq. 6.103] as

$$\frac{\delta\omega_0}{\omega_0} \approx \frac{\delta W_m - \delta W_e}{W_{tot}}. \tag{4.69}$$

Our ring has a rectangular cross section $(w \times w)$ so that

$$\begin{aligned}\delta W_m &\approx 2\mu_0 w^3 \int |H_\phi(\rho = a, z = 0, \phi)|^2 d\phi \\ &= \frac{2\pi\mu_0 a^2 w^3}{(p_{11})^2}\left[\omega_0\epsilon_0 E_0 J_2(p_{11})\right]^2.\end{aligned} \tag{4.70}$$

Whereas, the total energy is

$$W_{tot} = \frac{\pi\mu_0 a^4 d}{8(p_{11})^2}\left[\omega_0\epsilon_0 E_0 J_2(p_{11})\right]^2. \tag{4.71}$$

The ratio therefore gives

$$\frac{\delta\omega_0}{\omega_0} \approx \frac{16w^3}{a^2 d}. \tag{4.72}$$

We seek to perturb the modes only modestly ($\delta\omega_0/\omega_0 \sim 0.1\%$) and therefore, choose $w = 0.032\,\text{in}$. The above expression would predict an induced detuning of the modes of $\delta\omega_0/2\pi \approx 10\,\text{MHz}$ for $a = 0.75\,\text{in}$, $d = 0.95\,\text{in}$, and $\omega_0/2\pi = 11.5\,\text{GHz}$. However, other effects, such as asymmetry introduced by machining imprecision, can further split

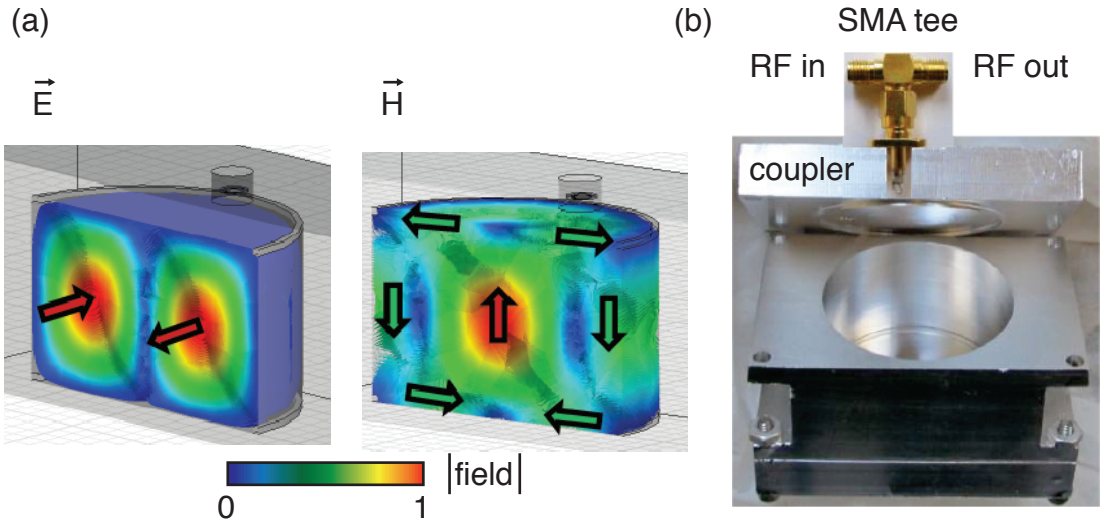

Figure 4.9: Cylindrical TE_{011} resonator. (a) Field distribution of the TE_{011} mode. The electric field is concentrated in a torus about the cylindrical $\hat{z}$axis, and the electric field vectors point along $\hat{\phi}$. It is visible on the plot that the electric field goes to zero on all the cavity wall. The magnetic field is zero at the the corners of the cavity and a maximum at the center. **(b)** Physical realization of the cylindrical cavity. Two lids close the cylindrical cavity along the region of minimum magnetic field. Additionally, the small ring perturbation on the lids, which detunes the degenerate TM_{111} modes, is visible. An SMA tee allows this cavity to be measured with the shunt technique. The coupling from SMA to cavity is accomplished via a loop coupler as described in Section 4.5.2. (Figure used with permission from [100]. See Copyright Permissions.)

degeneracies at this small of a limit. The above estimates serve as a lower bound then for the splitting between modes. Experimentally, we observe a detuning between TE_{011} and TM_{111} modes of $\delta\omega/2\pi \approx 30\,\text{MHz}$.

The other modes of the cylinder are useful to study many dissipation mechanisms at once, since they will all have various sensitivities to materials and assembly. For instance, if the TE_{011} mode is significantly higher Q than any of these other modes, we require loss mechanisms beyond conductor loss to explain the other modes (see Table 4.2) [100].

4.5.2 Input-output coupling

As shown in Figure 4.10, coupling to the cylindrical cavity is achieved in a similar manner as before (see Sec. 4.4.2). However, due to the special configuration of the TE_{011} mode, magnetic dipole coupling is required here. Additionally, several other considerations are

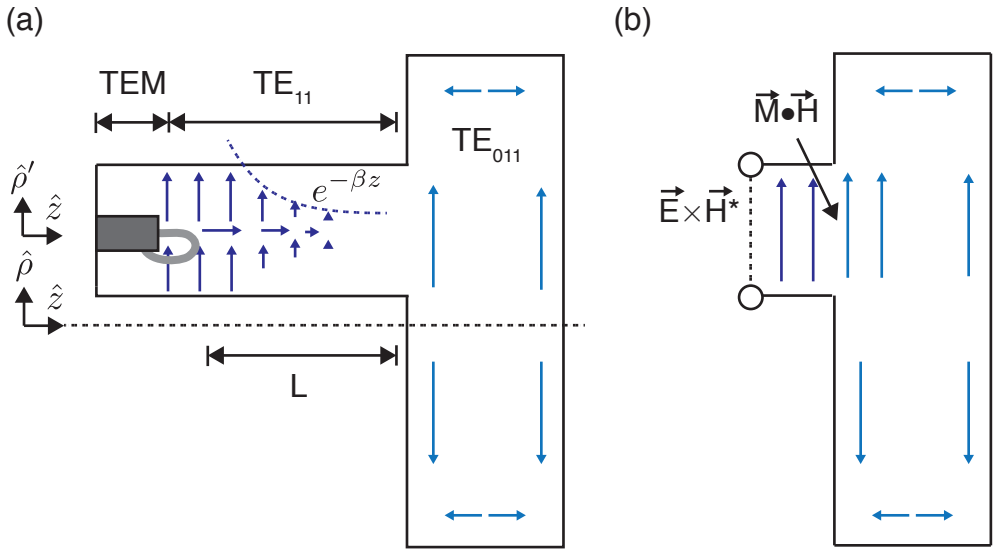

Figure 4.10: Input-output coupling for cylindrical cavities. (a) Coupling to the cylindrical TE_{011} is accomplished in an analogous manner to the rectangular cavity geometry. The center pin of a coaxial cable is soldered to the outer shield, forming a loop. The dipole moment of the loop is aligned to the local orientation of the magnetic field of the cavity. A propagating circulating waveguide mode (TE_{11}) translates this dipole moment to the resonator with an exponentially reduced amplitude. **(b)** A circular aperture acts as magnetic dipole in the cavity.

taken into account when implementing a coupling scheme for the cylindrical cavity. In particular, the presence of the TM_{111} modes necessitates caution. This section provides an overview of these choices.

In general, the coupling design problem begins with selecting which field component of the resonator to excite. For the TE_{011} mode, only H_ρ is remains nonzero at the lids of the cavity, where machining is easiest. Furthermore, H_ρ has its maximum at $\rho/a = 0.48$, making this location particularly attractive.

To couple to the cavity's H_ρ, we must choose which sub-cutoff waveguide mode to excite. We treat the cavity's field as a constant vector across the face of our sub-cutoff waveguide (magnetic dipole approximation) [137]. In the cylindrical coordinate frame of the sub-cutoff waveguide, the magnetic field therefore actually reverses polarity under (ϕ' $\Rightarrow$ -ρ'). Therefore, only those propagating modes with $H_{\rho'}$ that changes polarity under

this transformation will contribute to this coupling scheme. Looking at the $H_{\rho'}$ component of our propagating modes, we have

$$H_{\rho',TE} = \frac{-j\beta}{k_c}\cos(n\phi)J_n'(k_c\rho') \tag{4.73}$$

$$H_{\rho',TM} = \frac{-j\omega\epsilon n}{k_c^2\rho}\sin(n\phi)J_n(k_c\rho') \tag{4.74}$$

A loop or iris has a magnetic moment that is constant in the direction of its orientation (surface area $\hat{n}$ for the loop) as pictured in [138, op. cit. Fig. 4.32]. Therefore, we align the coupling loop to the $\hat{\rho}$ vector of the cavity [100]. Actually, this orientation couples to both TE_{nm} and TM_{nm} modes. Therefore, we need to consider all propagating modes.

In the experimental realization, the sub-cutoff waveguide has a radius r = 1.8 mm, which sets a propagation constant for each mode (calculated explicitly in Appendix C). As for the rectangular cavity (Section 4.4.2), we expect the lowest mode to dominate the transport. We observe that the propagation constant for the TE_{11} mode is about a factor of two smaller than that of the next-lowest mode, the TM_{11} mode. Therefore, we expect the TE_{11} mode to propagate signals in and out of the cavity. Thus for the cavity's resonant TE_{011} mode, the scaling of Q_{ext} should be

$$Q_{ext} \propto e^{2\beta_{TE11}L}, \tag{4.75}$$

which is the scaling observed experimentally (Appendix C).

4.5.3 Losses

The formulas for three main participation ratios for general TE_{nml} and TM_{nml} modes are given in Appendix D. We give the specific expressions for the TE_{011} here for completeness. We calculate the losses for a resonator with radius a and height d.

Dielectric loss

The dielectric participation ratio is exactly zero for a TE_{011} mode. Introducing the shape perturbation to the cavity causes some electric field to reach the walls of the geometry. Finite element techniques are the most accurate method for determining the resulting p_{diel}. For the implemented geometry, we have $p_{diel} \approx 4 \times 10^{-11}$. Therefore, an unphysically

low q_{diel} would be necessary to damp the TE_{011} mode at the levels we observe ($Q \lesssim 10^9$) [100].

Conductor loss

The magnetic participation ratio is [138, op. cit. Eq 7.55]

$$p_{mag} = \frac{2\omega\mu_0\lambda}{\eta} \frac{\left[(p_{11})^2 + \frac{2\pi^2 a^3}{d^3}\right]}{\left[(p_{11})^2 + \left(\frac{\pi a}{d}\right)^2\right]^{3/2}} \tag{4.76}$$

which gives $p_{mag} = 6 \times 10^{-6}$ [100]. A measured $Q_{tot} = 7 \times 10^8$ for this mode puts our best bound on $q_{cond} \gtrsim 4 \times 10^3$.

Seam loss

We do not rely on stringent machining tolerances to achieve zero surface currents at the seams for the TE_{011} mode. However, other modes in the cylindrical resonator do participate with this loss mechanism. We give expressions for the seam-admittances of these modes in Appendix D since these also shed light on other geometries which rely on small $g_{\varnothing}$.

4.5.4 Hurdles to transmon integration

Despite the high quality factors achieved for the TE_{011} mode, several obstacles must be overcome in order to successfully integrate this mode with a transmon. The first of these issues is the frequency spectrum of cylindrical cavities [111]. As previously described, the TE_{011} mode is not the fundamental mode of the cylindrical cavity. Therefore, any cQED experiment must deal with multi-mode dynamics, and these modes will lie below any low pass filtering. Moreover, the degenerate TM_{111} modes, which are lower Q, will always be a nuisance for large-bandwidth pulses that are typically used to control resonators.

Beyond the spectral concerns, the field pattern of the TE_{011} is not obviously beneficial for cQED. The geometry has a larger mode-volume than the rectangular cavities, necessitating a larger transmon to maintain strong coupling. Also, the toroidal electric fields, with field vectors along $\hat{\phi}$, makes the standard electric-dipole coupling difficult in the limit of large dipoles. The location of the field maxima in the interior of the cavity further requires a large amount of sapphire to be loaded into the cavity for strong coupling.

Finally, as we consider in Chapter 6, coupling the transmon to a resonator causes the resonator to acquire new dissipation channels. If the same transmon dissipation and coupling strength as used for Chapter 6 had been used to realize a quantum memory with the cylindrical TE_{011} mode, the resulting T_2 of the memory would at most have been improved by $\sim 30\%$, despite the massive undertaking required. With better qubits though [106, 114], the cylindrical resonator may eventually prove a useful resource.

4.6 Coaxial $\lambda/4$ resonators

We developed a new type of resonator for cQED [52] in order to avoid the integration issues faced by the rectangular cavity design as discussed in subsection 4.4.4. We present the design and realization of the architecture here, and a detailed analysis of the coherent dynamics of the system is presented in Chapter 6.

4.6.1 Resonant modes

The coaxial transmission line (TL) supports a TEM mode [111] with fields

$$\mathbf{E} = \frac{V_0 e^{-\gamma z}}{\rho \ln b/a}\hat{\rho} \tag{4.77a}$$

$$\mathbf{H} = \frac{V_0 e^{-\gamma z}}{2\pi\eta\rho}\hat{\phi} \tag{4.77b}$$

where $a = 1.6\,\mathrm{mm}$ and $b = 4.8\,\mathrm{mm}$ are the radii of the inner and outer conductors, Our coaxial $\lambda/4$ resonator (Fig. 4.11) is formed by such a TL that is short-circuited on one end and open-circuited on the other by virtue of a narrow circular waveguide [136]. The fundamental resonance frequency, f_0, is determined by the length of the transmission line, $\ell \approx \lambda/4$ (for instance, $\ell = 20\,\mathrm{mm}$ results in $f_0 = 4.25\,\mathrm{GHz}$).

We rely on a length L of circular waveguide, located between the $\lambda/4$ section and our light-tight seal, to protect the $\lambda/4$ mode from contact resistance at that joint. Because we design the resonator to be well below the waveguide's cutoff frequency ($f_0 < f_c$), the fundamental mode's energy density decreases exponentially into the waveguide section, at a rate determined by the radius of the outer conductor, as discussed in detail in subsection 4.6.4. This is one of the key innovations that enables long lifetimes while integrating a transmon qubit [52].

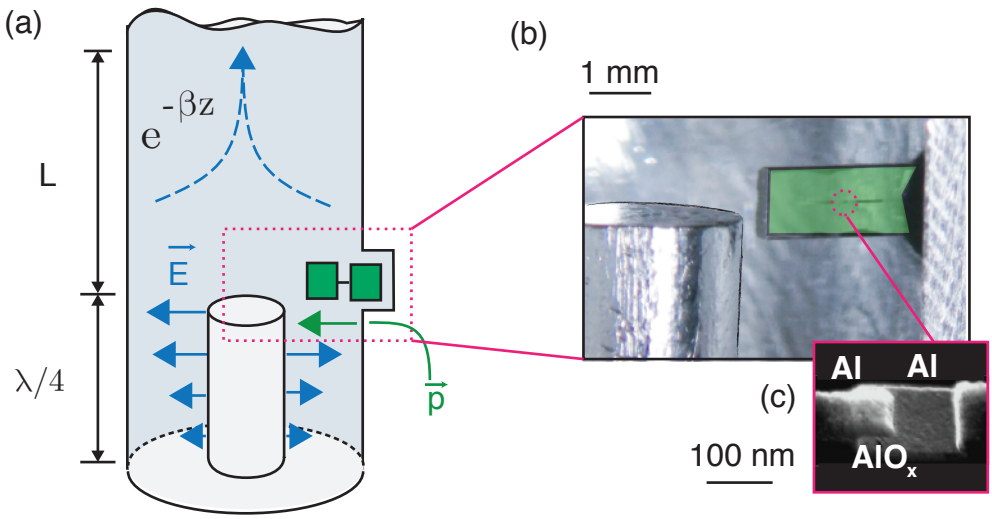

Figure 4.11: Coaxial $\lambda/4$ resonator. **(a)** A quarter-wave coaxial resonator is defined by shorting a coaxial transmission line's inner and outer conductors at one location on the transmission line (bottom) and open-circuiting the line a distance $\lambda/4$ away (upward). A superconducting transmon qubit (green) can be coupled to the $\lambda/4$ mode by aligning the electric dipole moment of the transmon $\vec{p}$ to the electric field of the resonator $\vec{E}$. In the section above the coaxial resonator, the outer conductor's cylindrical waveguide TE/TM modes are well below cutoff. Placing a light-tight seam a distance L away from the resonator thus allows the perturbation to be exponentially eliminated. This is the same effect as described in Section 4.4.2. **(b)** A superconducting transmon qubit on sapphire (green) is inserted through a 1.5 mm hole. The qubit is also coupled to a second cavity used for readout that is not shown here. **(c)** Electron beam microscopy image of a Josephson junction that provides the nonlinearity to the system. (Figure used with permission from [52]. See Copyright Permissions.)

Because the cavity is a $\lambda/4$ resonator, we expect the next transmission line mode at $f_0 \approx 3\lambda/4$. The separation in frequency between the fundamental mode and the next TEM harmonic is actually double the fundamental frequency itself, which provides a remarkably 'clean' spectrum. In fact, waveguide modes of the coax, in particular the TE_{11} mode, can be lower-lying than the second TEM harmonic. The TE_{11} mode begins to play a role when $\omega \approx 2c/(a+b) = (2\pi) \times 15\,\text{GHz}$. Simulations show that these box modes do indeed appear at $\omega_0/2\pi \approx 18\,\text{GHz}$.

4.6.2 Input-output coupling

This cavity is driven in a nearly-identical manner to the rectangular cavities (Sec. 4.4.2), via a coaxial pin coupler through a hole in the side wall of the cavity [114]. We have measured coaxial $\lambda/4$ modes strongly under-coupled at the levels of $\kappa_{\text{ext}}/2\pi \approx 1\,\text{Hz}$, as well as strongly over-coupled at the levels of $\kappa_{\text{ext}}/2\pi \approx 1\,\text{MHz}$.

4.6.3 Integrating a transmon

The small mode volume makes this quarter-wave resonator particularly attractive for integration with transmon qubits. By inserting a sapphire chip holding the qubit as shown in Figure 4.11, we are able to achieve strong coupling between the qubit and the resonator [52]. For the memory experiment, the qubit is also coupled to a second, over-coupled cavity used for qubit control and readout. We set the coupling strength between the transmon and each resonator by the location, orientation, and size of the antenna pads of the transmon.

The sapphire chip that contains the transmon device is diced to a narrow width (1 mm). That chip is inserted into the resonant cavity via a small diameter hole, in a manner that is analogous to the coaxial signal probes. Indeed, the strength of the qubit-resonator coupling is set by the depth of this insertion.

We estimate how the position of the qubit affects the qubit-resonator coupling through simulations that solve the full BBQ model [10, 149] at several insertion locations. The results of those simulations are given in Figure 4.12. For small deviations from the target junction location, the coupling strength can be approximated as linear in the distance (dashed line). An uncertainty in position at the 100 μm level is determined to be an uncertainty in dispersive coupling strength χ of $\delta\chi/\chi = 20\%$. Therefore, a technique for the careful assembly of this package is necessary to achieve reasonable predictive power over the system Hamiltonian.

To align the sapphire chip to such a precise location, we monitor the frequency of the cavity as we insert the chip. The high dielectric of the sapphire pulls the resonant frequency of the mode downward as more material is added to the cavity. The fractional frequency change of the mode is [111, op. cit. Eq. 6.95]

$$\frac{\delta\omega_0}{\omega_0} \approx -\frac{\int \delta\epsilon_r |E_0|^2 dV}{\int |E_0|^2 dV}, \tag{4.78}$$

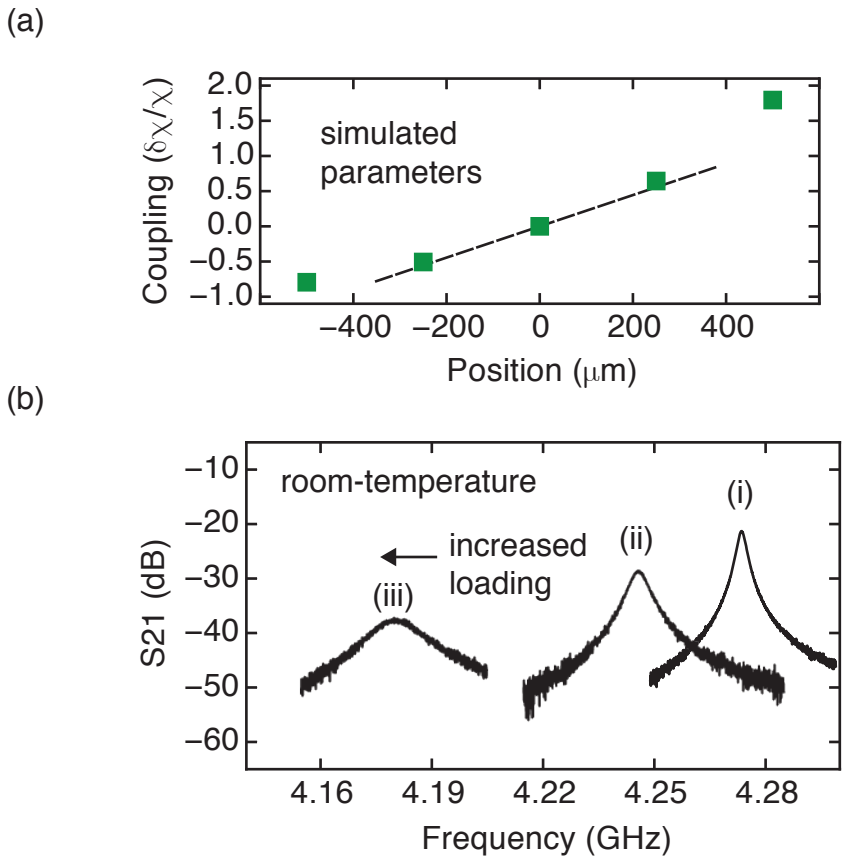

Figure 4.12: Assembling a coaxial quarter-wave cQED device. (a) Simulations provide a means for estimating how the system's degree of freedom in transmon location affect the dispersive coupling strength χ between the transmon and resonator. For small deviations ($\delta x_0 \lesssim 0.2\,\mathrm{mm}$), we find a linear approximation (dashed line) for the change in χ as $\delta\chi/\chi \approx \delta x_0/(0.5\,\mathrm{mm})$. **(b)** To achieve this precision in the transmon location, we rely on the frequency pull of the sapphire dielectric on the resonator. We monitor the center frequency of the resonator empty (i), with the sapphire fully inserted (iii), and for the final assembled device (iii). Equation 4.79 is used to solve for the resulting transmon location.

where $\delta\epsilon_r = 9.4$ for sapphire. We evaluate the above integral assuming that the field is constant across a width w and thickness t of the substrate, giving

$$\frac{\delta\omega_0}{\omega_0} \approx -\frac{\delta\epsilon_r wt}{\pi\ell(ln(b/a))^2}\left(\frac{1}{x}-\frac{1}{b}\right). \tag{4.79}$$

where x is the extent of the sapphire into the cavity. This expression holds whenever the mode is not significantly distorted by the presence of the dielectric. Remarkably though, Equation 4.79 predicts the correct frequency shift for the sapphire fully inserted in the resonator ($x = a$), with the above expression giving $\delta\omega_0/2\pi \approx 107\,\text{MHz}$ as compared the observed value $\delta\omega_0/2\pi = 93\,\text{MHz}$. In fact, the 15% frequency difference equates to approximately 50 μm of location uncertainty, a difference that may arise from chipping and kerf uncertainty of the sapphire chip itself.

Table 4.1: Predicted and extracted parameters for the full device device Hamiltonian.

$H/\hbar$	Experiment (Hz)	Simulation (Hz)	Deviation (%)
$\omega_s/2\pi$	4.250 $\times 10^9$	4.246 $\times 10^9$	< 1
$\omega_q/2\pi$	7.906 $\times 10^9$	7.878 $\times 10^9$	< 1
$\omega_r/2\pi$	9.777 $\times 10^9$	9.653 $\times 10^9$	1
$\chi_{sq}/2\pi$	4.99 $\times 10^5$	5.56 $\times 10^5$	11
$\chi_{rq}/2\pi$	8.25 $\times 10^5$	7.77 $\times 10^5$	6
$\chi_{sr}/2\pi$	-	1.60 $\times 10^3$	-
$K_s/2\pi$	4.50 $\times 10^2$	5.20 $\times 10^2$	16
$K_q/2\pi$	1.46 $\times 10^8$	1.41 $\times 10^8$	3
$K_r/2\pi$	-	1.20 $\times 10^3$	-

As shown in Figure 4.12, we can use Equation 4.79 to solve for the sapphire location for a given assembly. This process can be done iteratively at room-temperature. However, we caution the reader that low VNA powers ($\lesssim -40\,\text{dB}$) should be used for this technique to avoid breaking the AlO_x tunnel junction. The achieved transmon parameters are listed in Table 4.2.

4.6.4 Losses

The dimensions for the inner and outer conductors for the coax resonator are $a = 1.6\,\text{mm}$ and $b = 4.8\,\text{mm}$ respectively [52]. We calculate the participation ratios for the fundamental mode here.

Dielectric loss

The dielectric participation ratio for the coaxial cavity is

$$p_{diel} \approx \frac{t_{ox}}{\epsilon_{r,ox}} \left(\frac{1}{a \ln(b/a)} \right) \tag{4.80}$$

For the standard assumptions, $t_{ox} = 3\,\text{nm}$ and $\epsilon_{r,ox} = 10$ and our geometry we have $p_{diel} \approx 2 \times 10^{-7}$.

Conductor loss

The magnetic participation ratio for the coaxial cavity is

$$p_{diel} \approx \lambda \left(\frac{1}{a \ln(b/a)} \right) \tag{4.81}$$

For the standard $\lambda = 50\,\text{nm}$ and our geometry we have $p_{mag} \approx 4 \times 10^{-7}$.

Seam loss

If the 'open-circuit' termination of this resonator was exact, placing the seam location anywhere above the center conductor of the coax would have zero seam-participation. However, the waveguide coupling weakens this effect. We use finite element techniques to evaluate $y_{\varnothing}$ numerically, finding $y_{\varnothing} = 1.3 \times 10^{-3}\,/\Omega\text{m}$ at the interface of the transmission line and waveguide sections. We expect $y_{\varnothing}$ to decay exactly as Q_{ext}, as described in section 4.4.2, except with a different e-folding length.

The TM_{01} mode sets the $\lambda/4$ mode's propagation into the waveguide. The evanescent TM_{01} mode has a propagation constant $\beta = \sqrt{k^2 - (2.41/a)^2}$, where $k = 2\pi/\lambda$ is the wavenumber, and $a = 5\,\text{mm}$ is the radius of the circular waveguide section. At our transmission line's fundamental resonance frequency of 4.25 GHz, the propagation constant is $\beta = \imath/2.03\,\text{mm}$, below cutoff. Therefore, the $\lambda/4$ mode's current-energy density falls

as $|H|^2 \propto e^{-2|\beta|z}$ into the waveguide section. Finite element simulations, which take into account all possible waveguide modes, confirm these simple predictions to within 5%.

We seal the cavity for light-tightness after a length of waveguide section that is $L \approx 10/|\beta|$. The resonator's energy has been suppressed at this location by a factor of about e^{-20}. We therefore rule out assembly defects such as contact resistance as a potentially limiting dissipation mechanism at internal quality factors of $Q_{\rm int} \sim 10^9$.

4.7 Summary of modes and quality factors

In Table 4.2, we provide a compiled list of the different types of resonators presented in this chapter and the observed quality factors of each mode. As is clear from the table, the TE_{011} has essentially no sensitivity to dielectrics and seams. Conductor loss is the main culprit for the dissipation of this mode. Therefore, the bound on q_{mag} obtained from these experiments is potentially a real measure of the conductivity of our high purity, machined aluminum. It is interesting then that the coaxial $\lambda/4$ cavities achieve very similar bounds for q_{mag}. We can deduce by this comparison that the $\lambda/4$ cavities are likely also limited by conductor loss. Vortices and nonequilibrium quasiparticles are known to cause conductor loss in superconductors. Investigating these loss mechanisms could be a fruitful path forward for improving these devices further.

Table 4.2: Resonant modes and quality factors for high purity aluminum.. Results for rectangular cavities (R), cylindrical cavities (C), and coaxial $\lambda/4$ cavities (Q). All cavities have undergone the surface preparation described in Chapter 5. Material bounds ($q \geq$ or $g_{\varnothing} \geq$) are under the assumptions provided in Section 4.2. We use bold font to denote the best bounds obtained. Unphysical bounds are left as a dash.

Device	Mode	f_0 (GHz)	Q_{int}	q_{diel}	q_{mag}	$g_{\varnothing}(/\Omega m)$	cite
R1	TE_{101}	9.455	4.2×10^7	5.0	1.3×10^3	7.8×10^3	[100]
R2	TE_{101}	9.481	4.3×10^7	5.1	1.3×10^3	7.9×10^3	[100]
R2	TE_{101}	9.481	6.9×10^7	8.1	2.1×10^3	1.3×10^4	[100]
C1	TE_{111}	7.700	3.1×10^7	-	3.4×10^2	$\mathbf{1.0\times10^6}$	[100]
C1	TM_{111}	11.448	1.4×10^7	-	2.3×10^2	1.4×10^5	[100]
C1	TE_{011}	11.417	6.1×10^8	-	3.7×10^3	-	[100]
C2	TE_{011}	11.440	7.4×10^8	-	$\mathbf{4.5\times10^3}$	-	[100]
C2	TE_{011}	11.442	5.2×10^8	-	3.2×10^3	-	[100]
Q1	$\lambda/4$	7.881	8.7×10^7	**20.**	3.3×10^3	-	
Q2	$\lambda/4$	7.858	8.6×10^7	20.	3.3×10^3	-	
Q3	$\lambda/4$	7.992	8.0×10^7	18.	3.0×10^3	-	
Q4	$\lambda/4$	4.280	7.0×10^7	16.	2.7×10^3	-	[52]

CHAPTER 5

Measuring resonators and transmons

This chapter presents the core cQED techniques used throughout this thesis. Two basic types of measurements are considered. First, we present the characterization of linear resonators that are intended for use in full cQED devices. How to achieve high quality factors, as well as how to extract Q from measurements, is presented in detail. Then, we discuss methods for transmon experiments. We focus here on experiments that illuminate properties of a transmon as an individual circuit element. The next chapter concerns the coupling between a transmon and a resonator, as well as new experiments enabled by the coupling (besides qubit readout), in detail.

Many of the techniques in this chapter have a long history in cQED. For a complimentary review of techniques for resonator measurements, we refer the reader to Geerlings's thesis [110]. A step-by-step manual for transmon characterization can be found in Sears's thesis [43], and many transmon control techniques are presented in detail in Reed's thesis [144]. However, a number of new techniques are also explored here.

5.1 Linear resonator experiments

Being able to fabricate and probe high quality bare resonators ($Q > 10^8$) is an important step toward using such objects as coherent quantum memories for cQED [100]. Moreover, their existence in standard cQED setups (dilution refrigerator, coaxial input-output lines,

etc.), shows that there are not fundamental barriers to these long lifetimes using the technology already common for cQED experiments. Additionally, resonators can be sensitive to the same dissipation mechanisms that may limit qubits. Optimizing resonator performance can therefore be a powerful path forward for improving qubits [104].

In this section, we describe the methods to prepare, measure, and analyze superconducting aluminum cavity resonators [100]. Preparing these cavities for cryogenic measurement involves a surface etching step, calibrating the microwave couplers, and finally, integrating the cavities into a dilution refrigerator measurement setup. The central technique for vetting the performance of a superconducting cavity is via measurements with a Vector Network Analyzer (VNA) in a quasi-reflection mode. Fully interpreting these measurements is only possible by repeating them across a range of circulating RF energies and elevated temperatures since a resonator's sensitivity to loss mechanisms, such as quasiparticle loss, can be revealed through these schemes.

5.1.1 Surface preparation

In order to achieve the highest quality factors in superconducting niobium cavity resonators, it has been commonly observed that 100-200 μm of surface layer should be removed prior to those measurements [147]. Preparing superconducting surfaces via etching has been a well-established technique for niobium cavities used in particle accelerators [147]. There, a combination of buffered chemical polishing (BCP) and electro-polishing (EP) is used to mitigate a damaged surface layer.

For high purity aluminum ($\gtrsim$ 99.99% pure), we have found that chemically etching cavities is essential to realize their optimum performance [100]. The commercially available $Aluminum\ Etch\ A$ by Transene Co is a combination of nitric and phosphoric acid that has an etch rate of pure aluminum of 100 Å/s at 50°C [150]. The nitric acid attacks the aluminum directly, which results in an aluminum oxide layer that is dissolved by the phosphoric acid [151], as

$$7\mathrm{A} + 5\mathrm{HNO_3} + 21\mathrm{H_3PO_4} \Rightarrow +7\mathrm{Al(H_2PO_4)_3} + 13\mathrm{H_2O} + 2\mathrm{N_2} + \mathrm{NO_2}. \tag{5.1}$$

These alternating processes should remove 150 μm of material in approximately four hours. However, the etch rate for is highly dependent on temperature (550 Å/s at 75°C) and the process is exothermal [151]. Therefore, care must be taken to measure the total etch rate for a given setup.

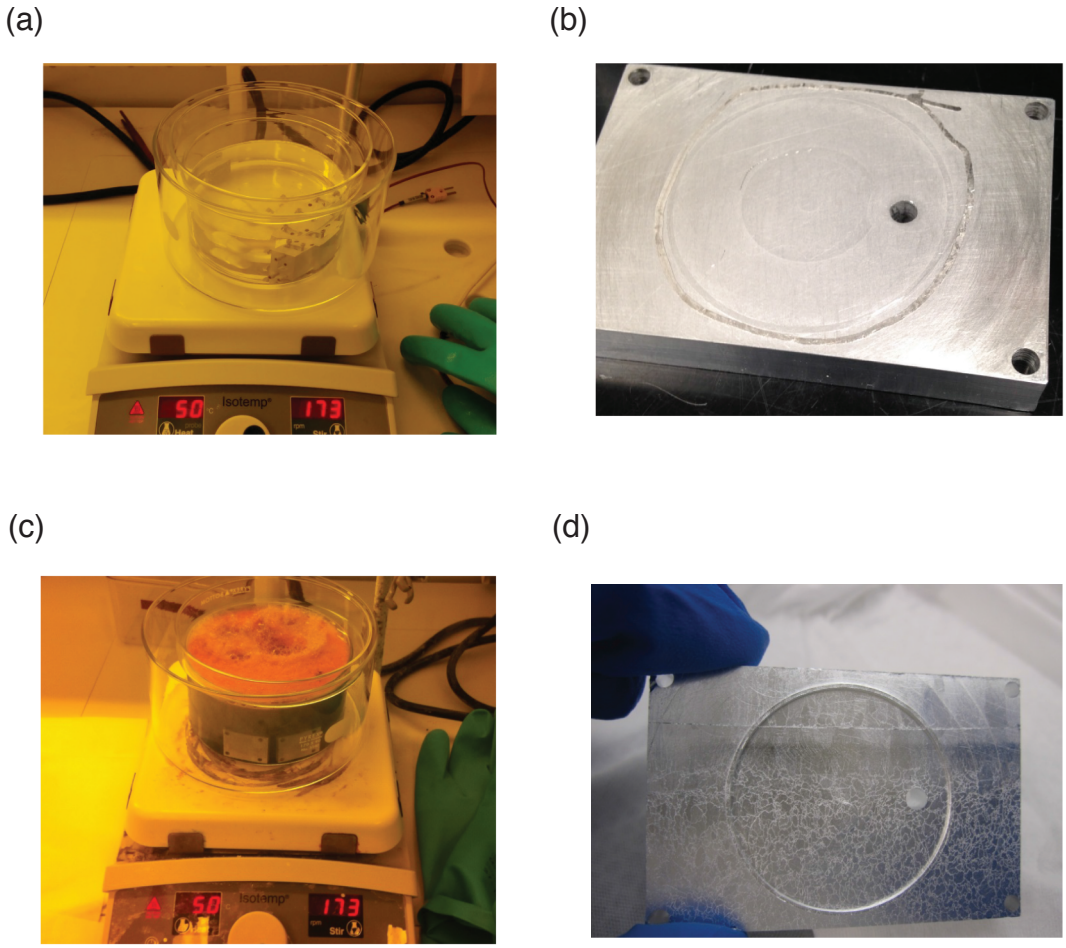

Figure 5.1: Surface preparation of superconducting cavities. **(a)** A high purity aluminum cavity is placed in a bath of *Aluminum Etch A* to remove the damaged surface layer. This process is conducted on a hot plate in the vented acid bench of the Becton cleanroom. Nested beakers with an additional lid prevents overflow and contamination. **(b)** High purity aluminum sample before etching. Clear signs of machining scratches are visible. **(c)** The acid bath at the end of a two-hour cycle. The liquid has been turned green by aluminum phosphate salt. Between the liquid and lid, nitrous oxide is trapped and vents in bursts whenever the pressure exceeds the weight of the lid. If the process is left to continue, the bath may eventually run clear again as a runaway reaction will begin to attack the salt itself. Unreliable etch rates and surface impedance results follow this runaway effect. **(d)** After two cycles of the two-hour process, the high purity sample is highly reflective with grain boundaries that are easily visible in the picture.

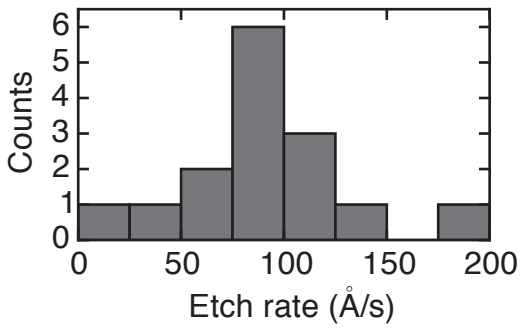

Figure 5.2: Calibrating the etch rate of *Aluminum Etch A*. Several samples are measured during the etching process to calibrate the etch rate of our process. The manufacturer-specified value of 100Å/s is indeed met on average, indicating that our process is well-regulated despite the large total volume of pure aluminum in the bath.

Rectangular cavities turn out to be a useful mechanism for extracting an etch rate. We perform room temperature VNA measurements to find the resonant frequency of cavities before and after a surface preparation step. While the etch is an isotropic process, only one dimension that is etched causes a frequency shift. Therefore, for the TE_{101} mode, we get

$$\frac{\delta f_0}{\delta t} = \frac{c}{2\pi}\frac{\delta}{\delta t}\sqrt{\left(\frac{\pi}{a}\right)^2 + \left(\frac{\pi}{d(t)}\right)^2} \tag{5.2}$$

which can be evaluated to solve for the etch rate as

$$\frac{\delta d}{\delta t} \approx \frac{4 f_0 d^3}{c^2}\left(\frac{\delta f_0}{\delta t}\right). \tag{5.3}$$

A histogram of etch-rate measurements performed on aluminum in the Becton cleanroom is given in Figure 5.2. We start the etching process at room temperature and bring the bath up to 50°C to avoid the run-away process from the exothermal heat load. During the process, a teflon stirring bean to agitate the bath at 175 RPM. We replace the bath with fresh acid after two hours in the four-hour process. The resulting surface finishes are mirror-like, and the highest purity samples have visible centimeter-sized grain boundaries. Cryogenic measurements on the penetration depths of these samples, as detailed in a later section, indicate that the microscopic description of the superconducting condensate has also been affected by the acid treatment. After surface preparation, a shift toward the 'clean' limit of superconductivity is observed [100], as we discuss later in Section 5.1.5.

5.1.2 Resonator measurement setup

As pictured in Figure 5.3, the cavity quality factor measurements in this thesis and in [100] were performed with the resonators attached to the base ($T \approx 15$ mK) cooling stage of a dilution refrigerator. Stainless steel cables carry signals from room temperature to the base stage. Physical attenuation of 20 dB and 30 dB is located on the 4 K and base stages to thermalize the input signals. The impedance of the device under study is introduced to the signal chain by an SMA tee. The third port of the tee continues through two isolators and through superconducting coaxial cable to the 4 K stage. At 4 K, the signal passes through a low noise HEMT amplifier. Stainless steel cable carriers the signal to room temperature, where the output passes through two low noise Miteq amplifiers. The input and output ports of this signal chain are measured in transmission via a vector network analyzer (VNA). This setup is similar to other quasi-transmission techniques as described in Section 5.1.3.

The cavities are mounted on copper brackets that are bolted to the base plate of the refrigerator. These samples are housed in mu-metal shielding (Amuneal 4K) [62], and only nonmagnetic components are used within the mu-metal shield to maintain low magnetic fields. Probing the magnetic field near the sample with a calibrated magnetometer, we detect field strengths of milligauss in the full measurement setup.

5.1.3 Extracting quality factors

The resonator measurement setup described in the previous subsection allows us to measure in the quasi-transmission method referred to as the shunt, hanger, or notch technique [104, 130, 133, 152]. Essentially, the signal-carrying transmission line is shunted by the impedance of a resonator under study as shown in Figure 5.5. The scattering matrix can be calculated taking into account imperfections, such as cable delay and reflections, that arise from a lack of calibration in the cryogenic environment. The far off-resonant behavior of these measurements serve as an in-situ calibration. Importantly, this calibration allows us to extract the external and internal quality factors independently.

Several derivations for this technique have been presented in papers [130, 133, 152] and theses [110, 112]. We provide the main results here, beginning with the ideal shunt resonant circuit (Fig. 5.5). If it has no internal dissipation, the resonant circuit simply

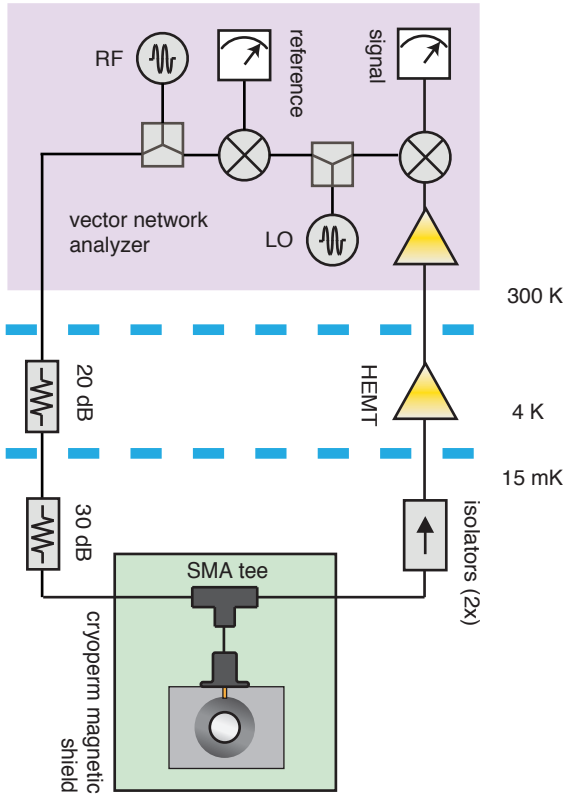

Figure 5.3: Experimental schematic for resonator testing. To extract the quality factor of a resonator, phase-resolved (vector) network analysis is performed on a transmission line circuit that includes the resonator. The analysis compares the full circuit response (large loop) to a reference branch. Two generators are used to bring the measurement frequency down to match an ADC digitizing rate. Cryogenic attenuators reduce the blackbody radiation from 300 K. An SMA-tee is used to introduce the impedance of the resonator to the coaxial transmission line. A low noise amplifier boosts the signal before the room temperature amplification and demodulation.

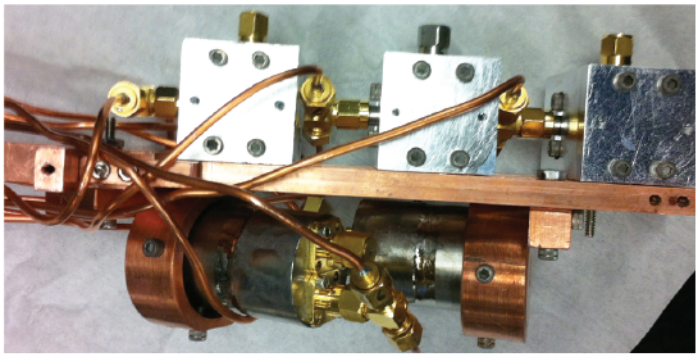

Figure 5.4: Picture of resonator payload. Three high purity aluminum coaxial resonators and two niobium TM_{010} cavities. Thermalization is provided by bolting each resonator to a copper bracket, which itself will be bolted to the mixing chamber. This payload will be inserted into a magnetic shield for measurement. Copper inner-outer coaxial cable is used inside the shield, and non-magnetic RF and mechanical assembly components are used to maintain milligauss fields inside the shield.

creates a phase interference effect in the transmitted signal that is a Lorentzian as

$$S_{21} = 1 - \frac{\kappa_{\text{ext}}}{\kappa_{\text{ext}} + 2\imath(\omega - \omega_0)} \tag{5.4}$$

Note that on resonance the phase inversion leads to complete destructive interference for the outgoing signal ($S_{21} = 0$), regardless of the coupling strength κ_{ext}. Essentially, this resonator is always infinitely over coupled. If instead the resonator has a finite internal energy decay rate (κ_{int}), the resonance frequency acquires an imaginary component [110], $\tilde{\omega} = \omega_0 + \imath\kappa_{\text{int}}/2$, to account for its lack of a natural frequency response. Now, the transmitted signal is given by

$$S_{21} = 1 - \frac{\kappa_{\text{ext}}}{\kappa_{\text{ext}} + \kappa_{\text{int}} + 2\imath(\omega - \omega_0)}, \tag{5.5}$$

or using quality factors to re-parameterize the expression ($Q_{tot} \equiv \omega/\kappa_{tot}$), we have

$$S_{21} = 1 - \frac{Q_{\text{tot}}}{Q_{\text{ext}} + 2\imath Q_{\text{tot}} Q_{\text{ext}}(\omega/\omega_0 - 1)}. \tag{5.6}$$

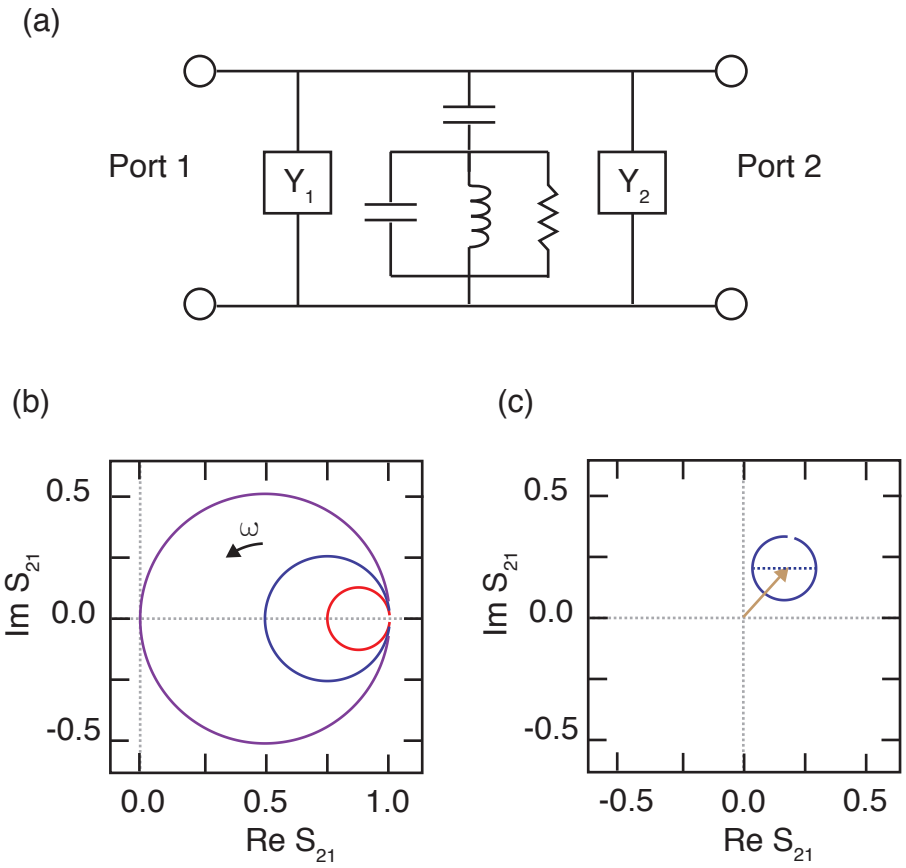

Figure 5.5: Shunt resonances along a transmission line. (a). The two-port circuit of a resonator measured via the shunt-technique. For an ideal transmission line that has no additional reflections or crosstalk, the other shunt impedances Y_1, Y_2 would be infinite. However, the response of the resonant circuit can be extracted for nearly-arbitrary Y_1, Y_2. **(b)** The transmission response of the ideal circuit. Far detuned from resonance, the transmission is unaffected by the resonator ($S_{21} = 1$). Resonance traces out a circle on the complex plane of the transmitted signal (Re(S_{21}, Im(S_{21})), the rate at which phase is acquired along this circle ($\theta[\omega]$) gives the total quality factor of the resonance. The distance from the origin at resonance gives the ratio of internal to external quality factors. For completely over-coupled resonators, the transmission approaches zero on resonance (purple). Critically coupled ($Q_{int} = Q_{ext}$) gives transmission of one-half on resonance (blue). Finally, under-coupled resonances give transmission closer to unity (red). **(c)** Imperfections in the transmission line Y_1, Y_2 cause displacements and rotations of the resonant circle. However importantly, the environmental admittances do not alter the rate of $\theta[\omega]$, which gives the total quality factor. Moreover, these effects can be calibrated out by taking into account the far detuned transmission, which gives access to the ratio of Q_{tot}/Q_{ext}.

In the complex transmitted voltages, the transmitted signal traces out a circle in the IQ plane. To see why this is a circle, it is useful to define an angle [152]

$$\theta(\omega) = \tan^{-1}\left[2Q_{\text{tot}}(\omega/\omega_0 - 1)\right], \tag{5.7}$$

so that the transmission signal is given by

$$S_{21} = 1 - \frac{Q_{\text{tot}}}{Q_{\text{ext}}}\left(\frac{1}{1 - \imath\tan\theta}\right). \tag{5.8}$$

Bringing the imaginary component to the numerator and using the trigonometric identity $1 + \tan^2\theta = \sec^2\theta$, we have

$$S_{21} = 1 - \frac{Q_{\text{tot}}}{Q_{\text{ext}}}\left(\cos^2\theta + \imath\cos\theta\sin\theta\right). \tag{5.9}$$

Finally, using the double-angle identities,

$$\begin{aligned}\cos^2\theta &= \frac{1}{2}(1 + \cos 2\theta)\\ \cos\theta\sin\theta &= \frac{1}{2}\sin 2\theta,\end{aligned} \tag{5.10}$$

we obtain a simple form for S_{21} as

$$S_{21} = 1 - \frac{Q_{\text{tot}}}{2Q_{\text{ext}}}\left(1 + e^{2\imath\theta}\right). \tag{5.11}$$

We recognize the diameter of the circle to be $2Q_{\text{tot}}/Q_{\text{ext}}$ and from the transmission circle's progression along θ as a function of frequency, we obtain Q_{tot} independently from Q_{ext} [152]. Thus, we can completely determine our internal and external dissipation.

Impedance mismatches, crosstalk and other imperfections in our measurement chain can be accounted for by allowing an imaginary component of the external quality factor $\tilde{Q}_{ext} = Q_{ext}e^{\imath\varepsilon}$ [152]. Additionally, loss and the electric phase-delay accumulated through the meters of coaxial cable can be lumped into a single complex scaling term $Ge^{j\omega\tau}$, where τ is the electrical delay time and G is a complex gain term. These perturbation have the effect of scaling, rotating, and displacing the resonant transmission circle while preserving the separation of Q_{int} and Q_{ext}. The imperfections can be combined [152] as

$$S_{21} = Ge^{j\omega\tau}\left[1 - \frac{Q_{\text{tot}}}{2Q_{\text{ext}}}\left(1 + e^{2\imath\theta}\right)e^{-\imath\varepsilon}\right]. \tag{5.12}$$

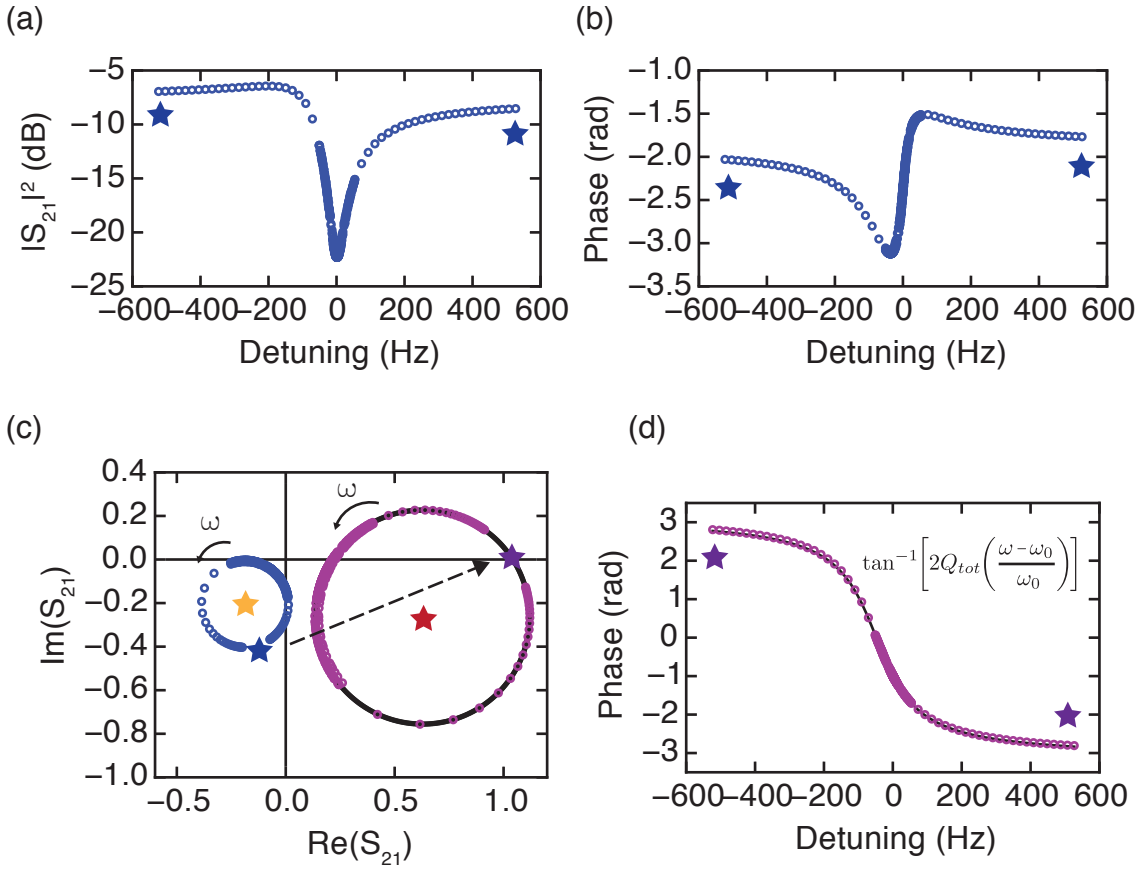

Figure 5.6: Fitting quality factors on the complex plane. (a). Raw data for the transmitted signal through a shunt resonator. Because the VNA cannot be calibrated directly at the device, we must transform the signal in post-processing by the far detuned signal levels. **(b)** A convenient representation for the signal is to evaluate the best-fit circle along the parametric angle $\theta[\omega]$. The phase wraps at a rate given by Q_{tot} alone.

As shown in Figure 5.6, resonator data is fit to Equation 5.12 by taking a best-fit circle to the data in the IQ plane of $(\mathcal{R}(S_{21}), \mathcal{I}(S_{21}))$, which gives the ratio of $Q_{\rm tot}/Q_{\rm ext}$. Then the data is parametrized by $\theta(\omega)$ and fit to an arctangent function to obtain $Q_{\rm tot}$.

5.1.4 Power dependence

While the loss mechanisms that dominate planar resonators are often observe to have loss tangents which depend on the field energy circulating in the device [153, 154, e.g.], most of the 3D cavities presented in this thesis do not show this behavior to a measurable

degree [100]. A notable exception is the coaxial $\lambda/4$ resonator. These resonators can have higher quality factors (by a factor of two or four) at large circulating energies ($\bar{n} \sim 10^6$), compared to the single-photon level [52].

To conduct these measurements, vanishingly small drive powers must be used since the circulating energy is directly proportional to the resonator's quality factor for a given drive power, $\bar{n} \approx P_{\mathrm{in}} Q_{\mathrm{tot}}/\hbar\omega^2$. To see how this comes about, consider the simplest case of the resonator being measured in reflection with P_{in}. This is equivalent to a shunt measurement if P_{in} is referenced after the microwave tee. Following Aspelmeyer [20], the input power is equivalent to an incoming photon flux,

$$P_{\mathrm{in}} = \hbar\omega \langle \hat{a}_{\mathrm{in}}^\dagger \hat{a}_{\mathrm{in}} \rangle \tag{5.13}$$

This provides an input-output relation for the resonator as

$$\dot{\hat{a}} = -\frac{\kappa_{\mathrm{tot}}}{2}\hat{a} + \sqrt{\kappa_{\mathrm{ext}}}\hat{a}_{\mathrm{in}} + \sqrt{\kappa_{\mathrm{int}}}\hat{h}, \tag{5.14}$$

where $\hat{h}$ is a noise term that we can ignore for calculating the expectation of $\langle \hat{a}^\dagger \hat{a} \rangle$. In steady state we require that $\dot{\hat{a}} \equiv 0$ which reduces the above equations of motion to

$$\hat{a} = \frac{2\sqrt{\kappa_{\mathrm{ext}}}}{\kappa_{\mathrm{tot}}}\hat{a}_{\mathrm{in}}, \tag{5.15}$$

so that the expectation value is

$$\langle \hat{a}^\dagger \hat{a} \rangle = \frac{4\kappa_{\mathrm{ext}}}{\kappa_{\mathrm{tot}}^2} \langle \hat{a}_{\mathrm{in}}^\dagger \hat{a}_{\mathrm{in}} \rangle. \tag{5.16}$$

Using the definition of Equation 5.13, we have then that for this measurement setup, the average circulating photon number is

$$\bar{n} = \frac{4Q_{\mathrm{tot}}^2 P_{\mathrm{in}}}{Q_{\mathrm{ext}} \hbar\omega^2}. \tag{5.17}$$

For nearly critically coupled measurements ($Q_{\mathrm{tot}} = Q_{\mathrm{ext}}/2$) at 10 GHz, the achieved quality factors of $Q_{\mathrm{tot}} \approx 7 \times 10^8$ require an input power of $P_{\mathrm{in}} \approx -175$ dBm at the port. We typically have approximately 70 dB of attenuation in a dilution refrigerator setup (Section 5.1.2). Therefore, drive powers on the order of -100 dBm are required at room temperature. The resulting output signal at these exceedingly low drive levels demands more than 24 Hr of integration for a single trace [100].

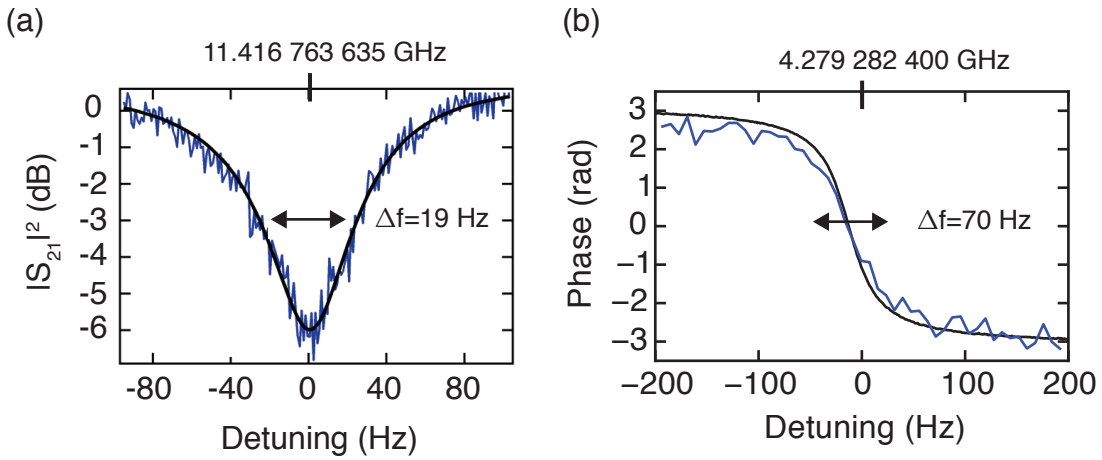

Figure 5.7: Power dependence of two cavity resonators. (a). The cylindrical TE_{011} resonator shows no measurable power dependence. Shown in blue is the transmission at single-photon levels, while the black trace is not a fit, but rather the transmission through the same circuit at circulating energies equivalent to 10^9 photons. This stability could be associated with the lack of dielectric sensitivity in the mode. **(b)** The coaxial $\lambda/4$ resonator, however, is observed here to have a degraded Q by approximately a factor of two at low powers as compared to high powers. Data from the two regimes of powers, low and high, are shown in blue and black, respectively. These saturable defects are a natural consequence of the coax resonator's increased sensitivity to materials.

We present data at high and low powers for the coaxial $\lambda/4$ resonator. The change in the observed $Q_{\rm int}$ corresponds to a saturable loss mechanism that changes the effective decay rate as

$$\kappa_{\rm tot}(P_{\rm in}) = \kappa_0 + \kappa_x(P_{\rm in}) \tag{5.18}$$

If the unknown loss mechanism completely staturates ($\kappa_x = 0$) at high powers, the above indicates that $\kappa_x/2\pi \approx 50\,$Hz would limit the otherwise lossless mode to $Q_{\rm tot} \approx 10^8$.

Dielectric loss is a central suspect for this behavior since the bound on $q_{\rm mag}$ obtained for the coaxial $\lambda/4$ resonators is similar to the bound obtained for cylindrical TE_{011} resonators. Therefore, we do not expect this device to probe the conductive properties of our aluminum cavities in qualitatively new ways. However, the TE_{011} modes have essentially no dielectric sensitivity. Therefore, the new power dependence for the coaxial $\lambda/4$ device might be attributable to dissipation in the amorphous aluminum-oxide layer of the device.

5.1.5 Temperature dependence

The response of superconducting resonators to a thermal bias reveals a number of important clues about the microscopic description of the BCS state [121] as well as the device's sensitivity to quasiparticle dissipation (p_{mag} from Section 4.2.3) [100, 122]. Similarly, temperature dependent measurements also provide a means to extract a direct bound on the density of nonequilibrium quasiparticles [114].

In general, a superconducting resonator is a sensitive probe to the complex surface impedance ($Z_s = R_s + j\delta X_s$) [121], where the differential surface reactance δX_s is used because the exact cavity volume is not accessible. Measurements on the cavity provide access to the superconducting surface impedance Z_s as

$$Z_s = \frac{\omega\mu_0\lambda}{p_{\mathrm{mag}}}\left(\frac{1}{Q_{\mathrm{mag}}} + 2j\frac{\delta f}{f}\right) \tag{5.19}$$

where λ is the penetration depth, p_{mag} is the magnetic participation ratio, Q_{mag} is the quality of the surface conductor, and the $\delta f/f$ term is the frequency shift of the resonator from the $\lambda = 0$ limit (i.e. the physical dimensions of the cavity) or, with an offset, the zero temperature value $\lambda(T = 0)$.

To extract useful information about the BCS state of our resonators from these measurements, Gianluigi Catelani translated fundamental formulas to an applied notebook found in Appendix []. That tool set was developed by Catelani and Glazman following the theory of Nam [155, 156], which we review here.

The behavior of BCS superconductors can be classified into two limits, comparing the mean free path (ℓ) to to the coherence length (ξ) [18]. Our aluminum samples are strongly in the Pippard, or dirty-superconductor, limit ($\ell \ll \xi$), which we determine by comparing the observed behavior to predictions of the dirty and clean (or London) limits of BCS predictions [100]. In the dirty and clean limits of superconductors, this impedance is related to the normal state impedance Z_n by a pair of conductivities σ_1, σ_2 (which we define later) such that the superconducting surface impedance can be written

$$Z_s \propto Z_n \times (\sigma_1 - \imath\sigma_2)^{\nu}\,, \tag{5.20}$$

where $\nu = -1/2$ for the dirty limit and $\nu = -1/3$ for the clean limit [155, 156]. Determining the proper exponent in Equation 5.20 is equivalent to determining the correct limit of BCS for a given material. We point out that a normal state conductor has $X_n/R_n = 1$ in the

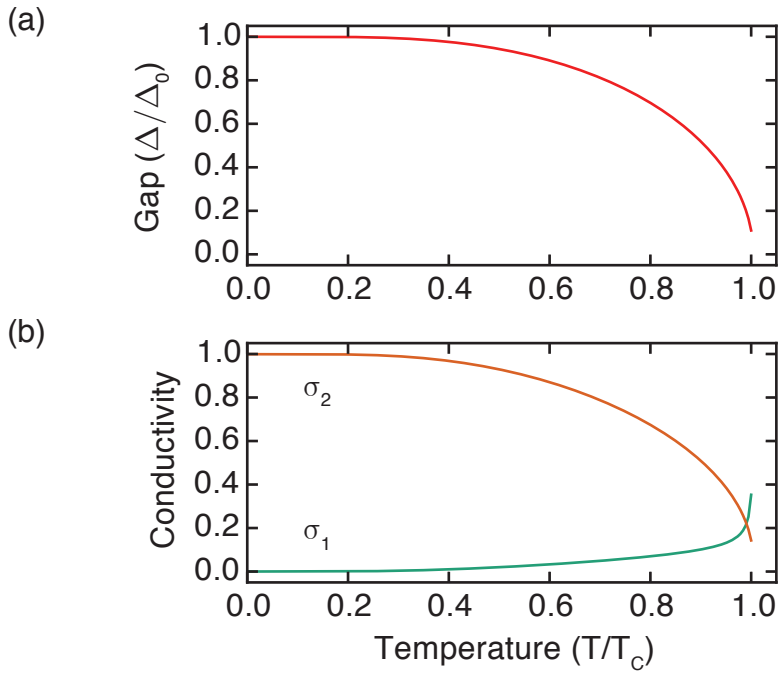

Figure 5.8: BCS theory for surface impedance of a superconductor. (a) The energy gap between free quasiparticles and bound pairs rolls off at the transition temperature T_c with a characteristic shape for all BCS superconductors. **(b)** The real and imaginary conductivity components (σ_1, σ_2 respectively) for the AC response of superconductors depends only on the frequency of the AC field and the gap of the superconductor. However because the gap is temperature dependent, these conductivities must be evaluated at each value of gap (implicitly, temperature) to capture the full behavior of the superconductor. The decreasing σ_2 is equivalent to an increasing kinetic inductance.

dirty limit and $X_n/R_n = \sqrt{3}$ for the clean limit due to the anomalous skin depth [111]. Yet, we will see that for superconductors the surface reactance can be much larger than the surface resistance.

At low temperatures, we can make the following useful approximation. For superconductors of both types, we will have $\sigma_2 \gg \sigma_1$ [18]. Therefore, we can factor Equation 5.20 to prepare for an expansion

$$Z_s \propto Z_n \sigma_2^{\nu} \left|1 + s^2\right|^{\nu/2} e^{\imath \mathrm{Arg}(s-\imath)}, \tag{5.21}$$

where we have introduced $s = \sigma_1/\sigma_2$ for convenience in the following calculations. Using

the definition of Arg(z) [157] with $z \notin$ reals

$$\mathrm{Arg}(z) = 2\arctan\left[\frac{\mathcal{I}(z)}{|z| + \mathcal{R}(z)}\right]. \tag{5.22}$$

Expanding the Arg function in $s \ll 1$ reduces to expanding an arctangent function, giving

$$\mathrm{Arg}(s - \imath) \approx -\frac{\pi}{2} + s + \mathcal{O}(s^3). \tag{5.23}$$

Then, expanding the polynomial

$$(1+s)^{\nu/2} \approx 1 + \frac{\nu s^2}{2} + \mathcal{O}(s^4), \tag{5.24}$$

we have for the full surface impedance

$$Z_s \propto Z_n \sigma_2^{\nu}\left(1 + \frac{\nu s^2}{2} + \mathcal{O}(s^4)\right)(-\imath)\left(1 + \imath s - \frac{s^2}{2} + \mathcal{O}(s^3)\right). \tag{5.25}$$

Keeping the leading order terms, we have that

$$R_s \propto R_n \sigma_1 \sigma_2^{\nu-1} \tag{5.26a}$$

$$X_s \propto R_n \sigma_2^{\nu}. \tag{5.26b}$$

Equation 5.26b allows us to define a penetration depth $\lambda \equiv X_s/(\omega\mu_0)$.

The surface Q_{mag} (as Section 4.2.3) can now be written as $Q_{\mathrm{mag}} \approx \sigma_2/\sigma_1$, which is evaluated by calculating σ_1, σ_2 explicitly. For a superconductor with gap $E = \hbar\Delta(T)$, at reduced temperature $\mathcal{T} = k_B T/\hbar$, and operated in low-frequency limit ($\omega \ll 2\Delta$), the dimensionless conductivities are given in [18] as

$$\sigma_1 = \frac{1}{\omega}\int_{\Delta}^{\infty} d\epsilon \frac{(\epsilon+\omega)\epsilon + \Delta^2}{\sqrt{(\epsilon+\omega)^2 - \Delta^2}\sqrt{\epsilon^2 - \Delta^2}}\left[\tanh\frac{\epsilon+\omega}{2\mathcal{T}} - \tanh\frac{\epsilon}{2\mathcal{T}}\right] \tag{5.27a}$$

$$\sigma_2 = \frac{1}{\omega}\int_{\Delta-\omega}^{\Delta} d\epsilon \frac{(\epsilon+\omega)\epsilon + \Delta^2}{\sqrt{(\epsilon+\omega)^2 - \Delta^2}\sqrt{\Delta^2 - \epsilon^2}}\left[\tanh\frac{\epsilon+\omega}{2\mathcal{T}}\right] \tag{5.27b}$$

These equations are readily integrated numerically. Remarkably within BCS theory, we find that the general response of a superconductor to an RF field only depends on the temperature and frequency of operation with respect to the gap and not any materials properties [18]. The specific choice of materials affects the realization of σ_i by providing particular gap and scaling these with the normal state impedance as Equation 5.26.

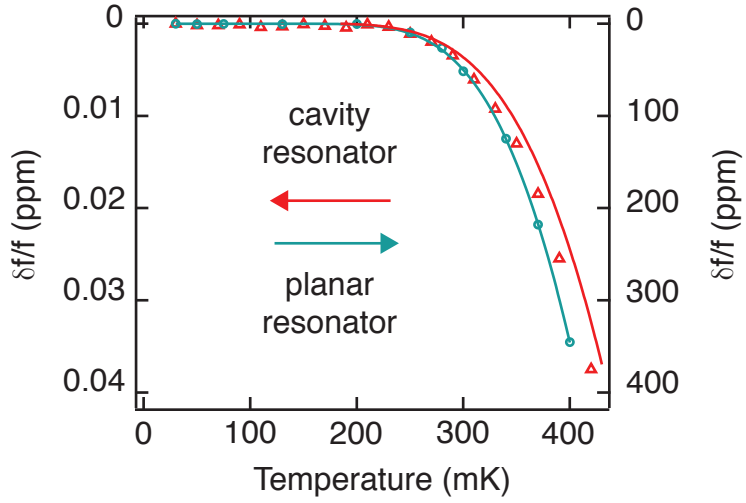

Figure 5.9: Temperature dependence of two superconducting resonators. The resonant frequencies of two superconducting aluminum resonators depend strongly on the temperature of the system. The physical realization of the two resonators are considerably different. One is a cylindrical TE_{011} cavity resonator, while the other is a traditional CPW planar resonator. These two devices share a similar transition temperature since they are both aluminum. That temperature response of the resonators is related by only a scaling factor demonstrates the universality of the BCS predictions. The factor of 10^5 difference between the two frequency shifts indicates the significantly smaller magnetic participation of the cavity resonator.

The BCS gap itself has a temperature dependence that is universal with respect to the reduced temperature ($\bar{t} = T/T_c$). It can be numerically solved [18, op. cit. Sec. 3.6.2] using

$$\frac{1}{N(0)V} = \int_0^{\omega_c} \frac{\tanh\left(\frac{1}{2}\beta\sqrt{\xi^2+\Delta^2}\right)}{\sqrt{\xi^2+\Delta^2}} d\xi. \tag{5.28}$$

where $\beta = 1/\mathcal{T}$, $N(0)$ is the number of Cooper pairs at zero temperature and V is the BCS interaction strength.

We can use Equation 5.28 to tabulate values of $\Delta(\bar{t})$ (Appendix []) and plug these values in Equation 5.27 with the frequency of interest to obtain a universal description for the complex impedance of a superconductor across a wide range of temperatures. A small modification to Equation 5.27 needs to be taken into account when $\omega \gtrsim \Delta(\bar{t})$ (Appendix []), which will always occur for finite frequency since $\Delta(\bar{t} = 1) = 0$. Because everything in this treatment has been universal thus far, the temperature dependence

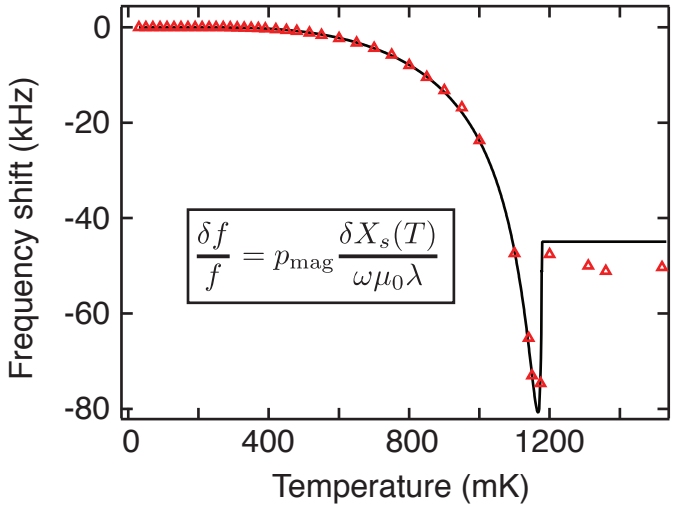

Figure 5.10: Fitting temperature dependence to BCS theory. The frequency of an aluminum cavity resonator can be tracked from base temperatures across the transition temperature of approximately 1.2 K. The BCS integrals allow the accurate and independent determination of T_c and the magnetic participation ratio p_{mag}. Knowing the field distribution of the mode allows us to extract the penetration depth λ from the scaling.

of a superconducting resonator reduces to scaling the temperature axis to find T_c and determining the proper clean/dirty limit by the exponent ν.

An example of such a fitting process is shown in Figure 5.10. Moreover, because we can calculate p_{mag} independently (see Section 4.2.3), scaling the magnitude of the frequency shift gives us the penetration depth immediately

$$\frac{\delta f(T)}{f} = \frac{1}{\lambda} \left(\frac{p_{\mathrm{mag}}}{\omega \mu_0} \right) \delta X_s(T). \tag{5.29}$$

Before and after etching, we find for a high purity aluminum cavity resonator $\lambda = 65 \pm 2$ nm and $\lambda = 52 \pm 2$ nm [52]. While both data sets are better described by the dirty-limit BCS description, the decreased penetration depth indicates that etching has increased the mean free path [155, 156]. Additionally, the real part of the superconducting surface can be extracted from quality factor measurements (Fig. 5.11).

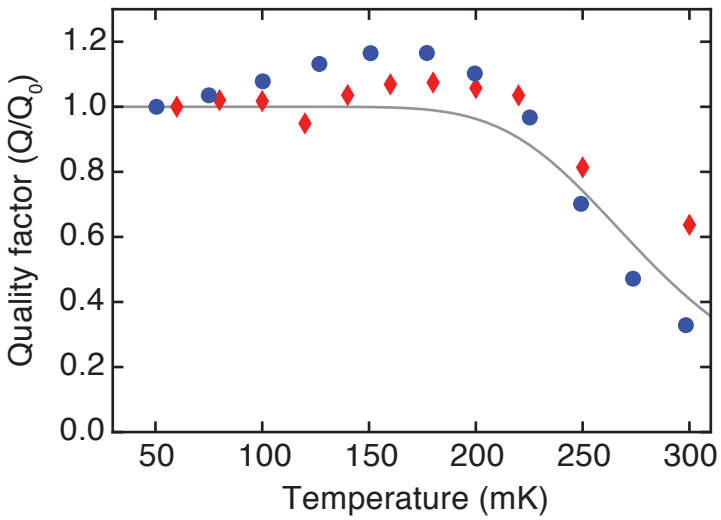

Figure 5.11: Observed quality factors compared to BCS theory. Temperature dependence of the internal quality factors for the cylindrical TE_{011} resonator (red diamonds) and the coax resonator (blue circles). The behavior of the imaginary conductivity allows us to predict the shape of the quality factor roll-off (grey) accounting for a residual Q_0 that is of unknown origin. Without an additional loss mechanism, the upward trend of the theory line at low temperatures would continue. We observe a maximum Q for the coax resonator at an elevated temperature ($T \approx 180\,\mathrm{mK}$), which is consistent with the power-dependent behavior of the mode, as these defects may be saturable via thermal energy in addition to RF excitation.

5.2 Transmon measurements

Measuring transmon qubits in the dispersive limit of cQED has been the focus of several theses at Yale and elsewhere. A recent development for these techniques has been the introduction of FPGA controllers as specialized tools for cQED experiments [48]. A dedicated undertaking by Shoelkopf and Devoret group members Nissim Ofek, Yehan Liu, Reinier Heeres, and many others has resulted in a stable set of FPGA hardware and software interface that has refined the capabilities of the Yale cQED team. These developments have made possible a new set of experiments [158]. The central impact of that work for this thesis has been enabling more efficient and stable experiments.

Here, we briefly review the experimental techniques used to fabricate, measure, and control a transmon qubit.

5.2.1 Fabrication

The transmon qubit is fabricated on a 430 μm thick sapphire wafer with a standard Dolan bridge process [159]. A bilayer of resists (MMA/PMMA) support a suspended structure at the Josephson tunnel junction location and are completely stripped where the antenna is to be deposited. Both exposures are completed in a single step of electron-beam lithography. Before deposition, the sapphire surface is cleaned with ion etching, an Ar/O_2 descum at 250 V and 160 mA for 30 s. We deposit aluminum with double-angle evaporation ($\pm 28^\circ$) with thicknesses of 20 nm and 60 nm, exposing the chamber to oxygen in between these depositions (720 seconds in 2000 Pa static pressure of a gaseous mixture of 85% argon and 15% oxygen) and again before removing the sample (600 seconds, 400 Pa). We liftoff the aluminum that is deposited on undeveloped resist. The full recipe is given in [129].

For the memory experiment, our tunnel junction has a normal-state resistance of R_n =3.5 kΩ at room temperature. We use the Ambegaokar Baratoff relations [160] to translate this junction resistance to a predicted Josephson energy, as

$$E_J = \frac{\Phi_0 \pi \Delta}{2e R_n'} = 150\,\mu\text{eV} \tag{5.30}$$

where $R_n' = 1.17 R_n$ is the equivalent low temperature value of the tunnel resistance. Applying Equation 2.41, we can translate the normal state resistance to a predicted Josephson inductance of $L_0 = 4.5$ nH.

5.2.2 Measurement setup

Figure 5.12 shows the experimental setup for qubit measurements. These measurements require two new types of low pass filtering at the base temperature stage [43] in addition to the attenuation chain in Section 5.1.2. These are necessary to remove for residual thermal radiation, which is detrimental for cQED experiments while being difficult to detect for bare resonator experiments. However, the setup presented here has also been used for resonator measurements to no effect.

The first additional filter is a multi-stage cavity low pass filter sourced for this thesis through K&L Microwave Inc [43]. They are constructed by concatenated sections of waveguide cavity resonators. The K&L filters have a rapid roll-off above cutoff ($\omega_c/2\pi = 10 \text{ or } 12$ GHz). Their purpose is to shield the cQED device from intermediate radiation frequencies ($\omega_{\text{rad}}/2\pi \lesssim 20$ GHz) which cause can T_2 degradation via photon-shot noise

[140]. However, because the K&L filters are based on resonant techniques, these devices will have unspecified transmission at very high frequencies ($\omega_{\rm rad} \gtrsim 2\omega_c$). Their metallic construction suggests that these filters will actually be good transmitters of infrared radiation, which could be leaking from higher temperatures stages of the dilution refrigerator or generated by the amplification chain.

Eccosorb filters are used to 'clean up' the high frequency spectrum [110]. These filters are fabricated in house via coaxial sections that have purposefully lossy dielectric. The dielectric of choice is Eccosorb CR-110 by Emerson & Cumming. The material is commonly used for making waveguide terminations and for anti-reflection coatings in radar applications. For our purposes, eccosorb imbues these filters with a slow, mostly linear roll-off that is provided by the conductivity of the activated carbon loading the dielectric [110]. These type of filters are important because they do not have a fundamental high frequency limit. Therefore, any infrared leakage will likely be absorbed by these sections.

Another modification to the measurement chain is the addition of a nearly quantum limited parametric amplifier to boost qubit readout [27]. We discuss its operation in Section 5.2.5.

5.2.3 Control signals

As we showed in Chapter 2, the transmon qubit is a strongly nonlinear Kerr resonator. To address its first Fock state, which we label $|e\rangle$, without populating the higher states of the transmon, we must use a frequency selective pulse. For universal control, the phase of that drive must be programmable. Single-sideband (SSB) modulation fulfills both of these requirements [62]. SSB is a technique developed a century ago to shape the amplitude and phase of a local oscillator (LO) signal without the penalty of spurious signal bands [67].

To realize a control signal, we play two envelopes on the FPGA DAC output that are modulated at some frequency $\omega_{\rm IF}$ and having some phase ϕ_0 at t=0 defined as the start of the experiment. Those signals are

$$I(t) = i(t)\sin(\omega t + \phi_0) \tag{5.31a}$$

$$Q(t) = q(t)\cos(\omega t + \phi_0) \tag{5.31b}$$

Usually, the two envelope functions are chosen to be Gaussians to minimize distortion [144], i.e.

$$i(t) = q(t) = Ae^{-(t-t_0)^2/2\sigma_t}, \text{ for } t \in [t_0 \pm 2\sigma_t], \tag{5.32}$$

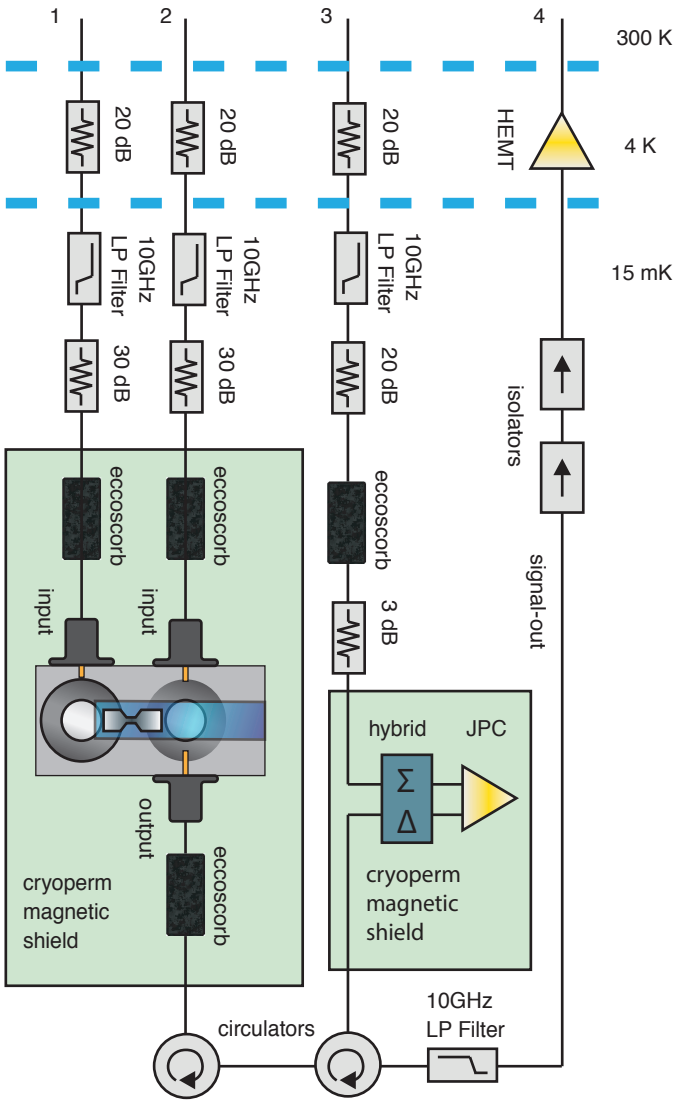

Figure 5.12: Low-temperature schematic for cQED device testing. The schematic for the memory experiment includes a number of important components in dilution refrigerator. Three input control lines (1,2,3) are heavily filtered to reduce thermal population and dephasing in any of our cQED modes. Circulators are used to introduce the output signal to the JPA amplifier, which amplifies the signal in reflection. The signal is further amplified by a low-noise HEMT amplifier and continues to the room-temperature demodulation chain (4).

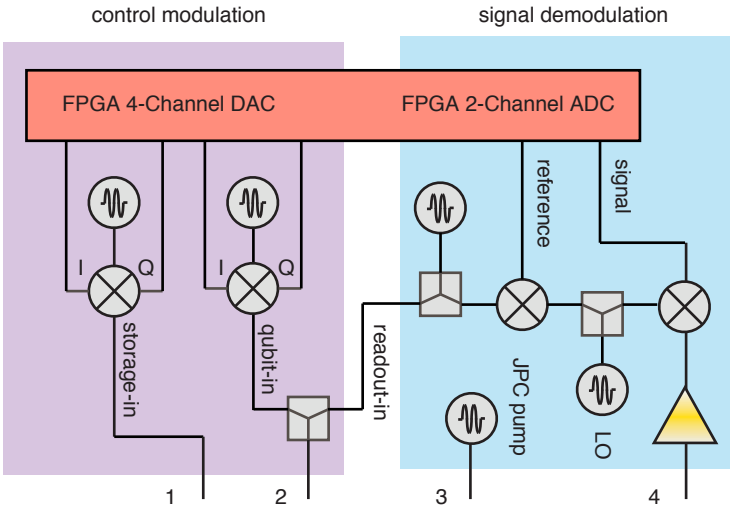

Figure 5.13: Room-temperature schematic for modulation and demodulation. The scheme for generating control signals and performing measurements is shown. The control chain (blue) depends on IQ modulating carrier tones for full phase and amplitude control, which are delivered to the cryogenic setup via lines (1,2). The resulting signal channel (4) is down converted by a phase-resolving, phase-stable interferometer, which compares the signal to a reference branch. The similarity of the measurement block to the VNA schematic is not a coincidence, since its primary function here too is to determine the resonant frequency of a circuit.

which is a pulse centered on some time t_0 and has width σ_t. These signals are often truncated to have $4\sigma_t$ duration to save DAC memory. This pulse has a frequency bandwidth of $\sigma_f = 1/(2\pi\sigma_t)$.

The conjugate signals are delivered to an IQ mixer on the I and Q ports respectively. For a mixer driven on the LO port at ω the resulting tone on the RF output will be delivered at $\omega - \omega_{IF}$. Additionally, tuning DC voltage offsets and phase unbalance can be used to account for imperfections in the IQ mixer that cause spurious sidebands [129].

5.2.4 Readout signals

A pulse is delivered to the readout mode in order to probe its frequency as discussed in Section 2.5 [64]. While techniques for pulse-shaping this tone can yield enhanced functionality [161], a square pulse is sufficient for most readout schemes. Therefore, a

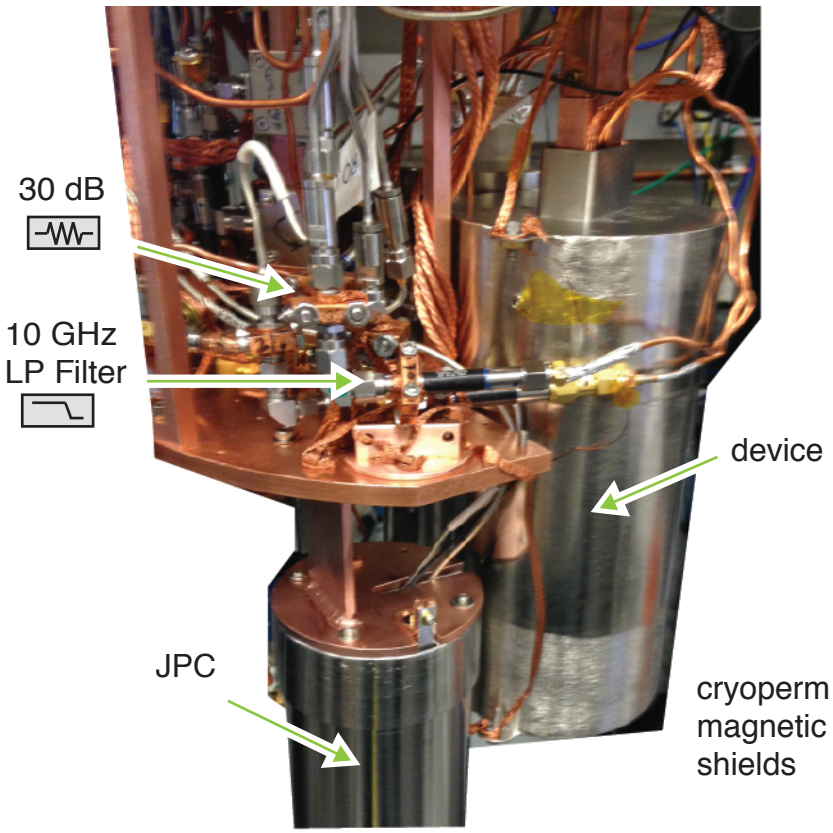

Figure 5.14: Picture of cQED setup. The assembled experiment in a cryogen-free dilution refrigerator. In the foreground, an input line, with two of its key filters, is visible. The third filter (eccosorb) is inside the device magnetic shield. Also visible is the magnetic shield of the experiments JPC. The two coaxial cables into this shield carry the pump and signal tones. Thermalization via copper braid and OHFC copper brackets is visible throughout the image.

digital marker from the FPGA is used to trigger a readout generator whenever the state of the qubit is to be determined.

For the memory experiment, the readout resonator was relatively long-lived ($\kappa/2\pi = 30\,\text{kHz} \ll \chi/2\pi = 1\,\text{MHz}$) [52]. Therefore, driving at the bias point halfway between the ground and excited state transitions required impractically large driving amplitudes. Instead, the readout was biased at the frequency resonant with readout mode conditioned on the ground state of the qubit ($\omega_r/2\pi = 9.78\,\text{GHz}$). The readout signal was therefore mostly an amplitude response. However, phase-resolving techniques still allowed for the most accurate state discrimination.

The readout mode in [52] was strongly over-coupled via the output port of the device. Therefore, signal leaked into our integration chain much faster than it was lost to the dissipation of the system. Our heterodyne interferometer (Fig. 5.13) mixed the readout signal with a detuned local oscillator ($\omega_{LO}/2\pi = 9.78\,\text{GHz}$+50 MHz) so that the signal could be digitized by our FPGA's gigasample-per-second DAC. The trajectory of the digitized signal, conditioned on preparing the state $|g\rangle$ or $|e\rangle$ is shown in Figure 5.15.

We generate an optimal filter by taking the difference of these two trajectories. That filter is applied to each qubit measurement by integrating the associated trajectory with the difference filter to obtain a single complex voltage (I_m, Q_m). Many such measurements allow a histogram to be assembled (Fig. 5.15). With a nearly quantum-limited JPC amplifier in the signal chain, we observe a large separation of the two distributions. This bimodal distribution can be thresholded at the bisection of the two Gaussians, so that each measurement record is converted into a binary result (g or e). Summing up these records gives us the probability that the qubit was detected in the excited state P_e, which we use throughout this thesis as our main detection mechanism.

5.2.5 JPC-backed dispersive readout

The memory experiment benefited immensely from a JPC pre-amplification stage [93]. The JPC is a nearly quantum-limited, phase-insensitive parametric amplifier. It provides a large gain (18 dB) to the readout chain, while introducing significantly less noise than the following HEMT amplifier at the 4 K temperature stage. Katrina Sliwa designed and fabricated the JPC used in this experiment.

A Wheatsone bridge of Josephson junctions at the center of the JPC allows for frequency tuning of the linear resonators that determine the amplification frequency of the device

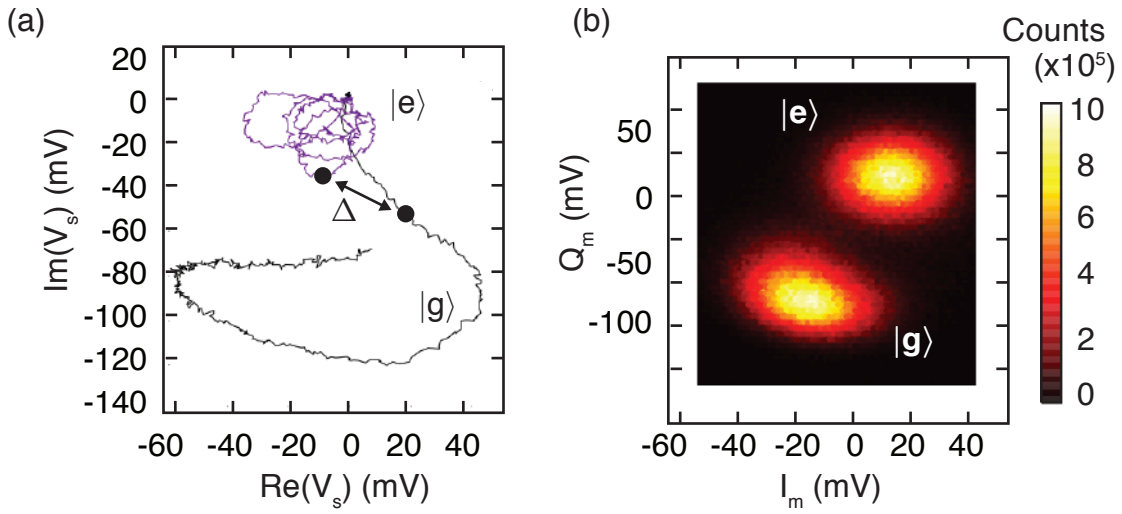

Figure 5.15: Dispersive readout signal. Many single-shot trajectories are averaged for the qubit initially prepared in the ground or excited state. Here, the readout frequency is resonant with the ground-state transition, which causes a large amplitude response of the readout signal. An optimal filter for detecting the qubit state is constructed by taking the vector difference between these two signals. **(b)**Many measurements of a prepared qubit state, here σ_x, are conducted by integrating the resulting signals through the optimal filter to obtain many single measurement records I_m, Q_m which can be plotted as a histogram. The separation of the distributions gives an indication of the measurement fidelity, boosted here by a JPC.

[93]. The bridge is biased with a magnetic field coil. Before tuning up the gain of the amplifier, the current bias that puts the linear mode of the JPC on resonance with the readout tone must be found. This is done by taking a flux curve of the amplifier that traces out the linear frequency of JPC as a function of current (Fig. 5.16).

After the desired current-bias point is found $\omega_s = \omega_r$. The frequency of the idler mode of the JPC needs to be determined ω_i. Then the condition on the pump $\omega_p = \omega_s + \omega_i$ is approximately known. The tune-up process involves small deviations about the ideal ω_p while increasing the pump strength. We operated the JPC at a gain point of $G = 18\,\text{dB}$ with a bandwidth of approximately $B = 7\,\text{MHz}$, which provided the high signal to noise ratio shown in Figure 5.15.

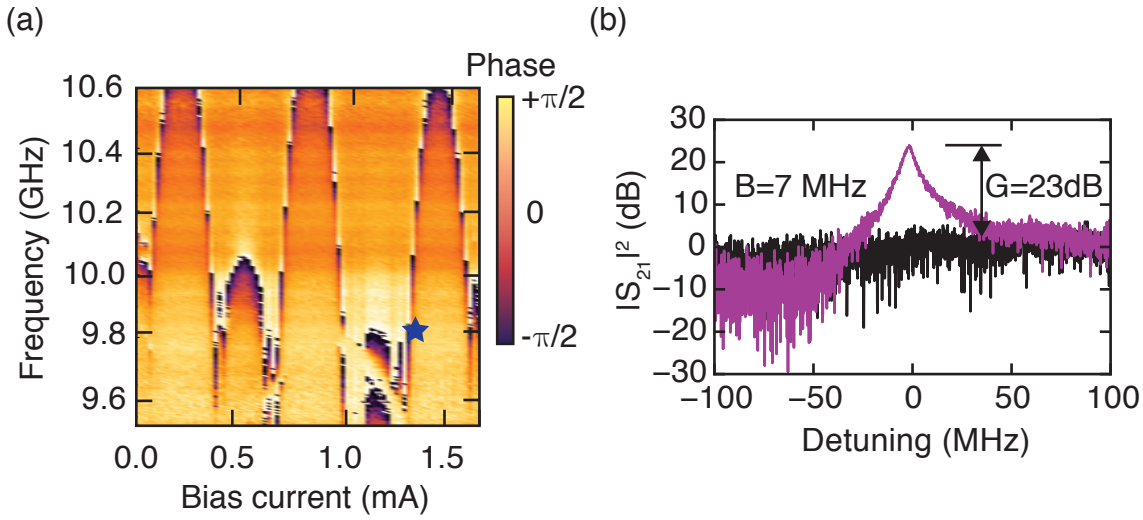

Figure 5.16: JPC tuneup and gain curve. (a) A flux curve is taken of a JPC's signal mode during the experiment to find a conversion between current bias and JPC frequency. The goal is to put the JPC on the resonance frequency of the readout mode. Because we operate the JPC at the 'bottom' of the flux curve (star), our JPC parameters are highly susceptible to fluctuating flux offsets. A cryoperm magnetic shield is crucial for stable operation. **(b)** After finding the correct bias current, the pump is tuned to drive the signal-plus-idler mode of the circuit at a power which gives the correct gain and bandwidth for optimum readout. In practice, this is an iterative process with single-shot readout histograms, although the gain provides a good indication of performance.

5.2.6 Spectroscopy

Without knowing the qubit parameters, a precise tune up of the readout signal is impossible. But if the device is in the strong-dispersive limit of cQED, the result of an otherwise-resonance drive of the readout mode will be mostly ineffective whenever the transmon is populated. We rely on this key observation to perform transmon spectroscopy and determine its frequency [43].

A pulsed generator is swept across the frequency region that the transmon is expected to occupy. The pulse duration and amplitude determine of this pulse determine the spectral content of the probe. For precise determination of the fundamental transmission frequency of the transmon, a relatively long, weak pulse is required $\sigma_t \approx T_2$. As shown in Figure 5.17, at higher powers, additional transmission peaks emerge as discussed at the conclusion of Chapter 2. These spectral lines allow the determination of other Hamiltonian parameters, such as the Kerr nonlinearity of the transmon [9].

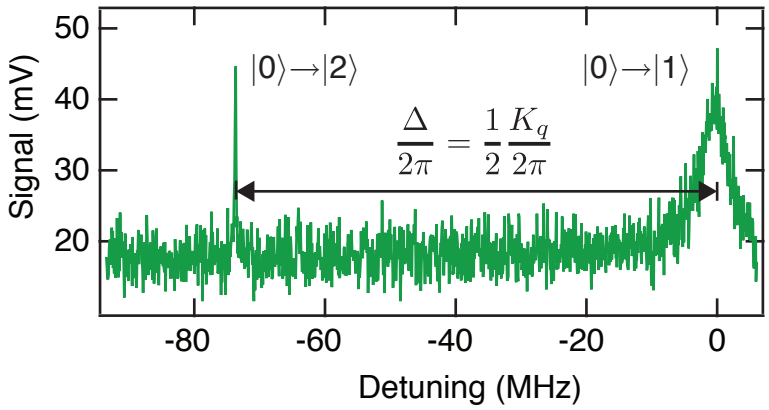

Figure 5.17: Transmon spectroscopy. The fundamental transition frequency of the transmon is determined by the large signal response of the readout signal whenever the spectroscopy generator is resonant with the $|0\rangle \rightarrow |1\rangle$ transition (used as $|g\rangle \rightarrow |e\rangle$ when operating the transmon as a qubit). At high powers, the two-photon transition $|0\rangle \rightarrow |2\rangle$ is also clearly visible and provides a direct measurement of the transmon's nonlinearity.

5.2.7 Rabi oscillations

After the frequency of the transmon is determined, we can selectively drive its fundamental transition frequency, thereby treating the transmon as a two-level qubit system. The most basic experiment that one can perform on such a system is Rabi-type experiment [39]. In a Rabi experiment (Fig. 5.18), a resonant drive causes the qubit to rotate around the Bloch sphere. The rate at which the Bloch vector rotates is given by the amplitude of the driving field, while the final location on the Bloch sphere is also affected by the duration of the drive. Measuring the final Bloch vector angle gives a calibration for the π pulses used throughout this thesis [144].

There are two main classes of Rabi-type experiments, 'power-Rabi' and 'time-Rabi' that are associated with the two main parameters for any family of drives, amplitude and duration [39]. Each experiment varies a single pulse parameter, e.g. duration, and equates the maximum P_e location to a π pulse. Usually the 'power'-type experiments are preferred since the experiment may already have timing constraints.

A few complications to these experiments warrant mention. A detuned drive will result in a slightly deformed shape to the Rabi oscillations. This can cause an experimentalist to

locate a local maximum of P_e, rather than the global. Therefore, the calibration of the π pulse will not take the qubit to the excited state, but rather some state which is mostly the $|e\rangle$ with some coherent superposition remaining in $|g\rangle$. If the drive is resonant instead with the two-photon transition, the resulting oscillations will be non-sinusoidal. In fact, the measurements (which are now indicative of population in the second-excited state) will oscillate at frequency that is dependent on the amplitude of the drive.

5.2.8 Lifetime

Once a π pulse is calibrated, a T_1-style experiment is readily possible [39]. We simply put the qubit in the excited state and monitor its population as a function of time (Fig. 5.18). If the qubit is experiencing a single decay rate, the decay will be a single exponential with time constant T_1.

5.2.9 Coherence

The coherence time of the qubit can be revealed by performing a Ramsey-type measurement with the qubit [39]. We put the qubit in a superposition state $|\psi\rangle = (|g\rangle + |e\rangle)/\sqrt{2}$ with a calibrated $\pi/2$ pulse. After some time, another $\pi/2$ pulse puts the qubit to the excited state if the phase angle between the generator and qubit is maintained (Fig. 5.18). In practice, we use a detuning between the generator and qubit to create an oscillatory signal. This prevents small-detuning effects that can lead to an incorrect exponential time constant. The resulting decay is an exponential envelope on the oscillations, with the exponential envelope decaying as T_2.

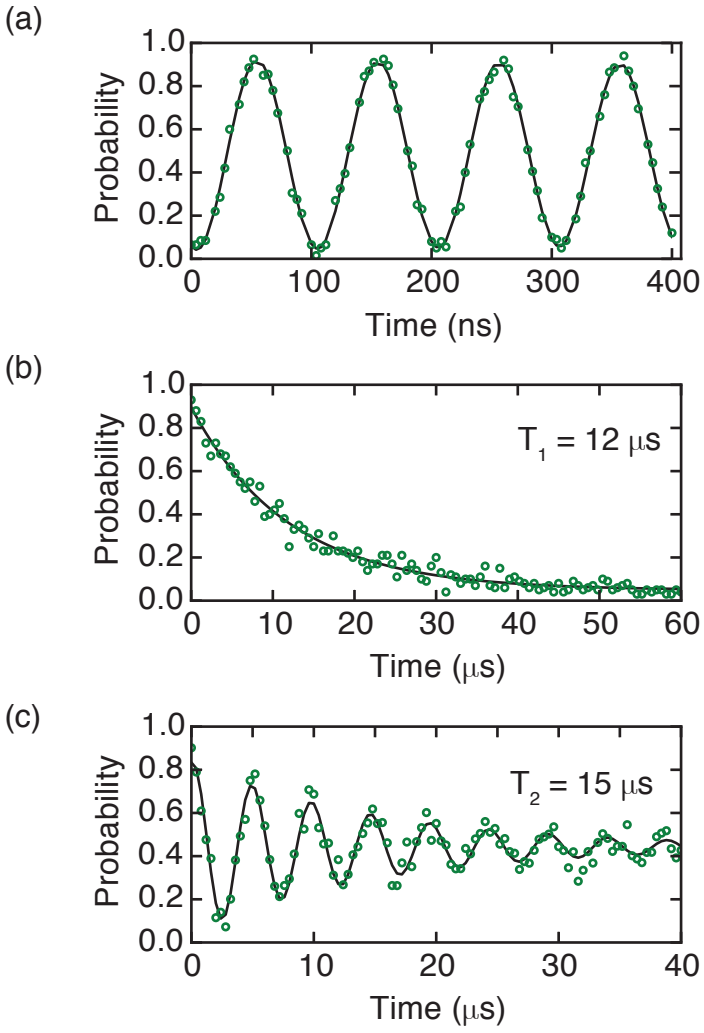

Figure 5.18: Transmon qubit characterization measurements. Operating the transmon as a two-level system, we can perform the standard suite of qubit experiments that enable tuneup and characterization. **(a)** Rabi oscillations are driven in the qubit for a fixed amplitude tone of variable duration (dt). This technique, colloquially the 'time-Rabi' experiment, converts a digitization parameter dt to a π pulse by the location of the maximum of the sinusoid. Alternatively, a 'power-Rabi' could be used, which fixes dt and varies the amplitude of the pulse. The Rabi experiments serve as a basic calibration of qubit control pulses. **b** The lifetime T_1 is measured by performing a calibrated π pulse and measuring the decay of the resulting signal. **(c)** The coherence time T_2 is performed by two $\pi/2$ pulses separated by a delay and, preferably, a digital phase that makes the experiment less susceptible to small-detuning effects.

CHAPTER 6

Characterizing near-millisecond coherence in a cQED oscillator

We have now seen several architectures for cQED, as well as the potential for resonators to act as quantum memories in these systems. In this chapter, we review a central result of this thesis, the realization of near-millisecond coherence times in a resonator that is strongly coupled to a transmon qubit [52]. We present the experimental techniques that allow for the characterization and utilization of such a quantum memory.

6.1 Dispersive coupling

In our coupled system of detuned modes, the interaction Hamiltonian (see Section 2.4.1) is given by

$$\hat{H}_{\text{int}}/\hbar \approx \chi \hat{a}^\dagger \hat{a} \hat{b}^\dagger \hat{b}. \tag{6.1}$$

The dispersive interaction strength χ constrains many of the cQED experiments that utilize qubit-mediated control or readout of resonators. Therefore, knowing χ to the highest precision is of paramount importance for the results in this thesis. Here, we review how χ is measured, as well as the resonator-drive calibration techniques enabled by the dispersive measurements.

6.1.1 Number-splitting spectroscopy

As shown in Figure 6.1, for strong-dispersive interactions, the qubit acquires a discrete set of transitions in its spectrum that are dependent on the state of the coupled resonator, as $|g,m\rangle \rightarrow |e,m\rangle$ [62]. In addition, the resonator spectrum is split by an equal amount for states of the transmon, as $|g,m\rangle \rightarrow |g,m\pm 1\rangle$. When no drives are present, these transitions are separated by χ. Therefore, precise measurements of the qubit or resonator spectrum allows a straightforward extraction of χ [62].

We stress however that if another drive is present, and particularly if it is at a frequency close to a transition of the system, the observed spectrum can be difficult to interpret [34, 64]. Therefore, pulsed spectroscopy is the preferred method for extracting χ in the frequency domain. The experimental sequence is shown in Figure 6.1. First, a resonant drive populates one of the modes (the i^{th} mode). If a short pulse is used for this purpose ($\sigma_f \gg K_i$), we expect that a coherent state should result. Then, a second pulse of variable frequency scans the spectrum of the j^{th} mode. To achieve a discrete spectrum, this pulse should be long so that $\sigma_f \ll \chi$ and of sufficiently weak amplitude to avoid power broadening the j^{th} mode (FWHM$_j \ll \chi$). A form of spectroscopy known as π-pulse spectroscopy sweeps the frequency of a pulse calibrated to take the qubit $|g\rangle \rightarrow |e\rangle$ to achieve these goals while maximizing the population of the transmon in $|e\rangle$, thus increasing signal levels. The resulting spectrum can be fit to a sum of Gaussians or Lorentzian functions depending on the amplitude of the probe tone and the phase noise of the j^{th} mode.

We also point out that there are always higher order interaction Hamiltonian terms of the form

$$\hat{H}'_{\text{int}}/\hbar = \chi'_{ab}\hat{a}^\dagger\hat{a}^\dagger\hat{a}\hat{a}\hat{b}^\dagger\hat{b}^\dagger + \chi'_{ba}\hat{a}^\dagger\hat{a}\hat{b}^\dagger\hat{b}^\dagger\hat{b}\hat{b}, \tag{6.2}$$

which yield a dispersive shift which itself is number dependent [69], i.e. there is no longer a single χ_{ab} that describes all dynamics. However, these higher terms can often be neglected because

$$\frac{\chi'_{ab}}{\chi_{ab}} \approx \varphi_a^2 \ll 1 \tag{6.3}$$

where φ_a is the zero point fluctuations of the resonator mode. While the magnitude of χ'_{ba} is not small, the transmon is typically operated with $\langle\hat{b}^\dagger\hat{b}\rangle \leq 1$. Therefore, this term does not contribute to our dynamics. However, measurements of χ' are possible [69]. These techniques allow confirmation of our Hamiltonian model.

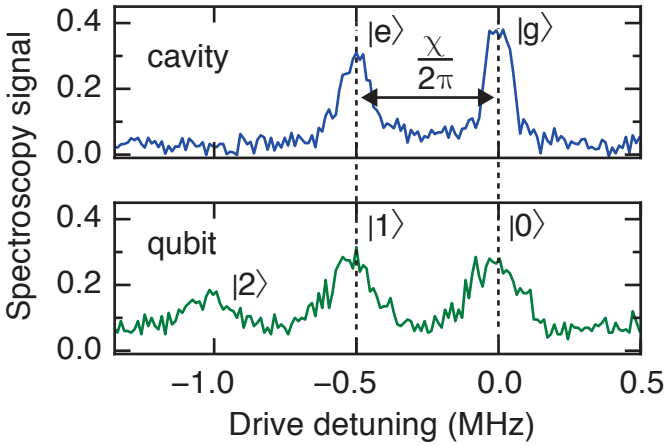

Figure 6.1: Number-splitting spectroscopy. (top) With the qubit in an equal superposition of $|g\rangle$ and $|e\rangle$ the cavity has an equal probability of being detected at two frequencies detuned by the dispersive shift $\chi/2\pi$. **(bottom)** A small displacement on the cavity causes the qubit to acquire multiple transition frequencies whose weights are proportional to P_n. Either of these techniques therefore provides a straightforward measurement of χ.

6.1.2 Time-domain techniques

While the frequency domain allows a simple extraction of χ, the fine tuning of the drive amplitudes and frequency spans can become onerous for large amplitude states. Measuring in the time domain can provide an arguably simpler experiment, involving only resonant drives, at the cost of a highly nonlinear output [11, 68]. Further, because many of the techniques for cQED operations involve essentially time domain modulation of excitation numbers [68], performing time domain measurements of χ is crucial. For instance, such a measurement is nearly equivalent to the calibration of the QND parity measurement scheme [80].

The measurement, shown in Figure 6.2, requires only a small modification to the basic qubit T_2 protocol. Essentially, the resonator is displaced to some, potentially unknown, amplitude. Then, a $T_{2,q}$ experiment is performed on the qubit. In the strong-dispersive regime, the qubit's coherence will decay much more rapidly than the the bare $T_{2,q}$ [68]. However, this extra decay is only caused by entanglement with the resonator. Measuring solely the qubit mode traces out the information in the resonator, causing a false decoherence signal [79]. In fact, at some time later, $t = 2\pi/\chi$, the state will

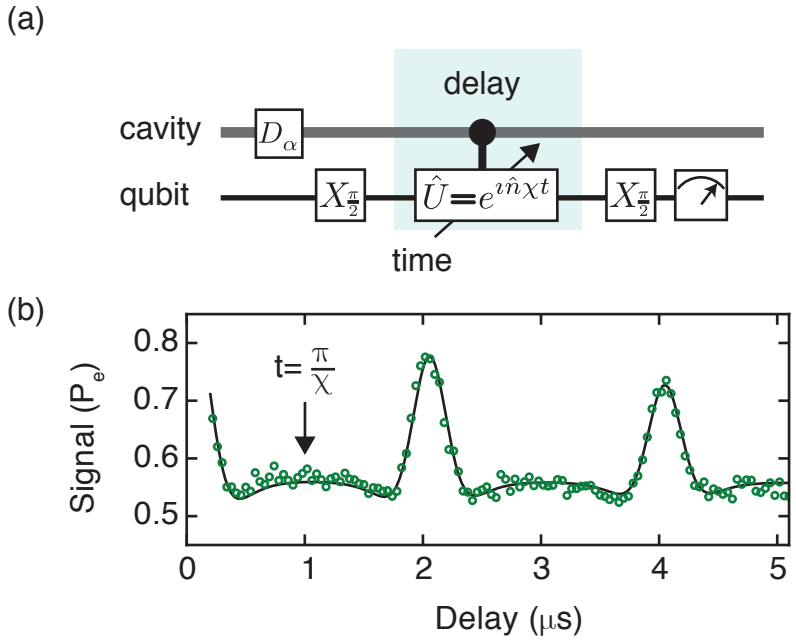

Figure 6.2: Time-domain χ measurement. (a) Experimental sequence to extract the dispersive interaction strength via time-domain techniques. A displacement pulse on the cavity puts the cavity state in a superposition of many Fock states. With the qubit on the equator of the Bloch sphere, the superposition of cavity Fock states causes a frequency dispersion of the qubit, which revives at times $t = 2\pi/\chi$. A second π pulse on the qubit maps the oscillating phase coherence back onto the qubit state. **(b)** Experimental results from the time-domain technique. The fully-coherent evolution of Equation 6.4 (grey) over-predicts the revival strength then the delay becomes comparable to the lowest T_2 of the system.

completely revive (although reduced by at least a factor of $e^{-\chi T_2}$). Locating the period of these revivals then is equivalent to determining χ.

The form of these oscillations with a coherent state in the cavity [68] is

$$\begin{aligned} P_e &= \frac{1}{2}\left[1 + \mathrm{Re}\left(\langle\beta|\beta e^{\imath\chi t}\rangle\right)\right] \\ &= \frac{1}{2}\left[1 + e^{|\beta|^2(\cos(\chi t)-1)}\cos(|\beta|^2\sin\chi t)\right] \end{aligned} \tag{6.4}$$

One advantage of the time domain technique is that many different displacements on the resonator can be performed with a single protocol, rather than for the frequency

domain which requires several different frequency spans to be stitched together. This allows for rapid assessment of χ' effects.

6.2 Classical energy decay rate

6.2.1 Calibrating control pulses

Once χ is well understood, we immediately know how to perform selective drives on the system which act as effective $CNOT$ operations between different system observables [38]. The most straightforward of these is the detection of individual Fock states. This same technique turns out to also be a calibration tool for making displacement pulses of known amplitude [38].

In the number-splitting spectroscopy measurement (Section 6.1.1), we have already seen the selective drive in action, resulting in an increased signal whenever the drive was resonant with an allowed $|g,m\rangle \rightarrow |e,m\rangle$ transition, provided $\sigma_f \ll \chi/2\pi$. However, spectroscopy is an over-complete measurement. Essentially, each of the peak-widths will be equal. Therefore, the height of each peak, or equivalently, the effectiveness of each selective π-pulse, is sufficient to determine the P_n distribution [38].

Remarkably, that tool gives us the ability to convert DAC voltages for a pulse to a coherent state displacement amplitude β for drives on the resonator. Because the statistics of the photon number distribution is a well known set of Poissonian functions, those statistics should provide a linear scaling term between the DAC voltage (V_{DAC}) and β, [38] i.e.

$$P_n(\beta) \propto P_n(cV_{\mathrm{DAC}}), \tag{6.5}$$

where c has units of inverse-Volts. The proportionality relation is used instead of equality to acknowledge finite measurement fidelity, which provides false counts (mainly in $|g\rangle\langle g|$ due to $T_{1,q}$) but does so equally along each number state. While each Fock state can be measured, again this provides over-complete information since only a single scaling term is required.

A subtle effect in these measurements can arise from direct resonator-resonator interactions. For large displacements, typically $\alpha \gtrsim 2$, an upward quadratic signal can be observed in dispersive measurement signals [38]. This arises from Hamiltonain terms like $\chi_{r1r2}|\beta|^2$, where the readout mode is shifted in frequency by the population of the resonator under calibration. This effect was dramatic in [162], which observed number-splitting directly

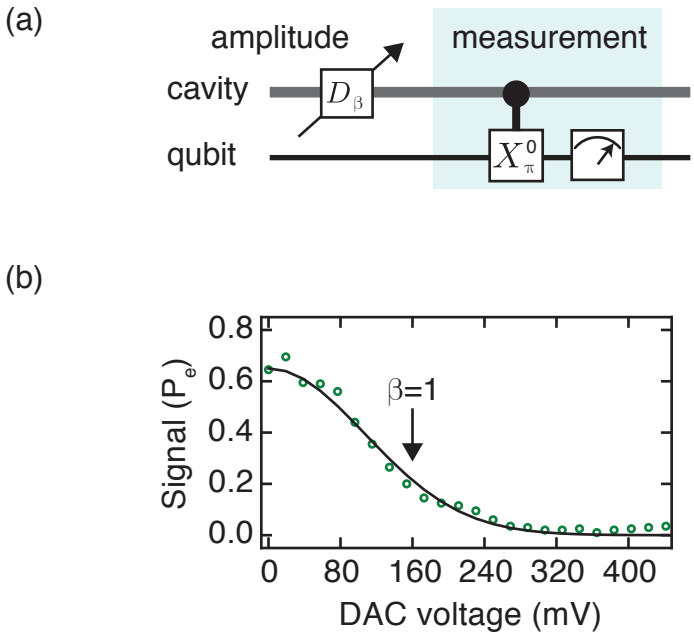

Figure 6.3: Calibrating cavity displacement pulses. **(a)** Experimental sequence to convert classical pulse strengths to displacement amplitudes. Variable amplitude pulses displace the cavity from the origin. Then, a number-selective π pulse on the qubit measures the remaining population in the vacuum. **(b)** The signal falls as a Gaussian, whose width serves as a conversion from DAC units to photons. The height of the curve being lower than unity indicates that the long qubit pulse acts on a timescale comparable to the decoherence of the system. This procedure is identical to measuring the Husimi-Q function of the resonator along an axis on the IQ plane.

between two cavities. For small perturbations, a background subtraction (retaking the data without the qubit π pulse and subtracting the two signals) is used to remove this artifact and restore a signal proportional to simply P_n.

6.2.2 Coherent state κ experiment

In order to determine the classical energy decay rate that bounds the coherence of our resonator memory we perform the experiment shown in Figure 6.4. This experiment essentially repeats the coherent state calibration, but includes a delay between state generation and detection. Since the coherent state preserves its statistics during the decay,

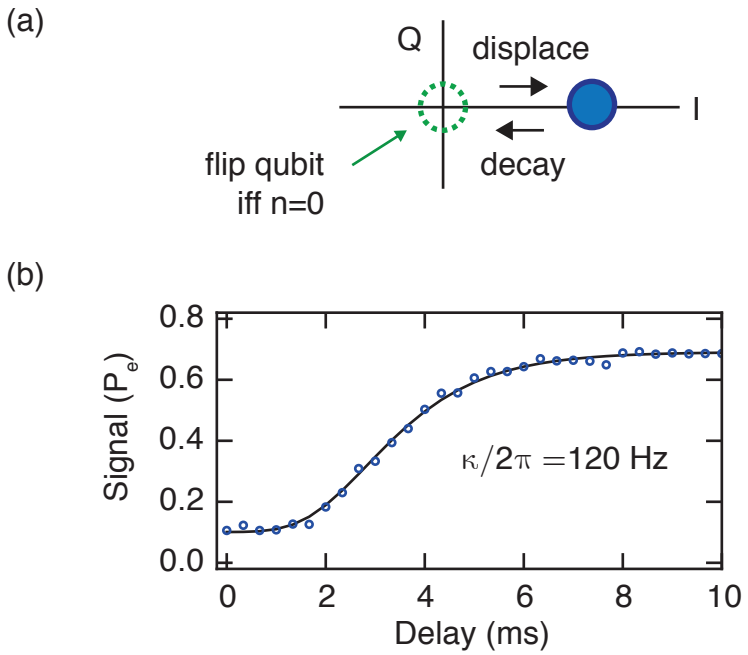

Figure 6.4: Energy decay of a qubit-coupled resonator. (a) Schematic representation of the experiment to extract the energy decay rate of a cavity. A calibrated displacement pulse on the cavity puts it in a state with average photon number $\bar{n} = |\beta|^2 \gg 1$. This state falls to the origin with a characteristic rate κ, which is probed by measuring the population of the vacuum P_0. **(b)** Experimental results from the coherent state κ technique. At first, the signal is flat because the state is still far from the origin $|\beta(1 - \kappa dt/2)|^2 \gg 1$. At the end of the experiment, the curve is again flat since the vacuum state is equilibrium. The duration of time that separates these two flat regions gives κ for any sufficiently large amplitude input coherent state. We find in this experiment that $\kappa = 120 \pm 5\,\text{Hz}$.

we can even use the same description for P_n. After displacing the resonator, we probe the population of the vacuum state [52], giving

$$P_n(\beta(t)) = P_n(\beta_0 e^{-\kappa t/2}) = e^{-|\beta_0|^2 \exp(-\kappa t)} \tag{6.6}$$

The double exponential form requires some care for choosing β_0. It is important to displace the resonator sufficiently high $\beta_0 \gtrsim 3$ that P_0 remains approximately zero for some time. Then, one can more easily separate the two distinct curvatures. While the ring down appears quite different than qubit $T_{1,q}$ decays, we can gain additional confidence in our work by using calibrating displacements, reducing the problem to essentially three fit

parameters, an offset, a scaling, and κ. Of these, only κ causes nontrivial behavior in the decay curve.

In Figure 6.4 [52], we extract $\kappa/2\pi = 120 \pm 5$ Hz, corresponding to a quality factor of $Q = 3.5 \pm 0.1 \times 10^7$. We expect from this classical decay rate that a single excitation in the mode would have a lifetime $T_1 = 1/\kappa = 1.33 \pm 0.06$ ms.

6.3 Coherence experiments

The coherence of the resonator is directly accessible if one can create and measure the decay of non-classical photonic states in the mode [39]. Fortunately, techniques for preparing arbitrary quantum states in resonators were recently developed for the dispersive cQED Hamiltonian at our disposal [69, 95]. This section provides an overview of how input states, analogous to those commonly used for experiments on two-level system coherence, are generated and how their decay is recorded. We then recover the simple exponential decays of T_1 and T_2.

6.3.1 Oscillator T_1

A two-level system T_1 experiment begins with a complete inversion of the qubit's population from ground to excited state. At zero-temperature, the qubit population will be left in the excited state with probability that is simply $P_e = e^{-t/T_1}$. State-of-the-art superconducting qubits have reached $T_1 \approx 1$ ms for fluxonioum-type qubits at a flux bias point of $\Phi = \Phi_0/2$ [119]. Transmon-type qubits have been observed at the $T_1 \approx 0.1$ ms level [106, 114, 141].

If an oscillator is prepared in the first Fock state $|1\rangle$, a similar description follows. The energy decay is given by a simple exponential $P_1 = e^{-t/T_1}$ [52]. Alternatively, the probability of detecting the resonator in its ground state is $P_0 = 1 - e^{-t/T_1}$. We have already shown how SNAP can be used to generate such an input state for a dispersively-coupled resonator (Section 3.3.2). In addition, the selective qubit rotations described in P_n complete the required control and measurement channels. The protocol for conducting a T_1-type experiment on a resonator is therefore readily available with these elements. First, we use SNAP to generate $|\psi_0\rangle = |1\rangle$, then we monitor P_0 as a function of delay, which we expect to yield a single exponential term.

In practice, SNAP does not prepare a perfect $|1\rangle$ Fock state. Because the photon number selective qubit rotation has duration $\sim 1/\chi$, the cavity and qubit are completely

entangled for some finite time [79], which can be comparable to the decay rates of the system. In particular, the qubit's coherence time in the memory experiment was observed to be $T_{2,q} = 6\,\mu$s, while the Gaussian sigma of the SNAP gate was chosen to be $T_{\text{gate}} \approx 1.5\,\mu$s. A naive estimation of fidelity $\mathcal{F} \sim e^{-T_{\text{gate}}/T_{2,q}}$ would predict that approximately 80% of the resonator should be prepared in the target state.

We indeed confirm a similar result experimentally (Fig. 6.5). By performing qubit spectroscopy we measure the distribution of P_n after the SNAP preparation step. We point out that a complication to this spectroscopy technique can arise for coherent SNAP gate errors. Essentially, if the qubit does not return to the ground state upon completion of the SNAP gate, the n^{th} Fock state undergoing the SNAP rotation may be mistakenly found to have excess P_n. Resetting the qubit between preparing the cavity state and detecting its probability distribution can avoid this source of error. Luckily, for the memory experiment [52], the ratio of lifetimes between qubit and cavity was approximately 100. We are therefore able to reset the qubit passively before measuring P_n to reset. A delay of three qubit lifetimes changes the cavity statistics by only 3%. Therefore, we include this delay before extracting the distribution P_n. We find the resonator state to be a distribution of Fock states as $P_0 = 0.21 \pm 0.02$, $P_1 = 0.75 \pm 0.02$, $P_2 = 0.0.04 \pm 0.02$, and all other states below the noise of our detection. Any off-diagonal matrix elements are not resolved by this method. However, for the purposes of a T_1 experiment, this characterization is sufficient.

The T_1 decay is obtained by incrementing a delay between preparation and measuring the population of P_0 or P_1. As expected, a single exponential is observed in the signal, with a time constant that is within the uncertainty of measurements on coherent states. The two measurement techniques trade ease of state preparation (Fock states are harder to generate than coherent states) for ease of decay signal interpretation (decay of coherent states is a double exponential). Therefore, it is reassuring to obtain the two types of measurements. Indeed, in Figure 6.6 [52], we extract $T_1 = 1.22 \pm 0.06$ ms, in agreement with the classical energy decay rate extracted from coherent states.

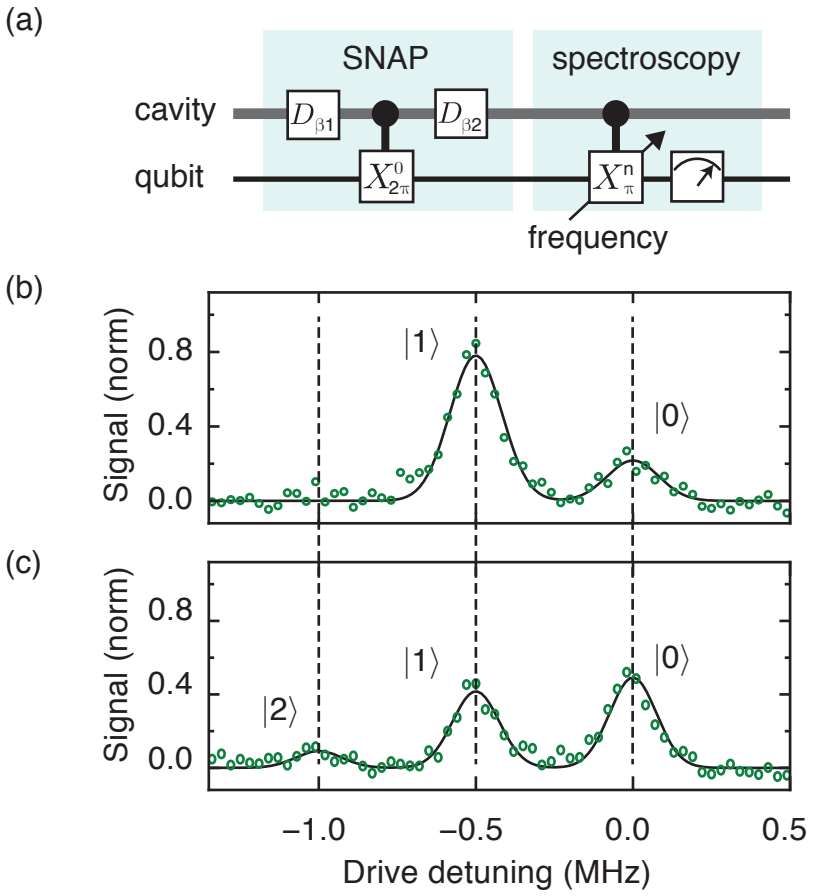

Figure 6.5: Preparation of nonclassical states via SNAP. (a) Experimental sequence to characterize the resulting photon statistics of a resonator state prepared by SNAP. Two displacement pulses on the resonator are separated by a single number-selective qubit 2π rotation that takes $|g,0\rangle \Rightarrow e^{i\pi}|g,0\rangle$ via a geometric phase. This phase rotation causes a nontrivial interference effect between the displacement operators. (b) Spectroscopy on the qubit reveals the results of this preparation step. When the cavity is mostly in the first Fock state, $|1\rangle$, the qubit's frequency distribution reflects these statistics. By the normalized area under each peak, we determine that the population of each Fock state (P_n) is $P_0 = 0.21 \pm 0.02$, $P_1 = 0.75 \pm 0.02$, $P_2 = 0.04 \pm 0.02$ **(c)** After preparing a superposition of $|0\rangle$ and $|1\rangle$, we find the distribution to be $P_0 = 0.49 \pm 0.02$, $P_1 = 0.41 \pm 0.02$, $P_2 = 0.10 \pm 0.02$. This experiment alone is not sufficient to distinguish between a statistical mixture of these states and a coherent superposition. However, the phase coherence is revealed in the sinusoidal oscillations of the subsequent T_2 experiment.

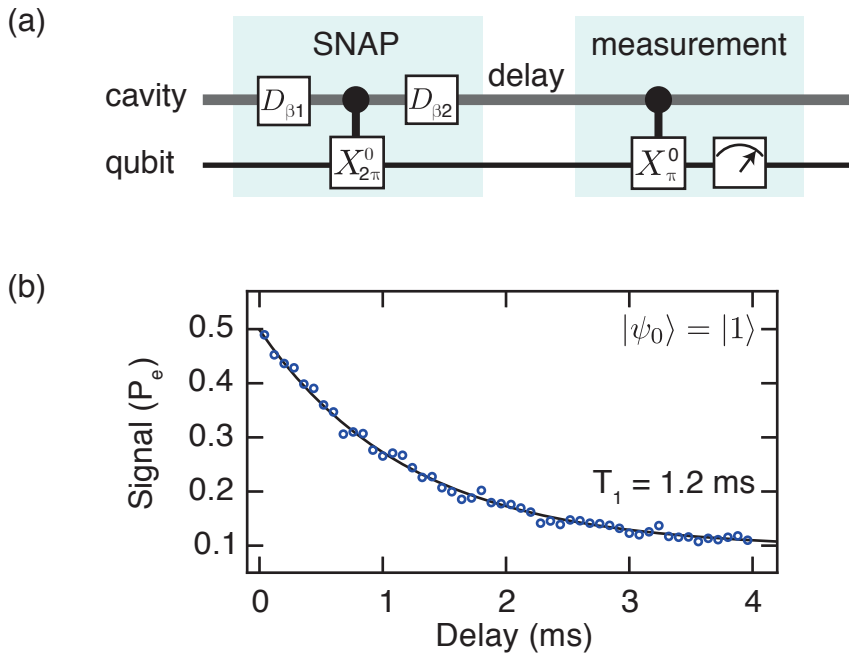

Figure 6.6: T_1 decay of an $|1\rangle$ Fock state. (a) Experimental sequence to measure T_1 of a resonator via SNAP. After the $|1\rangle$ state is prepared, a delay is incremented. Then, a selective qubit rotation is used to probe the population of the vacuum as the first Fock state decays. **b** We observe a single exponential with $T_1 = 1.22 \pm 0.06$ ms.

6.3.2 Oscillator T_2

A typical T_2-type coherence measurement on a two-level system [39] begins with a $\pi/2$ pulse that takes the state to a superposition along the equator of the Bloch sphere like

$$|\psi_0\rangle = \frac{1}{\sqrt{2}}(|g\rangle + |e\rangle). \tag{6.7}$$

After some time, the state has evolved with some phase to a state

$$|\psi(t)\rangle = (|g\rangle + e^{-\imath\theta(t)}|e\rangle)/\sqrt{2}. \tag{6.8}$$

Without decoherence, a second $\pi/2$ pulse along the same axis on the Bloch sphere will restore the state whenever $\theta = 2\pi$. For a frequency detuning between the pulse and two-level system (Δ), the revival will be sinusoidal with period $T_{rev} = 2\pi/\Delta$. The decay

of the phase coherence (T_2) leads to an envelope on this oscillatory signal that is related to the energy decay and phase noise of the system.

With SNAP, we can prepare a state along the equator of the pseudo-Bloch sphere of the resonator's subspace spanned by $\{|0\rangle, |1\rangle\}$ [95], such as

$$|\psi_0\rangle \approx \frac{1}{\sqrt{2}}(|0\rangle + |1\rangle). \tag{6.9}$$

The detailed calculation of how SNAP accomplishes this state preparation is included in Appendix B for completeness. This resonator state will evolve analogously to the two-level system (Eq. 6.8). Then, we are left with the task of detecting the phase coherence between the two states. A displacement pulse on the resonator accomplishes just this [69], as shown in the theoretical results of Figure 6.8.

Because the SNAP gate is similar here to the one used for the creation of a single Fock state, we expect similar over all fidelities to the target superposition state. Experimentally, we can reconstruct the statistics of the prepared state of the resonator. Again, we use the frequency spectrum on the qubit to reveal the P_n distribution after a reset time. We find for the distribution that $P_0 = 0.49 \pm 0.02$, $P_1 = 0.44 \pm 0.02$, $P_2 = 0.1 \pm 0.02$, and the remainder of the Fock states having populations below the noise level of our detection [52]. However, the off-diagonal components of the density matrix, which contain the coherences between individual Fock states, are not captured by this characterization. That coherence is revealed by the application of the final displacement pulse at varying phase angles.

Using this state as an input to our T_2 experiment, we observe an exponentially decaying envelope with time constant $T_2 = 0.72 \pm 0.03\,\text{ms}$ [52]. The resonator exhibits some excess phase noise such that $T_2 < 2T_1$. We can parameterize this excess noise by a pure dephasing time T_ϕ such that

$$\frac{1}{T_2} = \frac{1}{2T_1} + \frac{1}{T_\phi}. \tag{6.10}$$

Using our observed T_1 for this expression, we conclude that $T_\phi = 0.98 \pm 0.05\,\text{ms}$, or a pure dephasing rate $\Gamma_\phi = 1/T_\phi = (2\pi) \times 1\,\text{kHz}$. This is a surprising result for the memory since VNA measurements on empty resonators [100], which probe frequency stability (T_2), have agreed with pulsed ring-down energy decay measurements (T_1) for the same devices.

The source of the excess dephasing can be traced to the qubit, as we show in the next section.

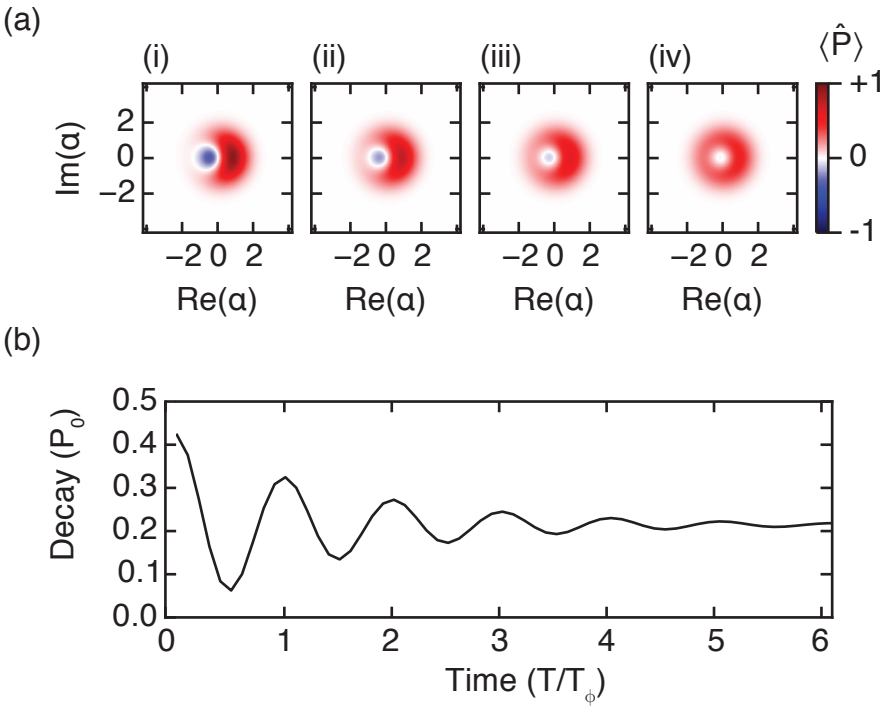

Figure 6.7: Theoretical analysis of pure dephasing in a resonator. **(a)** Simulated Wigner functions for a superposition state $|\psi\rangle = (|0\rangle + |1\rangle)/\sqrt{2}$ undergoing pure dephasing as described by Section 3.4.2. Across the panel, the initial state **(i)** has a large negativity in the Wigner function, but after a few pure dephasing times **(iv)**, the negativity has been completely washed out. The radial asymmetry in the state also decays in this process. **(b)** We simulate the process used experimentally to probe the phase coherence of the cavity state. The same state shown in (a) is displaced by an amplitude $\beta e^{i\Delta t}$. The resulting population in the vacuum state is plotted as a function of time. The oscillations damp as the state becomes more radially symmetric.

6.4 Qubit-induced decoherence

To understand how imperfections in the qubit mode can affect the performance of our cavity memory, we study two processes in detail. First, we examine how energy decay in the qubit can damp the strongly coupled cavity mode. Next, we show how thermal excitations in the qubit mode can dephase cavity states. Both of these processes have been subject to detailed study in the opposite limit. Low-Q resonators have been 'usual suspects' for inducing short qubit lifetimes [56]. Additionally, thermal excitations in low-Q resonator modes have been shown to cause pure dephasing of qubits [140, 141]. The

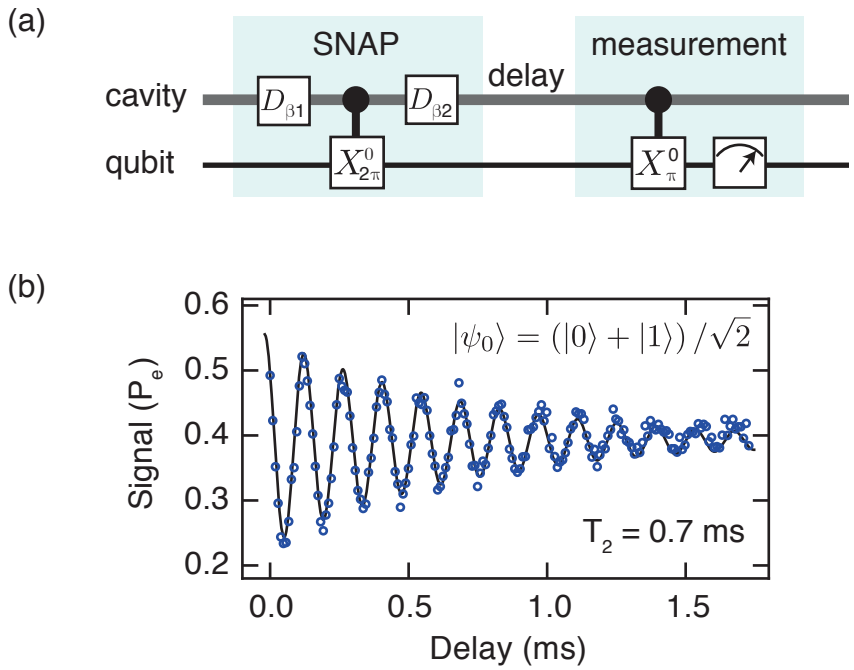

Figure 6.8: T_2 decay of an $|0\rangle$ and $|1\rangle$ superposition state. (a) Experimental sequence to measure T_2 of a resonator via SNAP and a final displacement. After the superposition state is prepared, a delay is incremented. Then, a final displacement pulse is used to measure the remaining phase coherence of the state via interference. A selective qubit rotation is used to measure the resulting interference by probing the population of the vacuum. **b** We observe an exponentially decaying sinusoid with $T_1 = 0.72 \pm 0.03$ ms. This indicates a pure dephasing time $T_\phi = 0.98 \pm 0.05$ ms

symmetry of cQED suggests that both of these effects become important in the reverse when we find ourselves in the low-Q qubit limit.

6.4.1 Reverse-Purcell effects

Black box quantization [10], as we discussed in Chapter 2 gives a framework for predicting the behavior of coupled QED circuits by first solving the linear system. If one of the coupled modes suffers from (linear) damping then, the dynamics of the linear system should exactly translate to the decay rates observed in the quantum regime [163]. The quantum memory experiment is a good test system for these predictions because the qubit

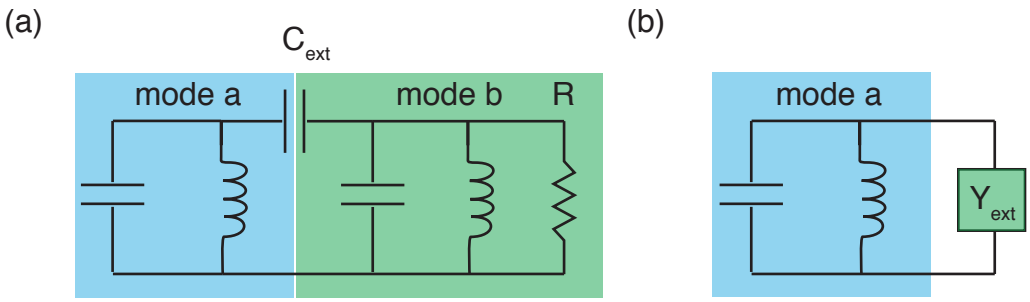

Figure 6.9: Capturing Purcell effects with linear LC circuits. (a) Two modes a and b are capacitively coupled, identically to the circuit considered in Chapter 2. Here however, mode b is damped with a resistor R. **(b)** To solve this circuit, we recast the admittance of mode b through the coupling capacitor. The real part of this admittance will show up as a damping term in mode a

mode has an energy decay rate of approximately one hundred times that of the cavity. We expect that the qubit's damping could influence observed lifetime of the memory.

Consider the following model (Fig. 6.11) to show how that cross-damping should behave. Two parallel LC oscillators (ω_a, ω_b) are coupled via a capacitor (C_{ext}). In addition, mode b is explicitly damped via a resistor R. The following calculation is similar to the one used to solve damping from ports (Q_{ext}) in Section 4.2.1. Here however, the real impedance R is transformed by mode b in a nontrivial way.

We saw earlier that the quality factor of a generic resonant circuit, like mode a, can be written (Eq. 4.6) as

$$Q_a = \frac{1}{Z_a^0 \mathrm{Re}Y[\omega = \omega_a]}, \tag{6.11}$$

where $Z_a^0 = \sqrt{L_a/C_a}$ is the characteristic impedance of the mode. In order to solve for the effect of R on mode a, we again recast the admittance of the coupling capacitor and load impedance as

$$Y_{ext} = \frac{1}{\frac{1}{j\omega C_{ext}} + Z_b[\omega]}, \tag{6.12}$$

where Z_b is the impedance of mode b,

$$Z_b = R + j\omega L_b + \frac{1}{j\omega C_b}. \tag{6.13}$$

The imaginary component of Y_{ext} will shift the resonant frequency of mode a, but in the

detuned limit, we expect this effect to be negligible and concern ourselves with the real part of the admittance. Expanding Equation 6.12 in the high Q limit ($R \gg Z^0_{a,b}$) gives

$$\mathrm{Re}Y[\omega = \omega_a] \approx \frac{\omega_a^4 L_b^2 C_{ext}^2}{R\left(1 - \omega_a^2 L_b (C_b + C_{ext})\right)^2}. \tag{6.14}$$

We introduce a detuning Δ such that $\omega_a = \omega_b - \Delta$ and constrain our model such that $\Delta \ll \omega$. By expanding to lowest order in Δ/ω, we get that

$$\mathrm{Re}Y[\omega = \omega_a] \approx \frac{C_{ext}^2 L_b^2 \omega_a^4}{\left(\frac{4R\Delta^2}{\omega_b^2}\right)}. \tag{6.15}$$

We have now that the quality factor of mode a due to R is

$$Q_a = \frac{1}{Z_a} \frac{\left(\frac{4R\Delta^2}{\omega_b^2}\right)}{C_{ext}^2 L_b^2 \omega_a^4}. \tag{6.16}$$

The resulting expression for Q_a can be made considerably more intuitive by grouping terms,

$$Q_a \approx 4 \left(\frac{1}{Z_a^0 \omega_a^4 C_{ext}^2 \omega_b L_b}\right) \Delta^2 \frac{R}{\omega_b L_b}, \tag{6.17}$$

which we recognize as

$$Q_a \approx \frac{\Delta^2}{g^2} Q_b. \tag{6.18}$$

where

$$g^2 = \frac{\omega_a^2}{4} \left(Z_a^0 \omega_a^2 C_{ext}^2 Z_b^0\right). \tag{6.19}$$

This coupling strength g is similar to the splitting term of two resonant LC oscillators [110]. We also point out the similarities between Equation 6.19 and the expression for Q_{ext}.

In practice, this circuit model does not allow us to make predictions for our distributed resonant modes. However, we do have access to a fully three-dimensional finite element solver which can handle dissipation natively (HFSS). The Eigenmode-type solutions can diagonalize the linear system and report quality factors for each resonant mode if there is dissipation in the simulation. To get a prediction for the cross-damping between qubit and cavity, we add a lumped element resistor in parallel to the Josephson junction - in an otherwise lossless simulation - generating some generic Q_q. The output of the simulation reports some value for the resonator Q_r which is caused only by the linear hybridization between the two modes. If the simulation is accurate, i.e. predicts the correct dispersive

coupling strength, we expect this ratio of quality factors to be the maximum possible separation between resonator and qubit lifetimes. For the device in the memory experiment, this ratio was $Q_r/Q_q = 590$

6.4.2 Testing the reverse Purcell effect

If an experimentalist has *in situ* control to any parameter in g, e.g. C_{ext}, or frequency tunability over one of the modes (Δ), there are well established techniques to test for Purcell effects in a coupled system [56]. However, for 3D transmons and in the memory experiment, we lack either of these knobs. Instead, we seek to tune Q_b (here, the qubit's lifetime) and monitor the effect on the coupled-cavity [52].

In order to perform this measurement, we rely on the high sensitivity to quasiparticles in the qubit mode [114]. Essentially, the qubit has near unity kinetic inductance fraction since most of its inductance comes from the Josephson junction [164], while the distributed nature of cavity surface currents gives the cavity orders of magnitude smaller participation [100]. Therefore, at elevated temperatures, thermally excited quasiparticles will be a nearly-selective damping mechanism. The total decay rate for the resonator is then

$$\kappa = \kappa_q(T) + \kappa_0 \tag{6.20}$$

where κ_q is the g^2/Δ^2 like Purcell term under study, which is strongly temperature dependent, and κ_0 is the intrinsic decay of the resonator, which should ideally be equal to the bare cavity results.

Previous measurements would suggest this is feasible for our experiment. Temperature dependent measurements of the $T_{1,q}$ of other 3D transmons have observed that the lifetime can be greatly reduced at temperatures as low as 120 mK [114], while indeed resonator measurements like those in Section 5.1.5 typically show no quality factor degradation until 150-180 mK.

First, we performed temperature dependent quality factor measurements on a nominally identical, empty resonator. We find that its lifetime monotonically increases on the range of 50-180 mK (dashed line in Fig. 6.10). We also monitored the lifetimes of the qubit and qubit-coupled resonator across the same temperature range. All three modes show a trend toward improved lifetime at slightly elevated temperatures (below 150 mK). However, the qubit and qubit-coupled cavity lifetimes sharply decrease above this threshold.

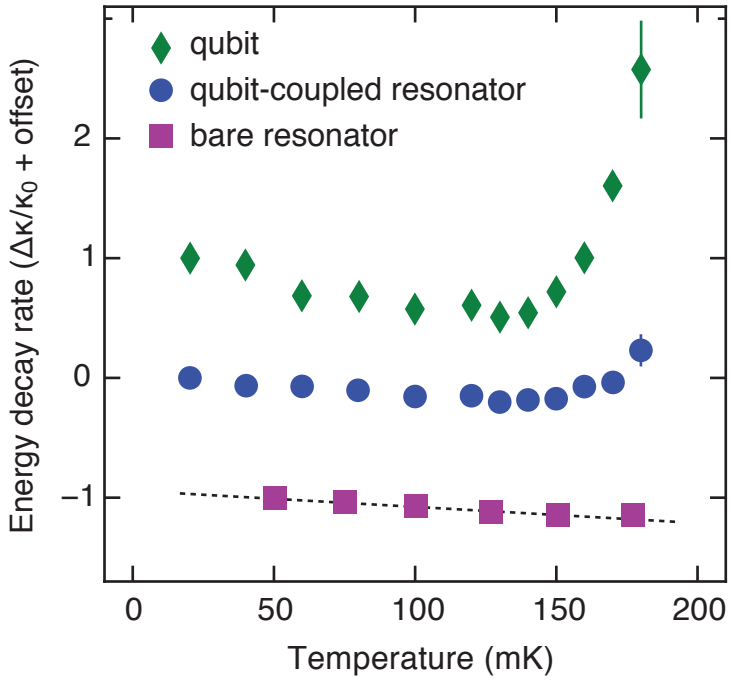

Figure 6.10: Temperature dependence of a cQED system. We monitor the decay rates of the qubit (green diamonds), qubit-coupled memory resonator (blue circles), and an empty resonator (purple squares) as a function of temperature. We present the relative change in those decay rates, offset to aide visualization. Decreases in the decay rates (improvements in lifetime) are observed for all three modes at elevated temperatures below 150 mK. The dashed line is a best linear fit to the bare resonator's temperature dependence in this range. Above 150 mK, the quasiparticle sensitivity of the qubit causes at a sharp increase in the decay rate for both the qubit and the qubit-coupled resonator, while the bare resonator continues its trend toward improvement. Figure 6.11 is an unnormalized, parameterized version of this plot, with the qubit-coupled resonator decay rates plotted against the qubit decay rates.

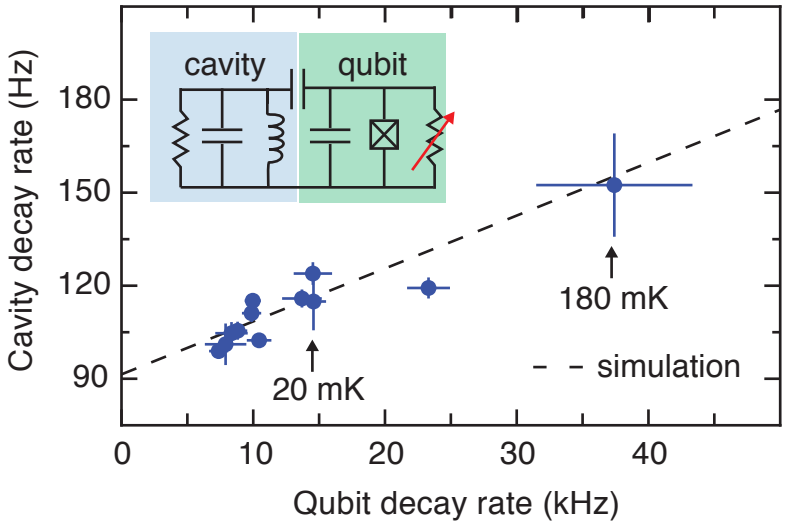

Figure 6.11: Revealing reverse-Purcell effects in a resonator. (inset) We expect the cavity to inherit a photon-loss channel from coupling to the lossy qubit. This effect can be revealed by tuning the decay rate of the qubit *in situ*. **(main)** We measure the decay rates of the cavity and qubit across a temperature range of 20-180 mK. The observed correlation agrees with the predicted qubit-induced loss channel from a three-dimensional electromagnetic simulation of the device

The qualitative difference between the bare cavity and the qubit-coupled cavity in this range is due to the reverse-Purcell effects that we are seeking to elucidate. We correlate the decay rates of the qubit and cavity and indeed observe a linear relationship (Fig. 6.11). The best-fit slope between the two modes is $\kappa_q = (650 \pm 200)^{-1}\gamma$, where the large uncertainty is caused by the somewhat small range of observed lifetime variation, since we required that $\gamma > \chi$ during the procedure. However, the scaling between the two modes agrees quite well with our predicted scaling of $\kappa_q \approx \gamma/600$.

We note however that the bare resonator's lifetime improves up to 15% at these elevated temperatures. To estimate how this behavior affects the extracted qubit-induced decay rate of the qubit-coupled resonator, we re-express the total decay rate for this coupled resonator as

$$\kappa_{\mathrm{tot}}(T) = \kappa_{\mathrm{q}}(T) + \kappa_0(T) \tag{6.21}$$

where the internal resonator dissipation ($\kappa_0(T)$) is taken to be the temperature-dependent behavior of an empty resonator. We subtract the best fit linear trend that is obtained from empty resonator measurements, $\kappa_0(T)$ (dashed line in Fig. 6.10), from the observed decay

rate of the qubit-coupled resonator, $\kappa_{\mathrm{tot}}(T)$. Finally, we correlate the qubit's decay rate to this scaled resonator decay rate for all recorded temperatures. The more thorough analysis changes the best fit result from the main text for $\kappa_{\mathrm{q}} = (650 \pm 200)^{-1}\gamma$ by only 2%, well within the 30% uncertainty in the value from our measurements. Our approximation was therefore well-justified.

We can also conclude from these measurements that with the qubit lifetime of this sample $T_{1,q} \approx 6 - 10\,\mu$s, the maximum memory lifetime obtainable due to our system Hamiltonian is $T_1 \lesssim 4 - 6\,$ms. Therefore, an otherwise-perfect resonator would only have been able to achieve a factor of three or four longer lifetime in this setup. We conclude that an optimal quantity of graduate student resources has thus been put into the development of this cavity. For the optimist, improvements in qubit lifetime should be readily available by implementing 3D transmons in this architecture. This strategy could push the obtainable cavity lifetimes to as much as $T_1 \lesssim 60\,$ms.

The correlation between decay rates also reveals the intrinsic dissipation of the resonator $\kappa_0/2\pi = 80\,$Hz via the y-intercept of the best-fit. This corresponds to a quality factor of $Q_r \approx 5 \times 10^7$, in good agreement with the measurements conducted on empty resonators. Therefore, no significant, unexplained dissipation was likely introduced by the qubit-integration process.

6.4.3 Shot-noise dephasing in cQED

Pure dephasing, as we saw in Section 3.4.2, is caused by environmental interactions that shift the frequency of a mode without exchanging energy directly. As shown in Figure 6.12, our dispersive interaction can become a dephasing channel when the excitation of a coupled mode is stochastic [140, 141, 165]. An exact model for the pure-dephasing of a qubit due to thermal photons in strongly coupled, lossy resonators has been developed for the dispersive regime of cQED in which we operate [141, 165]. Because the cQED Hamiltonian is symmetric, this model is directly applicable to resonators being subjected to the reverse process of thermal shot-noise in the qubit mode. The dephasing rate Γ_ϕ derived in [141, 165], can thus be used for our case of a resonator coupled to a single, thermally populated qubit as

$$\Gamma_\phi = \frac{\gamma}{2}\mathrm{Re}\left[\sqrt{\left(1 + \frac{2\imath\chi}{\gamma}\right)^2 + \frac{8\imath\chi P_e}{\gamma}} - 1\right], \tag{6.22}$$

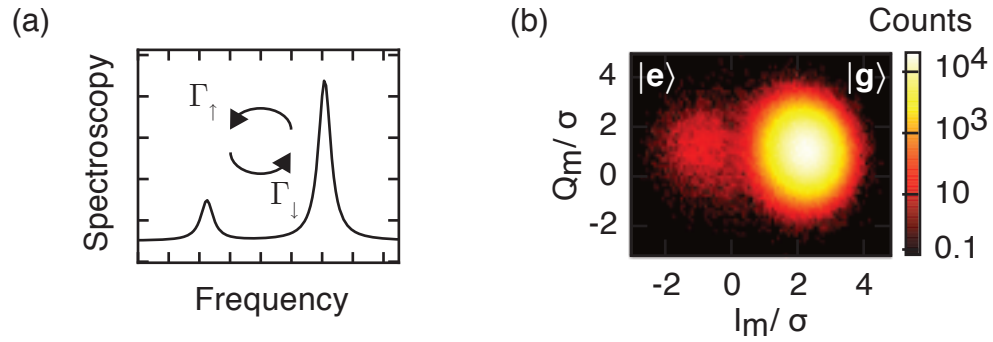

Figure 6.12: Shot-noise dephasing in cQED. (a) In the strong dispersive limit of QED, the presence of a single quantum of energy in one mode shifts the other by more than a linewidth. If one of these modes is thermally excited (at a rate $\Gamma_\uparrow$), the corresponding frequency shift will lead to a rapid phase accumulation for the other mode. Because this process is stochastic and uncorrected, it leads to a pure dephasing channel. **(b)** A histogram of qubit measurement records for the system in equilibrium. The relative weights of the two distributions give the thermal population of the qubit to be $P_e = 0.008$, which corresponds to a thermal hopping rate of $\Gamma_\uparrow \approx$ kHz.

where P_e is the excited state population of the qubit and γ is the decay rate of the qubit. Expanding this expression in the strong dispersive limit ($\chi \gg \gamma$) gives

$$\Gamma_\phi \approx P_e \gamma \left[1 - \mathcal{O}\left(\frac{\gamma}{\chi}\right)^2\right]. \tag{6.23}$$

The quadratic term is of order 1×10^{-4} and thus neglected in our analysis here.

To get an estimate for the size of this effect on our resonator, we perform measurements on the steady-state population of the qubit (Fig. 6.12). We detect the qubit in the excited state in equilibrium 0.8% of the measurement records corresponding to an effective temperature of 80 mK. For our observed qubit decay rate $\gamma/2\pi = 27 \pm 2$ kHz, we therefore expect a pure dephasing rate for the cavity of $\Gamma_\phi/2\pi \approx 216 \pm 16$ Hz. The dephasing rate we extract for the cavity via T_1 and T_2 measurements is $\Gamma_\phi/2\pi = 162 \pm 8$ Hz. These two rates are suspiciously close.

In order to test the shot-model more precisely, we follow Sears et al. [140] by populating the spurious mode (in our case, the qubit) intentionally with a calibrated thermal field and monitoring the induced dephasing. As shown in Figure 6.13, we use a resonant drive on the qubit of weak amplitude $\Omega \ll \gamma$ to cause a new equilibrium state of the qubit which is

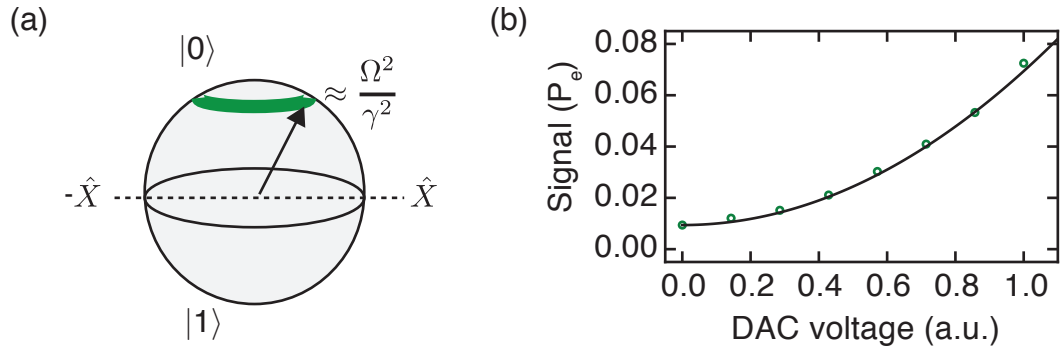

Figure 6.13: Increasing qubit population with weak drives. (a) To test the shot-noise dephasing model, we drive the qubit weakly ($\Omega \ll \gamma$), which results in an incoherent mixture of ground and excited state (green region). **(b)** The resulting P_e population as a function of drive amplitude. Each population is measured via readout histograms as shown in Figure 6.12. We find that we are well within the quadratic drive limit (fit in black is Ω^2).

an incoherent mixture of ground and excited states with

$$P_e \approx \frac{\Omega^2}{\gamma^2}. \tag{6.24}$$

We can essentially calibrate Ω by performing repeated measurements of the qubit state after the driven system has reached equilibrium at many drive powers. As expected, we observe a quadratic rise in P_e for weak drive amplitudes, indicating that a thermal jump rate of $\Gamma_\uparrow = P_e\gamma$ has been achieved.

Finally, we create this enhanced thermal state of the qubit while performing Ramsey-type measurements on the cavity (Fig. 6.14). We find a decreasing T_2 of the cavity for increasing Ω, indicating enhanced pure dephasing. Further, by using our calibration for $P_e(\Omega)$ we can correlate the dephasing rate directly with the shot-noise of the qubit mode. The total dephasing rate should follow

$$\Gamma_\phi = P_e\gamma + \Gamma_\phi^0 \tag{6.25}$$

where Γ_ϕ^0 is an intrinsic dephasing of the cavity not explained by the shot-noise model.

To obtain a bound on Γ_ϕ^0, we fit the observed data to a linear model while constraining the slope to be given by γ. The best-fit y-intercept then would be Γ_ϕ^0. In fact, the error on Γ_ϕ^0 for this data set overwhelms the actual value [52]. Therefore, we cite the uncertainty

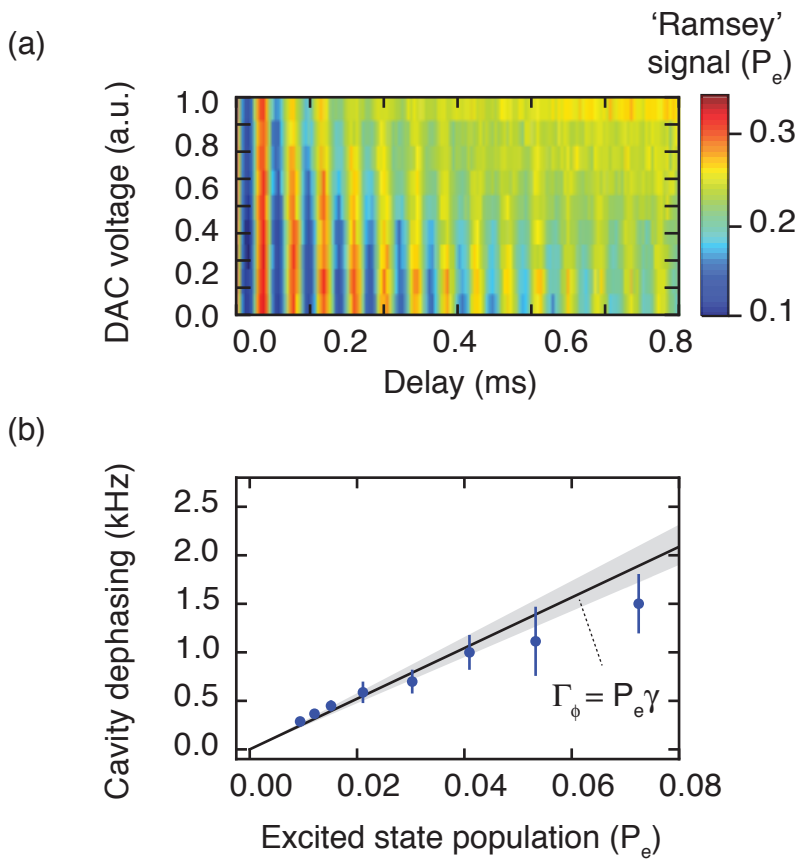

Figure 6.14: Revealing shot-noise dephasing of a cQED resonator. (a) A cavity T_2 measurement is performed for each qubit drive amplitude. The qubit drive is left on for the duration of the T_2 experiment. **(b)** We use the calibration P_e experiments to correlate the observed pure dephasing rate Γ_ϕ versus P_e. Because we also know the qubit decay rate γ from independent measurements, we include the theory line for shot-noise dephasing in the strong dispersive limit $\Gamma_\phi = P_e\gamma$ (black). The grey shading represents the uncertainty in qubit decay rate, $\gamma/2\pi = 27 \pm 2$ kHz

on Γ_ϕ^0 as the bound. We find that the data is consistent with the resonator undergoing intrinsic dephasing at only the level of $\Gamma_\phi^0/2\pi \lesssim 40$ Hz.

Reducing $P_e\gamma$ will therefore result in a more coherent quantum memory. These results are particularly encouraging because the shot-noise of the qubit mode is a potentially solvable challenge. Several groups have made progress on improvements in qubit thermalization [110, 166, 167]. The current record for thermalized transmons is $T_{1,q} = 80\,\mu$s

and $P_e = 0.1\%$ [168]. This same device would only weakly dephase our cavity memory $\Gamma_\phi \approx 2\,\text{Hz}$.

In addition, during storage operation of the cavity memory, coupling to the qubit may be unnecessary. Therefore, schemes which involve decoupling the qubit could be used turn off dephasing during storage operation [107, 169]. These techniques could be just as useful as physically thermalizing the device for improving the performance of the memory.

6.5 Outlook for resonator quantum memories

Putting this architecture to use is exciting prospect. Besides the types of coherent quantum optics experiments that such a device could enable [170], we consider two applications for quantum information here. These provide an outlook on the future impact of highly coherent cavities for cQED.

One potential application is to use the cavity itself as a qubit, rather than as simply a quantum memory. The timescale at which we can apply gates to this resource is on the order of $T_{\text{gate}} \approx 2\pi/\chi$ [68, 95]. Therefore, the maximum fidelities one would expect for controlling the cavity on this timescale are on the order of $\mathcal{F} \sim 1 - 2T_1/T_{\text{gate}} \approx 8 \times 10^3$. This is a respectable gate operation [39], comparable to a qubit with $T_{\text{gate}} = 20\,\text{ns}$ and $2T_{1,q} = 80\,\mu\text{s}$. However, the dispersive control schemes presented in this thesis rely on complete entanglement with the transmon qubit. Therefore, equivalently coherent transmons would be needed to reach these optimal values (at which point gates on the transmon would still outperform those on the resonator by a ratio of $\sim K_q/\chi \approx 10^3$). In the absence of new controls, the cavity is doomed to always be a worse qubit, though potentially better quantum memory, than the transmon.

Using this architecture for experiments on an error-correctable quantum memory is a potential win for system performance (see Section 3.5). To see how this comes about, consider the decay of the two-cat under QND parity measurements as in [80]. With monitoring, the effective decay of the state is

$$\kappa_{\text{eff}} = \left[\frac{(\bar{n}\kappa)^2(\tau_m + \tau_w)^2}{2} + \frac{\tau_m}{T_{1,q}}\right]\frac{1}{\tau_m + \tau_w}, \tag{6.26}$$

where τ_m is the time of a single-shot parity measurement, τ_w is a wait time between

measurements. The minimum of this expression occurs for a waiting time

$$\tau_w = \frac{1}{\bar{n}\kappa}\sqrt{\frac{2\tau_m}{T_{1,q}}} - \tau_m, \tag{6.27}$$

which gives

$$\kappa_{\text{eff}} = \bar{n}\kappa\sqrt{\frac{2\tau_m}{T_{1,q}}}. \tag{6.28}$$

Clearly, if we take the ratio of $\kappa_{\text{eff}}/\kappa$ as the only metric, the resulting improvement is independent of the intrinsic energy decay rate of the resonator. However, in order for the optimal wait time to be physical, we require that $\tau_w \gg \tau_m$ in order for the system to reset between measurements. This gives an additional constraint on κ as

$$\kappa \ll \frac{1}{\bar{n}\tau_m}\sqrt{\frac{2\tau_m}{T_{1,q}}}. \tag{6.29}$$

Working with smaller κ resonators is thus more forgiving to the experimentalist who seeks to work with distinguishable (large $\bar{n}$) cat states for a fixed parity measurement time and qubit performance [80].

Another important goal of logical cat-qubit operation are the so-called cat-pumping schemes [34]. There, parametric processes restore the deterministic energy decay rate of coherent states. The important metric for these schemes are $\kappa_\uparrow/\kappa$, where $\kappa_\uparrow$ is the restorative pumping rate. These parametric processes have strengths that are independent of κ [70]. Therefore implementing a long lived cavity could provide a potentially large gain for these systems.

CHAPTER 7

Conclusion

In this chapter, we conclude with an outlook on two fundamental concepts that have been touched on throughout this thesis. The first concerns the scaling-law for the coherence of cQED devices, known as Schoelkopf's Law. Building off the arguments from this section, we suggest radically re-thinking how the most coherent objects in cQED are controlled today.

7.1 Continuing Schoelkopf's Law

Gordon Moore predicted in 1965 that the number of transistors patterned on a production integrated circuit would double about every two years [171]. That prediction heralded the semiconductor industry's sustained, rapid progress in developing new ways of extending the computational power available on chip, keeping pace with Moore's Law [172]. Unbelievably insightful, Moore made his prediction when, only three years earlier, state-of-the-art integrated circuits had only ten components.

Today, quantum circuits are on a similar trajectory. As pointed out in previous theses and in the review [16], the coherence of circuits has doubled approximately every nine months. The 'one-figure' summary of this thesis is shown in Figure 7.1, as the quantum memory presented here can be thought of as the state-of-the-art in circuit coherence at $T_2 \approx 1$ ms level [52].

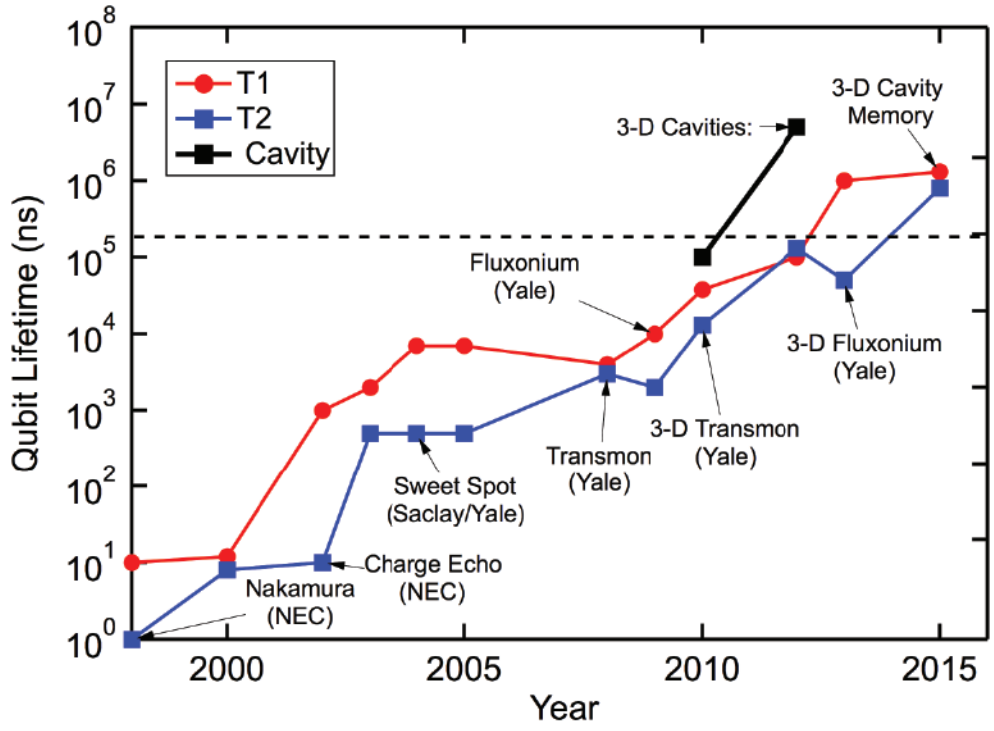

Figure 7.1: Schoelkopf's Law for the coherence times of circuits. The coherence of state-of-the-art superconducting quantum circuits has doubled approximately every nine months. Maintaining this trend is a continuing challenge for the field. (Figure used with permission from [16]. See Copyright Permissions.)

An important corollary to Schoelkopf's Law was pointed out by Bishop [173]. It was observed that each improvement on the way up the coherence trajectory was accompanied by a sacrifice of some access channel to the circuit. The step from Cooper-Pair-Box [33] to Quantronium [174] sacrificed always-on charge-sensor readout [174]. The change to cQED devices gave up charge-sensor readout altogether [55]. Transmon qubits are accompanied by finite anharmonicity [9]. Finally, the pristine environment of 3D transmons sacrifices fast-flux control [114]. Perhaps including cQED resonators on Figure 7.1 is the extreme limit of Bishop's Corollary - these devices are nearly-harmonic oscillators after all.

Finally, there is strong hope that these cQED resonators will be improved upon by future experiments. The coaxial $\lambda/4$ resonator places our best bound on the loss properties of bulk aluminum. On the other hand, planar, thin-film aluminum resonators require significantly better materials performance to achieve their observed lifetimes [103, 104].

Understanding the key differences between these two types of devices will potentially unlock huge gains for cavity based quantum memories in cQED.

Coherence is only as important as what we can do with it however. For that matter, we consider an extension to the control schemes in this thesis and comment on the desired tool set for controlling cQED resonators.

7.2 Controlling quantum states in resonators

With the dispersive interaction, many resonator Fock states can be manipulated in parallel [68]. Gates like QCMap can create very complex resonator states with only simple pulses because of the high symmetry of this scheme. However, there are two intrinsic limitations to dispersive control.

The first is that the rate of the control applications ($\sim$ MHz) is necessarily slower than qubit control ($\sim 100\,MHz$). This constraint arises because the dispersive interaction strength is the geometric mean of the control rate of the qubit ($\sim 100\,MHz$) and the direct-control rate of the cavity ($\sim$1 kHz). These relatively slow gates diminish the gains of highly coherent cavities.

Driving other terms in the dispersive Hamiltonian may speed up the gates on resonators. Consider the sideband pulses described at the conclusion of Chapter 2. There, individual excitations are swapped between qubit and resonator. In particular, the choice of pump frequency $2\omega_p = \omega_q + \omega_r$ enhances the Hamiltonian term

$$H_{sb} = \hbar g \left(\hat{a}\hat{b}^\dagger + \hat{a}^\dagger \hat{b} \right), \tag{7.1}$$

where the exchange rate g is proportional to the pump power. This resonant-like exchange interaction can likely be made quite large ($g \gg \chi$) if other side-effects of the pump are avoided. Equation 7.1 is sufficient for Law-Eberly type arbitrary control via SWAP gates [175], the type used to prepare cQED resonators in [71]. To use this interaction, on would sacrifice parallel control for rapid single Fock state addressability for speed.

Yet, a more subtle issue fundamentally limits the fidelity of both dispersive and Law-Eberly type controls. When exciting the qubit for control, the decoherence of the qubit enters into the limit for gate fidelities. For instance, during the evolution time of the QCMap gate, the resonator and qubit become completely entangled. Any phase or quantum jumps of the qubit will completely scramble the resulting resonator state. It is an intriguing

question whether schemes can be implemented which control quantum states of resonators without suffering from qubit decoherence.

At least one such gate has been already proposed. The idea is essentially to use a pump to create a trapping potential for cavity states (in $\hat{X}, \hat{Y}$) [70]. Then, applying classical drives on the cavity can rotate the state. This type of nonlinearity-by-driving is related to the ideas of Quantum-Zeno-Dynamics (QZD) [170], except, importantly, the qubit here is left nominally in the ground state throughout the protocol, whereas for QZD protocols we are again forced to excite the qubit. The challenge for this scheme is the complex potential well that needs to be created. Methods for creating simpler potentials, for instance in $\hat{n}$ instead (as in QZD), might lessen the system-constraints and allow for gate fidelities that exceed the qubit-limited performance in a qudit-like subspace of a resonator.

Indeed, if any system has the flexibility and coherence to explore these important ideas, it is likely cQED.

Bibliography

1. R. de Bruyn Ouboter, "Superconductivity: Discoveries during the early years of low temperature research at leiden 1908-1914," *Magnetics, IEEE Transactions on* **23**, 355–370 (1987). Cited on page 1.

2. H. Rogalla and P. H. Kes, *100 Years of Superconductivity*. CRC Press, 2011. Cited on pages 1 & 2.

3. A. Einstein, B. Podolsky, and N. Rosen, "Can Quantum-Mechanical Description of Physical Reality Be Considered Complete?," *Physical Review* **47**, 777–780 (1935). Cited on page 2.

4. B. M. Terhal, "Quantum error correction for quantum memories," *Rev. Mod. Phys.* **87**, 307–346 (2015). Cited on page 2.

5. J. Preskill, "Fault-tolerant quantum computation," *eprint arXiv:quant-ph/9712048* (1997), quant-ph/9712048. Cited on page 2.

6. E. Verlinde and H. Verlinde, "Black hole entanglement and quantum error correction," *Journal of High Energy Physics* **10**, 107 (2013), 1211.6913 [hep-th]. Cited on page 2.

7. M. H. Devoret, "Quantum fluctuations in electrical circuits," in *Mesoscopic Quantum Physics: Lecture Notes of the Les Houches Summer School: Volume 61, July 1994*, E. Akkermans, G. Montambaux, J. L. Pichard, and J. Zinn-Justin, eds., Lecture Notes of the Les Houches Summer School: Volume 61, July 1994. Elsevier Science Ltd, Feb., 1996. Cited on pages 3, 5, 7, 8, 10, 16 & 18.

8. B. D. Josephson, "The discovery of tunnelling supercurrents," *Rev. Mod. Phys.* **46**, 251–254 (1974). Cited on pages 3 & 15.

9. A. Houck, J. Koch, M. Devoret, S. Girvin, and R. Schoelkopf, "Life after charge noise: recent results with transmon qubits," *Quantum Information Processing* **8**, 105–115 (2009). Cited on pages 3, 19, 28, 29, 67, 137 & 167.

10. S. E. Nigg, H. Paik, B. Vlastakis, G. Kirchmair, S. Shankar, L. Frunzio, M. H. Devoret, R. J. Schoelkopf, and S. M. Girvin, "Black-box superconducting circuit quantization," *Phys. Rev. Lett.* **108**, 240502 (2012). Cited on pages 3, 5, 18, 19, 20, 31, 33, 73, 106 & 154.

11. S. Haroche and J. M. Raimond, *Exploring the Quantum: Atoms, Cavities, and Photons*. Oxford Univ. Press, Oxford, UK, 2006. Cited on pages 3, 14, 21, 24, 29, 33, 35, 37, 42, 45, 46, 49, 59, 60, 62, 65, 68, 143 & 188.

12. D. Gottesman, A. Kitaev, and J. Preskill, "Encoding a qubit in an oscillator," *Phys. Rev. A* **64**, 012310 (2001), quant-ph/0008040. Cited on page 3.

13. S. D. Bartlett, H. de Guise, and B. C. Sanders, "Quantum encodings in spin systems and harmonic oscillators," *Phys. Rev. A* **65**, 052316 (2002). Cited on page 3.

14. S. M. Girvin, "Superconducting qubits and circuits: Artificial atoms coupled to microwave photons," in *Quantum Machines: Measurement and Control of Engineered Quantum Systems: Lecture Notes of the Les Houches Summer School: Volume 96, July 2011*, M. Devoret, B. Huard, R. Schoelkopf, and L. F. Cugliandolo, eds., Lecture Notes of the Les Houches Summer School: Volume 96, July 2011. OUP Oxford, June, 2014. Cited on pages 5, 7, 8, 9, 13, 36, 37, 39 & 72.

15. J. Clarke and F. K. Wilhelm, "Superconducting quantum bits," *Nature* **453**, 1031–1042 (2008). Cited on pages 6 & 19.

16. M. H. Devoret and R. J. Schoelkopf, "Superconducting circuits for quantum information: An outlook," *Science* **339**, 1169–1174 (2013), http://www.sciencemag.org/content/339/6124/1169.full.pdf. Cited on pages 6, 19, 85, 166 & 167.

17. C. Kittel, *Introduction to Solid State Physics*. Wiley, 2004. https://books.google.com/books?id=kym4QgAACAAJ. Cited on page 6.

18. M. Tinkham, *Introduction to Superconductivity*. Dover Books on Physics Series. Dover Publications, 1996. Cited on pages 6, 16, 79, 124, 125, 126 & 127.

19. V. B. Braginsky, Y. I. Vorontsov, and K. S. Thorne, "Quantum nondemolition measurements," *Science* **209**, 547–557 (1980), http://www.sciencemag.org/content/209/4456/547.full.pdf. Cited on page 9.

20. M. Aspelmeyer, T. J. Kippenberg, and F. Marquardt, "Cavity optomechanics," *Rev. Mod. Phys.* **86**, 1391–1452 (2014). Cited on pages 10, 65 & 122.

21. R. J. Glauber, *Quantum Theory of Optical Coherence: Selected Papers and Lectures*. Wiley, 2007. Cited on pages 10, 11, 14, 45, 47, 49, 51, 52, 53 & 67.

22. R. J. Glauber, "Coherent and incoherent states of the radiation field," *Phys. Rev.* **131**, 2766–2788 (1963). Cited on pages 11, 13 & 14.

23. W. M. Itano, C. R. Monroe, D. M. Meekhof, D. Leibfried, B. E. King, and D. J. Wineland, "Quantum harmonic oscillator state synthesis and analysis," in *Atom Optics*, M. G. Prentiss and W. D. Phillips, eds., vol. 2995 of *Society of Photo-Optical Instrumentation Engineers (SPIE) Conference Series*, pp. 43–55. May, 1997. quant-ph/9702038. Cited on pages 13, 14, 188, 189 & 190.

24. B. D. Josephson, "Possible new effects in superconductive tunnelling," *Physics Letters* **1**, 251–253 (1962). Cited on page 16.

25. Y. Makhlin, G. Schön, and A. Shnirman, "Quantum-state engineering with josephson-junction devices," *Rev. Mod. Phys.* **73**, 357–400 (2001). Cited on page 16.

26. J. Q. You and F. Nori, "Atomic physics and quantum optics using superconducting circuits," *Nature* **474**, 589–597 (2011). Cited on pages 18 & 42.

27. N. Bergeal, F. Schackert, M. Metcalfe, R. Vijay, V. E. Manucharyan, L. Frunzio, D. E. Prober, R. J. Schoelkopf, S. M. Girvin, and M. H. Devoret, "Phase-preserving amplification near the quantum limit with a Josephson ring modulator," *Nature* **465**, 64–68 (2010). Cited on pages 19 & 131.

28. B. Abdo, K. Sliwa, F. Schackert, N. Bergeal, M. Hatridge, L. Frunzio, A. D. Stone, and M. Devoret, "Full coherent frequency conversion between two propagating microwave modes," *Phys. Rev. Lett.* **110**, 173902 (2013). Cited on page 19.

29. K. M. Sliwa, M. Hatridge, A. Narla, S. Shankar, L. Frunzio, R. J. Schoelkopf, and M. H. Devoret, "The reconfigurable Josephson circulator/directional amplifier," *ArXiv e-prints* (2015), 1503.00209 [quant-ph]. Cited on page 19.

30. J. Koch, T. M. Yu, J. Gambetta, A. A. Houck, D. I. Schuster, J. Majer, A. Blais, M. H. Devoret, S. M. Girvin, and R. J. Schoelkopf, "Charge-insensitive qubit design derived from the cooper pair box," *Phys. Rev. A* **76**, 042319 (2007). Cited on pages 19 & 20.

31. J. A. Schreier, A. A. Houck, J. Koch, D. I. Schuster, B. R. Johnson, J. M. Chow, J. M. Gambetta, J. Majer, L. Frunzio, M. H. Devoret, S. M. Girvin, and R. J. Schoelkopf, "Suppressing charge noise decoherence in superconducting charge qubits," *Phys. Rev. B* **77**, 180502 (2008). Cited on page 19.

32. L. Sun, L. DiCarlo, M. D. Reed, G. Catelani, L. S. Bishop, D. I. Schuster, B. R. Johnson, G. A. Yang, L. Frunzio, L. Glazman, M. H. Devoret, and R. J. Schoelkopf, "Measurements of Quasiparticle Tunneling Dynamics in a Band-Gap-Engineered Transmon Qubit," *Physical Review Letters* **108**, 230509 (2012), 1112.2621 [cond-mat.mes-hall]. Cited on page 20.

33. Y. Nakamura, Y. A. Pashkin, and J. S. Tsai, "Coherent control of macroscopic quantum states in a single-Cooper-pair box," *Nature* **398**, 786–788 (1999), cond-mat/9904003. Cited on pages 21 & 167.

34. Z. Leghtas, S. Touzard, I. M. Pop, A. Kou, B. Vlastakis, A. Petrenko, K. M. Sliwa, A. Narla, S. Shankar, M. J. Hatridge, M. Reagor, L. Frunzio, R. J. Schoelkopf, M. Mirrahimi, and M. H. Devoret, "Confining the state of light to a quantum manifold by engineered two-photon loss," *Science* **347**, 853–857 (2015). Cited on pages 21, 22, 23, 39, 40, 70, 142 & 165.

35. H. J. Carmichael, *Statistical Methods in Quantum Optics 2: Non-Classical Fields, Theoretical and Mathematical Physics*. Springer Berlin Heidelberg, 2007. Cited on pages 22, 63, 64, 65 & 66.

36. P. Blasiak, *Combinatorics of boson normal ordering and some applications*. PhD thesis, PhD Thesis, 2005, 2005. Cited on page 23.

37. B. E. A. Saleh and M. C. Teich, *Fundamentals of Photonics*. John Wiley and Sons, New Jersey, USA, 2006. Cited on pages 24 & 40.

38. G. Kirchmair, B. Vlastakis, Z. Leghtas, S. E. Nigg, H. Paik, E. Ginossar, M. Mirrahimi, L. Frunzio, S. M. Girvin, and R. J. Schoelkopf, "Observation of quantum state collapse and revival due to the single-photon Kerr effect," *Nature* **495**, 205–209 (2013), 1211.2228 [quant-ph]. Cited on pages 24, 46, 47, 49 & 145.

39. M. A. Nielsen and I. L. Chuang, *Quantum Computation and Quantum Information, 10^{th} Anniversary Ed.* Cambridge University Press, New York, 2011. Cited on pages 25, 27, 28, 45, 65, 138, 139, 148, 151 & 164.

40. M. J. Peterer, S. J. Bader, X. Jin, F. Yan, A. Kamal, T. J. Gudmundsen, P. J. Leek, T. P. Orlando, W. D. Oliver, and S. Gustavsson, "Coherence and Decay of Higher Energy Levels of a Superconducting Transmon Qubit," *Physical Review Letters* **114**, 010501 (2015), 1409.6031 [quant-ph]. Cited on page 26.

41. S. H. Autler and C. H. Townes, "Stark Effect in Rapidly Varying Fields," *Physical Review* **100**, 703–722 (1955). Cited on page 27.

42. D. I. Schuster, A. Wallraff, A. Blais, L. Frunzio, R.-S. Huang, J. Majer, S. M. Girvin, and R. J. Schoelkopf, "ac Stark Shift and Dephasing of a Superconducting Qubit Strongly Coupled to a Cavity Field," *Physical Review Letters* **94**, 123602 (2005), cond-mat/0408367. Cited on page 27.

43. A. Sears, *Extending Coherence of Superconducting Qubits: from Microseconds to Milliseconds*. PhD thesis, Yale University, 2013. http://www.eng.yale.edu/rslab/papers/theses/sears.pdf. Cited on pages 29, 87, 112, 130 & 137.

44. L. Dicarlo, J. M. Chow, J. M. Gambetta, L. S. Bishop, B. R. Johnson, D. I. Schuster, J. Majer, A. Blais, L. Frunzio, S. M. Girvin, and R. J. Schoelkopf, "Demonstration of two-qubit algorithms with a superconducting quantum processor," *Nature* **460**, 240–244 (2009), 0903.2030 [cond-mat.mes-hall]. Cited on page 29.

45. M. D. Reed, L. Dicarlo, S. E. Nigg, L. Sun, L. Frunzio, S. M. Girvin, and R. J. Schoelkopf, "Realization of three-qubit quantum error correction with superconducting circuits," *Nature* **482**, 382–385 (2012), 1109.4948 [quant-ph]. Cited on pages 29 & 30.

46. J. Kelly, R. Barends, A. G. Fowler, A. Megrant, E. Jeffrey, T. C. White, D. Sank, J. Y. Mutus, B. Campbell, Y. Chen, Z. Chen, B. Chiaro, A. Dunsworth, I.-C. Hoi, C. Neill, P. J. J. O'Malley, C. Quintana, P. Roushan, A. Vainsencher, J. Wenner, A. N. Cleland, and J. M. Martinis, "State preservation by repetitive error detection in a superconducting quantum circuit," *Nature* **519**, 66–69 (2015), 1411.7403 [quant-ph]. Cited on pages 29 & 85.

47. A. D. Corcoles, E. Magesan, S. J. Srinivasan, A. W. Cross, M. Steffen, J. M. Gambetta, and J. M. Chow, "Demonstration of a quantum error detection code using a square lattice of four superconducting qubits," *Nature Communications* **6**, 6979 (2015). Cited on page 29.

48. D. Ristè, S. Poletto, M.-Z. Huang, A. Bruno, V. Vesterinen, O.-P. Saira, and L. Dicarlo, "Detecting bit-flip errors in a logical qubit using stabilizer measurements," *Nature Communications* **6**, 6983 (2015), 1411.5542 [quant-ph]. Cited on pages 29 & 129.

49. G. Kurizki, P. Bertet, Y. Kubo, K. Mølmer, D. Petrosyan, P. Rabl, and J. Schmiedmayer, "Quantum technologies with hybrid systems," *Proceedings of the National Academy of Sciences* **112**, 3866–3873 (2015). Cited on pages 29, 94 & 95.

50. X. Zhu, S. Saito, A. Kemp, K. Kakuyanagi, S.-I. Karimoto, H. Nakano, W. J. Munro, Y. Tokura, M. S. Everitt, K. Nemoto, M. Kasu, N. Mizuochi, and K. Semba, "Coherent coupling of a superconducting flux qubit to an electron spin ensemble in diamond," *Nature* **478**, 221–224 (2011), 1111.5399 [quant-ph]. Cited on page 29.

51. Y. Kubo, C. Grezes, A. Dewes, T. Umeda, J. Isoya, H. Sumiya, N. Morishita, H. Abe, S. Onoda, T. Ohshima, V. Jacques, A. Dréau, J.-F. Roch, I. Diniz, A. Auffeves, D. Vion, D. Esteve, and P. Bertet, "Hybrid quantum circuit with a superconducting qubit coupled to a spin ensemble," *Phys. Rev. Lett.* **107**, 220501 (2011). Cited on page 29.

52. M. Reagor, W. Pfaff, C. Axline, R. W. Heeres, N. Ofek, K. Sliwa, E. Holland, C. Wang, J. Blumoff, K. Chou, M. J. Hatridge, L. Frunzio, M. H. Devoret, L. Jiang, and R. J. Schoelkopf, "A quantum memory with near-millisecond coherence in circuit QED," *ArXiv e-prints* (2015), 1508.05882 [quant-ph]. Cited on pages 29, 71, 104, 105, 106, 109, 111, 122, 128, 135, 141, 147, 148, 149, 152, 157, 162 & 166.

53. K. Stannigel, P. Rabl, A. S. Sørensen, P. Zoller, and M. D. Lukin, "Optomechanical Transducers for Long-Distance Quantum Communication," *Physical Review Letters* **105**, 220501 (2010), 1006.4361 [quant-ph]. Cited on page 29.

54. A. Blais, R.-S. Huang, A. Wallraff, S. M. Girvin, and R. J. Schoelkopf, "Cavity quantum electrodynamics for superconducting electrical circuits: An architecture for quantum computation," *Phys. Rev. A* **69**, 062320 (2004). Cited on pages 29, 36 & 37.

55. A. Wallraff, D. I. Schuster, A. Blais, L. Frunzio, R. S. Huang, J. Majer, S. Kumar, S. M. Girvin, and R. J. Schoelkopf, "Strong coupling of a single photon to a superconducting qubit using circuit quantum electrodynamics," *Nature* **431**, 162–167 (2004). Cited on pages 29, 36 & 167.

56. A. A. Houck, J. A. Schreier, B. R. Johnson, J. M. Chow, J. Koch, J. M. Gambetta, D. I. Schuster, L. Frunzio, M. H. Devoret, S. M. Girvin, and R. J. Schoelkopf, "Controlling the spontaneous emission of a superconducting transmon qubit," *Phys. Rev. Lett.* **101**, 080502 (2008). Cited on pages 29, 36, 71, 153 & 157.

57. M. A. Sillanpaa, J. I. Park, and R. W. Simmonds, "Coherent quantum state storage and transfer between two phase qubits via a resonant cavity," *Nature* **449**, 438–442 (2007). Cited on pages 29 & 71.

58. J. Majer, J. M. Chow, J. M. Gambetta, J. Koch, B. R. Johnson, J. A. Schreier, L. Frunzio, D. I. Schuster, A. A. Houck, A. Wallraff, A. Blais, M. H. Devoret, S. M. Girvin, and R. J. Schoelkopf, "Coupling superconducting qubits via a cavity bus," *Nature* **449**, 443–447 (2007). Cited on pages 29, 71 & 86.

59. R. Vijay, D. H. Slichter, and I. Siddiqi, "Observation of quantum jumps in a superconducting artificial atom," *Phys. Rev. Lett.* **106**, 110502 (2011). Cited on pages 29 & 36.

60. M. Hatridge, S. Shankar, M. Mirrahimi, F. Schackert, K. Geerlings, T. Brecht, K. M. Sliwa, B. Abdo, L. Frunzio, S. M. Girvin, R. J. Schoelkopf, and M. H. Devoret, "Quantum back-action of an individual variable-strength measurement," *Science* **339**, 178–181 (2013), http://www.sciencemag.org/content/339/6116/178.full.pdf. Cited on pages 29, 36 & 94.

61. R. M. Foster, "A Reactance Theorem," *Bell System Technical Journal* **3**, 259–267 (1924). Cited on page 31.

62. D. I. Schuster, A. A. Houck, J. A. Schreier, A. Wallraff, J. M. Gambetta, A. Blais, L. Frunzio, J. Majer, B. Johnson, M. H. Devoret, S. M. Girvin, and R. J. Schoelkopf, "Resolving photon number states in a superconducting circuit," *Nature* **445**, 515–518 (2007), cond-mat/0608693. Cited on pages 35, 46, 47, 76, 80, 82, 84, 85, 94, 116, 131 & 142.

63. I. C. Hoi, C. M. Wilson, G. Johansson, T. Palomaki, B. Peropadre, and P. Delsing, "Demonstration of a single-photon router in the microwave regime," *Phys. Rev. Lett.* **107**, 073601 (2011). Cited on page 36.

64. J. Gambetta, A. Blais, D. I. Schuster, A. Wallraff, L. Frunzio, J. Majer, M. H. Devoret, S. M. Girvin, and R. J. Schoelkopf, "Qubit-photon interactions in a cavity: Measurement-induced dephasing and number splitting," *Phys. Rev. A* **74**, 042318 (2006), cond-mat/0602322. Cited on pages 36, 37, 46, 57, 58, 71, 133 & 142.

65. M. Neeley, R. C. Bialczak, M. Lenander, E. Lucero, M. Mariantoni, A. D. O'Connell, D. Sank, H. Wang, M. Weides, J. Wenner, Y. Yin, T. Yamamoto, A. N. Cleland, and J. M. Martinis, "Generation of three-qubit entangled states using superconducting phase qubits," *Nature* **467**, 570–573 (2010), 1004.4246 [cond-mat.supr-con]. Cited on page 40.

66. S. L. Braunstein and P. van Loock, "Quantum information with continuous variables," *Reviews of Modern Physics* **77**, 513–577 (2005), quant-ph/0410100. Cited on page 42.

67. H. Stern, S. Mahmoud, and L. Stern, *Communication Systems: Analysis and Design*. Pearson Prentice Hall, 2004. https://books.google.com/books?id=-McoAAAACAAJ. Cited on pages 42, 43, 45 & 131.

68. B. Vlastakis, G. Kirchmair, Z. Leghtas, S. E. Nigg, L. Frunzio, S. M. Girvin, M. Mirrahimi, M. H. Devoret, and R. J. Schoelkopf, "Deterministically encoding quantum information using 100-photon schrödinger cat states," *Science* **342**, 607–610 (2013), http://www.sciencemag.org/content/342/6158/607.full.pdf. Cited on pages 42, 43, 52, 53, 54, 58, 59, 60, 70, 143, 144, 164 & 168.

69. R. W. Heeres, B. Vlastakis, E. Holland, S. Krastanov, V. V. Albert, L. Frunzio, L. Jiang, and R. J. Schoelkopf, "Cavity State Manipulation Using Photon-Number Selective Phase Gates," *ArXiv e-prints* (2015), 1503.01496 [quant-ph]. Cited on pages 42, 58, 60, 61, 70, 142, 148 & 152.

70. M. Mirrahimi, Z. Leghtas, V. V. Albert, S. Touzard, R. J. Schoelkopf, L. Jiang, and M. H. Devoret, "Dynamically protected cat-qubits: a new paradigm for universal quantum computation," *New Journal of Physics* **16**, 045014 (2014), 1312.2017 [quant-ph]. Cited on pages 42, 59, 62, 67, 68, 70, 165 & 169.

71. M. Hofheinz, H. Wang, M. Ansmann, R. C. Bialczak, E. Lucero, M. Neeley, A. D. O'Connell, D. Sank, J. Wenner, J. M. Martinis, and A. N. Cleland, "Synthesizing arbitrary quantum states in a superconducting resonator," *Nature* **459**, 546–549 (2009). Cited on pages 42, 49 & 168.

72. I. Chiorescu, P. Bertet, K. Semba, Y. Nakamura, C. J. P. M. Harmans, and J. E. Mooij, "Coherent dynamics of a flux qubit coupled to a harmonic oscillator," *Nature* **431**, 159–162 (2004). Cited on page 42.

73. Y.-X. Liu, L. F. Wei, J. R. Johansson, J. S. Tsai, and F. Nori, "Superconducting qubits can be coupled and addressed as trapped ions," *Phys. Rev. B* **76**, 144518 (2007), cond-mat/0509236. Cited on page 42.

74. A. Wallraff, D. I. Schuster, A. Blais, J. M. Gambetta, J. Schreier, L. Frunzio, M. H. Devoret, S. M. Girvin, and R. J. Schoelkopf, "Sideband transitions and two-tone spectroscopy of a superconducting qubit strongly coupled to an on-chip cavity," *Phys. Rev. Lett.* **99**, 050501 (2007). Cited on page 42.

75. P. J. Leek, M. Baur, J. M. Fink, R. Bianchetti, L. Steffen, S. Filipp, and A. Wallraff, "Cavity Quantum Electrodynamics with Separate Photon Storage and Qubit Readout Modes," *Physical Review Letters* **104**, 100504 (2010), 0911.4951 [cond-mat.mes-hall]. Cited on pages 42 & 71.

76. W. H. Zurek, "Sub-Planck structure in phase space and its relevance for quantum decoherence," *Nature* **412**, 712–717 (2001). Cited on page 45.

77. K. Husimi, "Some formal properties of the density matrix," *Proc. Phys. Math. Soc. Jpn.* **22**, 264–314 . Cited on page 47.

78. L. Bretheau, P. Campagne-Ibarcq, E. Flurin, F. Mallet, and B. Huard, "Quantum dynamics of an electromagnetic mode that cannot contain n photons," *Science* **348**, 776–779 (2015), http://www.sciencemag.org/content/348/6236/776.full.pdf. Cited on page 47.

79. B. Vlastakis, A. Petrenko, N. Ofek, L. Sun, Z. Leghtas, K. Sliwa, Y. Liu, M. Hatridge, J. Blumoff, L. Frunzio, M. Mirrahimi, L. Jiang, M. H. Devoret, and R. J. Schoelkopf, "Violating Bell's inequality with an artificial atom and a cat state in a cavity," *ArXiv e-prints* (2015), 1504.02512 [quant-ph]. Cited on pages 47, 49, 54, 143 & 149.

80. L. Sun, A. Petrenko, Z. Leghtas, B. Vlastakis, G. Kirchmair, K. M. Sliwa, A. Narla, M. Hatridge, S. Shankar, J. Blumoff, L. Frunzio, M. Mirrahimi, M. H. Devoret, and R. J. Schoelkopf, "Tracking photon jumps with repeated quantum non-demolition parity measurements," *Nature* **511**, 444–448 (2014), 1311.2534 [quant-ph]. Cited on pages 49, 68, 70, 93, 143, 164 & 165.

81. P. Bertet, A. Auffeves, P. Maioli, S. Osnaghi, T. Meunier, M. Brune, J. M. Raimond, and S. Haroche, "Direct Measurement of the Wigner Function of a One-Photon Fock State in a Cavity," *Phys. Rev. Lett.* **89**, 200402 (2002). Cited on pages 52 & 53.

82. A. Kenfack and K. Zyczkowski, "Negativity of the Wigner function as an indicator of non-classicality," *Journal of Optics B: Quantum and Semiclassical Optics* **6**, 396–404 (2004), quant-ph/0406015. Cited on page 53.

83. E. F. Galvão, "Discrete Wigner functions and quantum computational speedup," *Phys. Rev. A* **71**, 042302 (2005), quant-ph/0405070. Cited on page 53.

84. V. Veitch, C. Ferrie, D. Gross, and J. Emerson, "Negative quasi-probability as a resource for quantum computation," *New Journal of Physics* **14**, 113011 (2012), 1201.1256 [quant-ph]. Cited on page 53.

85. S. Deléglise, I. Dotsenko, C. Sayrin, J. Bernu, M. Brune, J.-M. Raimond, and S. Haroche, "Reconstruction of non-classical cavity field states with snapshots of their decoherence," *Nature* **455**, 510–514 (2008), 0809.1064 [quant-ph]. Cited on page 53.

86. A. I. Lvovsky and M. G. Raymer, "Continuous-variable optical quantum-state tomography," *Reviews of Modern Physics* **81**, 299–332 (2009), quant-ph/0511044. Cited on page 54.

87. D.-G. Welsch, W. Vogel, and T. Opatrny, "Homodyne Detection and Quantum State Reconstruction," *ArXiv e-prints* (2009), 0907.1353 [quant-ph]. Cited on pages 54 & 56.

88. J. Bertrand and P. Bertrand, "A tomographic approach to wigner's function," *Foundations of Physics* **17**, 397–405 (1987). Cited on page 56.

89. Z. Hradil, "Quantum-state estimation," *Phys. Rev. A* **55**, R1561–R1564 (1997). Cited on page 56.

90. C. Eichler, D. Bozyigit, C. Lang, L. Steffen, J. Fink, and A. Wallraff, "Experimental State Tomography of Itinerant Single Microwave Photons," *Physical Review Letters* **106**, 220503 (2011), 1011.6668 [quant-ph]. Cited on pages 56 & 57.

91. C. W. Gardiner and M. J. Collett, "Input and output in damped quantum systems: Quantum stochastic differential equations and the master equation," *Phys. Rev. A* **31**, 3761–3774 (1985). Cited on page 57.

92. D. F. Walls and G. J. Milburn, *Quantum Optics*. Springer-Verlag, Berlin Heidelberg, 2008. Cited on page 57.

93. F. D. O. Schackert, *A Practical Quantum-Limited Parametric Amplifier Based on the Josephson Ring Modulator*. PhD thesis, Yale University, 2013. http://qulab.eng.yale.edu/documents/theses/Thesis_Flavius_A%20Practical%20Quantum-Limited%20Parametric%20Amplifier.pdf. Cited on pages 57, 135 & 136.

94. Z. Leghtas, G. Kirchmair, B. Vlastakis, M. H. Devoret, R. J. Schoelkopf, and M. Mirrahimi, "Deterministic protocol for mapping a qubit to coherent state superpositions in a cavity," *Phys. Rev. A* **87**, 042315 (2013), 1205.2401 [quant-ph]. Cited on page 58.

95. S. Krastanov, V. V. Albert, C. Shen, C.-L. Zou, R. W. Heeres, B. Vlastakis, R. J. Schoelkopf, and L. Jiang, "Universal Control of an Oscillator with Dispersive Coupling to a Qubit," *ArXiv e-prints* (2015), 1502.08015 [quant-ph]. Cited on pages 58, 60, 61, 148, 152 & 164.

96. P. J. Leek, J. M. Fink, A. Blais, R. Bianchetti, M. Göppl, J. M. Gambetta, D. I. Schuster, L. Frunzio, R. J. Schoelkopf, and A. Wallraff, "Observation of Berry's Phase in a Solid-State Qubit," *Science* **318**, 1889– (2007), 0711.0218. Cited on page 60.

97. S. Lloyd and S. L. Braunstein, "Quantum Computation over Continuous Variables," *Physical Review Letters* **82**, 1784–1787 (1999), quant-ph/9810082. Cited on page 61.

98. A. M. Steane, "Error correcting codes in quantum theory," *Phys. Rev. Lett.* **77**, 793–797 (1996). Cited on page 67.

99. Z. Leghtas, G. Kirchmair, B. Vlastakis, R. J. Schoelkopf, M. H. Devoret, and M. Mirrahimi, "Hardware-Efficient Autonomous Quantum Memory Protection," *Physical Review Letters* **111**, 120501 (2013), 1207.0679 [quant-ph]. Cited on pages 67 & 68.

100. M. Reagor, H. Paik, G. Catelani, L. Sun, C. Axline, E. Holland, I. M. Pop, N. A. Masluk, T. Brecht, L. Frunzio, M. H. Devoret, L. Glazman, and R. J. Schoelkopf, "Reaching 10 ms single photon lifetimes for superconducting aluminum cavities," *Applied Physics Letters* **102**, 192604 (2013), 1302.4408 [cond-mat.supr-con]. Cited on pages 67, 80, 95, 97, 98, 99, 100, 102, 103, 111, 112, 113, 115, 116, 122, 124, 152 & 157.

101. J. Gao, M. Daal, A. Vayonakis, S. Kumar, J. Zmuidzinas, B. Sadoulet, B. A. Mazin, P. K. Day, and H. G. Leduc, "Experimental evidence for a surface distribution of two-level systems in superconducting lithographed microwave resonators," *Applied Physics Letters* **92**, – (2008). Cited on page 71.

102. M. R. Vissers, J. Gao, D. S. Wisbey, D. A. Hite, C. C. Tsuei, A. D. Corcoles, M. Steffen, and D. P. Pappas, "Low loss superconducting titanium nitride coplanar waveguide resonators," *Applied Physics Letters* **97**, 232509 (2010), 1007.5096 [cond-mat.supr-con]. Cited on page 71.

103. A. Megrant, C. Neill, R. Barends, B. Chiaro, Y. Chen, L. Feigl, J. Kelly, E. Lucero, M. Mariantoni, P. J. J. O'Malley, D. Sank, A. Vainsencher, J. Wenner, T. C. White, Y. Yin, J. Zhao, C. J. Palmstrøm, J. M. Martinis, and A. N. Cleland, "Planar superconducting resonators with internal quality factors above one million," *Applied Physics Letters* **100**, 113510 (2012), 1201.3384 [cond-mat.mes-hall]. Cited on pages 71, 83, 85 & 167.

104. K. Geerlings, S. Shankar, E. Edwards, L. Frunzio, R. J. Schoelkopf, and M. H. Devoret, "Improving the quality factor of microwave compact resonators by optimizing their geometrical parameters," *Applied Physics Letters* **100**, 192601 (2012), 1204.0742 [cond-mat.supr-con]. Cited on pages 71, 75, 85, 113, 116 & 167.

105. C. Wang, C. Axline, Y. Y. Gao, T. Brecht, L. Frunzio, M. H. Devoret, and R. J. Schoelkopf, "Surface participation and dielectric loss in superconducting qubits," *ArXiv e-prints* (2015), 1509.01854 [quant-ph]. Cited on pages 71, 75, 78, 85, 93, 94 & 95.

106. O. Dial, D. T. McClure, S. Poletto, J. M. Gambetta, D. W. Abraham, J. M. Chow, and M. Steffen, "Bulk and surface loss in superconducting transmon qubits," *ArXiv e-prints* (2015), 1509.03859 [quant-ph]. Cited on pages 71, 75, 78, 93, 94, 104 & 148.

107. M. Mariantoni, H. Wang, T. Yamamoto, M. Neeley, R. C. Bialczak, Y. Chen, M. Lenander, E. Lucero, A. D. O'Connell, D. Sank, M. Weides, J. Wenner, Y. Yin, J. Zhao, A. N. Korotkov, A. N. Cleland, and J. M. Martinis, "Implementing the Quantum von Neumann Architecture with Superconducting Circuits," *Science* **334**, 61– (2011), 1109.3743 [cond-mat.mes-hall]. Cited on pages 71 & 164.

108. R. Feynman, R. Leighton, and M. Sands, *The Feynman Lectures on Physics: Mainly electromagnetism and matter. Volume 2*. Basic Books. Basic Books, 2011. https://books.google.com/books?id=hlRhwGK40fgC. Cited on page 72.

109. W. A. Al-Saidi and D. Stroud, "Eigenstates of a small Josephson junction coupled to a resonant cavity," *Phys. Rev. B* **65**, 014512 (2002), cond-mat/0110117. Cited on page 73.

110. K. L. Geerlings, *Improving Coherence of Superconducting Qubits and Resonators*. PhD thesis, Yale University, 2013. http://qulab.eng.yale.edu/documents/theses/Kurtis_ImprovingCoherenceSuperconductingQubits.pdf. Cited on pages 74, 112, 116, 118, 131, 156 & 163.

111. D. Pozar, *Microwave Engineering, 4th Edition*. Wiley, 2011. https://books.google.com/books?id=JegbAAAAQBAJ. Cited on pages 75, 76, 77, 79, 80, 82, 87, 89, 92, 98, 99, 103, 104, 106, 125 & 202.

112. J. Gao, *The Physics of Superconducting Microwave Resonators*. PhD thesis, California Institute of Technology, 2008. http://resolver.caltech.edu/CaltechETD:etd-06092008-235549. Cited on pages 75 & 116.

113. ROGERS Corporation, *RO4000 Series High Frequency Circuit Materials*, 2015. Cited on page 77.

114. H. Paik, D. I. Schuster, L. S. Bishop, G. Kirchmair, G. Catelani, A. P. Sears, B. R. Johnson, M. J. Reagor, L. Frunzio, L. I. Glazman, S. M. Girvin, M. H. Devoret, and R. J. Schoelkopf, "Observation of High Coherence in Josephson Junction Qubits Measured in a Three-Dimensional Circuit QED Architecture," *Physical Review Letters* **107**, 240501 (2011), 1105.4652 [quant-ph]. Cited on pages 77, 86, 87, 88, 93, 94, 95, 96, 104, 106, 124, 148, 157 & 167.

115. D. L. Creedon, Y. Reshitnyk, W. Farr, J. M. Martinis, T. L. Duty, and M. E. Tobar, "High Q-factor sapphire whispering gallery mode microwave resonator at single photon energies and millikelvin temperatures," *Applied Physics Letters* **98**, 222903 (2011), 1103.6094 [quant-ph]. Cited on page 77.

116. H. Padamsee, "The science and technology of superconducting cavities for accelerators," *Superconductor Science and Technology* **14**, R28–R51 (2001). Cited on pages 79 & 95.

117. R. Barends, J. Wenner, M. Lenander, Y. Chen, R. C. Bialczak, J. Kelly, E. Lucero, P. O'Malley, M. Mariantoni, D. Sank, H. Wang, T. C. White, Y. Yin, J. Zhao, A. N. Cleland, J. M. Martinis, and J. J. A. Baselmans, "Minimizing quasiparticle

generation from stray infrared light in superconducting quantum circuits," *Applied Physics Letters* **99**, 113507 (2011). Cited on page 79.

118. M. Lenander, H. Wang, R. C. Bialczak, E. Lucero, M. Mariantoni, M. Neeley, A. D. O'Connell, D. Sank, M. Weides, J. Wenner, T. Yamamoto, Y. Yin, J. Zhao, A. N. Cleland, and J. M. Martinis, "Measurement of energy decay in superconducting qubits from nonequilibrium quasiparticles," *Physical Review B* **84**, (2011). Cited on page 79.

119. I. M. Pop, K. Geerlings, G. Catelani, R. J. Schoelkopf, L. I. Glazman, and M. H. Devoret, "Coherent suppression of electromagnetic dissipation due to superconducting quasiparticles," *Nature* **508**, 369 (2014). Cited on pages 79 & 148.

120. C. Wang, Y. Y. Gao, I. M. Pop, U. Vool, C. Axline, T. Brecht, R. W. Heeres, L. Frunzio, M. H. Devoret, G. Catelani, L. I. Glazman, and R. J. Schoelkopf, "Measurement and control of quasiparticle dynamics in a superconducting qubit," *Nature Communications* **5**, 5836 (2014). Cited on pages 79 & 88.

121. J. Turneaure, J. Halbritter, and H. Schwettman, "The surface impedance of superconductors and normal conductors: The mattis-bardeen theory," *Journal of Superconductivity* **4**, 341–355 (1991). Cited on pages 80 & 124.

122. P. K. Day, H. G. LeDuc, B. A. Mazin, A. Vayonakis, and J. Zmuidzinas, "A broadband superconducting detector suitable for use in large arrays," *Nature* **425**, 817–821 (2003). Cited on pages 80 & 124.

123. T. Brecht, M. Reagor, Y. Chu, W. Pfaff, C. Wang, L. Frunzio, M. H. Devoret, and R. J. Schoelkopf, "Demonstration of superconducting micromachined cavities," *ArXiv e-prints* (2015), 1509.01119 [cond-mat.supr-con]. Cited on pages 80, 81, 93, 96 & 97.

124. J. P. Turneaure and N. T. Viet, "Superconducting Nb Tm010 Mode Electron-Beam Welded Cavities," *Applied Physics Letters* **16**, 333–& (1970). Cited on page 80.

125. G. Rebeiz, *RF MEMS: Theory, Design, and Technology*. Wiley, 2004. https://books.google.com/books?id=A7728XHtmzAC. Cited on page 80.

126. C. Wen, "Coplanar waveguide: A surface strip transmission line suitable for nonreciprocal gyromagnetic device applications," *Microwave Theory and Techniques, IEEE Transactions on* **17**, 1087–1090 (1969). Cited on page 82.

127. R. Simons, *Coplanar Waveguide Circuits, Components, and Systems*. Wiley Series in Microwave and Optical Engineering. Wiley, 2004. https://books.google.com/books?id=XgNMZ5YVJdgC. Cited on pages 82 & 83.

128. M. Goppl, A. Fragner, M. Baur, R. Bianchetti, S. Filipp, J. M. Fink, P. J. Leek, G. Puebla, L. Steffen, and A. Wallraff, "Coplanar waveguide resonators for circuit quantum electrodynamics," *Journal of Applied Physics* **104**, – (2008). Cited on page 84.

129. B. R. Johnson, *Controlling Photons in Superconducting Electrical Circuits*. PhD thesis, Yale University, 2011. http://www.eng.yale.edu/rslab/papers/johnson-thesis.pdf. Cited on pages 84, 130 & 133.

130. P. J. Petersan and S. M. Anlage, "Measurement of resonant frequency and quality factor of microwave resonators: Comparison of methods," *Journal of Applied Physics* **84**, 3392–3402 (1998). Cited on pages 85 & 116.

131. J. Wenner, R. Barends, R. C. Bialczak, Y. Chen, J. Kelly, E. Lucero, M. Mariantoni, A. Megrant, P. J. J. O'Malley, D. Sank, A. Vainsencher, H. Wang, T. C. White, Y. Yin, J. Zhao, A. N. Cleland, and J. M. Martinis, "Surface loss simulations of superconducting coplanar waveguide resonators," *Applied Physics Letters* **99**, (2011). Cited on page 85.

132. J. M. Sage, V. Bolkhovsky, W. D. Oliver, B. Turek, and P. B. Welander, "Study of loss in superconducting coplanar waveguide resonators," *Journal of Applied Physics* **109**, (2011). Cited on page 85.

133. M. S. Khalil, M. J. A. Stoutimore, F. C. Wellstood, and K. D. Osborn, "An analysis method for asymmetric resonator transmission applied to superconducting devices," *Journal of Applied Physics* **111**, – (2012). Cited on pages 85 & 116.

134. M. Sandberg, M. R. Vissers, T. A. Ohki, J. Gao, J. Aumentado, M. Weides, and D. P. Pappas, "Radiation-suppressed superconducting quantum bit in a planar geometry," *Applied Physics Letters* **102**, 072601 (2013). Cited on pages 85 & 93.

135. C. Wang, C. Axline, Y. Y. Gao, T. Brecht, Y. Chu, L. Frunzio, M. H. Devoret, and R. J. Schoelkopf, "Surface Participation and Dielectric Loss in Superconducting Qubits," *Applied Physics Letters* **107**, 162601 (2015). Cited on page 86.

136. B. Bianco, A. Corana, L. Gogioso, S. Ridella, and M. Parodi, "Open-circuited coaxial lines as standards for microwave measurements," *Electronics Letters* **16**, 373–374(1) (1980). Cited on pages 88, 92 & 104.

137. H. A. Bethe, "Theory of diffraction by small holes," *Phys. Rev.* **66**, 163–182 (1944). Cited on pages 90 & 101.

138. R. Collin, *Foundations for Microwave Engineering*. IEEE Press Series on Electromagnetic Wave Theory. Wiley, 2001. https://books.google.com/books?id=2SxoQgAACAAJ. Cited on pages 90, 91, 102 & 103.

139. S. B. Cohn, "Microwave coupling by large apertures," *Proceedings of the IRE* **40**, 696–699 (1952). Cited on page 90.

140. A. P. Sears, A. Petrenko, G. Catelani, L. Sun, H. Paik, G. Kirchmair, L. Frunzio, L. I. Glazman, S. M. Girvin, and R. J. Schoelkopf, "Photon shot noise dephasing in the strong-dispersive limit of circuit QED," *Physical Review B* **86**, (2012). Cited on pages 93, 131, 153, 160 & 161.

141. C. Rigetti, J. M. Gambetta, S. Poletto, B. L. T. Plourde, J. M. Chow, A. D. Corcoles, J. A. Smolin, S. T. Merkel, J. R. Rozen, G. A. Keefe, M. B. Rothwell, M. B. Ketchen, and M. Steffen, "Superconducting qubit in a waveguide cavity with a coherence time approaching 0.1 ms," *Physical Review B* **86**, 100506 (2012). Cited on pages 94, 148, 153 & 160.

142. A. Sears, D. Hover, T. Gudmundsen, J. Yoder, A. Kamal, F. Yan, S. Gustavsson, A. Kerman, and W. Oliver, "Probing an Ensemble of Superconducting Devices," in *APS March Meeting*, p. M39.00013. 2015. Cited on page 94.

143. S. E. Nigg and S. M. Girvin, "Stabilizer Quantum Error Correction Toolbox for Superconducting Qubits," *Physical Review Letters* **110**, 243604 (2013), 1212.4000 [quant-ph]. Cited on page 94.

144. M. D. Reed, *Entanglement and Quantum Error Correction with Superconducting Qubits*. PhD thesis, Yale University, 2013. http://www.eng.yale.edu/rslab/papers/theses/reed.pdf. Cited on pages 94, 112, 131 & 138.

145. Y. Tabuchi, S. Ishino, A. Noguchi, T. Ishikawa, R. Yamazaki, K. Usami, and Y. Nakamura, "Coherent coupling between a ferromagnetic magnon and a superconducting qubit," *Science* **349**, 405–408 (2015), http://www.sciencemag.org/content/349/6246/405.full.pdf. Cited on page 94.

146. S. Kuhr, S. Gleyzes, C. Guerlin, J. Bernu, U. B. Hoff, S. Deleglise, S. Osnaghi, M. Brune, J. M. Raimond, S. Haroche, E. Jacques, P. Bosland, and B. Visentin, "Ultrahigh finesse Fabry-Perot superconducting resonator," *Applied Physics Letters* **90**, (2007). Cited on page 95.

147. H. Padamsee, *RF Superconductivity: Volume II: Science, Technology and Applications*. Wiley series in beam physics and accelerator technology. Wiley, 2009. https://books.google.com/books?id=Pfo2js9IdrIC. Cited on pages 97 & 113.

148. J. P. Turneaure and I. Weissman, "Microwave Surface Resistance of Superconducting Niobium," *Journal of Applied Physics* **39**, 4417–4427 (1968). Cited on pages 97, 98 & 99.

149. B. Vlastakis, *Controlling Coherent State Superpositions with Superconducting Circuits*. PhD thesis, Yale University, 2015. Cited on page 106.

150. Transense Company, Inc., *Aluminum Etchants*, 2015. Cited on page 113.

151. PotashCorp, *Bright Dipping Aluminum*, 2015. Cited on page 113.

152. S. Probst, F. B. Song, P. A. Bushev, A. V. Ustinov, and M. Weides, "Efficient and Robust Analysis of Complex Scattering Data Under Noise in Microwave Resonators," *Review of Scientific Instruments* **86**, 024706 (2015), 1410.3365 [cond-mat.supr-con]. Cited on pages 116 & 120.

153. H. Wang, M. Hofheinz, J. Wenner, M. Ansmann, R. C. Bialczak, M. Lenander, E. Lucero, M. Neeley, A. D. O'Connell, D. Sank, M. Weides, A. N. Cleland, and J. M. Martinis, "Improving the coherence time of superconducting coplanar resonators," *Applied Physics Letters* **95**, 233508 (2009). Cited on page 121.

154. P. Macha, S. H. W. van der Ploeg, G. Oelsner, E. Il'ichev, H.-G. Meyer, S. Wünsch, and M. Siegel, "Losses in coplanar waveguide resonators at millikelvin temperatures," *Applied Physics Letters* **96**, 062503 (2010), 0910.0685 [cond-mat.supr-con]. Cited on page 121.

155. S. B. Nam, "Theory of electromagnetic properties of superconducting and normal systems. i," *Phys. Rev.* **156**, 470–486 (1967). Cited on pages 124 & 128.

156. S. B. Nam, "Theory of electromagnetic properties of strong-coupling and impure superconductors. ii," *Phys. Rev.* **156**, 487–493 (1967). Cited on pages 124 & 128.

157. E. W. Weisstein, "Inverse Tangent," *Mathworld-A Wolfram Web Resource* . Cited on page 126.

158. Y. Liu, S. Shankar, N. Ofek, M. Hatridge, A. Narla, K. Sliwa, L. Frunzio, R. J. Schoelkopf, and M. H. Devoret, "Comparing and combining measurement-based and driven-dissipative entanglement stabilization," *ArXiv e-prints* (2015), 1509.00860 [quant-ph]. Cited on page 129.

159. G. J. Dolan, "Offset masks for liftâĂŘoff photoprocessing," *Applied Physics Letters* **31**, (1977). Cited on page 130.

160. V. Ambegaokar and A. Baratoff, "Tunneling between superconductors," *Phys. Rev. Lett.* **10**, 486–489 (1963). Cited on page 130.

161. D. T. McClure, H. Paik, L. S. Bishop, M. Steffen, J. M. Chow, and J. M. Gambetta, "Rapid Driven Reset of a Qubit Readout Resonator," *ArXiv e-prints* (2015), 1503.01456 [quant-ph]. Cited on page 133.

162. E. T. Holland, B. Vlastakis, R. W. Heeres, M. J. Reagor, U. Vool, Z. Leghtas, L. Frunzio, G. Kirchmair, M. H. Devoret, M. Mirrahimi, and R. J. Schoelkopf, "Single-photon Resolved Cross-Kerr Interaction for Autonomous Stabilization of Photon-number States," *ArXiv e-prints* (2015), 1504.03382 [quant-ph]. Cited on page 145.

163. F. Solgun, D. W. Abraham, and D. P. DiVincenzo, "Blackbox quantization of superconducting circuits using exact impedance synthesis," *Phys. Rev. B* **90**, 134504 (2014), 1403.7341 [quant-ph]. Cited on page 154.

164. G. Catelani, S. E. Nigg, S. M. Girvin, R. J. Schoelkopf, and L. I. Glazman, "Decoherence of superconducting qubits caused by quasiparticle tunneling," *Phys. Rev. B* **86**, 184514 (2012), 1207.7084 [cond-mat.mes-hall]. Cited on page 157.

165. A. A. Clerk and D. W. Utami, "Using a qubit to measure photon-number statistics of a driven thermal oscillator," *Phys. Rev. A* **75**, 042302 (2007). Cited on page 160.

166. R. Barends, J. Wenner, M. Lenander, Y. Chen, R. C. Bialczak, J. Kelly, E. Lucero, P. O'Malley, M. Mariantoni, D. Sank, H. Wang, T. C. White, Y. Yin, J. Zhao, A. N. Cleland, J. M. Martinis, and J. J. A. Baselmans, "Minimizing quasiparticle generation from stray infrared light in superconducting quantum circuits," *Applied Physics Letters* **99**, 113507 (2011). Cited on page 163.

167. A. D. Córcoles, J. M. Chow, J. M. Gambetta, C. Rigetti, J. R. Rozen, G. A. Keefe, M. B. Rothwell, M. B. Ketchen, and M. Steffen, "Protecting superconducting qubits from radiation," *Applied Physics Letters* **99**, 181906 (2011). Cited on page 163.

168. X. Y. Jin, A. Kamal, A. P. Sears, T. Gudmundsen, D. Hover, J. Miloshi, R. Slattery, F. Yan, J. Yoder, T. P. Orlando, S. Gustavsson, and W. D. Oliver, "Thermal and Residual Excited-State Population in a 3D Transmon Qubit," *Physical Review Letters* **114**, (2015). Cited on page 164.

169. S. J. Srinivasan, A. J. Hoffman, J. M. Gambetta, and A. A. Houck, "Tunable Coupling in Circuit Quantum Electrodynamics Using a Superconducting Charge Qubit with a V-Shaped Energy Level Diagram," *Physical Review Letters* **106**, 083601 (2011). Cited on page 164.

170. J. M. Raimond, C. Sayrin, S. Gleyzes, I. Dotsenko, M. Brune, S. Haroche, P. Facchi, and S. Pascazio, "Phase Space Tweezers for Tailoring Cavity Fields by Quantum Zeno Dynamics," *Physical Review Letters* **105**, 213601 (2010). Cited on pages 164 & 169.

171. G. Moore, "Cramming more components onto integrated circuits," *Electronics* 114–117 . Cited on page 166.

172. G. Moore, "Cramming more components onto integrated circuits," 1998. Cited on page 166.

173. L. Bishop, *Circuit Quantum Electrodynamics*. PhD thesis, Yale University, 2010. http://arxiv.org/pdf/1007.3520.pdf$$yThesis. Cited on page 167.

174. D. Vion, A. Aassime, A. Cottet, P. Joyez, H. Pothier, C. Urbina, D. Esteve, and M. H. Devoret, "Manipulating the quantum state of an electrical circuit," *Science* **296**, 886–889 (2002), http://www.sciencemag.org/content/296/5569/886.full.pdf. Cited on page 167.

175. C. K. Law and J. H. Eberly, "Arbitrary control of a quantum electromagnetic field," *Phys. Rev. Lett.* **76**, 1055–1058 (1996). Cited on page 168.

176. J. Johansson, P. Nation, and F. Nori, "Qutip: An open-source python framework for the dynamics of open quantum systems," *Computer Physics Communications* **183**, 1760 – 1772 (2012). Cited on pages 191 & 192.

APPENDIX A

Arbitrary classical drives on linear circuits

In this appendix we adapt the proof from Itano et al. [23] that an arbitrary force on a damped mechanical oscillator $\hat{F}(t) = k(t)\hat{x}$ always results in a coherent state. In particular, we are interested in the equivalent description for circuits.

Consider the effect of a time-dependent current bias on a simple LC circuit. This bias will couple to the flux through the inductor as $V(t) = -I(t)\hat{\Phi} = -\hbar\epsilon(t)(\hat{a} + \hat{a}^\dagger)$, where we have expressed the drive in convenient units. That now gives us a Hamiltonian of the driven circuit as

$$\hat{H} = \hbar\omega\hat{a}^\dagger\hat{a} - \hbar\epsilon(t)(\hat{a} + \hat{a}^\dagger). \tag{A.1}$$

We change to a rotating frame to simplify our derivation. This can be done with a unitary operator [11] as

$$\hat{U} = \exp(+\imath\omega t\hat{a}^\dagger\hat{a}), \tag{A.2}$$

which transforms our Hamiltonian as

$$\hat{H}' = \hat{U}\hat{H}\hat{U}^\dagger + \hat{U}\left[-\imath\frac{d}{dt}, \hat{U}\right]. \tag{A.3}$$

Clearly, $\hat{U}$ commutes with $\hat{a}^\dagger\hat{a}$. However, as a result of the lack of free-commutation between the number operator and single ladder operators, the time-evolution of the bare Hamiltonian gets acquired by the ladder operators as

$$\hat{H}_1(t) = \hbar\epsilon(t)\left(\hat{a}\exp(-\imath\omega t) + \hat{a}^\dagger\exp(\imath\omega t)\right). \tag{A.4}$$

We are interested in the time-evolution of states that begin as coherent states. Do they remain coherent states under arbitrary $\epsilon(t)$? If we assume that they do, then at any time we can write the resulting state, including a global phase [23], as

$$|\psi(t)\rangle = e^{\imath\theta(t)}|\alpha(t)\rangle. \tag{A.5}$$

From the Schrödigner equation, we can write out the time-dependence explicitly as

$$\imath\hbar\frac{d}{dt}|\psi(t)\rangle = \hat{H}_1(t)|\alpha(t)\rangle. \tag{A.6}$$

Our problem thus reduces to finding a coherent state amplitude $\alpha(t)$ that satisfies the Schrödinger equation [23]. Following Itano, we expand out the left hand side of this expression by using our Fock-state enumeration of Equation 2.22, as

$$\begin{aligned}\imath\hbar\frac{d}{dt}|\alpha(t)\rangle = \imath\hbar\left(\frac{d}{dt}e^{-|\alpha(t)|^2/2}\right)\sum_n\frac{\alpha(t)^n}{\sqrt{n!}}|n\rangle \\ + \imath\hbar e^{-|\alpha|^2/2}\frac{d}{dt}\sum_n\frac{\alpha(t)^n}{\sqrt{n!}}|n\rangle.\end{aligned} \tag{A.7}$$

The time derivative in the first term on the right hand side can be written as

$$\frac{d}{dt}e^{-|\alpha(t)|^2/2} = -\frac{1}{2}\left(\frac{d\alpha}{dt}\alpha^*(t) + \frac{d\alpha^*}{dt}\alpha(t)\right) \tag{A.8}$$

We also point out that the time derivative in second term on the right hand of Equation A.7 side will bring down an n from the exponent on $\alpha(t)$ in the summation as

$$\frac{d}{dt}\sum_n\frac{\alpha(t)^n}{\sqrt{n!}}|n\rangle = \sum_n\frac{n\alpha(t)^{n-1}}{\sqrt{n!}}\frac{d\alpha}{dt}|n\rangle \tag{A.9}$$

Now, we need to solve the right hand side of Equation A.6 so that we can find the correct

description of $\alpha(t)$

$$\hat{H}_1(t)|\alpha(t)\rangle = \hbar\epsilon(t)\left(\hat{a}e^{-\imath\omega t} + \hat{a}^\dagger e^{\imath\omega t}\right)|\alpha(t)\rangle. \tag{A.10}$$

Again, we rely on the Fock-state representation of coherent states in Equation 2.22 to write out the right hand side

$$\hat{H}_1(t)|\alpha(t)\rangle = \hbar\epsilon(t)\left(e^{-\imath\omega t}\sum_n \frac{\alpha(t)^{n+1}}{\sqrt{n!}}|n\rangle + e^{\imath\omega t}\sum_n \frac{\alpha(t)^{n-1}n}{\sqrt{n!}}|n\rangle\right). \tag{A.11}$$

Finally, we equation Equation A.7 to Equation A.11 and solve for $\alpha(t)$. Because Fock states are orthogonal, these relations must hold for each n in the summations independently. Furthermore, for this equality to hold for all n simultaneously, the summation terms with an explicit n dependence must cancel out [23]. Gathering these terms gives

$$\frac{d\alpha}{dt} - \imath\epsilon(t)e^{+\imath\omega t} = 0 \tag{A.12}$$

which can be solved as

$$\alpha(t) = \alpha(0) + \imath\int_0^t \epsilon(t')e^{\imath\omega t'}dt'. \tag{A.13}$$

One can plug this solution into Schrödinger equation to verify that it is indeed satisfied at all times, which provides another constraint for the global reference phase $\theta(t)$.

APPENDIX B

Superpositions with SNAP

In this appendix, we present the calculations and QuTiP code [176] for the series of SNAP gates that allow us to create a superposition of Fock states in a resonator.

First, a displacement of amplitude $\beta_1 = 0.56$ creates a small coherent state in the resonator. Then, the phase on the zeroth Fock state of the resonator is rotated by π via a selective rotation on the qubit. Finally, a displacement of $\beta_2 = -0.26$ centers the Fock state superposition, leaving the state mostly in $|\psi\rangle = (1/\sqrt{2})(|0\rangle + |1\rangle)$.

We can simulate this process in QuTip with a few simple commands. From the code in Figure B.1, we can inspect the state vector at each of these steps. Note that this model assumes perfect gate operations. We find a final state vector of

$$|\psi\rangle = -0.711|0\rangle + 0.703|1\rangle + 0.001|2\rangle + 0.022|3\rangle + ... \tag{B.1}$$

The probability of detecting the resonator in the first excited state is $P_1 = 0.494$ and the ground state with $P_0 = 0.505$. Furthermore, this is a coherent superposition, satisfying our requirement for the T_2-type experiment.

```
import qutip as qt
# initialize the ground state of a N=20 dim. Hilbert space
psi0 = qt.fock(20,0)
print psi0

# displace the resonator
beta1 = 0.56
psi1 = qt.
displace(20,beta) * psi0
print psi1

# flip the |0> state
psi1_SNAP = (qt.qeye(20)-2*qt.fock_dm(20,0)) * psi1
print psi1_SNAP

# final dislacement
beta2 = -0.26
psi2 = qt.displace(20,beta2) * psi1_SNAP
print psi2
```

Figure B.1: Python code for simulating SNAP processes. We use the open source QuTiP package [176] to calculate the evolution of a resonator under a sequence of gates. After two displacements and a single SNAP rotation, we achieve the desired superposition of Fock states.

APPENDIX C

Evanescent coupling to resonators

In this appendix, we present measurements and simulations of the coupling techniques used with the three dimensional cavity resonators discussed in Chapter 4.

Rectangular cavities

In Section 4.4.2, we showed that coupling to our rectangular cavities is mediated by a circular waveguide's TM_{0m} modes. The propagation constants of these propagating waves are imaginary, leading to the exponential decay we exploit for tunable coupling. We have for these modes a propagation constant

$$\beta_{TM_{0m}} = \sqrt{k^2 - \left(\frac{p_{0m}}{r_0}\right)^2}, \tag{C.1}$$

where k is the wave vector, p_{0m} is the m-th zero of the zeroth Bessel function, and $r_0 = 1.2\,\text{mm}$ is the radius of the sub-cutoff waveguide. In Table C.1, we tabulate the propagation constant for the first three modes at 10 GHz. We further expect that the dominant propagation constant will be that corresponding to the lowest cutoff mode. This

Mode	Propagation constant β (mm^{-1})
TM_{01}	2.05 $\imath$
TM_{02}	4.74 $\imath$
TM_{03}	7.41 $\imath$

Table C.1: Propagation constants for the lowest three sub-cutoff modes of a pin coupled circular waveguide.

mode will determine the scaling of $Q_{ext} \propto e^{-2j\beta_{TM_{01}}L}$, where $\beta_{TM_{01}}$ is the propagation constant for the lowest cutoff mode and L is the length of sub-cutoff waveguide.

In Figure C.1, we show the extracted external quality factor versus length of sub-cutoff waveguide. On a log scale, the best-fit slope gives the evanescent coupling scaling as $|\beta|$ = 1.83 mm^{-1}. This is in good agreement with the dominant waveguide mode, the TM_{01} mode ($|\beta|$ = 2.05mm^{-1}). The fact that the best-fit $|\beta|$ is smaller than expected indicates that higher waveguide modes are contributing to the power transmitted from the cavity at the 10% level.

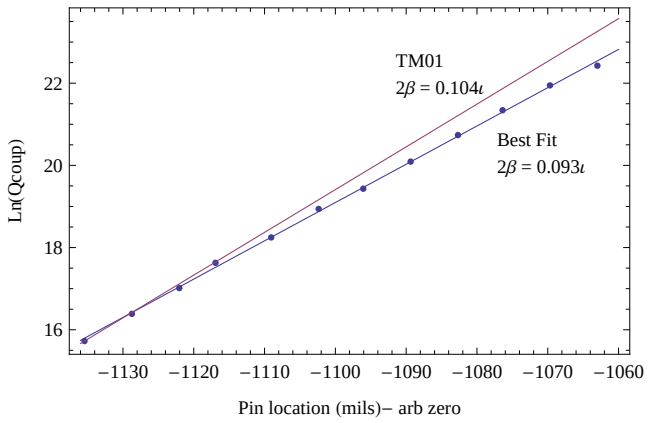

Figure C.1: Measured scaling of external coupling for rectangular cavity. Measured values of Q_{ext} versus length of evanescent circular waveguide shown in thousandths of an inch (mils). On a log scale, the propagation constant of the dominant waveguide mode is given by the best linear fit ($|\beta|$ = 1.83 mm^{-1}).

Cylindrical Cavity

Figure C.2 shows a constructed loop coupler of the type used to excite the cylindrical TE_{011} cavities through a section of narrow circular waveguide (see Section 4.5.2). With

Mode	Propagation constant β (mm^{-1})
TE_{11}	1.02 $\imath$
TM_{11}	2.13 $\imath$
TE_{12}	2.99 $\imath$
TM_{12}	3.94 $\imath$

Table C.2: Propagation constants for for the lowest three sub-cutoff modes of a loop coupled circular waveguide.

this method, both TE and TM types of circular waveguide contribute to the evanescent coupling. In Table C.2, we calculate the propagation constant for the four lowest modes at 10 GHz. We find that, here, the TE_{11} mode likely dominates the transport.

In Figure C.3, we show the scaling of the external coupling as a function of the length of sub-cutoff waveguide. To avoid issues with coupler-fabrication repeatability, we investigate the dependence with a single semi-rigid loop coupler (2.5 mm x 1.3 mm) (see Fig. C.2). Then, the length of sub-cutoff waveguide was varied by the addition of No. 8 washers ($\approx$1 mm thick) and a No. 8 hex nut (2.5 mm thick). These spacers were inserted between the SMA panel mount jack and the endcap (see Fig. C.2). The best linear fit to the log of Q_{ext} gives a propagation constant of $|\beta|$=0.94 mm^{-1}), which is in agreement with the predicted value of ($|\beta|$=1.02 mm^{-1}). Again, the observed propagation constant is smaller than the single-mode approximation due to the participation of higher modes.

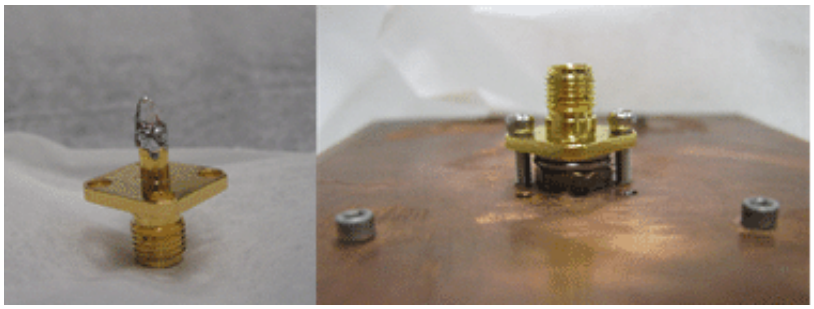

Figure C.2: Loop coupling scheme for cylindrical cavities. (Left) Soldered semi-rigid loop coupler attached to SMA panel mount jack. (Right) Coupling investigation set up - shown with two No.8 washers and a sanded No.8 hex nut.

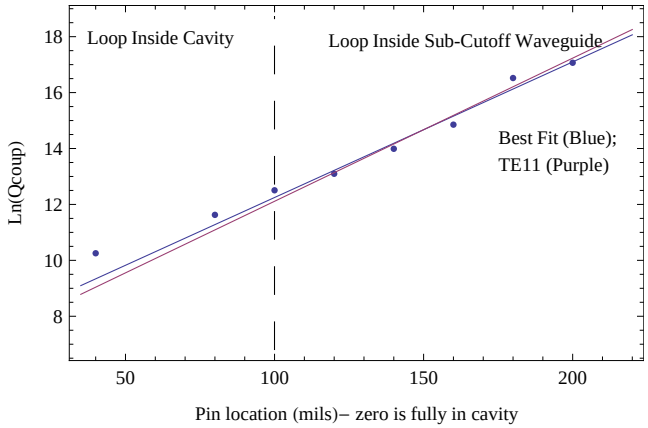

Figure C.3: Measured scaling of external coupling for cylindrical cavity. Measured values of Q_{ext} versus length of evanescent circular waveguide shown in thousandths of an inch (mils). On a log scale, the propagation constant of the dominant waveguide mode is given by the best linear fit (β=0.94 mm^{-1}).

APPENDIX D

Integrals and participation ratios for cylindrical cavities

In this appendix, we compute the sensitivity of the cylindrical geometry to various loss mechanisms. We consider a cavity with radius a and height d.

D.1 TM$_{nml}$ modes

The fields of the TM$_{nml}$ modes are

$$\begin{aligned}
E_\rho &= E_0 \frac{\beta}{k_c} \cos(n\phi) J_n'(k_c\rho) \sin\left(\frac{l\pi z}{d}\right) \\
E_\phi &= E_0 \frac{\beta n}{k_c^2 \rho} \sin(n\phi) J_n(k_c\rho) \sin\left(\frac{l\pi z}{d}\right) \\
E_z &= E_0 \cos(n\phi) J_n(k_c\rho) \cos\left(\frac{l\pi z}{d}\right) \\
H_\rho &= -E_0 \frac{j\omega\epsilon n}{k_c^2 \rho} \sin(n\phi) J_n(k_c\rho) \cos\left(\frac{l\pi z}{d}\right) \\
H_\phi &= -E_0 \frac{j\omega\epsilon}{k_c} \cos(n\phi) J_n'(k_c\rho) \cos\left(\frac{l\pi z}{d}\right) \\
H_z &= 0,
\end{aligned} \tag{D.1}$$

where $k = \omega\sqrt{\mu\epsilon}$ is the wave vector, and β is the propagation constant of the TM_{nm} mode given by

$$\begin{aligned}\beta &= \sqrt{k^2 - \left(\frac{p_{nm}}{a}\right)^2} \\ &= \sqrt{k^2 - k_c^2}.\end{aligned} \tag{D.2}$$

The resonance frequency of a TM_{nml} mode is

$$f_{nml} = \frac{c}{\sqrt{\mu_r\epsilon_r}}\sqrt{\left(\frac{l\pi}{d}\right)^2 + \left(\frac{p_{nm}}{a}\right)^2} \tag{D.3}$$

Conductor loss

To obtain the quality factor due to the conductor loss, we must calculate the stored electromagnetic energy W and the power loss P_c in the conducting walls on resonance. It is convenient to calculate W from the magnetic energy W_m for the TM mode since $W = 2W_m = 2W_e$ at resonance, as

$$W_m = \frac{\mu}{2}\int_0^a \rho d\rho \int_0^{2\pi} d\phi \int_0^d dz(|H_\rho|^2 + |H_\phi|^2) \tag{D.4}$$

and

$$\begin{aligned}|H_\rho|^2 &= E_0^2\left(\frac{\omega\epsilon n}{k_c^2\rho}\right)^2 \sin^2(n\phi)J_n^2(k_c\rho)\cos^2\left(\frac{l\pi z}{d}\right) \\ |H_\phi|^2 &= E_0^2\left(\frac{\omega\epsilon}{k_c}\right)^2 \cos^2(n\phi)J_n'^2(k_c\rho)\cos^2\left(\frac{l\pi z}{d}\right).\end{aligned} \tag{D.5}$$

We have that

$$\begin{aligned}\int_0^{2\pi}\sin^2(n\phi)d\phi &= \int_0^{2\pi}\frac{1}{2}\left(1-\cos(2n\phi)\right)d\phi = \pi(1-\delta_{0,n}) \\ \int_0^{2\pi}\cos^2(n\phi)d\phi &= \int_0^{2\pi}\frac{1}{2}\left(1+\cos(2n\phi)\right)d\phi = \pi(1+\delta_{0,n}) \\ \int_0^d \cos^2\left(\frac{l\pi z}{d}\right)dz &= \frac{d}{2}(1+\delta_{0,l}),\end{aligned} \tag{D.6}$$

where $\delta_{0,n}$ is the Dirac delta function. Then, Equation D.4 becomes

$$\begin{aligned} W_m &= \frac{\pi\mu d(1+\delta_{0,l})}{4}\left(\frac{E_0\omega\epsilon}{k_c}\right)^2 \int_0^a \rho d\rho \left[\left(\frac{n}{k_c\rho}\right)^2 J_n^2(k_c\rho) + J_n'^2(k_c\rho)\right] \\ &= \frac{\pi\mu d(1+\delta_{0,l})}{4}\left(\frac{E_0\omega\epsilon}{k_c}\right)^2 \int_0^{p_{nm}} \frac{x dx}{k_c^2} \left[\left(\frac{n}{x}\right)^2 J_n^2(x) + J_n'^2(x)\right] \\ &= \frac{\pi\mu d(1+\delta_{0,l})}{8}\left(\frac{E_0\omega\epsilon}{k_c^2}\right)^2 p_{nm}^2 J_n'^2(p_{nm}). \end{aligned} \tag{D.7}$$

The conductor loss on the cavity wall is given by

$$\begin{aligned} P_c &= \frac{R_s}{2}\left[\int_0^d dz \int_0^{2\pi} d\phi |H_\phi(\rho=a)|^2 + 2\int_0^a \rho d\rho \int_0^{2\pi} d\phi \left(|H_\rho(z=0)|^2 + |H_\phi(z=0)|^2\right)\right] \\ &= \frac{R_s}{2}\left(\frac{E_0\omega\epsilon}{k_c}\right)^2 J_n'^2(p_{nm})\left[\frac{ad\pi}{2}(1+\delta_{0,l}) + \pi a^2\right]. \end{aligned} \tag{D.8}$$

Therefore, the quality factor is

$$\begin{aligned} Q_m &= \frac{\omega\pi\mu d(1+\delta_{0,l})a^2}{4R_s((ad\pi/2)(1+\delta_{0,l}) + \pi a^2)} \\ &= \frac{\eta}{2R_s}\frac{\sqrt{p_{nm}^2 + (l\pi a/d)^2}}{(1+(a/d)(2-\delta_{0,l}))} \end{aligned} \tag{D.9}$$

Further, keeping track of the side wall ($|H_\phi(\rho=a)|^2$) and end cap ($|H_\rho(z=0)|^2 + |H_\phi(z=0)|^2$) contributions to P_c separately, we can distinguish between conductive losses in the two locations.

$$\begin{aligned} Q_{m,walls} &= \frac{\eta}{2R_s}\sqrt{p_{nm}^2 + (l\pi a/d)^2} \\ Q_{m,caps} &= \frac{\eta}{2R_s}\frac{\sqrt{p_{nm}^2 + (l\pi a/d)^2}}{(a/d)(2-\delta_{l,o})} \end{aligned} \tag{D.10}$$

We recognize the magnetic participation ratio from Chapter 4 in these expressions since

$$p_{mag} = \frac{1}{\omega\mu\lambda}\frac{R_s}{Q_m}. \tag{D.11}$$

Dielectric loss

It useful to rewrite the total energy calculated previously (Eq. D.7) as

$$\begin{aligned} W_{total} &= \frac{\pi\mu d}{8}\left(\frac{E_0\omega\epsilon_0}{k_c}\right)^2 p_{nm}^2 J_n'^2(p_{nm})(1+\delta_{n,0}) \\ &= \frac{\pi d}{8}\epsilon_0\left[\left(\frac{p_{nm}}{a}\right)^2+\left(\frac{l\pi}{d}\right)^2\right]E_0^2\frac{a^4}{p_{nm}^2}J_n'^2(p_{nm})(1+\delta_{n,0}). \end{aligned} \tag{D.12}$$

To proceed with calculating the dielectric participation ratios, we must consider the cavity side walls and caps separately. On the side walls, E_ρ is the only non-vanishing field component, leaving for a dielectric film of thickness t and relative dielectric constant ϵ_r,

$$\begin{aligned} W_{walls} &= \frac{t}{2\epsilon_r}\left(\frac{E_0 al\pi}{(p_{nm})d}\right)^2\int_0^d\int_0^{2\pi}\left[J_n'^2(p_{nm})\cos^2(n\phi)\sin^2(\frac{l\pi z}{d})\right]ad\phi dz \\ &= \frac{E_0^2a^3t\pi^3l^2}{4\epsilon_r p_{nm}^2 d}J_n'^2(p_{nm})(1+\delta_{n,0}). \end{aligned} \tag{D.13}$$

Taking the ratio between W_{walls} and W_{total} we find for TM modes

$$p_{walls} = \frac{t}{\epsilon_r a}\left(\frac{2\pi^2l^2}{p_{nm}^2\left(\frac{d}{a}\right)^2+(l\pi)^2}\right). \tag{D.14}$$

The numerical term in the parenthesis is of order unity for our aspect ratio.

Finally, we turn our attention to the end caps of TM modes. Here, E_ρ and E_ϕ will go to zero, leaving E_z as the only contributor.

$$W_{caps} = \frac{\epsilon_{caps}2t}{2}E_0^2\int_0^a\int_0^{2\pi}\left[J_n^2(\frac{p_{nm}\rho}{a})\cos^2(n\phi)\right]\rho d\rho d\phi. \tag{D.15}$$

Using the Bessel identity

$$\int_0^{p_{nm}} J_n^2(x)xdx = \frac{p_{nm}^2}{2}J_{n+1}^2(p_{nm}), \tag{D.16}$$

we have that

$$W_{caps} = \frac{E_0^2a^2t}{\epsilon_r 2}J_{n+1}^2(p_{nm})\pi(1+\delta_{n,0}), \tag{D.17}$$

which gives us the end caps participation ratio for TM modes

$$p_{caps} = \frac{t}{\epsilon_r d}\left(\frac{4p_{nm}^2 J_{n+1}^2(p_{nm})}{J_{nm}'^2(p_{nm})\left(p_{nm}^2 + (l\pi)^2\left(\frac{a}{d}\right)^2\right)}\right), \tag{D.18}$$

Again, the term in the parenthesis is of order unity for our aspect ratio. Intuitively, the TM mode's p_{caps} depends on the ratio of cavity height to surface thickness, rather than the ratio of thickness to radius like in the side wall calculation.

Seam loss

We assemble the cylindrical geometry as a tube with end caps. We are therefore sensitive to currents flowing in the $\hat{z}$ direction across the resuling seam. For TM modes,

$$|H_\phi(z_0)|^2 = \left(E_0\frac{\omega\epsilon}{k_c}\cos(n\phi)J_n'(k_c\rho)\right)^2\cos^2\left(\frac{l\pi z_0}{d}\right) \tag{D.19}$$

where $k_c = p_{nm}/a$. The power dissipated is

$$\begin{aligned} P_\varnothing &= \frac{1}{2g_\varnothing}\left(\frac{\omega\epsilon a E_0 J_n'(p_{nm})}{p_{nm}}\right)^2\left(\cos\frac{\ell\pi z_0}{d}\right)^2\int_0^{2\pi}\cos^2 n\phi a d\phi \\ &= \frac{1}{2g_\varnothing}\left(\frac{\omega\epsilon a E_0 J_n'(p_{nm})}{p_{nm}}\right)^2\left(\cos\frac{\ell\pi z_0}{d}\right)^2 a\pi(1+\delta_{n,0}), \end{aligned} \tag{D.20}$$

and the quality factor due to this dissipation is

$$\begin{aligned} Q_\varnothing &= \frac{\frac{\pi d\epsilon}{8}\left[\left(\frac{p_{nm}}{a}\right)^2 + \left(\frac{\ell\pi}{d}\right)^2\right]E_0^2\frac{a^4}{p_{nm}^2}J_n'^2(p_{nm})}{\frac{1}{2g_\varnothing}\left(\frac{\omega\epsilon a E_0 J_n'(p_{nm})}{p_{nm}}\right)^2\cos^2\left(\frac{\ell\pi z_0}{d}\right)a\pi} \\ &= \frac{\eta a g_\varnothing\left[\left(\frac{p_{nm}d}{a}\right)^2 + (\ell\pi)^2\right]^{1/2}}{4\cos^2\left(\frac{\ell\pi z_0}{d}\right)} \end{aligned} \tag{D.21}$$

which gives us the total admittance for the seam as

$$y_\varnothing = g_\varnothing/Q_\varnothing. \tag{D.22}$$

D.2 TE_{nml} modes

The fields of the TE_{nml} modes are

$$\begin{aligned}
E_\rho &= \frac{jk\eta a^2 nH_0}{p'^2_{nm}\rho}\sin(n\phi)J_n\left(\frac{p'_{nm}\rho}{a}\right)\sin\left(\frac{l\pi z}{d}\right)\\
E_\phi &= \frac{jk\eta a^2 H_0}{p'^2_{nm}\rho}\cos(n\phi)J'_n\left(\frac{p'_{nm}\rho}{a}\right)\sin\left(\frac{l\pi z}{d}\right)\\
E_z &= 0\\
H_\rho &= \frac{\beta a H_0}{p'_{nm}}\cos(n\phi)J'_n\left(\frac{p'_{nm}\rho}{a}\right)\cos\left(\frac{l\pi z}{d}\right)\\
H_\phi &= \frac{-\beta a^2 nH_0}{p'^2_{nm}\rho}\sin(n\phi)J_n\left(\frac{p'_{nm}\rho}{a}\right)\cos\left(\frac{l\pi z}{d}\right)\\
H_z &= H_0\cos(n\phi)J_n\left(\frac{p'_{nm}\rho}{a}\right)\sin\left(\frac{l\pi z}{d}\right)
\end{aligned} \tag{D.23}$$

Conductor loss

From similar calculations to the previous section (also see [111, op. cit. Eq. 6.56]), we have

$$Q_m = \frac{\eta\left[1-\left(\frac{n}{p'_{nm}}\right)^2\right]\left[(p'_{nm})^2+\left(\frac{l\pi a}{d}\right)^2\right]^{3/2}}{2R_s\left[(p'_{nm})^2+\frac{2a}{d}\left(\frac{l\pi a}{d}\right)^2+\left(1-\frac{2a}{d}\right)\left(\frac{nl\pi a}{p'_{nm}d}\right)^2\right]}. \tag{D.24}$$

We can further separate the contributions from the walls and end caps for these modes.

$$\begin{aligned}
Q_{m,walls} &= \frac{\eta\left[1-\left(\frac{n}{p'_{nm}}\right)^2\right]\left[(p'_{nm})^2+\left(\frac{l\pi a}{d}\right)^2\right]^{3/2}}{2R_s\left[(p'_{nm})^2+\left(\frac{nl\pi a}{p'_{nm}d}\right)^2\right]}\\
Q_{m,caps} &= \frac{\eta\left[1-\left(\frac{n}{p'_{nm}}\right)^2\right]\left[(p'_{nm})^2+\left(\frac{l\pi a}{d}\right)^2\right]^{3/2}}{2R_s\left[\frac{2a}{d}\left(\frac{l\pi a}{d}\right)^2-\left(\frac{2a}{d}\right)\left(\frac{nl\pi a}{p'_{nm}d}\right)^2\right]}
\end{aligned} \tag{D.25}$$

Dielectric loss

For the case of the TE_{nml} end caps, we see that both E_ρ and E_ϕ go to zero at (z=0) and (z=d) due to the $\sin(\frac{l\pi z}{d})$ term. Thus, the TE modes have zero participation of end cap

dielectric. Therefore, calculating the dielectric participation ratio reduces to solving for the fields on the walls. Following similar calculations to the previous section, we have

$$p_{diel} = \frac{t}{\epsilon_r a}\left(\frac{n^2}{(p'_{nm})^2 - n^2}\right)(1-\delta_{n,0}). \tag{D.26}$$

Note that the Dirac delta function nulls this expression exactly for $n = 0$, as for the TE_{011} mode.

Seam loss

For TE modes, the relevant surface current is

$$|J_z(z_0)|^2 = \left(\frac{\ell\pi a n H_0 J_n(p'_{nm})}{d(p'_{nm})^2}\right)^2 \left(\cos\frac{\ell\pi z_0}{d}\right)^2 \sin^2 n\phi \tag{D.27}$$

and the dissipated power is

$$\begin{aligned} P_{\varnothing} &= \frac{1}{2g_{\varnothing}}\left(\frac{\ell\pi a n H_0 J_n(p'_{nm})}{d(p'_{nm})^2}\right)^2 \left(\cos\frac{\ell\pi z_0}{d}\right)^2 \int_0^{2\pi} \sin^2 n\phi a d\phi \\ &= \frac{1}{2g_{\varnothing}}\left(\frac{\ell\pi a n H_0 J_n(p'_{nm})}{d(p'_{nm})^2}\right)^2 \left(\cos\frac{\ell\pi z_0}{d}\right)^2 a\pi(1-\delta_{n,0}). \end{aligned} \tag{D.28}$$

The quality factor due to the loss from the contact resistance at the seam is then

$$\begin{aligned} Q_{\varnothing} &= \omega \frac{\frac{\epsilon k^2 \eta^2 a^4 H_0^2 \pi d}{8(p'_{nm})^2}\left[1-(n/p'_{nm})^2\right] J_n^2(p'_{nm})}{\frac{1}{2g_{\varnothing}}\left(\frac{\ell\pi a n H_0 J_n(p'_{nm})}{d(p'_{nm})^2}\right)^2 \left(\cos\frac{\ell\pi z_0}{d}\right)^2 a\pi} \\ &= \frac{\eta a g_{\varnothing}\left[(p'_{nm})^2 - n^2\right]\left[(p'_{nm}d/a)^2 - (\ell\pi)^2\right]^{3/2}}{4\ell^2\pi^2 n^2 \cos^2\left(\frac{\ell\pi z_0}{d}\right)}. \end{aligned} \tag{D.29}$$

From which we recover $y_{\varnothing}$ for TE modes.

APPENDIX E

BCS Calculations

In this appendix, we include calculations by Gianluigi Catelani for evaluating the surface impedance of a BCS superconductor. Mathematica is used to numerically evaluate the integrals in Chapter 5.

```
(* BCS Gap *)
dt = {{0.05,1.},{0.35,0.992},{0.4,0.985},{0.5,0.957},
{0.55,0.935},{0.575,0.921},{0.6,0.906},{0.625,0.890},
{0.65,0.871},{0.675,0.851},{0.7,0.828},{0.725,0.803},
{0.75,0.775},{0.775,0.745},{0.8,0.711},{0.825,0.673},
{0.85,0.630},{0.875,0.581},{0.9,0.526},{0.925,0.460},
{0.95,0.380},{0.975,0.272063},{1., 0.}};
dtf = Interpolation[dt,InterpolationOrder
  -> 5, Method -> "Spline"];

(* BCS Conductivity Integrals *)
st1[o_, t_] :=
  NIntegrate[(x (x + o) + 1)/Sqrt[x^2 - 1]/
     Sqrt[(x + o)^2 - 1] (Tanh[(x + o)/(2 tc t)] -
     Tanh[x/(2 tc t)]), {x, 1, Infinity},
     WorkingPrecision -> 18]/ Pi + If[o < 2, 0,
  NIntegrate[(x (x + o) + 1)/Sqrt[x^2 - 1]/
     Sqrt[(x + o)^2 - 1]*Tanh[x/(2 tc t)],
     {x, 1 - o, -1}, WorkingPrecision -> 18,
     MaxRecursion -> 13]/Pi];

st2[o_, t_] :=
  NIntegrate[(x (x + o) + 1)/Sqrt[1 - x^2]/
     Sqrt[(x + o)^2 - 1] Tanh[(x + o)/(2 tc t)],
     {x, Max[{-1, 1 - o}],1}]/Pi;

(* BCS Surface Impedance *)
xsf[o1_, t1_, n_] :=
  Im[-Exp[-I Pi/2 (1 - n)]
     ((st1f[t1/dtf[t1], o1/dtf[t1]] -
     I st2f[t1/dtf[t1], o1/dtf[t1]]) Pi*dtf[t1]/o1)^n]

rsf[o1_, t1_, n_] :=
  Re[-Exp[-I Pi/2 (1 - n)]
     ((st1f[t1/dtf[t1], o1/dtf[t1]] -
     I st2f[t1/dtf[t1], o1/dtf[t1]]) Pi*dtf[t1]/o1)^n]
```

Figure E.1: Mathematica code for evaluating the BCS surface impedance. The temperature dependence of the BCS gap (Eq. 5.28) is given as a table for convenience. This table is interpolated for fitting purposes. We numerically evaluate the expressions BCS conductivities (Eq. 5.27) to calculate the surface impedance (Eq. 5.20).

Copyright Permissions

- Figure 2.7 is reproduced or adapted with permission from:
  Reed et al., Nature 482, 382 (2012) [45].
- Figure 4.5 is reproduced or adapted with permission from:
  Majer et al., Nature 449, 7161 (2007) [58].
- Figure 4.6 is reproduced or adapted with permission from:
  Wang et al., Nature Communications 5, 55836 (2015) [120].
- Figure 4.9 is reproduced or adapted with permission from:
  Reagor et al., Applied Physics Letters 102, 19 (2013) [100].
- Figure 4.11 is reproduced or adapted with permission from:
  Reagor et al., ArXiv e-prints, arXiv1508.05882 (2015) [100].
- Figure 7.1 is reproduced or adapted with permission from:
  Devoret and Schoelkopf, Science 339, 1169 (2013) [100].